

Università degli Studi di Trieste  
Dipartimento di Astronomia  
Dottorato di Ricerca in Fisica - Ciclo XXII



TESI DI DOTTORATO

# Chemical and Physical Evolution of the Intergalactic Medium

Dottorando: Edoardo Tescari

a.a. 2008/2009

Relatore: Dr. Matteo Viel  
Supervisore: Prof. Stefano Borgani



*ai miei genitori (e un po' anche a mio fratello)*



We shall go on to the end, we shall fight in France, we shall fight on the seas and oceans, we shall fight with growing confidence and growing strength in the air, we shall defend our Island, whatever the cost may be, we shall fight on the beaches, we shall fight on the landing grounds, we shall fight in the fields and in the streets, we shall fight in the hills; we shall never surrender...

Winston Churchill – June 4, 1940



# Contents

<b>Contents</b>	<b>7</b>
<b>Introduction</b>	<b>9</b>
<b>1 The Intergalactic Medium</b>	<b>13</b>
1.1 The Gunn-Peterson test . . . . .	13
1.2 Lyman- $\alpha$ absorption line systems . . . . .	15
1.3 Absorption line properties . . . . .	17
1.3.1 High resolution spectroscopy: Voigt profile decomposition . . . . .	17
1.3.2 The column density distribution . . . . .	18
1.3.3 The Doppler parameter distribution . . . . .	19
1.3.4 Evolution in the number density of the Lyman- $\alpha$ forest . . . . .	21
1.4 Statistics of the transmitted flux . . . . .	23
1.5 Damped Lyman- $\alpha$ systems . . . . .	26
1.6 Metal absorption systems . . . . .	28
1.7 Early models of the IGM . . . . .	31
1.7.1 The semianalytical model of Bi & Davidsen (1997) . . . . .	34
1.8 Physical insights into the nature of the Lyman- $\alpha$ forest . . . . .	37
1.8.1 Physical properties . . . . .	38
<b>2 Numerical Cosmology</b>	<b>41</b>
2.1 Methods of numerical simulations . . . . .	41
2.2 Gravitational force description: N-body simulations . . . . .	41
2.3 Gravity + gas physics: GADGET-2 . . . . .	43
2.3.1 Collisionless dynamics . . . . .	45
2.3.2 Hydrodynamics . . . . .	46
2.4 Additional physics . . . . .	49
2.4.1 Radiative processes . . . . .	49
2.4.2 The star formation model . . . . .	52
2.4.3 The chemical evolution model . . . . .	55
2.4.4 Feedback schemes . . . . .	59
2.4.5 Gas distribution . . . . .	63

<b>3</b>	<b>DLAs in high-resolution hydrodynamical simulations</b>	<b>67</b>
3.1	The simulations . . . . .	68
3.2	Global properties of the simulations . . . . .	70
3.2.1	IGM temperature and metallicity relations at $z = 3$ . . . . .	70
3.2.2	Star formation rates and evolution of ion species . . . . .	74
3.3	The neutral hydrogen distribution . . . . .	78
3.3.1	Identifying haloes . . . . .	78
3.3.2	Properties of the haloes . . . . .	81
3.3.3	The DLA cross-section . . . . .	83
3.3.4	The incidence rate of DLA systems . . . . .	85
3.3.5	The column density distribution function . . . . .	87
3.4	Simulated QSO spectra . . . . .	91
3.4.1	Velocity width distribution . . . . .	93
3.4.2	Correlation between Metallicity and Velocity Widths . . . . .	96
3.5	Main results . . . . .	98
<b>4</b>	<b>Cosmic evolution of the CIV</b>	<b>101</b>
4.1	Observational data sample . . . . .	102
4.2	The simulations . . . . .	105
4.3	Statistics of HI . . . . .	107
4.3.1	The HI column density distribution function . . . . .	107
4.3.2	Probability distribution function of the HI Doppler parameter . . . . .	109
4.3.3	Column density-Doppler parameter relation . . . . .	109
4.4	The CIV column density distribution function . . . . .	113
4.5	The evolution of the CIV cosmological mass density . . . . .	116
4.6	Probability distribution function of the CIV Doppler parameter . . . . .	120
4.7	The CIV column density-Doppler parameter relation . . . . .	121
4.8	Final Remarks . . . . .	126
<b>5</b>	<b>Conclusions</b>	<b>129</b>
<b>A</b>	<b>First Principles</b>	<b>135</b>
A.1	Standard Model . . . . .	135
A.2	The Cosmological Constant . . . . .	136
A.3	Dark Matter . . . . .	138
A.4	Structure formation and evolution . . . . .	139
A.5	$\Lambda$ CDM model . . . . .	141
	<b>List of Figures</b>	<b>143</b>
	<b>Bibliography</b>	<b>149</b>

# Introduction

The aim of this thesis work is to explore different aspects related to the properties of the Intergalactic Medium (IGM): the all-pervading cosmic gas that fills the spaces between the galaxies. We focussed on the IGM chemical and physical evolution from high to low redshift, considering in particular the metal enrichment mechanism and the impact that different galactic feedback processes have on the IGM properties.

Our present understanding of the evolution of the Universe is based on the Standard Hot Big Bang Model (see Appendix A). The expansion of the Universe, the synthesis of the light elements and the Cosmic Microwave Background (CMB) radiation are the pillars of this model. Its observational confirmation was the CMB accidental detection in 1965 by Penzias & Wilson. In the 1990s the COBE (COsmic Background Explorer) satellite improved on the previous observation and measured an almost isotropic blackbody radiation with temperature  $T_{\text{CMB}} = 2.726 \pm 0.010$  K (Mather et al. 1994), together with temperature anisotropies on angular scales  $\approx 90^\circ$  (Smoot et al. 1992). The isotropy of the microwave background indicates that on large scales ( $\geq 200$  Mpc) the Universe is indeed very smooth, as postulated by the “cosmological principle” (i.e. the assertion that, on sufficiently large scales, beyond those traced by the large-scale structure of the distribution of galaxies, the Universe is both homogeneous and isotropic). On small scales, in contrast, it presents inhomogeneities, from planets and stars, to galaxy clusters and super-clusters of galaxies. These structures are not uniformly distributed, but show some spatial correlation, and regions of space almost totally devoid of galaxies are alternated to high density regions. The commonly adopted theory for the formation of these structures is the gravitational instability scenario, in which primordial density perturbations grow through gravitational Jeans instability to form all the structures we observe today (Appendix A.4).

Once the gas has virialized in the potential wells of pre-existing dark matter haloes, it collapses and cools. At this point star formation (SF) is ignited. After the first sources have formed, their mass deposition, energy injection and emitted radiation can deeply affect the subsequent galaxy formation process and influence the evolution of the intergalactic medium via a number of so-called “feedback” effects. Although a rigorous classification of the various effects is not feasible, they can be divided into three broad classes: radiative, mechanical and chemical feedback. Into the first class fall all those effects associated, in particular, with ionization/dissociation of hydrogen atoms/molecules. The second class is produced by the mechanical energy injection of massive stars in form of winds or supernova (SN) explosions. Finally, the chemical feedback is related to the metal ejection efficiency, transport and mixing in the intergalactic medium.

In the last years, high resolution spectroscopic observations have shown that the neutral hydrogen (HI) in the IGM at redshift around three, traced by the Lyman- $\alpha$  forest lines in

absorption, is subjected to metal pollution down to very low column density ( $10^{13}$  atoms  $\text{cm}^{-2}$ ) with a metallicity of about  $10^{-3}$  in solar units. Since metals are produced only by stars inside galaxies, the diffuse metals in the IGM retain an important trace of the star formation and of the feedback processes from the galaxies to the IGM.

The purpose of the thesis is to identify, using high-resolution and large box-size hydrodynamical simulations, the mechanisms responsible of the enrichment, propose some physically motivated theoretical models and compare the prediction of the models with the latest observational data. In particular we focussed on two different type of enrichment: galactic (energy and momentum driven) winds produced by “starburst” galaxies at redshift  $z = 1.5 - 4$  and Active Galactic Nuclei (AGN) feedback associated to the energy released by gas accretion onto super-massive black holes. We analysed in detail the following aspects: dynamic and energetic of wind and AGN feedbacks, IGM contamination efficiency as a function of different astrophysical and cosmological parameters, temperature and chemical composition of the metal systems, nature of the ultraviolet ionizing background. Part of the thesis is dedicated to Damped Lyman- $\alpha$  systems (DLAs), historically defined as quasar absorption systems with neutral hydrogen column density  $N_{\text{HI}} > 2 \times 10^{20}$  atoms  $\text{cm}^{-2}$  (Wolfe et al. 1986). DLAs are one of the best probe of structure formation in the early Universe and are closely linked to the formation of galaxies and stars at high redshift. Finally, we studied the cosmic evolution of the CIV (triply ionized carbon), which is considered the best tracer of the IGM metallicity. Most studies of the high redshift IGM have focussed on CIV absorption, because it is strong and lies redward of the Lyman- $\alpha$  forest. Moreover the absorption line is actually a doublet with rest frame wavelengths 1548.204 Å and 1550.781 Å, so its identification in the observational spectra is easier because of the fixed ratio between the wavelengths of the two components.

The plan of the thesis can be summarized as follows:

- **Chapter 1:** in this Chapter we introduce the intergalactic medium characteristics. We start describing some observational features of the IGM like the Gunn-Peterson test, the different Lyman- $\alpha$  absorption line systems and their properties. Then we move on the statistics of the HI transmitted flux and we focus on the Damped Lyman- $\alpha$  systems and the metal absorption systems. We conclude this Chapter by discussing the early models of the IGM, especially the semianalytical model of Bi & Davidsen (1997), and some physical insights on the nature of the Lyman- $\alpha$  forest given by Schaye (2001). These latter models describe in a very simple way the properties of the intergalactic medium and are very useful for the comparison and calibration the hydrodynamical simulations predictions.
- **Chapter 2:** we describe the numerical background of the entire work: the cosmological hydrodynamical simulations. At first, we briefly review the current techniques for describing the gravitational force using different N-body simulations methods. Then we present GADGET-2: a massively parallel TreePM-SPH (Tree Particle Mesh-Smoothed Particle Hydrodynamics) code, capable of following a collisionless fluid with the N-body method, and an ideal gas by means of smoothed particle hydrodynamics. In the last part of the Chapter we focus on the additional physics implemented in GADGET-2 by our group: in fact, our version of the code contains a self consistent implementation of the metal enrichment mechanism (Tornatore et al. 2007) and some new feedback schemes (one of

them, the so called momentum-driven winds feedback, developed as a part of the Ph.D. project).

- **Chapter 3:** in this Chapter we report the results of our work about the Damped Lyman- $\alpha$  systems and the chemical enrichment of the intergalactic medium at high redshift. We use the self consistent chemo-dynamical code introduced in Chapter 2 with the aim of matching some observed properties of the metal and neutral hydrogen distribution. After having addressed some global properties and evolution of IGM low-ionization species, we focus on DLAs because their statistical properties are well measured over a wide redshift range by Sloan Digital Sky Survey and high resolution data and they could provide a useful benchmark for the physics implemented in our simulations. By interpolating physical quantities along line-of-sights through massive haloes we check how different galactic wind models impact on the IGM around DLAs. Furthermore, we analyse statistics related to the velocity widths of SiII associated to DLAs. The results of this work are published in the paper: *Damped Lyman- $\alpha$  systems in high-resolution hydrodynamical simulations*, E. Tescari, M. Viel, L. Tornatore & S. Borgani, 2009, MNRAS, 397, 411.
- **Chapter 4:** we present our work on the cosmic evolution of the CIV. The cosmological mass density of CIV,  $\Omega_{\text{CIV}}$ , observed as a function of redshift is a fundamental quantity closely related to the metal enrichment of the IGM. Our work is the theoretical counterpart of the observational analysis performed by D’Odorico et al. (2009) using high resolution data. We firstly introduce the observational data sample and the cosmological simulations used, then we reproduce some HI statistics and finally move to the CIV. In particular, we study the redshift variation of: the CIV column density distribution function, the cosmological mass density, the CIV Doppler parameter ( $b_{\text{CIV}}$ ) probability distribution function and the  $b_{\text{CIV}} - N_{\text{CIV}}$  relation. A paper containing the results of this work will be soon submitted to MNRAS (Tescari et al. 2010, in preparation).
- **Chapter 5:** in this Chapter we summarize our main results and draw some conclusions.
- **Appendix A:** we briefly resume some basic principles of cosmology on which our work is based. We introduce the standard model, the cosmological constant and the dark matter. We also present the hierarchical scenario for structure formation and evolution and our reference cosmological model: the  $\Lambda$ CDM model.



# Chapter 1

## The Intergalactic Medium

About half a million years after the Big Bang, the cosmic blackbody radiation cooled below 3000 K and shifted first into the infrared and then into the radio, and the smooth baryonic plasma that filled the Universe became neutral. The Universe then entered a “dark age” which persisted until the first cosmic structures collapsed into gravitationally-bound systems, and evolved into stars, galaxies, and galaxy clusters that lit up the Universe again. Some time between redshift of 7 and 15, stars within protogalaxies created the first heavy elements; these systems, together perhaps with an early population of quasars (QSOs), generated the ultraviolet radiation that reheated and reionized the cosmos. The history of the Universe during and soon after these crucial formative stages is recorded in the Intergalactic Medium, which is believed to contain most of the ordinary baryonic material left over from the Big Bang. Throughout the epoch of structure formation, the IGM becomes clumpy and acquires peculiar motions under the influence of gravity, and acts as a source for the gas that gets accreted, cools, and forms stars within galaxies, and as a sink for the metal enriched material, energy, and radiation which they eject. Observations of absorption lines in quasar spectra at high redshifts provide insights into the chemical composition of the IGM and primordial density fluctuations spectrum of some of the earliest formed cosmological structures, as well as of the ultraviolet background radiation that ionizes them. Absorption or scattering of light during its journey to us can, in principle, be detected by its effect upon the spectrum of the quasar. This, in turn, can be used to constrain the number and properties of absorbers, which, whatever they are, must be associated with the baryonic content of the intergalactic medium. To summarize, the IGM is the ordinary matter between galaxies and its physical and chemical state is closely interconnected to that of the galaxies over a large fraction of the cosmic time.

The goal of this Chapter is to describe the main observational aspects and the underlying physics of the IGM, both considering neutral hydrogen and metals.

### 1.1 The Gunn-Peterson test

Neutral hydrogen has a resonant scattering feature associated with the Lyman- $\alpha$  atomic transition. This resonance is so strong that it is possible for a relatively low neutral-hydrogen column density (i.e number density per unit area of atoms, integrated along the line of sight) to cause a significant apparent absorption at the appropriate wavelength for the transition. Let

us suppose that light travels towards us through a uniform background of neutral hydrogen. The optical depth for scattering is

$$\tau(\lambda_0) = \frac{c}{H_0} \int \sigma(\lambda_0 a/a_0) n_{\text{HI}}(t) \Omega_{\text{0m}}^{-1/2} \left(\frac{a_0}{a}\right)^{-3/2} \frac{da}{a}, \quad (1.1)$$

where  $\sigma(\lambda)$  is the cross-section at resonance and  $n_{\text{HI}}$  is the proper density of neutral hydrogen atoms at the redshift corresponding to this resonance (the usual convention is that HI refers to neutral and HII to ionized hydrogen). We have assumed in Eq. (1.1) that the Universe is matter dominated. The integral is taken over the width of the resonance line (which is very narrow and can therefore be approximated by a delta function) and yields a result for  $\tau$  at some observed wavelength  $\lambda_0$ . It therefore follows that

$$\tau = \frac{3\Lambda\lambda_\alpha^3 n_{\text{HI}}}{8\pi H_0 \Omega_{\text{0m}}^{1/2}} (1+z)^{-3/2}, \quad (1.2)$$

where  $\Lambda = 6.25 \times 10^8 \text{ s}^{-1}$  is the rate of spontaneous decays from the 2p to 1s level of hydrogen (the Lyman- $\alpha$  emission transition) and  $\lambda_\alpha$  is the wavelength corresponding to this transition, i.e. 1215.67 Å. Equation (1.2) can be inverted to yield

$$n_{\text{HI}} = 2.4 \times 10^{-11} \Omega_{\text{0m}}^{1/2} h (1+z)^{3/2} \tau \text{ cm}^{-3}. \quad (1.3)$$

This corresponds to the optical depth  $\tau$  at  $z = (\lambda_0/\lambda_\alpha) - 1$ , when observed at a wavelength  $\lambda_0$ .

The Gunn-Peterson test (Gunn & Peterson 1965) shows that there is no apparent drop between the long-wavelength side of the Lyman- $\alpha$  emission line in quasar spectra and the short-wavelength side, where extinction by scattering might be expected. Observations suggest a (conservative) upper limit on  $\tau$  of order 0.1, which translates into a very tight bound on  $n_{\text{HI}}$ :

$$n_{\text{HI}} < 2 \times 10^{-12} \Omega_{\text{0m}}^{1/2} h (1+z)^{3/2} \tau \text{ cm}^{-3}. \quad (1.4)$$

The mean number density of baryons as a function of redshift reads:

$$n_{\text{b}} \simeq 1.1 \times 10^{-5} \Omega_{\text{0b}} h^2 (1+z)^3 \text{ cm}^{-3}. \quad (1.5)$$

Comparing Eq. (1.4) with Eq. (1.5) with  $\Omega_{\text{0b}} = 1$ , yields a constraint on the contribution to the critical density due to neutral hydrogen:

$$\Omega(n_{\text{HI}}) < 2 \times 10^{-7} \Omega_{\text{0m}}^{1/2} h^{-1} (1+z)^{-3/2}. \quad (1.6)$$

There is no alternative but to assume that, by the epoch one can probe directly with quasar spectra (which corresponds to  $z \simeq 4$ ), the density of any uniform neutral component of the IGM was very small indeed.

One can translate this result for the neutral hydrogen into a constraint on the plasma density at high temperatures by considering the balance between collisional ionization reactions



and recombination reactions of the form



The physics of this balance is complicated by the fact that the cross-sections for these reactions are functions of temperature. It turns out that the ratio of neutral to ionized hydrogen,  $n_{\text{HI}}/n_{\text{HII}}$ , has a minimum at a temperature around  $10^6$  K, and at this temperature the equilibrium ratio is

$$\frac{n_{\text{HI}}}{n_{\text{HII}}} \simeq 5 \times 10^{-7}. \quad (1.9)$$

Since this is the minimum possible value, the upper limit on  $n_{\text{HI}}$  therefore gives an upper limit on the total density in the IGM, which we can assume to be made entirely of hydrogen:

$$\Omega_{\text{IGM}} < 0.4\Omega_{\text{0m}}^{1/2}h^{-1}(1+z)^{-3/2}. \quad (1.10)$$

If the temperature is much lower than  $10^6$  K, the dominant mechanism for ionization could be electromagnetic radiation. In this case one must consider the equilibrium between radiative ionization and recombination, which is more complex and requires some assumptions about the ionizing flux. There are probably enough high-energy photons from quasars at around  $z \simeq 3$  to ionize most of the baryons if the value of  $\Omega_{\text{b}}$  is not near unity, and there is also the possibility that early star formation in protogalaxies could contribute substantially. Another complication is that the spatial distribution of the IGM might be clumpy, which alters the average rate of recombination reactions but not the mean rate of ionizations. One can show that, for temperatures around  $10^4$  K, the constraint becomes

$$\Omega_{\text{IGM}} < 0.4I_{21}\Omega_{\text{0m}}^{1/2}h^{-3/2}(1+z)^{9/4}, \quad (1.11)$$

if the medium is not clumpy and the ionizing flux,  $I_{21}$ , is measured in units of  $10^{-21}$  erg cm $^{-2}$  s $^{-1}$  Hz $^{-1}$  ster $^{-1}$ .

These results suggest that the total IGM density cannot have been more than  $\Omega_{\text{IGM}} \simeq 0.03$  at  $z \simeq 3$ , whatever the temperature of plasma. This limit is compatible with the cosmological nucleosynthesis value for  $\Omega_{\text{b}}$ .

## 1.2 Lyman- $\alpha$ absorption line systems

Almost immediately after Gunn & Peterson published their results in 1965, it was recognized that individual Lyman- $\alpha$  absorption features should appear from neutral hydrogen concentrated into cosmological structures (Bahcall & Salpeter 1965; Wagoner 1967). Although quasar spectra do not exhibit any general absorption consistent with a smoothly distributed hydrogen component, there are many absorption lines in such spectra which are interpreted as being due to clouds intervening between the quasar and the observer and absorbing at the Lyman- $\alpha$  resonance.

The clouds are grouped into four categories depending on their column density, which can be obtained from the strength of the absorption line. The strongest absorbers have column densities  $N_{\text{HI}} = 2 \times 10^{20}$  atoms cm $^{-2}$  or more, which are comparable with the column densities of

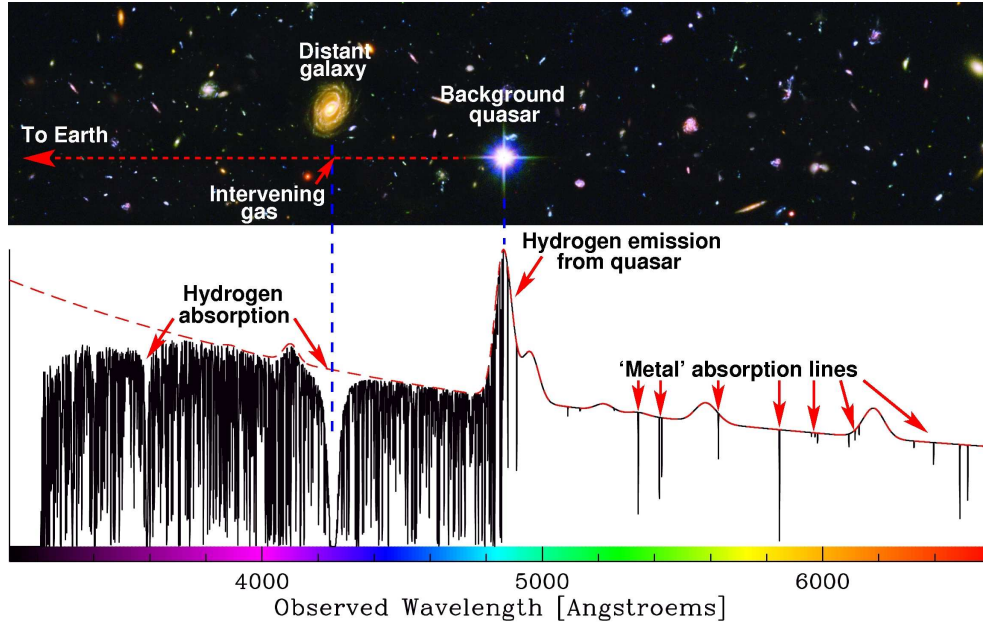


Figure 1.1: Illustrative example of high redshift QSO spectrum with both hydrogen (blueward, i.e. at lower redshifts, of the Lyman- $\alpha$  emission of the quasar) and metal (redward of the Lyman- $\alpha$  emission) absorption lines.

interstellar gas in a present-day spiral galaxy. This is enough to produce a very wide absorption trough at the Lyman- $\alpha$  wavelength and these systems are usually called *Damped Lyman- $\alpha$  systems* or *Damped Lyman- $\alpha$  Absorbers* (DLAs). These are relatively rare, and are usually interpreted as being the progenitors of spiral discs, even if up to date there are different models proposed to explain their nature (see Section 1.5 for more details). In the category of *sub-DLAs* fall those systems with  $10^{19} < N_{\text{HI}} < 2 \times 10^{20}$  atoms  $\text{cm}^{-2}$ . There is an important physical distinction between DLAs and sub-DLAs: the hydrogen in the DLAs is essentially neutral, while the sub-DLAs are sufficiently penetrated by the UV metagalactic background as to be partially ionized.

A more abundant type of objects are the *Lyman limit systems*. These have  $10^{17} < N_{\text{HI}} < 10^{19}$  atoms  $\text{cm}^{-2}$  and are dense enough to block radiation at wavelengths near the photoionization edge of the Lyman series of lines. Smaller features, with  $N_{\text{HI}} \lesssim 10^{17}$  atoms  $\text{cm}^{-2}$  appear as sharp absorption lines at the Lyman- $\alpha$  wavelength<sup>1</sup>. These are very common, and reveal themselves as a “forest” of lines in the spectra of quasars, hence the term *Lyman- $\alpha$  forest*. The importance of the Lyman limit is that, at this column density, the material at the centre of the cloud will be shielded from ionizing radiation by the material at its edge. At lower densities this cannot happen. In Figure 1.1 we show an illustrative example of high redshift QSO spectrum with both hydrogen and metal absorption lines.

The Lyman- $\alpha$  forest clouds have a number of interesting properties. Firstly, they provide evidence that quasars are capable of ionizing the IGM. The number densities of systems observed along lines of sight towards different quasars are similar, which strengthens the impression that

<sup>1</sup>For simplicity, in the rest of the thesis we will change the notation of the column density dimensions from [atoms  $\text{cm}^{-2}$ ] to [ $\text{cm}^{-2}$ ].

they are intervening objects and not connected with the quasar environment. At redshifts near of that of the quasar the number density decreases significantly, an effect known as the *proximity effect*. The idea here is that radiation from the quasar substantially reduces the neutral hydrogen fraction in the clouds by ionization, thus inhibiting absorption at the Lyman- $\alpha$  resonance. Secondly, the total mass in the clouds appears to be close to that in the damped systems or that seen in present-day galaxies. Thirdly, the comoving number density of such systems is changing strongly with redshift. Finally, and most interestingly from the point of view of structure formation, the absorption systems seem to be only weakly clustered, in contrast to the distribution of galaxies. How these smaller Lyman- $\alpha$  systems fit into a picture of galaxy formation is not absolutely certain, but it appears that they correspond to lines of sight passing through gas confined in the small-scale “cosmic-web” of filaments and voids that corresponds to an earlier stage of the clustering hierarchy than is visible in the local galaxy distribution, indicating that clouds’ properties are evolving (Rauch 1998).

## 1.3 Absorption line properties

### 1.3.1 High resolution spectroscopy: Voigt profile decomposition

If the Lyman- $\alpha$  forest is seen as an ensemble of redshifted lines the standard tools of notions and techniques from stellar spectroscopy becomes applicable. For lower resolution data, the equivalent width provides a combined measure of line width and strength. In high resolution spectra (FWHM  $< 25 \text{ km s}^{-1}$ ) where the typical Lyman- $\alpha$  line is resolved, the line shapes are found to be reasonably well approximated by Voigt profiles (Carswell et al 1984), and line width, column density  $N_{\text{HI}}$ , and redshift  $z$  of an absorption line are the basic observables. The statistics of the Lyman- $\alpha$  forest from high resolution studies have been cast in terms of the distribution functions of these three quantities and their correlations. The main advantage of the high resolution approach is the opportunity of determining the shape of these distribution functions without parametric prejudices, by directly counting lines with parameters in a certain range.

The standard approach to Voigt profile fitting (Carswell et al. 1987) relies on  $\chi^2$  minimization to achieve a complete decomposition of the spectrum into as many independent Voigt profile components as necessary to make the  $\chi^2$  probability consistent with random fluctuations. For stronger Lyman- $\alpha$  lines the higher order Lyman lines can provide additional constraints when fitted simultaneously. The absorption lines are measured against a QSO continuum estimated locally from polynomial fits to spectral regions deemed free of absorption.

Given sufficient spectral resolution, and assuming that Lyman- $\alpha$  clouds are discrete entities the profile fitting approach is the most physically meaningful way of extracting information from the Lyman- $\alpha$  forest. If the absorber is a gas cloud with a purely Gaussian velocity dispersion (a thermal Maxwell-Boltzmann distribution, plus any Gaussian contributions from turbulence) a Voigt profile provides an exact description of the absorption line shape:

$$H(a, x) = \frac{a}{\pi} \int_{-\infty}^{\infty} \frac{e^{-y^2}}{(x-y)^2 + a^2} dy, \quad (1.12)$$

where  $a = \Gamma_{\text{lu}}/(4\pi\Delta\nu_{\text{D}})$  is the ratio of the damping width to the Doppler width and  $x =$

$(\nu - \nu_{\text{lu}})/\Delta\nu_{\text{D}}$  is the frequency shift from line center in units of the Doppler width  $\Delta\nu_{\text{D}} = \nu_{\text{lu}}b/c$ . Here  $\nu_{\text{lu}}$  is the resonance line frequency, corresponding to the wavelength  $\lambda_{\text{lu}}$ , of the transition between an upper level broadened by radiation damping to a sharp level (the ground state),  $\Gamma_{\text{lu}} = (g_{\text{l}}f_{\text{lu}}/g_{\text{u}})[1/4\pi\epsilon_0]8\pi^2e^2/(m_e c\lambda_{\text{lu}}^2)$  is the damping width of the upper level, where  $g_{\text{l}}$  and  $g_{\text{u}}$  are the respective statistical weights of the lower and upper levels,  $f_{\text{lu}}$  is the upward oscillator strength,  $e$  is the electric charge of an electron and  $m_e$  the electron mass. The Doppler parameter  $b$ , related to the line width, can then be written as the quadratic sum of its individual (thermal + kinetical) contributions:

$$b = \sqrt{\frac{2k_{\text{B}}T}{m_{\text{a}}} + b_{\text{kin}}^2}, \quad (1.13)$$

where  $m_{\text{a}}$  is the mass of the scattering particle and  $k_{\text{B}}$  is the Boltzmann's constant. In this thesis work we used the analytic approximation to the Voigt function in Equation (1.12) given by Tepper García (2006):

$$H(a, x) = e^{-x^2} \left[ 1 - a \frac{2}{\sqrt{\pi}} K(x) \right], \quad (1.14)$$

where

$$K(x) = \frac{1}{2x^2} \left[ (4x^2 + 3)(x^2 + 1)e^{-x^2} - \frac{1}{x^2}(2x^2 + 3) \sinh x^2 \right]. \quad (1.15)$$

Unfortunately, in most more realistic models of the absorbing gas, finite velocity and density gradients invalidate the assumptions underlying Voigt profile fitting, and the line parameters may have less immediate physical meaning. Departures of the absorption line shape from a Voigt profile may contain valuable information about the underlying nature of the absorption systems, and different scenarios may have quite different observational signatures. Rotational motion (Weisheit 1978; Prochaska & Wolfe 1997), gravitational collapse (McGill 1990; Meiksin 1994) and galactic outflows (Fransson & Epstein 1982; Wang 1995) have been discussed in terms of the likely absorption line shapes they produce. As yet, the quantitative application of these results has proven difficult, because of the lack of realistic models for the actual line formation, the rather subtle departures from Voigt profiles expected, and the wide variety of profiles actually encountered.

Non-Voigt profiles can still be fitted as blends of several Voigt profiles, but the information about the non-thermal motion is encoded in the spatial correlations between the individual profiles (Rauch 1998). Also, there is no guarantee that the number of components necessary for a good fit converges with increasing signal-to-noise ratio. Clearly, for specific line formation models, the results of Voigt profile decomposition may have less immediate physical meaning, and global techniques of extracting the velocity information may be more appropriate.

### 1.3.2 The column density distribution

The neutral hydrogen column densities of the absorbers are measured to range from roughly  $10^{12} - 10^{22} \text{ cm}^{-2}$ . Lower column density systems may exist, but are difficult to detect. An upper cut-off at  $3 - 5 \times 10^{21} \text{ cm}^{-2}$  is suggested by Prochaska et al. (2005). It was early recognized by Tytler (1987) that the distribution function of the column densities is a power law,  $dN/dN_{\text{HI}} \propto N_{\text{HI}}^{-\beta}$ , with  $\beta = 1.5 - 1.7$  (Tytler 1987; Hu et al. 1995; Kim et al. 2002). A recent determination for absorption systems in the redshift range  $0.5 < z < 1.9$  is shown in Fig.

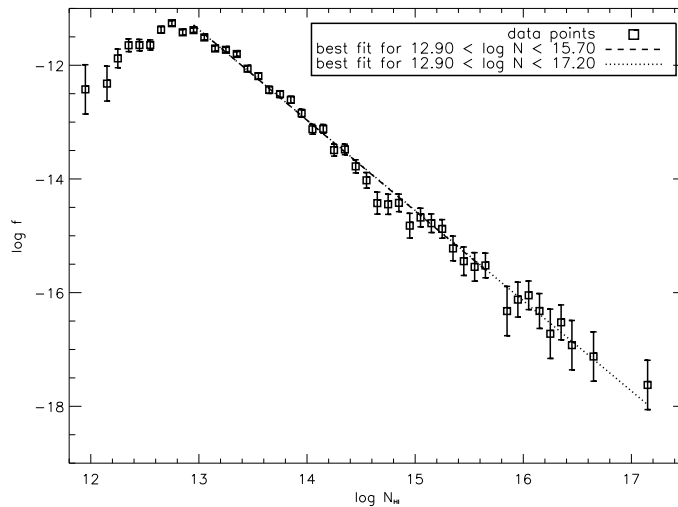


Figure 1.2: Distribution of Lyman- $\alpha$  forest column densities with fits for different ranges, for absorption systems in the redshift range  $0.5 < z < 1.9$ . For  $12.90 < \log N_{\text{HI}} < 15.70$ ,  $\beta = 1.60 \pm 0.03$ . For  $12.90 < \log N_{\text{HI}} < 17.20$ ,  $\beta = 1.59 \pm 0.02$ . Here  $f$  is the number of absorption systems per unit column density and per unit of absorption distance. From the work by Janknecht et al. (2006), where the authors used high-resolution ( $R \geq 30000$ ) UV (STIS) and optical (VLT/UVES and Keck/HIRES) spectra of nine bright quasars with  $z_{\text{em}} < 1.94$ .

1.2 (Janknecht et al. 2006). Although there may be small deviations from a perfect power law (Giallongo et al. 1993; Cristiani et al. 1993; Meiksin & Madau 1993; Petitjean et al. 1993), the almost perfect agreement to a single power law over such an enormous dynamic range strongly suggests a single formation mechanism.

### 1.3.3 The Doppler parameter distribution

The measured Doppler velocities  $b$  range over about  $10 < b < 100 \text{ km s}^{-1}$ , with the large majority concentrated between  $15 - 60 \text{ km s}^{-1}$  (Atwood et al. 1985; Carswell et al. 1991; Rauch et al. 1992; Hu et al. 1995; Lu et al. 1996; Kim et al. 1997; Kirkman & Tytler 1997). Typical distributions are shown in Fig. 1.3, for varying redshift ranges (Janknecht et al. 2006). Temperatures may in principle be inferred from Eq. (1.13), but in doing so there are basically two difficulties: (1) the systems may be broadened by a kinematic component and (2) the absorption features may be blends of more than a single system. Evidence for kinematic broadening is found when metal features are also detected. In general, there is no unique fit to an absorption feature, particularly in the presence of blending: several statistically acceptable fits are possible (Kirkman & Tytler 1997), and these will change as the signal-to-noise ratio or spectral resolution changes (Rauch et al. 1993).

Broadening is also expected from the line finding and fitting procedure. The systematic influence of procedures used to locate and fit the absorption lines on the resulting distributions of Doppler parameters has received limited attention. The potential usefulness of the

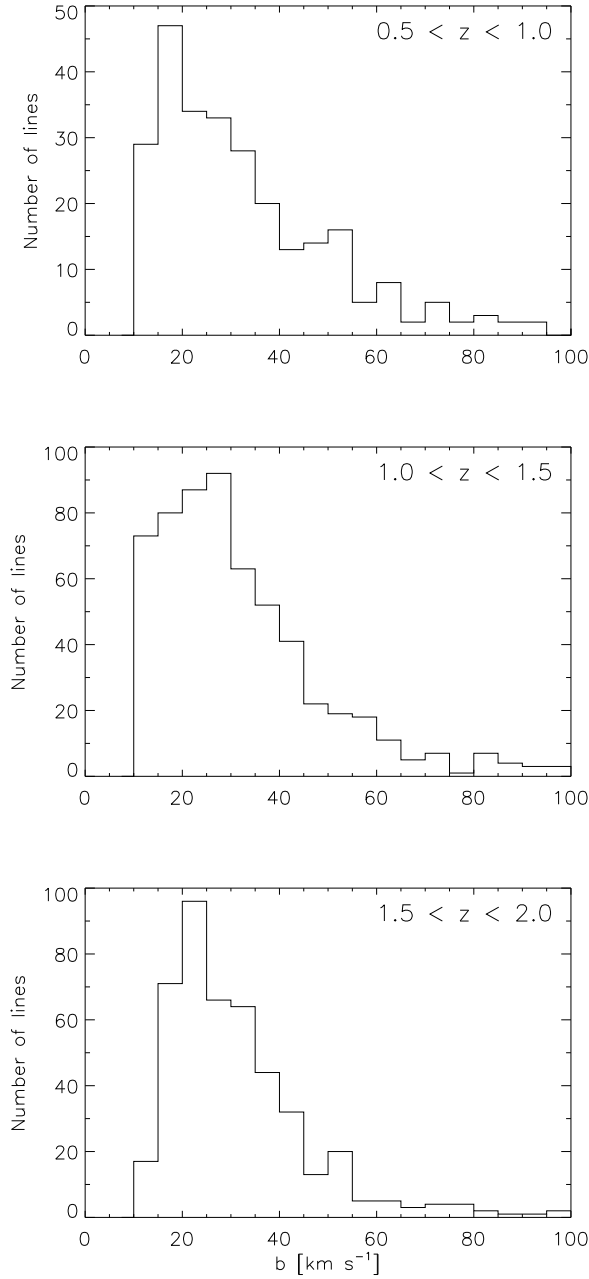


Figure 1.3: Distribution of the Lyman- $\alpha$  Doppler parameters in intervals  $\Delta b = 5 \text{ km s}^{-1}$ , varying redshift ranges. Data are the same of Figure 1.2, from Janknecht et al. (2006). CANDALF was used for the analysis of all quasar spectra except for HE 0515-4414. The lines found in the HST/STIS and VLT/UVES spectra of HE 0515-4414 were fit with the MIDAS software package FITLYMAN (Fontana & Ballester 1995).

Doppler parameter distribution for extracting physical information about the IGM, such as its temperature distribution, merits further study of the effect of fitting algorithms on the derived distribution. In general a lognormal distribution provides a good fit for the  $b$ -parameter distribution (Zhang et al. 1997; Kirkman and Tytler 1997; Meiksin et al. 2001). This suggests that the measured Doppler parameters may in part be induced by a lognormal-generating stochastic process. It is noted that the process need not arise entirely from the line-fitting, but could also originate from the physical processes that gave rise to the structures that produce discrete absorption features.

Uncertainty in the origin of the Doppler parameter distribution leaves the physical interpretation of the Doppler parameters with some ambiguity, but, although their relation to the gas temperature is not straightforward, the Doppler parameters are used to set upper limits on the gas temperature. Note that noise affects weak lines may also produce an artificial narrow line and spoils some statistics. For pure Doppler broadening, the range  $20 - 60 \text{ km s}^{-1}$  corresponds to temperatures of  $2.4 - 3.8 \times 10^4 \text{ K}$ , the range expected from photoionization at the moderate overdensities expected for the absorbers (Meiksin 1994; Hui & Gnedin 1997). Cooler temperatures are possible, however, particularly if the gas has been expanding sufficiently fast for adiabatic cooling to be appreciable.

### 1.3.4 Evolution in the number density of the Lyman- $\alpha$ forest

The number of absorption systems per unit redshift increases with redshift. Some evolution is expected as a result of the expansion of the Universe. For a proper number density  $n_a(z)$  of absorption systems at redshift  $z$ , with proper cross-section  $\sigma_a(z)$ , the expected number of absorbers per unit proper length is  $dN/dl_p = n_a(z)\sigma_a(z)$ . The proper line element is related to redshift according to  $dl_p/dz = c/[H(z)(1+z)]$ , where  $H(z) = H_0E(z)$  is the Hubble parameter. For a flat Universe and standard cosmological parameters,  $E(z) \simeq 0.55(1+z)^{3/2}[1 + 2.3/(1+z)^3]^{1/2}$ . The evolution in the number density is then given by

$$\frac{dN}{dz} \simeq (2100 \text{ Mpc})n_{a,c}(z)\sigma_a(z)(1+z)^{1/2} \left[ 1 + \frac{2.3}{(1+z)^3} \right]^{-1/2}, \quad (1.16)$$

where  $n_{a,c}(z) = n_a(z)(1+z)^{-3}$  is the comoving number density of systems. For a constant comoving number density and fixed proper cross-section, only moderate evolution is expected,  $dN/dz \propto (1+z)^{1/2}$ . At low redshifts, this gives a reasonable description of the evolution. Using Hubble Space Telescope (HST) observations, Weymann et al. (1998) find for all system with equivalent widths above  $0.24 \text{ \AA}$ ,  $dN/dz = (32.7 \pm 4.2)(1+z)^{0.26 \pm 0.22}$  for  $z < 1.5$ . Subsequent higher spectral resolution surveys using HST have extended the statistics to systems with equivalent widths below  $0.1 \text{ \AA}$  at  $z < 0.1$  (Penton et al. 2000, 2004). The large survey of Danforth & Shull (2008) obtains  $dN/dz = 129_{-5}^{+6}$  down to  $0.030 \text{ \AA}$  at  $z < 0.4$  with  $\langle z \rangle \simeq 0.14$ .

For  $z > 1.5$ , however, the number density evolves considerably faster than the constant comoving rate (Tytler 1987b). Kim et al. (2002) obtain  $dN/dz = 6.1(1+z)^{2.47 \pm 0.18}$  for systems with column densities in the range  $13.64 < \log N_{\text{HI}} < 17$ : this corresponds to considerable evolution in the product  $n_{a,c}(z)\sigma_a(z)$ . A smooth transition is found over the redshift range  $0.5 < z < 1.9$  by Janknecht et al. (2006), with a dependence of the evolution rate on column density. High column density systems corresponding to Lyman Limit Systems evolve somewhat

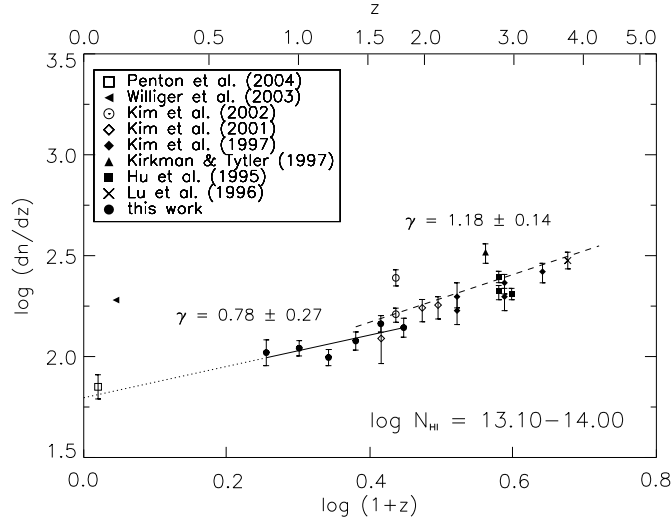


Figure 1.4: Evolution of the number density of Lyman- $\alpha$  systems with  $13.10 < \log N_{\text{HI}} < 14.00$ , including best-fits to the solid and open circles over the ranges indicated, as represented by the solid and dashed lines, respectively, taking  $dN/dz \propto (1+z)^\gamma$ . The dotted line extrapolates the lower redshift fit to  $z = 0$ . From Janknecht et al. (2006).

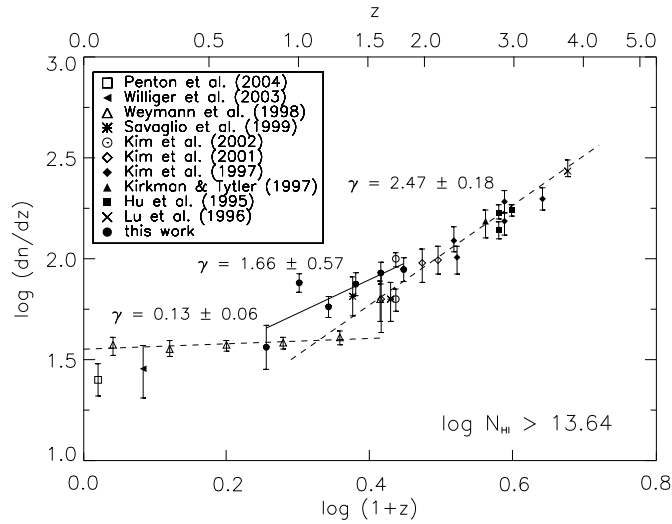


Figure 1.5: Evolution of the number density of Lyman- $\alpha$  systems with  $\log N_{\text{HI}} > 13.64$ , including best-fits to the solid and open circles over the ranges indicated, as represented by the solid and dashed lines, taking  $dN/dz \propto (1+z)^\gamma$ . The additional low redshift dashed line is the best fit to the open triangles. The open square, left-pointing solid triangle, and stars correspond to systems with  $\log N_{\text{HI}} > 14.00$ . From Janknecht et al. (2006).

more slowly than lower column density systems. Stengler-Larrea et al. (1995) find for systems with  $\tau_L > 1$ ,  $dN/dz = 0.25_{-0.10}^{+0.17}(1+z)^{1.50 \pm 0.39}$  over the redshift range  $0.32 < z < 4.11$ . Based on a larger, higher redshift sample, Péroux et al. (2003) find somewhat more rapid evolution, with  $dN/dz = 0.07_{-0.04}^{+0.13}(1+z)^{2.45_{-0.65}^{+0.75}}$  over the redshift range  $2.4 < z < 5$ . Damped Lyman- $\alpha$  Absorbers show evolution comparable to that of the Lyman Limit Systems, with  $dN/dz$  increasing by about a factor of 2 from  $z = 2.5$  to  $z = 4$  Prochaska et al. (2005).

Numerical simulations show that the structure of the IGM evolves, although in the comoving frame the structure is remarkably stable. Because  $dN/dz$  is fit for a fixed HI column density range, the diminishing gas density towards decreasing redshifts will result in fewer systems satisfying the column density threshold, so that  $dN/dz$  will decrease towards decreasing redshift. Evolution in the ionizing background will also affect the number of absorption systems lying above the column density threshold, and this is a major factor in the evolution of  $dN/dz$ . The slowdown at  $z < 1.5$  in the evolution is in fact attributed predominantly to a reduction in the intensity of the ionizing background: as the ionizing rate decreases, fewer systems will slip below the column density threshold than under pure density evolution. As a result, the decrease in  $dN/dz$  towards lower  $z$  slows down (Bianchi et al. 2001). The difference in the rate of evolution between low and high column density systems found by Janknecht et al. (2006) and shown in Figures 1.4 and 1.5, points out that structural evolution in the IGM must also play a role.

## 1.4 Statistics of the transmitted flux

A different approach to study the Lyman- $\alpha$  forest is based on recovering the information encoded in the transmitted flux treating the flux as a continuous field with directly measurable statistical properties (e.g. Rauch et al. 1997; Rauch 1998; Theuns et al. 1998; Croft et al. 2002; Meiksin 2009). In this approach, measurement of the zero, one, two- or three-point Probability Distribution Functions (PDFs; i.e. the mean flux level, the flux PDF, the flux power and bispectrum) enable a variety of physical properties to be explored. Ideally, a given IGM model described by a set of cosmological and astrophysical parameters should agree with all the previous statistics including the results from Voigt profile decomposition at the same time. In the following we briefly describe some of these statistics and how they are related to different aspects of the IGM physics.

### The mean transmitted flux

The mean normalized flux of the Lyman- $\alpha$  forest:

$$\langle F \rangle = \langle I_{\text{observed}}/I_{\text{emitted}} \rangle, \quad (1.17)$$

is the simplest observable quantity, and it is often expressed as an effective optical depth:

$$\tau_{\text{eff}} = -\ln \langle F \rangle \equiv -\ln \langle e^{-\tau} \rangle, \quad (1.18)$$

where  $\tau$  is the underlying Lyman- $\alpha$  optical depth in each pixel of the spectrum from which  $\langle F \rangle$  is measured. Assuming (Bolton, Oh & Furlanetto 2009) the IGM is highly ionized and

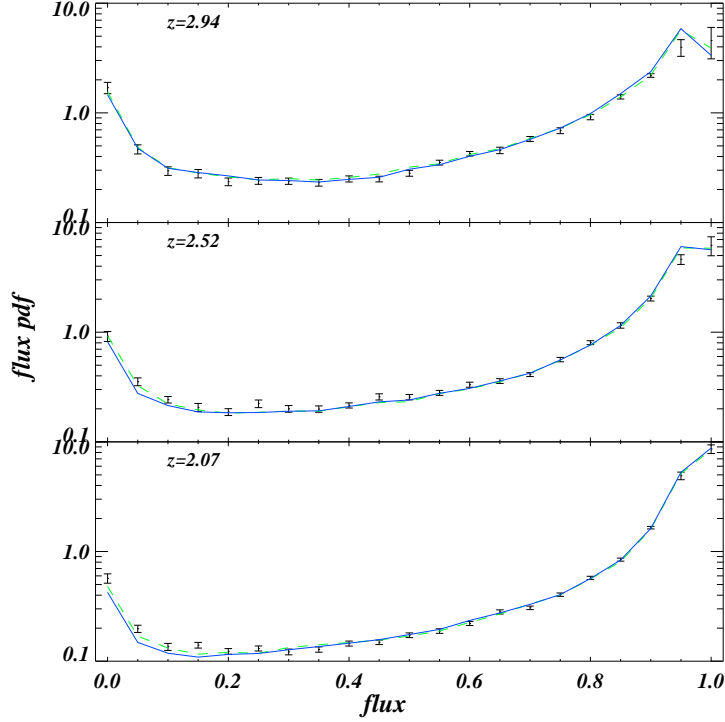


Figure 1.6: Best fit to the flux PDF for the two fiducial models (continuous blue and dashed green lines) of Viel et al. (2009), in the three redshift bins at  $\langle z \rangle = (2.07, 2.52, 2.94)$ . Data used for these investigations consist mainly of two kinds of sets of quasars spectra: the Sloan Digital Sky Survey low-resolution, low signal-to-noise ratio sample, and UVES/VLT or HIRES/KECK samples of high-resolution spectra. From Viel et al. (2009).

in photo-ionization equilibrium with the metagalactic UV background, and the low density IGM ( $\Delta = \rho/\langle \rho \rangle \leq 10$ ) follows a power law temperature density relation,  $T = T_0 \Delta^{\gamma-1}$  (Hui & Gnedin 1997; Valageas et al. 2002), the Lyman- $\alpha$  optical depth at  $z \lesssim 2$  may be written as (e.g. McDonald & Miralda-Escudé 2001):

$$\tau \simeq 1.0 \frac{(1 + \chi_{\text{He}})}{\Gamma_{-12}} \left( \frac{T_0}{10^4 \text{ K}} \right)^{-0.7} \left( \frac{\Omega_b h^2}{0.024} \right)^2 \left( \frac{\Omega_m h^2}{0.135} \right)^{-1/2} \left( \frac{1+z}{4} \right)^{9/2} \Delta^{2-0.7(\gamma-1)}, \quad (1.19)$$

where  $\Omega_b$  and  $\Omega_m$  are the present day baryon and matter densities as a fraction of the critical density,  $h = H_0/100 \text{ km s}^{-1} \text{ Mpc}^{-1}$  for the present day Hubble constant  $H_0$ ,  $\Delta = \rho/\langle \rho \rangle$  is the normalized gas density,  $T_0$  is the gas temperature at mean density,  $\gamma$  is the slope of the temperature density relation and  $\Gamma_{-12} = \Gamma_{\text{HI}}/10^{-12} \text{ s}^{-1}$  is the hydrogen photo-ionization rate.  $\chi_{\text{He}}$  accounts for the extra electrons liberated during HeII reionization;  $\chi_{\text{He}} = 1.08$  prior to HeII reionization and  $\chi_{\text{He}} = 1.16$  afterwards for a helium fraction by mass of  $Y = 0.24$  (Olive & Skillman 2004). The effective optical depth can then be estimated by integrating over all possible IGM densities  $\Delta$ .

Although Eq. (1.19) ignores the effect of redshift space distortions on the Lyman- $\alpha$  forest opacity, it clearly elucidates the relationship between the opacity and the underlying physical

properties of the IGM. A sudden decrease in the Lyman- $\alpha$  effective optical depth can thus be attributed to an increase in the IGM temperature, either by raising  $T_0$  or changing  $\gamma$ , an increase in the photo-ionization rate, or a combination of both. On the other hand, an increase in the free electron fraction will raise the opacity by reducing the recombination timescale.

### The flux PDF

The flux PDF is sensitive to the thermal evolution of the IGM and constrain the density-temperature distribution of the ionized gas (Viel et al. 2009; McQuinn et al. 2009; Bolton et al. 2009). Recently Viel et al. (2009) find results that corroborate the suggestion of an inverted temperature-density relation at  $z = 3$ . As for the analysis of the full flux range the statistical significance of the data favouring an inverted temperature-density relation  $\gamma < 1$  is about  $3\sigma$  at  $z \sim 3$ . At  $z < 3$  the data are consistent with an isothermal ( $\gamma \sim 1$ ) temperature-density relation. The results regarding the thermal state of the IGM do not change significantly when the authors omit the flux range  $F > 0.9$ . If they discard both the flux ranges at low and high emissivity and consider only the flux range  $F = [0.1 - 0.8]$ , there is still evidence for an inverted  $T - \rho$  relation, but at a reduced level of significance ( $1 - 1.5\sigma$  confidence level). In Figure 1.6 we show the Viel et al. (2009) best fit to the flux PDF.

### Power spectrum and bispectrum of the Lyman- $\alpha$ forest

The flux power spectrum has been used to constrain cosmological parameters and the behaviour of dark matter at small scales (Viel et al. 2004; Seljak et al. 2006; Viel et al. 2008). Equation (1.19) implies a tight correlation between the observable quantity  $F = e^{-\tau}$  and the underlying gas density  $\rho$ , which in turn follows the dark matter density because pressure gradients are weak in the diffuse, cool gas. Croft et al. (1998, 2002) show that the matter power spectrum  $P(k)$  is proportional to the flux power spectrum  $P_F(k)$  on large scales. The constant of proportionality depends on redshift, temperature,  $\Gamma_{-12}$  and some cosmological parameters, but it can be fixed empirically by matching a single observational constraint, such as the mean opacity of the forest at the redshift under consideration. The general assumption usually made is that  $P(k) = b^2(k)P_F(k)$ , where  $b(k)$  is a function calculated from simulations constrained to match the observed flux power spectrum. While the measurement of  $P_F(k)$  is quite precise, the determination of  $b(k)$  still suffers from some systematic uncertainties. The most important of these is the uncertainty in the mean opacity of the forest, measurement of which requires careful attention to continuum fitting. Other sources of uncertainty are the values of  $T_0$  and the numerical limitations of the simulations.

The bispectrum of the flux is the Fourier transform of the three-point correlation function. As the flux in the Lyman- $\alpha$  forest is a sensitive probe of the matter distribution it should probe the topology of the 3D matter distribution in more detail than the two-point correlation function or the power spectrum. It also can be used as a complementary tool to determine cosmological parameters (e.g. Fry 1994; Verde et al. 2002) and maybe also the physical state of the IGM. Gravitational growth induces correlations between large scale modes and small scale power which can be probed by the bispectrum. Zaldarriaga et al. (2001) pointed out that these correlations may be used to discriminate between fluctuations due to large-scale structure in the matter distribution and those produced by non-gravitational processes such as

fluctuations in the continuum emission of the quasar. Mandelbaum et al. (2003) showed that with the SDSS (Sloan Digital Sky Survey) QSO sample it should be possible to use higher order statistics such as the bispectrum to determine amplitude, slope and curvature of the slope of the matter power spectrum with an accuracy of a few percent provided systematic errors are under control. Viel et al. (2004b) found that the flux bispectrum of the observed spectra and that of synthetic spectra obtained from hydrodynamical simulations of a  $\Lambda$ CDM ( $\Lambda$  Cold Dark Matter, see Appendix A.5) model agree well within the errors, in the redshift range  $2 < z < 2.4$ . The flux bispectrum can also be used to search for signatures of non-gaussianities in the matter distribution (Viel et al. 2009b).

## 1.5 Damped Lyman- $\alpha$ systems

We already introduced Damped Lyman- $\alpha$  systems in Section 1.2. Part of this thesis work is dedicated to DLAs, therefore in this Section we further explore the characteristics of this class of cosmological objects.

Damped Lyman- $\alpha$  systems are defined as quasar absorption systems with neutral hydrogen column density  $N_{\text{HI}} > 2 \times 10^{20} \text{ cm}^{-2}$  (Wolfe et al. 1986). DLAs are considered as an important reservoir and/or sink of gas for the galaxy formation process in the high redshift Universe and their neutral hydrogen content dominate the total neutral hydrogen budget over a large fraction of the cosmic history. The fact that the hydrogen is mainly neutral in DLAs, distinguishes them from all the other classes of QSO absorption systems, in which the hydrogen is ionized. The neutrality of the gas is crucial: while stars are unlikely to form out of warm ionized gas, they are likely to descend from cold neutral clouds, which are the precursors of molecular clouds, the birthplace of stars (Wolfire et al. 2003). Therefore DLAs provide a window on the interplay between neutral gas and newly formed stars, i.e. they are the best, perhaps the only, example we have of an interstellar medium in the high-redshift Universe.

The most efficient method for locating quiescent layers of neutral gas is through the detection of damped Lyman- $\alpha$  absorption lines. In the rest frame of the atom, the absorption profile of any atomic transition is naturally broadened owing to the finite lifetime of the upper energy state. In the rest frame defined by the average velocity of the gas, the natural profile is Doppler broadened by the random motions of the atoms: the convolution of both effects results in the Voigt profile. Because the Doppler profile falls off from the central frequency,  $\nu_0$ , as  $\exp[-(\Delta\nu/\Delta\nu_{\text{D}})^2]$  (where  $\Delta\nu = |\nu - \nu_0|$  and  $\Delta\nu_{\text{D}} = \sqrt{2}\sigma_{\text{v}}\nu_0/c$  for an assumed Gaussian velocity distribution with dispersion  $\sigma_{\text{v}}$ ) and the natural or ‘‘damped’’ absorption profile falls off from  $\nu_0$  like  $1/(\Delta\nu)^2$ , at sufficiently large  $\Delta\nu$  the probability for damped absorption exceeds the probability for absorption in the Doppler profile. The frequency intervals in which natural broadening dominates Doppler broadening are called the damping wings of the profile function. Most atomic transitions of abundant ions are optically thin in their damping wings but optically thick near the core of the Doppler profile. Due to the higher values of  $N_{\text{HI}}$ , Lyman- $\alpha$  has unit optical depth in the damping wings at  $\Delta\nu_{\tau=1} \propto [A_{21}f_{21}N_{\text{HI}}]^{1/2}$  when  $N_{\text{HI}} > 10^{19} \text{ cm}^{-2}$  and  $\sigma_{\text{v}} < 70 \text{ km s}^{-1}$ :  $A_{21}$  and  $f_{21}$  are the Einstein spontaneous emission coefficient and oscillator strength for the Lyman- $\alpha$  transition. In this case, unit optical depth occurs in the damping wings, and therefore the equivalent width of a damped Lyman- $\alpha$  line is independent of the velocity structure of the gas for velocity dispersions within the range detected in most QSO

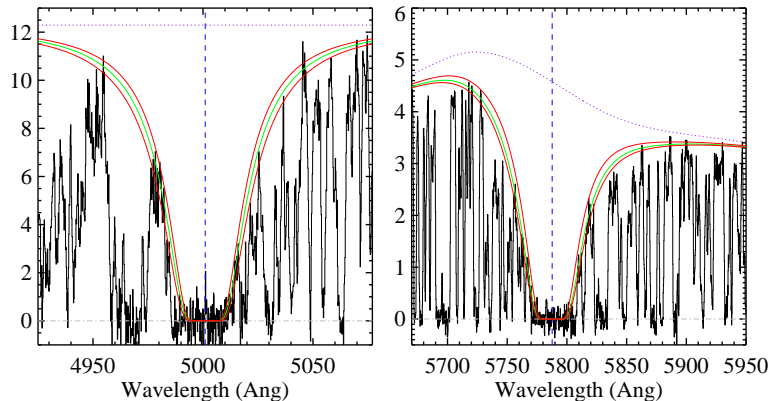


Figure 1.7: Example Voigt profile fits to two DLAs of the sample from Prochaska et al. (2003). In the y-axis is shown the relative flux. The vertical dashed line indicates the line centroid determined from metal-line transitions identified outside the Lyman- $\alpha$  forest. The dotted line traces the continuum of the QSO and the green and red lines trace the Voigt profile solution and the fits corresponding to  $1\sigma$  changes to  $N_{\text{HI}}$ . The fluctuations at the bottom of the damped Lyman- $\alpha$  absorption troughs indicate the level of sky noise.

absorption systems. As a result, the equivalent width will be large even when the velocity dispersion is small. In Figure 1.7 is shown an example of the Voigt profile fits to two DLAs.

Significant observational efforts have been made in order to understand the nature of DLAs (e.g. Wolfe et al. 1995; Storrie-Lombardi & Wolfe 2000; Rao & Turnshek 2000; Prochaska et al. 2001; Péroux et al. 2003; Chen & Lanzetta 2003; Prochaska et al. 2005; Wolfe & Chen 2006; Wolfe et al. 2008), while, on the theoretical side, semi-analytical models and high-resolution hydrodynamical simulations are routinely performed to investigate the relation between DLAs and dark matter haloes and to match their observed properties (e.g. Katz et al. 1996; Gardner et al. 1997, 2001; Haehnelt et al. 1998; Maller et al. 2001; Nagamine et al. 2004, 2007; Okoshi & Nagashima 2005; Pontzen et al. 2008; Barnes & Haehnelt 2009). Despite these efforts, the nature of DLAs is still unclear and the interpretation of the large observed velocity width of low-ionization species is not unambiguous. In fact, the disk-like model of Prochaska & Wolfe (1997) in which DLAs are thick rotating disks with speed typical of a present-day spiral galaxies and the alternative model based on the assumption that DLAs are protogalactic clumps (Haehnelt et al. 1998) seem to be both viable. More precisely, Haehnelt et al. (1998) showed that while the velocity width profiles of DLAs can be reproduced by rotation in disks as well as protogalactic clumps, the velocity width distribution cannot be reproduced by rotation in disks in the context of a cold dark matter model.

In order to make significant progress in this field observational and theoretical/numerical efforts are needed to tackle the problem under many different aspects. Recently, the Sloan Digital Sky Survey (SDSS) has allowed to measure to an unprecedented precision the statistical

properties of DLAs (incidence rates, column density distribution function, etc.) over a wide redshift range (Prochaska et al. 2005). Moreover, attempts to find the galaxy counterparts of DLAs represent the most promising way to understand their nature (e.g. Fynbo et al. 1999; Christensen et al. 2007). High-resolution spectroscopic studies have also played a crucial role since low-ionization metal lines, that are supposed to be good tracers of the neutral gas in DLAs, can be identified shedding light on the DLAs chemical and physical properties (Matteucci et al. 1997; Calura et al. 2003; Vladilo & Péroux 2005; Vladilo et al. 2006; Vladilo et al. 2008, Prochaska & Wolfe 2009).

Recently, Pontzen et al. (2008) analysed several different hydrodynamical simulations with and without feedback using an approximate *a posteriori* radiative transfer scheme. They matched most of the observed DLAs properties apart from a tension with the observed velocity widths. In their framework, haloes of virial masses between  $10^9$  and  $10^{11} h^{-1} M_{\odot}$  were the main contributors to the DLA cross-section. Barnes & Haehnelt (2009) with a semi-analytical model claimed instead that, in order to reproduce the velocity widths distribution, the cross-section of haloes less massive than  $10^{10} h^{-1} M_{\odot}$  should be exponentially suppressed. Observations of the HI distribution in the local Universe made by Zwaan et al. (2008) show that the link with galactic superwinds might be stronger than expected and favoured this explanation instead of the disk-like model to explain the observed velocity widths. Also some correlation properties of neutral hydrogen rich galaxies and HI absorbers in the local Universe seem to be better fit when galactic winds are taken into account (Pierleoni et al. 2008). However, the situation is quite confusing and potential problems for this interpretation are extensively discussed in Prochaska et al. (2008).

In the first part of this thesis work (Chapter 3), we will extend the analysis performed by Nagamine et al. (2007) that addressed the properties of DLAs in a  $\Lambda$ CDM universe. We will use simulations that have on average a factor 10 better mass resolution and a different version of the hydrodynamical code GADGET-2 that incorporates the dependence of the radiative cooling function on the global metallicity of the gas (following Sutherland & Dopita 1993) and a self consistent metal enrichment model (see next Chapter). The goal is to see which DLAs properties can be reproduced by the hydrodynamical simulations and to investigate closely the impact of galactic winds both on the neutral hydrogen and on the metal distribution around galactic environments in the high redshift Universe (mainly in the range  $z = 2 - 4$ ).

## 1.6 Metal absorption systems

The earliest identifications of intervening absorption systems were for elements heavier than helium, so called metals (Bahcall et al. 1968). Common elements are carbon, nitrogen, silicon and iron, but to date the list extends much further, including oxygen, magnesium, neon, sulfur, etc. The metals provide invaluable insight into the structure of the IGM in several different ways. The widths of metal absorption features allow direct estimates of the temperature of the IGM and its small-scale velocity structure. For example, the narrow widths of CIV (i.e. triply ionized Carbon) features were used by York et al. (1984) to demonstrate the absorbers had the characteristic temperatures of photoionized gas rather than collisionally ionized. Furthermore, the metal systems probe the impact star formation has had on the IGM, as the metals were most likely transported into the IGM through galactic winds, or introduced *in situ* by local small-scale

regions forming first generation, Population III, stars. In the nearby Universe, metals indicate the presence of shocked gas, as may accompany the formation of galaxy clusters. As such, the metals in principle document the history of cosmic structure and star formation. Ratios of the metal column densities may be used to constrain the spectral shape of the metagalactic ionizing UV background, which in turn puts constraints on the possible sources of the background and their relative contributions.

Searches for intervening metal absorbers have been facilitated by the exploitation of atomic line doublets for some of the stronger species. The most common doublets used are MgII  $\lambda\lambda$  2796, 2803 Å and CIV  $\lambda\lambda$  1548, 1551 Å. These are among the strongest lines detected in the Lyman- $\alpha$  forest. They also have the important advantage of wavelengths redward of Lyman- $\alpha$ , placing them outside the Lyman- $\alpha$  forest and avoiding this potential source of confusion (see Figure 1.1 for an illustrative example). Searches for MgII absorption systems are by far the most common because of their established connection to galaxies. Absorption features by OVI  $\lambda\lambda$  1032, 1038 Å are more difficult to identify since they lie within the Lyman- $\alpha$  forest, and so are not easily distinguished from the forest. Searches have been successful, however, and have moreover discovered a second and new IGM environment: while at high redshifts the OVIs systems probe the component of the IGM containing CIV, at low redshifts they are associated with a Warm-Hot Intergalactic Medium (WHIM). A search for OVI absorption systems as an indicator of a WHIM at high redshift was conducted by Simcoe et al. (2002). Efforts are currently underway to detect an intergalactic X-ray absorption line forest using the *XMM-Newton* and *Chandra* X-ray satellites. Tentative detections of low redshift OVIII have been reported by Fang et al. (2002, 2007) and Williams et al. (2007). Models for describing the WHIM properties, based on hydrodynamical simulations, have been proposed by Viel et al. (2003, 2005), Bertone et al. (2009) and Tornatore et al. (2009).

Attempts to infer the origin of the metals, whether distributed by galactic outflows or introduced locally by Population III stars, have led to various efforts to estimate the range in ambient metallicities and to determine their spatial distribution. Updated solar abundances useful for modeling the abundances of the metal absorption systems are provided by Grevesse & Sauval (1998), Holweger (2001), Allende Prieto et al. (2001, 2002), Lodders (2003), Asplund (2003) and Asplund et al. (2005). Early attempts to manage weak metal features were based either on a spectral shift-and-stack approach to generate a high signal-to-noise ratio composite CIV line (Lu et al. 1998) or through a pixel-by-pixel statistical analysis of the spectra (Songaila & Cowie 1996; Cowie & Songaila 1998).

An alternative is to perform long integrations of bright QSOs to obtain high resolution, high signal-to-noise ratio spectra. With signal-to-noise ratios of 200-300 per spectral resolution element, Simcoe et al. (2004) detected metal lines in 70% of the Lyman- $\alpha$  forest systems. Absorption systems with HI column densities as low as  $N_{\text{HI}} > 10^{14} \text{ cm}^{-2}$  show CIV features, while systems with  $N_{\text{HI}} > 4 \times 10^{13} \text{ cm}^{-2}$  show OVI features. Although the inferred metallicities are model dependent (fixed in part by the assumed spectrum and intensity of the ionizing background), the measurements suggest metallicities as low as  $3 \times 10^{-4}$  that of the Sun. No evidence for a metallicity floor could be discovered. The metallicity distribution inferred is consistent with a lognormal distribution with a mean of  $\sim 0.006$  solar: this demonstrates that the Lyman- $\alpha$  forest, the main manifestation of the IGM, is contaminated by metals.

The mechanism and degree of metal mixing in the diffuse IGM are unclear. While the

mixing of metals in stellar interiors by convection and diffusion may produce a homogeneous composition, preserved in supernovae ejecta and winds, it is far from clear that the mixing of the ejecta will result in uniform metallicity. The mixing process is still poorly understood in the Interstellar Medium, and much more so in the IGM. The stirring produced by dynamical instabilities, such as the Kelvin-Helmholtz and Rayleigh-Taylor, mix metal enriched stellar ejecta with the surrounding primordial gas. Insufficient mixing, however, rather than a uniform mixture, will instead result in patches of high metallicity gas entrained within the primordial gas of essentially zero metallicity. Schaye et al. (2007) find evidence for just such inadequate mixing for diffuse absorption systems (with a median upper limit of 13.3 on  $\log N_{\text{HI}}$ ), at  $z \simeq 2.3$ . By combining CIV measurements with upper limits on HI, CIII, SiII, SiIII, NV and OVI, they place robust constraints on the metallicities and physical properties of the CIV absorption systems, with a median lower limit on the metallicities of  $[\text{C}/\text{H}] > -0.42$  and a median upper limit on the absorber sizes of  $R \lesssim 1.5$  kpc. They obtain typical median lower and upper limits on the hydrogen densities of  $10^8 < n_{\text{H}} < 10^9 \text{ cm}^{-3}$ , a range that suggests a cloud size of about 100 pc. The clouds, however, would likely be transient, either quickly dispersing if freely expanding or shorn apart by dynamical instabilities if moving relative to a confining medium, on a timescale of about  $10^7$  yrs. Schaye et al. (2007) propose a picture in which new clouds are continuously created through dynamical or thermal instabilities. In this picture, nearly all the metals in the IGM could be processed through just such a cloud phase. The dispersed clouds would retain their coherence as small patches, but of too low column density to be detectable. The resulting IGM metallicity would persist as patchy, not mixed.

Damped Lyman- $\alpha$  systems show a wide range of metals with both low and high ionization states, including boron, carbon, nitrogen, oxygen, magnesium, aluminum, silicon, phosphorus, sulfur, chlorine, argon, titanium, chromium, manganese, iron, cobalt, nickel, copper, zinc, germanium, arsenic and krypton (Lu et al. 1996b; Wolfe et al. 2005; Dessauges-Zavadsky et al. 2006). The metallicities evolve from about 0.03 solar at  $z \simeq 4$  to 0.15 solar at  $z \simeq 1$ , with few above 0.3 solar (Wolfe et al. 2005). No DLA is found with a metallicity smaller than 0.0025 solar, distinguishing them as a population from the Lyman- $\alpha$  forest. By contrast, sub-DLAs are found to have metallicities ranging from 0.1 solar to super-solar abundances with as much as 5 times solar in zinc (Kulkarni et al. 2007). Both these classes of systems are likely related to galaxies.

The presence of the metal lines in absorbers of all HI column densities in principle offers an opportunity to obtain a nearly model-free measurement of the gas temperature. Allowing for kinetic broadening of the Doppler parameters following Eq. (1.13), the measurements of the Doppler parameters from features corresponding to two or more elements permits the thermal and kinematic broadening components to be separated (in principle, instrumental broadening could be incorporated into the kinematic term). Given total Doppler parameter measurements  $b_i$  and  $b_j$  for two species  $i$  and  $j$  of masses  $m_i$  and  $m_j$ , the temperature may be solved for as

$$T = \frac{m_i m_j}{2k_{\text{B}}} \frac{b_i^2 - b_j^2}{m_j - m_i}. \quad (1.20)$$

Applying this method to CIV and SiIV features detected in three high redshift QSOs, and assuming that the CIV and SiIV features trace the same systems with the same temperature and velocity structure, Rauch et al. (1996) obtain a typical temperature of  $T \approx 38000$  K and

typical kinetic motions of  $b_{\text{kin}} \approx 6 \text{ km s}^{-1}$  for a select subsample of especially well-fit features. The large CIV column densities of the systems (typically exceeding  $10^{12} \text{ cm}^{-2}$ ), suggest large HI column densities of  $N_{\text{HI}} > 10^{15} \text{ cm}^{-2}$  (Simcoe et al. 2004).

A few other Lyman- $\alpha$  systems selected for quiescent velocity fields as part of a program of deuterium abundance measurements yield somewhat cooler temperatures. The Doppler parameters of CIV and SiIV measured by Kirkman et al. (2000) in a system with  $\log N_{\text{HI}} = 16.7$  yields a temperature of  $T \approx 30000 - 32000 \text{ K}$ . For a Lyman limit system with  $\log N_{\text{HI}} = 17.1$  at  $z = 0.7$  (Tytler et al. 1999), the Doppler parameter measured for MgII compared with that of HI gives  $T \approx 31000 \text{ K}$  and  $b_{\text{kin}} \approx 13 \text{ km s}^{-1}$ , assuming the hydrogen and metals sample the same velocity field, which is not an obvious assumption to make. For a sub-DLA system with  $\log N_{\text{HI}} = 19.42$ , O’Meara et al. (2001) find from a simultaneous fit to OI, NI and HI  $T = 1.15 \pm 0.02 \times 10^4 \text{ K}$  and  $b_{\text{kin}} = 2.56 \pm 0.12 \text{ km s}^{-1}$ . In all cases, the temperatures obtained are consistent with photoionization heated gas. Although direct gas density measurements are not possible, models generally suggest that higher column density systems correspond to higher densities, especially at these high values. The temperatures support the expected trend of decreasing temperature with increasing density for sufficiently dense absorption systems (Meiksin 1994).

The small kinetic contributions to the line broadening are in contrast to what is found for HeII absorption systems, which appear to be dominated by kinetic broadening (Zheng et al. 2004). The HeII features, however, were chosen for their clear isolation in the spectrum, and so may probe physically underdense regions, in contrast to the higher column density systems above. An attempt to estimate temperatures from a larger sample of HeII and HI systems has not been able to produce secure values, but nonetheless shows that only  $\sim 45\%$  of the lines are dominated by kinematic broadening (Fechner & Reimers 2007).

In the second part of this thesis work (Chapter 4), we will focus on the cosmic evolution of the CIV. Our work is the theoretical counterpart of the D’Odorico et al. (2009) paper in which the authors present a new measurement of the CIV cosmological mass density,  $\Omega_{\text{CIV}}$ , in the redshift range  $1.5 - 4$ , based on a sample of 25 high resolution, high signal-to-noise QSO spectra plus an additional sample of 8 QSO spectra from the literature. Using high resolution and large box size cosmological simulations we reproduce the  $\Omega_{\text{CIV}}$  evolution, at least in the range  $z = 1.5 - 3$ , by extracting mock but realistic QSO spectra inside the cosmological boxes and subsequently fit the CIV lines with the public available software package VPFIT<sup>2</sup>. We also investigate the CIV column density distribution function, the  $b_{\text{CIV}}$  parameter probability distribution function and the  $b_{\text{CIV}} - N_{\text{CIV}}$  relation.

## 1.7 Early models of the IGM

Several models have been suggested for describing the physical structure of the Lyman- $\alpha$  forest absorption systems. All of the early models have been superseded by numerical cosmological simulations, which provide a largely successful description of the Lyman- $\alpha$  forest and associated absorption systems within the broader context of cosmological structure formation, and overall accuracy at the 10 percent level between prediction and observational properties

---

<sup>2</sup><http://www.ast.cam.ac.uk/~rfc/vpfit.html>

is achieved. Cosmological simulations will be extensively discussed in the next Chapter, while in this Section elements of those models are discussed since they continue to provide physical insight, and may still offer viable alternative descriptions of some absorption systems.

### Pressure-confined clouds

The earliest physical model for the absorbers was one in which the absorption features arise from distinct clouds pressure-confined by a hot IGM (Sargent et al. 1980). Denoting the cloud temperature and hydrogen number density by  $T_c$  and  $n_c$ , and those of the IGM by  $T_{\text{IGM}}$  and  $n_{\text{IGM}}$ , the condition of pressure equilibrium is  $n_c T_c = n_{\text{IGM}} T_{\text{IGM}}$ . Allowing for clouds photoionized by a QSO/AGN-dominated UV background, small enough to be Jeans stable and able to withstand thermal evaporation by the hot confining medium, while requiring the IGM to meet the Gunn-Peterson constraint, Sargent et al. (1980) found for the cloud parameters at  $z \approx 2.4$ ,  $n_c = 100 \text{ m}^{-3}$ ,  $T_c = 3 \times 10^4 \text{ K}$ ,  $n_{\text{IGM}} = 10 \text{ m}^{-3}$  and  $T_{\text{IGM}} = 3 \times 10^5 \text{ K}$ .

The pressure-confined models suffered from a serious shortcoming: a wide range of sizes was required to reproduce the range in observed HI column densities. The higher column density systems would need to be so large that they would become unstable under their own gravity. Jeans stability limits the size of a self-gravitating cloud of density  $n_c$  and temperature  $T_c$  to be sufficiently small that a sound wave can cross it in less than the time for it to gravitationally collapse (to ensure the internal gas pressure gradient of the cloud is able to balance its weight). A further failure of the model is that a system with a column density of  $N_{\text{HI}} = 10^{14} \text{ cm}^{-2}$  would have a typical size of 17 kpc. This conflicts with the sizes inferred from coincident absorbers along neighboring lines of sight to lensed QSO images, which give cloud sizes in excess of 70 kpc for systems with  $N_{\text{HI}} < 10^{14} \text{ cm}^{-2}$ .

Elements of the pressure-confined model, however, may still describe some absorption systems. The clouds could, for example, be confined by a wide range of pressures in different environments, which are themselves gravitationally confined (Baron et al. 1989). The association of metal absorption systems with galaxies suggests they may be pressure-confined systems within galactic haloes, as may be Lyman Limit Systems (Mo & Miralda-Escudé 1996).

### Dark matter minihaloes

A more viable physical model for the absorbers is the gravitational confinement by a dark matter halo. Rees (1986) recognized that the Lyman- $\alpha$  forest is a necessary consequence of the Cold Dark Matter scenario for structure formation (see Appendix A.4). The gas trapped in these haloes will produce absorption features with HI column densities and line widths comparable to those observed (Ikeuchi 1986; Rees 1986). A minihalo virialized at  $z_v = 3$  will be only a few kiloparsecs in size. A minihalo of mass  $10^9 M_\odot$  would have an adequate circular velocity to confine the gas. The HI column densities produced will range roughly over  $13 < \log_{10} N_{\text{HI}} < 16$ .

Bond et al. (1988) point out that the gas will in general be in a dynamical state, either collapsing with an increasing core density or expanding after photoionization. Gas associated with the minihaloes gives rise to absorption features with  $N_{\text{HI}} \lesssim 10^{13} \text{ cm}^{-2}$  on scales of 100 kpc at  $z = 3$ . Even though the gas is in motion, the line profiles are found to remain nearly Doppler in shape, although broadened by the gas motion. In the idealized case of an isothermal gas in

free expansion, so that the gas profile is gaussian with a linear velocity profile  $v = v_c(r/r_c)$ , the Voigt profile is exactly preserved for lines of sight passing through the cloud, but with the Doppler parameter broadened to  $b = (2k_B T/m_H + v_c^2)^{1/2}$ . Typical temperatures in the inner region of minihaloes with circular velocities of  $v_c \simeq 40 \text{ km s}^{-1}$  (which give rise to systems with  $N_{\text{HI}} > 10^{15} \text{ cm}^{-2}$ ) are  $30 - 40 \times 10^4 \text{ K}$ , consistent with the measurements of Rauch et al. (1996) for metal absorption systems expected to be associated with comparable HI column densities. In the inner  $10 - 30 \text{ kpc}$ , temperatures of  $T \simeq 30 - 60 \times 10^4 \text{ K}$  are predicted, with substantial deviations from thermal equilibrium due to adiabatic heating of the infalling gas. In the outer  $10 - 100 \text{ kpc}$ , the gas is significantly adiabatically cooled by Hubble expansion. Temperatures half these values are expected in smaller haloes of  $v_c \simeq 20 \text{ km s}^{-1}$ .

Of course, there is a limit to the degree of realism with which this model can describe the observed properties of gas clouds, and even the notion of distinct “objects” is misleading. In fact, hydrodynamical simulations show that in a hierarchical universe at intermediate redshift ( $z \sim 2$ ), most baryonic matter may not have settled in spherical, or rotationally supported virialized objects.

## Caustics and sheets

A gravitational perturbation will generically form sheets since the enhanced density along a given direction will accelerate the collapse along that direction. Once a growing density fluctuation becomes non-linear, it will produce a caustic. The caustic formation is well-described by the Zel’dovich approximation (Zel’dovich 1970)

$$\mathbf{x}(\mathbf{q}, t) = \mathbf{q} - D(t)\nabla\Psi(\mathbf{q}); \quad \mathbf{v}(\mathbf{q}, t) = -a\dot{D}(t)\nabla\Psi(\mathbf{q}), \quad (1.21)$$

where  $\mathbf{x}$  is the actual comoving position of a particle with initial comoving position  $\mathbf{q}$ ,  $\mathbf{v} = a\dot{\mathbf{x}}$  is the peculiar velocity,  $\Psi(\mathbf{q})$  describes the initial deformation of the density field, the gradient is with respect to  $\mathbf{q}$ , and  $D(t)$  is the growth factor for linear perturbations  $D(t) = (\dot{a}/a) \int^a da/\dot{a}^3$  (Peebles 1993). The physical radius is related to the comoving radius through  $\mathbf{r} = a(t)\mathbf{x}$ , where  $a(t) = 1/(1+z)$  is the expansion factor of the Universe at the epoch corresponding to redshift  $z$ . Conservation of mass gives for the density, up until the time of caustic formation,  $\rho(\mathbf{x}, t) = \rho(\mathbf{q})/|d^3\mathbf{x}/d^3\mathbf{q}|$ , where the denominator is the determinant of the Jacobian of the coordinate transformation. For one dimensional collapse, the density prior to caustic formation grows as  $\rho(x, t) = \rho_0 a(t)^{-3}/[1 - D(t)d^2\Psi/dq^2]$ , which is exact for the 1D collapse of a slab. Gravitational instability ensures that a uniform ellipsoidal density perturbation will collapse most rapidly along its shortest axis, forming a “Zel’dovich pancake”.

Some IGM models were built by using this approximation or simple modifications to account for baryonic pressure. Baryons infalling along with the dark matter will produce Lyman- $\alpha$  forest absorption features. The line profiles will become distorted at the time the caustic forms before the baryons come into dynamical equilibrium (McGill 1990; Miralda-Escudé & Rees 1993; Meiksin 1994). The HI column densities produced will range over about  $13 < \log_{10} N_{\text{HI}} < 15$ , with post-shock temperatures peaking at  $50 - 60 \times 10^4 \text{ K}$  (Meiksin 1994).

## Galactic models

Ever since the earliest papers on the Lyman- $\alpha$  forest, it was recognized that galaxies should give rise to intervening absorption systems. Their characteristics and frequency, however, are unclear. The interstellar medium of disk galaxies is expected to produce damped Lyman- $\alpha$  forest absorbers, although relatively few DLAs have been shown to arise from disks. Other suggestions include condensates in cooling outflows from dwarf galaxies (Wang 1995), the gas-rich dwarf galaxies themselves (York et al. 1986), debris from satellite galaxies lost through tidal stripping by a central galaxy or expelled by supernovae (Morris & van den Bergh 1994; Wang 1993), or pressure-confined clouds in a two-phase gaseous galactic halo medium (Mo & Miralda-Escudé 1996). The outflow model in particular may give rise to distorted absorption line features if a line of sight intercepts the outflowing diffuse gas.

Another suggestion (Salpeter 1993) is that the absorption lines arise from gas in extended disks with too low surface density to produce many stars. In this model, an inner disk gravitationally-confined region of radius about 15 kpc is surrounded by an extended pressure-confined disk of radius about 250 kpc. The inner region has a low gas surface density compared with most disk galaxies, but sufficiently large to produce a DLA feature in any line of sight passing through it. The outer region has such a low surface density that the hydrogen is photoionized by the metagalactic UV background. The outer region will give rise to Lyman- $\alpha$  forest features. The relative abundances of the various HI column densities is accounted for by the progressively diminishing geometric cross-section for increasing column densities. Once star formation begins, producing a starburst galaxy, metal-enriched gas ejected by the stars will accelerate the cooling and strengthen the burst, resulting in the expulsion of the gas in the central region and quenching further star formation. The result will be an outer gaseous disk, possibly enriched in gas and metals by a galactic fountain if material from the starburst falls onto the disk, and a very low surface brightness galaxy in the center.

### 1.7.1 The semianalytical model of Bi & Davidsen (1997)

In this Section we present the first model that overcame all the problems of the previous models and gave a consistent picture of the IGM. Bi & Davidsen (1997) performed a detailed statistical study of the evolution of structure in a photoionized intergalactic medium using analytical simulations to extend the calculation into the mildly non-linear density regime. Their work is based on a simple fundamental conjecture: that the probability distribution function of the density of baryonic diffuse matter in the universe is described by a lognormal (LN) random field. Starting with a suitably normalized power spectrum of primordial fluctuations in a universe dominated by cold dark matter, Bi & Davidsen (1997) compute the behavior of the baryonic matter, which moves slowly toward minima in the dark matter potential on scales larger than the Jeans length.

In their model the Lyman- $\alpha$  forest is not due to discrete clouds, but rather to fluctuations in a continuous intergalactic medium. At  $z = 3$ , typical clouds with measured neutral hydrogen column densities  $N_{\text{HI}} = 10^{15.3}, 10^{13.5}$ , and  $10^{11.5} \text{ cm}^{-2}$  correspond to fluctuations with mean total densities approximately 10, 1, and 0.1 times the universal mean baryon density. Perhaps surprisingly, fluctuations whose amplitudes are less than or equal to the mean density still appear as “clouds” because in their model more than 70% of the volume of the IGM at  $z = 3$

is filled with gas at densities below the mean value. The model predicts that about 80% of the baryons in the universe are associated with Lyman- $\alpha$  forest features with  $13 < \log N_{\text{HI}} < 15$  at  $z = 3$ , while 10% are in more diffuse gas with smaller column densities and 10% are in higher column density clouds and in collapsed structures, such as galaxies and quasars. It also requires that absorbers at  $z = 3$  with column densities higher than about  $10^{16} \text{ cm}^{-2}$  – Lyman limit systems, sub-DLAs and Damped Lyman- $\alpha$  Systems – represent a separate population that has collapsed out of the IGM.

The approach of Bi & Davidsen (1997) has the merit of great simplicity, with numerous predictions following from a small number of fundamental assumptions. As just mentioned the most important of these assumptions is that the probability distribution function of the density of diffuse matter in the Universe is described by a lognormal random field. The lognormal distribution has the correct asymptotic behavior on large scales or at very early times where the IGM evolves linearly, and it matches the isothermal hydrostatic solution on very small scales such as that for intracluster gas. They further assume that the IGM is photoionized by a metagalactic UV radiation field whose intensity is sufficient at  $z = 2 - 4$  to reduce the neutral fraction of hydrogen to less than  $10^{-5}$  for gas at the mean density.

### The lognormal density field

The density distribution of the IGM is assumed to be a lognormal random field,

$$n(\mathbf{x}) = n_0 \exp \left[ \delta_0(\mathbf{x}) - \frac{\langle \delta_0^2 \rangle}{2} \right], \quad (1.22)$$

where  $n_0$  is the mean number density and  $\delta_0$  is a Gaussian random field derived from the density contrast  $\delta_{\text{DM}}$  of dark matter :

$$\delta_0(\mathbf{x}) \equiv \frac{1}{4\pi x_b^2} \int \frac{\delta_{\text{DM}}(\mathbf{x}_1)}{|\mathbf{x} - \mathbf{x}_1|} e^{-\frac{|\mathbf{x} - \mathbf{x}_1|}{x_b}} d\mathbf{x}_1 \quad \text{or} \quad \delta_0(\mathbf{k}) \equiv \frac{\delta_{\text{DM}}(\mathbf{k})}{1 + x_b^2 k^2}, \quad (1.23)$$

in the comoving space or the Fourier space, respectively. The comoving scale  $x_b$  is defined by

$$x_b \equiv \frac{1}{H_0} \left( \frac{2\gamma k T_m}{3\mu m_p \Omega(1+z)} \right)^{\frac{1}{2}}, \quad (1.24)$$

where  $T_m$  and  $\mu$  are the mean temperature and molecular weight of the IGM,  $\Omega$  is the cosmological density parameter of total mass and  $\gamma$  is the ratio of specific heats. The scale  $x_b$  is  $2\pi$  times smaller than the standard Jeans length  $\lambda_b \equiv v_s(\pi/G\rho_c)^{1/2}$ , where  $v_s$  is the sound speed in the IGM and  $\rho_c$  is the total cosmological mass density (Peebles 1980).

The LN approach was introduced by Coles & Jones (1991) to describe the non-linear evolution of dark matter. Here it is applied to the baryonic matter in the IGM. We first discuss the physical background of the LN approach.

At early epochs  $z \gg 1$  or on large scales  $x \rightarrow \infty$ , fluctuations are small, so we have  $\delta(\equiv n/n_0 - 1) \simeq \delta_0$  in Eq. (1.22). This is just the expected linear evolution of the IGM (Peebles 1974; Fang et al. 1993). On very small scales, we have  $|\mathbf{x} - \mathbf{x}_1| \ll x_b$  in Eq. 1.23;

thus Eq. 1.22 becomes the well-known isothermal hydrostatic solution, which describes highly clumped structures such as intracluster gas,

$$n \propto \exp\left(-\frac{\mu m_p}{\gamma k T} \psi_{\text{DM}}\right), \quad (1.25)$$

where  $\psi_{\text{DM}}$  is the dark matter potential (Sarazin & Bahcall 1977).

During the linear evolution of dark matter fluctuations,  $\psi_{\text{DM}}$  is constant, being as small as that at the decoupling time. Therefore, one expects that the potential would remain linear much longer than the density; consequently one can simply use the unchanged primordial potential in the whole calculation. As long as the dark matter potential is fixed, baryons will move toward the minima in the potential, which are 2-dimensional pancakes. If the evolution is long enough, the final configuration will be the isothermal hydrostatic solution. In the LN distribution, the 3-D configuration of the IGM is uniquely determined by the primordial distribution. Among all smooth functions that can link the known linear solution and the hydrostatic solution asymptotically, the LN function is the simplest one.

Hydrogen atoms in the IGM are photo-ionized by the UV background radiation, which is assumed to be  $J(\nu) = J_{21} \times 10^{-21} (\nu_0/\nu)^{1.5}$  ergs s<sup>-1</sup> Hz<sup>-1</sup> cm<sup>-2</sup> sr<sup>-1</sup>, where  $\nu_0$  is the frequency of the HI ionization threshold. The optical depth is proportional to the combination of  $J_{21}$ ,  $\Omega_b$  and  $h$  through  $\frac{(\Omega_b h)^2}{h J_{21}}$ . Bi & Davidsen (1997) fix  $\Omega_b$  to the primordial density,  $\Omega_b = 0.015 h^{-2}$  (Walker et al. 1991) and let  $J_{21}$  be a free parameter.

## Outcomes of the model

In the following we report the main conclusions of the Bi & Davidsen (1997) semianalytical model, later confirmed and extended by hydrodynamical simulations (e.g. Theuns et al. 1998):

- *The nature of the IGM in the redshift range  $z = 2 - 4$ .* The fluctuation variance of the density field of the IGM is close to unity in the redshift range ( $z = 2 \rightarrow 4$ ) where most of the Lyman- $\alpha$  forest is observed. This is a special phase in the evolution of the IGM when both overdense and underdense clumps are significant in appearance. Mass is moving generally from low densities to high densities, but has not yet arrived at the final virialized stage when the clumps are stable in proper space. Dark matter fluctuations would act like magnets that attract the baryonic medium to their potential wells, but do not necessarily confine the baryons. There are no distinguished thermal phases in the medium from which it is possible to discriminate different thermal components. The whole medium appears as one diffuse and continuous fluid. This median fluctuation of the IGM is important in producing the correct HI opacity and the number of Lyman- $\alpha$  lines observed. The lognormal hypothesis appears to provide an excellent description of the density distribution of intergalactic gas in the non-linear regime at  $z < 4$ .
- *The structure within Lyman- $\alpha$  clouds.* In the diffuse IGM, the term ‘‘clouds’’ actually refers to all fluctuated density clumps which have either overdensity above the mean or underdensity below the mean. In fact, typical clouds and thus typical Lyman- $\alpha$  lines have just the mean mass density. For example, at redshift 3, clouds of column density  $10^{11.5}$ ,  $10^{13.5}$  and  $10^{15.3}$  cm<sup>-2</sup> have mass density that is 0.1, 1 and 10 times the mean. The

variation of (neutral) density within a cloud is best described by an exponential profile that peaks at the cloud center and declines outside the Jeans length. The origin of the density wing is actually due to the fluctuation nature of the IGM in which it is impossible to distinguish one cloud from another in space. The peculiar velocity causes mass to fall toward the cloud center where the dark matter potential is minimized in comoving space. However, all clouds below  $10^{16} \text{ cm}^{-2}$  are still expanding in proper space, because the peculiar velocity is not large enough to overcome the Hubble velocity. For clouds above  $10^{13.5} \text{ cm}^{-2}$ , the velocity is comparable to the thermal  $b$  parameter, so the resulting profile will be narrower. For an individual cloud, the velocity could appear as turbulent motions because it is not necessarily symmetric.

- *The number density of clouds.* The total number of all clumps in the IGM is determined by the number of dark matter potential wells when smoothed on the Jeans scale. Since the Jeans length is roughly a constant in comoving space, the “global” number will be more or less fixed. The same cloud with a high column density will evolve to lower and lower column densities at later times because the proper density is decreasing. The column density distribution function at one redshift can be identified with that at a lower redshift by shifting the column density by a constant decreasing factor. Thus we expect to have more low column density absorbers at  $z = 2$  than at  $z = 4$ .

## 1.8 Physical insights into the nature of the Lyman- $\alpha$ forest

Schaye (2001) showed that many aspects of the physical picture of the forest, in particular the fact that the absorption arises in extended structures of moderate overdensities that contain a large fraction of the baryons in the Universe, can be derived directly from the observations without making any specific assumptions about the presence and distribution of dark matter, the values of the cosmological parameters or the mechanism for structure formation. The key physical argument is that the absorbers will generally not be far from hydrostatic equilibrium, i.e. along any line of sight intersecting a gravitationally confined gas cloud, the size of the region over which the density is of order the maximum density is typically of order the local Jeans length. This is true for overdense absorbers, regardless of the shape of the cloud and regardless of whether the cloud as a whole is in dynamical equilibrium. The simple analytic model is used to derive the mass distribution of the photoionized gas directly from the observed column density distribution. It is demonstrated that the shape of the column density distribution, in particular the observed deviations from a single power law, and its evolution with redshift, reflect the shape of the matter distribution and can be understood in terms of the growth of structure via gravitational instability in an expanding universe.

### 1.8.1 Physical properties

Consider a cloud with characteristic density  $n_{\text{H}}$ , the dynamical (or free-fall) time is

$$t_{\text{dyn}} \equiv \frac{1}{\sqrt{G\rho}} \sim 1.0 \times 10^{15} \text{ s} \left( \frac{n_{\text{H}}}{1 \text{ cm}^{-3}} \right)^{-1/2} \left( \frac{1-Y}{X} \right)^{1/2} \left( \frac{f_{\text{g}}}{0.16} \right)^{1/2}, \quad (1.26)$$

where  $f_{\text{g}}$  is the gas mass fraction (stars and molecules do not contribute to  $f_{\text{g}}$ ), while  $X = 0.76$  and  $Y = 0.24$  are, respectively, the baryonic mass fraction in hydrogen and helium. In cold, collapsed clumps  $f_{\text{g}}$  could be close to unity, but on the scales of interest here  $f_{\text{g}}$  will not be far from its universal value,  $f_{\text{g}} \approx \Omega_{\text{b}}/\Omega_{\text{m}}$ . We define  $L$  to be the characteristic size of the cloud, i.e. the length of the part of the cloud over which the density is of order the characteristic density. The sound crossing time is then

$$t_{\text{sc}} \equiv \frac{L}{c_{\text{s}}} \sim 2.0 \times 10^{15} \text{ s} \left( \frac{L}{1 \text{ kpc}} \right) T_4^{-1/2} \left( \frac{\mu}{0.59} \right)^{1/2}, \quad (1.27)$$

where  $c_{\text{s}}$  is the sound speed in an ideal, monatomic gas with the ratio of specific heats  $\gamma = 5/3$ ,  $T \equiv T_4 \times 10^4 \text{ K}$ , and  $\mu$  is the mean molecular weight. In what follows  $\mu$  will be set equal to the value appropriate for a fully ionized, primordial plasma,  $\mu = 4/(8 - 5Y) \approx 0.59$ .

The hydrostatic equilibrium equation is  $dP/dr = -G\rho M/r^2$ , where  $M$  is the mass interior to  $r$ . Since the pressure  $P \sim c_{\text{s}}^2 \rho$ , this implies  $c_{\text{s}}^2 \rho/L \sim G\rho^2 L$ , i.e.  $t_{\text{sc}} \sim t_{\text{dyn}}$ . The condition  $t_{\text{sc}} = t_{\text{dyn}}$  defines the Jeans length,

$$L_{\text{J}} \equiv \frac{c_{\text{s}}}{\sqrt{G\rho}} \sim 0.52 \text{ kpc} n_{\text{H}}^{-1/2} T_4^{1/2} \left( \frac{f_{\text{g}}}{0.16} \right)^{1/2}, \quad (1.28)$$

and the related ‘‘Jeans column density’’ reads:

$$N_{\text{H,J}} \equiv n_{\text{H}} L_{\text{J}} \sim 1.6 \times 10^{21} \text{ cm}^{-2} n_{\text{H}}^{1/2} T_4^{1/2} \left( \frac{f_{\text{g}}}{0.16} \right)^{1/2}. \quad (1.29)$$

If  $t_{\text{sc}} \gg t_{\text{dyn}}$ , then the cloud is Jeans unstable and will either fragment or, since  $v \sim L/t_{\text{dyn}} \gg c_{\text{s}}$ , shock to the virial temperature. In either case, equilibrium will be restored on the dynamical timescale. If, on the other hand,  $t_{\text{sc}} \ll t_{\text{dyn}}$ , then the cloud will expand or evaporate and equilibrium will be restored on the sound crossing timescale.

It is useful to define the notion of ‘‘local hydrostatic equilibrium’’, i.e. the region of the cloud where  $t_{\text{sc}} \sim t_{\text{dyn}}$  locally, but not necessarily for the cloud as a whole. In other words, along any sightline through the evolving cloud, which will in general not be spherical, the length of the region for which the density is of order the maximum density, will be of order the local Jeans length. In case of substructures, the condition of local hydrostatic equilibrium applies to each density maximum along the sightline.

Large departures from local hydrostatic equilibrium do occur when the pressure changes on a timescale much shorter than  $t_{\text{dyn}}$ . For the Lyman- $\alpha$  forest, sudden heating is relevant: during reionization the temperature of the diffuse IGM is rapidly raised by several orders of magnitude to at least  $10^4 \text{ K}$ , but even to  $\gtrsim 10^5 \text{ K}$ , depending on the speed of reionization and

the spectrum of the ionizing radiation. Because of the sudden increase in the Jeans length during reionization,  $t_{\text{sc}} \ll t_{\text{dyn}}$  for most of the gas. Therefore the gas can be clumpy on scales smaller than the Jeans length, until pressure forces have had time to restore local hydrostatic equilibrium (e.g. Gnedin & Hui 1998).

Pressure forces can only smooth the gas distribution on scales smaller than the sound horizon, which is defined by the condition  $t_{\text{sc}} \sim H^{-1}$ . Hydrostatic equilibrium would then require  $t_{\text{dyn}} \sim H^{-1}$ , which implies  $\rho \sim \bar{\rho}$ . Hence, the assumption of local hydrostatic equilibrium may break down for absorbers with characteristic densities smaller than the cosmic mean. The precise value of the sound horizon depends on the thermal history of the IGM. After reionization, the temperature of the low density IGM is expected to drop. At very high redshift ( $z > 7$ ) the IGM can cool efficiently through inverse Compton scattering off the microwave background, but after that the main cooling mechanism is adiabatic expansion and the cooling time is thus of order the Hubble time. Then, for  $z < z_{\text{reion}}$ , the sound horizon is greater than  $c_s/H$ , which implies that the statement that local hydrostatic equilibrium is only a good approximation for overdense absorbers, is conservative.

Schaye (2001) considered only optically thin clouds ( $N_{\text{HI}} < 10^{17} \text{ cm}^{-2}$ ), for which the ionization correction can be computed analytically. The neutral fraction of a highly ionized, optically thin gas is

$$\frac{n_{\text{HI}}}{n_{\text{H}}} = n_{\text{e}} \beta_{\text{HII}} \Gamma^{-1} \sim 0.46 n_{\text{H}} T_4^{-0.76} \Gamma_{12}^{-1}, \quad (1.30)$$

where  $\beta_{\text{HII}} \approx 4 \times 10^{-13} T_4^{-0.76} \text{ cm}^3 \text{ s}^{-1}$  and  $\Gamma \equiv \Gamma_{12} \times 10^{-12} \text{ s}^{-1}$  are, respectively, the hydrogen recombination and photoionization rates and  $n_{\text{e}}$  is the number density of free electrons. The photoionization rate corresponding to a UV background intensity of  $J(\nu) \text{ erg s}^{-1} \text{ cm}^{-2} \text{ sr}^{-1} \text{ Hz}^{-1}$  is

$$\Gamma = \int_{\nu_{\text{L}}}^{\infty} \frac{4\pi J(\nu) \sigma(\nu)}{h\nu} d\nu, \quad (1.31)$$

where  $\sigma$  is the cross-section for photoionization and  $\nu_{\text{L}}$  is the frequency at the Lyman limit. At redshifts  $2 < z < 4$ , studies of the proximity effect find  $\Gamma \sim 10^{-12} \text{ s}^{-1}$  with a relative uncertainty of order unity (Scott et al. 2000), which is in reasonable agreement with models of the UV background from quasars (e.g. Haardt & Madau 1996). At low redshift ( $z \lesssim 0.5$ ) the intensity of the UV background is thought to be considerably lower,  $\Gamma \approx 10^{-14} - 10^{-13} \text{ s}^{-1}$  (e.g. Davé & Tripp 2001).

Finally,  $T \sim 10^4 \text{ K}$  is likely to be a good approximation for the temperature of the Lyman- $\alpha$  forest, although a somewhat higher temperature could be appropriate at densities  $n_{\text{H}} \lesssim 10^{-4} \text{ cm}^{-3}$  ( $\delta \simeq 10$  at  $z \sim 3$ ), if galactic winds are important.

In conclusion, using just the condition  $t_{\text{sc}} \sim t_{\text{dyn}}$  and an estimate of the temperature ( $T \sim 10^4 \text{ K}$ ) and ionization rate ( $\Gamma \sim 10^{-12} \text{ s}^{-1}$  at  $z \sim 3$ ), Schaye (2001) showed that the Lyman- $\alpha$  forest absorbers must be extended structures of low overdensity. With these assumptions, the conclusion that the low column density absorbers contain a large fraction of the baryons, follows directly from the observed column density distribution.

Scaling relations were derived for the radial sizes and characteristic densities of the absorbers. This led to several new insights: the shape of the column density distribution, in particular the deviations from a single power law, and its evolution with redshift, reflect the

shape of the matter distribution, which agrees remarkably well with the shape of the distribution produced by the growth of structure in an expanding universe via gravitational instability.

Although the above derived properties of the Lyman- $\alpha$  forest absorbers are not particularly sensitive to the presence of dark matter, dark matter may still be required to form the observed structure in the forest from the small-amplitude fluctuations ( $\delta \sim 10^{-5}$ ) observed at  $z \sim 10^3$  in the cosmic microwave background. In fact, it is well known that if gravitational instability is responsible for structure formation, then dark matter (or a modification of gravity) is required to grow the observed (non-linear) structure.

# Chapter 2

## Numerical Cosmology

### 2.1 Methods of numerical simulations

In Appendix A.4 we introduced the basic equations that describe the structure formation and evolution in the gravitational instability scenario. Within the currently leading theoretical model for structure formation small fluctuations that were imprinted in the primordial density field are amplified by gravity, eventually leading to non-linear collapse and the formation of dark matter haloes. Gas then falls into the potential wells provided by the dark matter haloes where it is shock-heated and then cooled radiatively, allowing a fraction of the gas to collapse to such high densities that star formation can ensue. The formation of galaxies hence involves dissipative gas dynamics coupled to the nonlinear regime of gravitational growth of structure. The substantial difficulty of this problem is made worse by the inherent three-dimensional character of structure formation in a  $\Lambda$ CDM ( $\Lambda$  Cold Dark Matter, see Appendix A.5) universe, where, due to the shape of the primordial power spectrum, a large range of wave modes becomes nonlinear in a very short time, resulting in the rapid formation of objects with a wide range of masses which merge in geometrically complex ways into ever more massive systems. Therefore, direct numerical simulations of structure formation which include hydrodynamics arguably provide the only method for studying this problem in its full generality.

Hydrodynamic methods used in cosmological simulations of galaxy formation can be broken down into two primary classes: techniques using an *Eulerian* grid, including Adaptive Mesh Refinement (AMR) techniques, and those which follow the fluid elements in a *Lagrangian* manner using gas particles, such as Smoothed Particle Hydrodynamics (SPH).

### 2.2 Gravitational force description: N-body simulations

It is possible to represent part of the expanding Universe as a “box” containing a large number  $N$  of point masses interacting through their mutual gravity. This box, typically a cube, must be at least as large as the scale at which the Universe becomes homogeneous if it is to provide a “fair sample” which is representative of the Universe as a whole. It is common practice to take the cube as having periodic boundary conditions in all directions, which also helps in some of the computational techniques by allowing Fourier methods to be employed in summing the N-body forces. A number of numerical techniques are available at the present

time; they differ, for the most part, only in the way the forces on each particle are calculated. We describe some of the most popular methods here:

- **Direct summation:** the simplest way to compute the non-linear evolution of a cosmological fluid is to represent it as a discrete set of particles, and then sum the (pairwise) interactions between them directly to calculate the Newtonian forces. Such calculations are often called particle-particle, or PP, calculations. With the adoption of a small timestep, one can use the resulting acceleration to update the particle velocity and then its position. New positions can then be used to recalculate the interparticle forces, and so on. However, there is a numerical problem with summation of the forces: the Newtonian gravitational force between two particles increases as the particles approach each other and it is therefore necessary to choose an extremely small timestep to resolve the large velocity changes this induces. A very small timestep would require the consumption of enormous amounts of CPU (Central Processing Unit) time and, in any case, computers cannot handle the formally divergent force terms when the particles are arbitrarily close to each other. One usually avoids these problems by treating each particle not as a point mass, but as an extended body. The practical consequence of this is that one modifies the Newtonian force between particles by putting

$$\mathbf{F}_{ij} = \frac{Gm^2(\mathbf{x}_j - \mathbf{x}_i)}{(\epsilon^2 + |\mathbf{x}_i - \mathbf{x}_j|^2)^{3/2}}, \quad (2.1)$$

where the particles are at positions  $\mathbf{x}_i$  and  $\mathbf{x}_j$  and they all have the same mass  $m$ ; the form of this equation avoids infinite forces at zero separations. The parameter  $\epsilon$  in Equation (2.1) is usually called the *softening length* and it acts to suppress two-body forces on small scales. This is equivalent to replacing point masses by extended bodies with a size of order  $\epsilon$ . Since we are not supposed to be dealing with the behaviour of a set of point masses anyway, the introduction of a softening length is quite reasonable but it means one cannot trust the distribution of matter on scales of order  $\epsilon$  or less. The crucial limitation of these methods is that they tend to be very slow, with the computational time required scaling roughly as  $N^2$  (where  $N$  is the number of particles and  $N(N-1)/2$  are the evaluations of Eq. (2.1) required at each timestep).

- **Particle-mesh techniques:** the usual method for improving upon direct N-body summation for computing inter-particle forces is some form of “particle-mesh”, or PM, scheme. In this scheme the forces are solved by assigning mass points to a regular grid and then solving Poisson’s equation on it. The use of a regular grid with periodic boundary conditions allows one to use Fast Fourier Transform (FFT) methods to recover the potential, which leads to a considerable increase in speed. Without enter in details, the calculation of the forces between particles can be speeded up by computing them in Fourier space. An FFT is basically of order  $N \log N$  in the number of grid points and this represents a substantial improvement for large  $N$  over the direct particle-particle summation technique. The price to be paid for this is that the Fourier summation method implicitly requires that the simulation box has periodic boundary conditions: this is probably the most reasonable choice for simulating a “representative” part of the Universe, so this

does not seem to be too high price. The potential weakness of this method is the comparatively poor force resolution on small scales because of the finite spatial size of the mesh. A substantial increase in spatial resolution can be achieved by using instead a hybrid “particle-particle-particle-mesh” method, which solves the short range forces directly (PP) but uses the mesh to compute those of longer range (PM); hence PP + PM = P<sup>3</sup>M, the usual name of such codes. Here, the short-range resolution of the algorithm is improved by adding a correction to the mesh force. This contribution is obtained by summing directly all the forces from neighbours within some fixed distance  $r_s$  of each particle. A typical choice for  $r_s$  will be around three grid units. Alternatively, one can use a modified force law on these small scales to assign particular density profile to the particles, similar to the softening procedure demonstrated in Equation (2.1). This part of the force may well be quite slow, so it is advantageous merely to calculate the short-range force at the start for a large number of points spaced linearly in radius and then find the actual force by simple interpolation. The long-range part of the force calculation is done by a variant of the PM method described earlier.

- **Tree codes:** An alternative procedure for enhancing the force resolution of a particle code whilst keeping the necessary demand on computational time within reasonable limits is to adopt a hierarchical subdivision procedure. The generic name given to this kind of technique is “tree code”. The basic idea is to treat distant clumps of particles as single massive pseudo-particles. The usual algorithm involves a mesh which is divided into cells hierarchically in such a way that every cell which contains more than one particle is divided into  $2^3$  sub-cells. If any of the resulting sub-cells contains more than one particle, that cell is subdivided again. There are some subtleties involved with communicating particle positions up and down the resulting “tree”, but it is basically quite straightforward to treat the distant forces using the coarsely grained distribution contained in the high level of the tree, while short-range forces use the finer grid. The greatest problem with such codes is that, although they run quite quickly in comparison with particle-mesh methods with the same resolution, they do require considerable memory resources. It is possible to improve the tree codes allowing the computation of long-range forces with a particle-mesh (PM) algorithm, with the tree algorithm supplying short-range gravitational interactions only. This TreePM method can substantially speed up the computation while maintaining the large dynamic range and flexibility of the tree algorithm. For our work we used the TreePM formulation of GADGET-2, presented in the next Session.

## 2.3 Gravity + gas physics: GADGET-2

In the previous Section we have dealt exclusively with the behaviour of (dark plus baryonic) matter under its self-gravity. Now we add the baryonic hydrodynamics treatment. Compared to gravity, much larger conceptual differences exist between the different hydrodynamical methods employed in current cosmological codes. Traditional Eulerian methods discretize space and represent fluid variables on a mesh, while Lagrangian methods discretize mass, using, for example, a set of fluid particles to model the flow. Both methods have many applications in cosmology. Mesh-based codes include algorithms with a fixed mesh and, more recently, also with adaptive

meshes. Lagrangian codes have almost all employed smoothed particle hydrodynamics thus far although this is not the only possibility.

Mesh codes offer better resolving power for hydrodynamical shocks, with some methods being able to capture shocks without artificial viscosity (see below), and with very low residual numerical viscosity. However, static meshes are only poorly suited for the high dynamic range encountered in cosmology. Even for meshes as large as  $1024^3$ , individual galaxies in a cosmological volume are poorly resolved, leaving no room for resolving internal structure such as bulge and disk components. A potential solution is provided by new generations of adaptive mesh refinement codes, which begin to be more widely used in cosmology. Some drawbacks of the mesh remain however even here. For example, the dynamics is in general not Galilean invariant, there are advection errors, and there can be spurious generation of entropy due to mixing (e.g. Abel et al. 2002; Kravtsov et al. 2002; Refregier & Teyssier 2002; Motl et al. 2004).

In contrast, Lagrangian methods like SPH are particularly well-suited to follow the gravitational growth of structure, and to automatically increase the resolution in the central regions of galactic haloes, which are the regions of primary interest in cosmology. The accurate treatment of self-gravity of the gas in a fashion consistent with that of the dark matter is a further strength of the particle-based SPH method. Another fundamental difference with mesh based schemes is that thermodynamic quantities advected with the flow do not mix between different fluid elements at all, unless explicitly modelled. An important disadvantage of SPH is that the method has to rely on an artificial viscosity for supplying the necessary entropy injection in shocks. The latter are broadened over the SPH smoothing scale and not resolved as true discontinuities (Springel et al. 2001; Springel 2005).

In this Section we focus on the cosmological simulation code GADGET-2<sup>1</sup> and, in particular, on the “entropy conserving” formulation of SPH presented in Springel & Hernquist (2002) and Springel (2005). GADGET-2 is a massively parallel TreePM-SPH code, capable of following a collisionless fluid with the N-body method, and an ideal gas by means of smoothed particle hydrodynamics. The implementation of SPH manifestly conserves energy and entropy in regions free of dissipation, while allowing for fully adaptive smoothing lengths. Gravitational forces are computed with a hierarchical multipole expansion, which can optionally be applied in the form of a TreePM algorithm, where only short-range forces are computed with the tree method while long-range forces are determined with Fourier techniques. Time integration is based on a quasi-symplectic scheme where long-range and short-range forces can be integrated with different timesteps. Individual and adaptive short-range timesteps may also be employed. The domain decomposition used in the parallelization algorithm is based on a space-filling curve, resulting in high flexibility and tree force errors that do not depend on the way the domains are cut. The code is efficient in terms of memory consumption and required communication bandwidth. It has been used to compute the first cosmological N-body simulation with more than  $10^{10}$  dark matter particles, reaching a homogeneous spatial dynamic range of  $10^5$  per dimension in a three-dimensional box. It has also been used to carry out very large cosmological SPH simulations that account for radiative cooling and star formation, reaching total particle numbers of more than 250 millions.

---

<sup>1</sup><http://www.MPA-Garching.MPG.DE/gadget>

### 2.3.1 Collisionless dynamics

In GADGET-2 the continuum limit of non-interacting dark matter is described by the collisionless Boltzmann equation coupled to the Poisson equation in an expanding background universe, the latter taken normally as a Friedman-Lemaître model. Due to the high-dimensionality of this problem, these equations are best solved with the N-body method, where phase-space density is sampled with a finite number  $N$  of tracer particles.

The dynamics of these particles is then described by the Hamiltonian

$$H = \sum_i \frac{\mathbf{p}_i^2}{2m_i a(t)^2} + \frac{1}{2} \sum_{ij} \frac{m_i m_j \varphi(\mathbf{x}_i - \mathbf{x}_j)}{a(t)}, \quad (2.2)$$

where  $H = H(\mathbf{p}_1, \dots, \mathbf{p}_N, \mathbf{x}_1, \dots, \mathbf{x}_N, t)$ . The  $\mathbf{x}_i$  are comoving coordinate vectors, and the corresponding canonical momenta are given by  $\mathbf{p}_i = a^2 m_i \dot{\mathbf{x}}_i$ . The explicit time dependence of the Hamiltonian arises from the evolution of the scale factor  $a(t)$ , which is given by the Friedman-Lemaître model.

If periodic boundary conditions are assumed for a cube of size  $L^3$ , the interaction potential  $\varphi(\mathbf{x})$  is the solution of

$$\nabla^2 \varphi(\mathbf{x}) = 4\pi G \left[ -\frac{1}{L^3} + \sum_{\mathbf{n}} \tilde{\delta}(\mathbf{x} - \mathbf{n}L) \right], \quad (2.3)$$

where the sum over  $\mathbf{n} = (n_1, n_2, n_3)$  extends over all integer triplets. Note that the mean density is subtracted here, so the solution corresponds to the ‘‘peculiar potential’’, where the dynamics of the system is governed by  $\nabla^2 \phi(\mathbf{x}) = 4\pi G [\rho(\mathbf{x}) - \bar{\rho}]$ . For the discretized particle system, the peculiar potential is defined as

$$\phi(\mathbf{x}) = \sum_i m_i \varphi(\mathbf{x} - \mathbf{x}_i). \quad (2.4)$$

The single particle density distribution function  $\tilde{\delta}(\mathbf{x})$  is the Dirac  $\delta$ -function convolved with a normalized gravitational softening kernel of comoving scale  $\epsilon$ . For it, Springel (2005) employs the spline kernel (Monaghan & Lattanzio 1985) used in SPH and sets  $\tilde{\delta}(\mathbf{x}) = W(|\mathbf{x}|, 2.8\epsilon)$ , where  $W(r)$  is given by

$$W(r, h) = \frac{8}{\pi h^3} \begin{cases} 1 - 6 \left(\frac{r}{h}\right)^2 + 6 \left(\frac{r}{h}\right)^3 & 0 \leq \frac{r}{h} \leq \frac{1}{2}, \\ 2 \left(1 - \frac{r}{h}\right)^3 & \frac{1}{2} < \frac{r}{h} \leq 1, \\ 0 & \frac{r}{h} > 1. \end{cases} \quad (2.5)$$

For this choice, the Newtonian potential of a point mass at zero lag in non-periodic space is  $-Gm/\epsilon$ , the same as for a Plummer ‘‘sphere’’ of size  $\epsilon$ .

If desired, it is possible to simplify to Newtonian space by setting  $a(t) = 1$ , so that the explicit time dependence of the Hamiltonian vanishes. For vacuum boundaries, the interaction potential simplifies to the usual Newtonian form, i.e. for point masses it is given by  $\varphi(\mathbf{x}) = -G/|\mathbf{x}|$  modified by the softening for small separations.

Note that independent of the type of boundary conditions, a complete force computation involves a double sum, resulting in a  $N^2$ -scaling of the computational cost. This reflects the long-range nature of gravity, where each particle interacts with every other particle, making high-accuracy solutions for the gravitational forces very expensive for large  $N$ . Fortunately, the force accuracy needed for collisionless dynamics is comparatively modest. Force errors up to  $\sim 1$  per cent tend to only slightly increase the numerical relaxation rate without compromising results (Hernquist et al. 1993), provided the force errors are random. We note however that the situation is different for collisional N-body systems, such as star clusters. Here direct summation can be necessary to deliver the required force accuracy.

### 2.3.2 Hydrodynamics

Smoothed particle hydrodynamics uses a set of discrete tracer particles to describe the state of a fluid, with continuous fluid quantities being defined by a kernel interpolation technique (Gingold & Monaghan 1977; Lucy 1977; Monaghan 1992; Katz et al. 1996b). The particles with coordinates  $\mathbf{r}_i$ , velocities  $\mathbf{v}_i$ , and masses  $m_i$  are best thought of as fluid elements that sample the gas in a Lagrangian sense. The thermodynamic state of each fluid element may either be defined in terms of its thermal energy per unit mass,  $u_i$ , or in terms of the entropy per unit mass,  $s_i$ . Some tests showed that is preferable to use the latter as the independent thermodynamic variable evolved in SPH (Springel & Hernquist 2002). The formulation of SPH in Springel (2005) manifestly conserves both energy and entropy even when fully adaptive smoothing lengths are used. Traditional formulations of SPH on the other hand can violate entropy conservation in certain situations.

We begin by noting that it is more convenient to work with an entropic function defined by  $A \equiv P/\rho^\gamma$ , instead of directly using the entropy  $s$  per unit mass. Because  $A = A(s)$  is only a function of  $s$  for an ideal gas, we will often refer to  $A$  as “entropy”.

Of fundamental importance for any SPH formulation is the density estimate, which GADGET-2 does in the form

$$\rho_i = \sum_{j=1}^N m_j W(|\mathbf{r}_{ij}|, h_i), \quad (2.6)$$

where  $\mathbf{r}_{ij} \equiv \mathbf{r}_i - \mathbf{r}_j$ , and  $W(r, h)$  is the SPH smoothing kernel defined in Equation (2.5). In the “entropy formulation” of SPH, the adaptive smoothing lengths  $h_i$  of each particle are defined such that their kernel volumes contain a constant mass for the estimated density, i.e. the smoothing lengths and the estimated densities obey the (implicit) equations

$$\frac{4\pi}{3} h_i^3 \rho_i = N_{\text{sph}} \bar{m}, \quad (2.7)$$

where  $N_{\text{sph}}$  is the typical number of smoothing neighbours, and  $\bar{m}$  is an average particle mass. Note that in many other formulations of SPH, smoothing lengths are typically chosen such that the number of particles inside the smoothing radius  $h_i$  is nearly equal to a constant value  $N_{\text{sph}}$ .

Starting from a discretized version of the fluid Lagrangian, one can show (Springel & Hernquist 2002) that the equations of motion for the SPH particles are given by

$$\frac{d\mathbf{v}_i}{dt} = - \sum_{j=1}^N m_j \left[ f_i \frac{P_i}{\rho_i^2} \nabla_i W_{ij}(h_i) + f_j \frac{P_j}{\rho_j^2} \nabla_i W_{ij}(h_j) \right], \quad (2.8)$$

where the coefficients  $f_i$  are defined by

$$f_i = \left(1 + \frac{h_i}{3\rho_i} \frac{\partial \rho_i}{\partial h_i}\right)^{-1}, \quad (2.9)$$

and the abbreviation  $W_{ij}(h) = W(|\mathbf{r}_i - \mathbf{r}_j|, h)$  has been used. The particle pressures are given by  $P_i = A_i \rho_i^\gamma$ . Provided there are no shocks and no external sources of heat, the equations above already fully define reversible fluid dynamics in SPH. The entropy  $A_i$  of each particle stays constant in such a flow.

However, flows of ideal gases can easily develop discontinuities, where entropy is generated by microphysics. Such shocks need to be captured by an artificial viscosity in SPH. To this end, GADGET-2 uses a viscous force

$$\left. \frac{d\mathbf{v}_i}{dt} \right|_{\text{visc}} = - \sum_{j=1}^N m_j \Pi_{ij} \nabla_i \overline{W}_{ij}, \quad (2.10)$$

where  $\Pi_{ij} \geq 0$  is non-zero only when particles approach each other in physical space. The viscosity generates entropy at a rate

$$\frac{dA_i}{dt} = \frac{1}{2} \frac{\gamma - 1}{\rho_i^{\gamma-1}} \sum_{j=1}^N m_j \Pi_{ij} \mathbf{v}_{ij} \cdot \nabla_i \overline{W}_{ij}, \quad (2.11)$$

transforming kinetic energy of gas motion irreversibly into heat. The symbol  $\overline{W}_{ij}$  is here the arithmetic average of the two kernels  $W_{ij}(h_i)$  and  $W_{ij}(h_j)$ .

The Monaghan-Balsara form of the artificial viscosity (Monaghan & Gingold 1983; Balsara 1995) is probably the most widely employed parametrization of the viscosity in SPH codes. It takes the form

$$\Pi_{ij} = \begin{cases} (-\alpha c_{ij} \mu_{ij} + \beta \mu_{ij}^2) / \rho_{ij} & \text{if } \mathbf{v}_{ij} \cdot \mathbf{r}_{ij} < 0, \\ 0 & \text{otherwise,} \end{cases} \quad (2.12)$$

with

$$\mu_{ij} = \frac{h_{ij} \mathbf{v}_{ij} \cdot \mathbf{r}_{ij}}{|\mathbf{r}_{ij}|^2}. \quad (2.13)$$

Here  $h_{ij}$  and  $\rho_{ij}$  denote arithmetic means of the corresponding quantities for the two particles  $i$  and  $j$ , with  $c_{ij}$  giving the mean sound speed. The strength of the viscosity is regulated by the parameters  $\alpha$  and  $\beta$ , with typical values in the range  $\alpha \simeq 0.5 - 1.0$  and the frequent choice of  $\beta = 2\alpha$ .

Based on an analogy with the Riemann problem and using the notion of a signal velocity  $v_{ij}^{\text{sig}}$  between two particles, Monaghan (1997) derived a slightly modified parametrization of the viscosity, namely the *ansatz*

$$\Pi_{ij} = -\frac{\alpha}{2} \frac{w_{ij} v_{ij}^{\text{sig}}}{\rho_{ij}}. \quad (2.14)$$

In the simplest form, the signal velocity can be estimated as

$$v_{ij}^{\text{sig}} = c_i + c_j - 3w_{ij}, \quad (2.15)$$

where  $w_{ij} = \mathbf{v}_{ij} \cdot \mathbf{r}_{ij}/|\mathbf{r}_{ij}|$  is the relative velocity projected onto the separation vector, provided the particles approach each other, i.e. for  $\mathbf{v}_{ij} \cdot \mathbf{r}_{ij} < 0$ ; otherwise is set  $w_{ij} = 0$ . This gives a viscosity of the form

$$\Pi_{ij} = -\frac{\alpha (c_i + c_j - 3w_{ij}) w_{ij}}{2 \rho_{ij}}, \quad (2.16)$$

which is identical to Equation (2.12) if one sets  $\beta = 3/2\alpha$  and replaces  $w_{ij}$  with  $\mu_{ij}$ . The main difference between the two viscosities lies therefore in the additional factor of  $h_{ij}/r_{ij}$  that  $\mu_{ij}$  carries with respect to  $w_{ij}$ . In Equations (2.12) and (2.13), this factor weights the viscous force towards particle pairs with small separations. In fact, after multiplying with the kernel derivative, this weighting is strong enough to make the viscous force diverge as  $\propto 1/r_{ij}$  for small pair separations, unless  $\mu_{ij}$  in Equation (2.13) is softened at small separations by adding some fraction of  $h_{ij}^2$  in the denominator, as it is often done in practice.

In the equation of motion, the viscosity acts like an excess pressure

$$P_{\text{visc}} \simeq \frac{1}{2} \Pi_{ij} \rho_{ij}^2, \quad (2.17)$$

assigned to the particles. For the new form of the viscosity in Equation (2.16), this is given by

$$P_{\text{visc}} \simeq \frac{\alpha}{2} \gamma \left[ \frac{w_{ij}}{c_{ij}} + \frac{3}{2} \left( \frac{w_{ij}}{c_{ij}} \right)^2 \right] P_{\text{therm}}, \quad (2.18)$$

assuming roughly equal sound speeds and densities of the two particles for the moment. This viscous pressure depends only on a Mach-number like quantity  $w/c$ , and not explicitly on the particle separation or smoothing length. Springel (2005) found that the modified viscosity of Equation (2.16) gives equivalent or improved results in their tests compared to the standard formulation of Equation (2.12). In simulations with dissipation it has the advantage that the occurrence of very large viscous accelerations is reduced, so that a more efficient and stable time integration results. For these reason, they usually adopt the viscosity given by Equation (2.16) in GADGET-2.

The signal velocity approach naturally leads to a Courant-like hydrodynamical timestep of the form

$$\Delta t_i^{(\text{hyd})} = \frac{C_{\text{courant}} h_i}{\max_j (c_i + c_j - 3w_{ij})}, \quad (2.19)$$

which is adopted by GADGET-2. The maximum is here determined with respect to all neighbours  $j$  of particle  $i$ .

Following Balsara (1995) and Steinmetz (1996), GADGET-2 also uses an additional viscosity-limiter to alleviate spurious angular momentum transport in the presence of shear flows. This is done by multiplying the viscous tensor with  $(f_i + f_j)/2$ , where

$$f_i = \frac{|\nabla \times \mathbf{v}|_i}{|\nabla \cdot \mathbf{v}|_i + |\nabla \times \mathbf{v}|_i}, \quad (2.20)$$

is a simple measure for the relative amount of shear in the flow around particle  $i$ , based on standard SPH estimates for divergence and curl (Monaghan 1992).

The above equations for the hydrodynamics were all expressed using physical coordinates and velocities. In the actual simulation code, we use comoving coordinates  $\mathbf{x}$ , comoving momenta  $\mathbf{p}$  and comoving densities as internal computational variables, which are related to physical variables in the usual way. Since we continue to use the physical entropy, adiabatic cooling due to expansion of the universe is automatically treated accurately.

## 2.4 Additional physics

We use GADGET-2 code as the starting point for our implementation of chemical evolution in cosmological hydrodynamical simulations. The original GADGET-2 contains a fully adaptive timestepping, an explicit entropy-conserving formulation of the SPH scheme (as we described in the previous Section), heating from a uniform evolving UV background (Haardt & Madau 1996), radiative cooling from a zero metallicity cooling function, a sub-resolution model for star formation in multiphase interstellar medium (Springel & Hernquist 2003, see below) and a phenomenological model for feedback from galactic ejecta powered by explosions of Type II supernovae. Chemical enrichment was originally implemented by accounting only for the contribution of the SNII expected for a Salpeter Initial Mass Function (Salpeter 1955), under the Instantaneous Recycling Approximation (IRA) using global stellar yields.

As we describe in this Section, for our work we used the improved version of this simplified model presented in Tornatore et al. (2007). In particular, the new model:

- Includes the contributions of Type II and Type Ia supernovae (SNII, SNIa), along with low and intermediate mass stars (LIMS), to the chemical enrichment. Both SNIa and SNII contribute to thermal feedback.
- Accounts for the age of different stellar populations, so that metals and energy are released over different timescales by stars of different mass.
- Allows for different Initial Mass Functions (IMFs), so as to check the effect of changing its shape both on the stellar populations and on the properties of the diffuse gas.
- Allows different choices for stellar yields from SNII, SNIa and LIMS.
- Considers different schemes to distribute SN ejecta around star forming regions, so as to check in detail the effect of changing the numerical treatment of metal and energy spreading.

### 2.4.1 Radiative processes

While dark matter moves under the only influence of gravity, when orbit crossing occurs the gas, in addition, shocks and heats, converting the kinetic energy of bulk motion into thermal energy. Furthermore when the first structures begin to form, gas cools and sinks into high-density cores inside dark matter haloes.

In our simulations we compute radiative cooling for the gas considering the following processes:

- collisional excitation,
- collisional ionization,
- photoionization,
- recombination,
- dielectric recombination,
- free-free (bremsstrahlung) emission with a Gaunt factor:

$$g_{\text{ff}} = 1.1 + 0.34 \exp[-(5.5 - \log T)^2/3.0]. \quad (2.21)$$

In addition we include inverse Compton cooling off the microwave background at the rate (Ikeuchi & Ostriker 1986):

$$\Lambda_{\text{C}} = 5.41 \times 10^{-36} n_{\text{e}} T(1+z)^4 \text{ erg s}^{-1} \text{ cm}^{-3}. \quad (2.22)$$

Each SPH particle carries information about its density and temperature. In order to compute the radiative cooling rates associated to the previous processes we need to know the abundances of the different ionic species of the gas. Assuming for simplicity an optically thin gas of primordial composition (i.e. made only of hydrogen and helium) in ionization equilibrium with a given UV background, the equilibrium implies a balance between the creation and destruction rates for each ionic species:

$$\Gamma_{\text{eHI}} n_{\text{e}} n_{\text{HI}} + \Gamma_{\gamma\text{HI}} n_{\text{HI}} = \alpha_{\text{HII}} n_{\text{HII}} n_{\text{e}}, \quad (2.23)$$

$$\Gamma_{\text{eHeI}} n_{\text{e}} n_{\text{HeI}} + \Gamma_{\gamma\text{HeI}} n_{\text{HeI}} = (\alpha_{\text{HeII}} + \alpha_{\text{d}}) n_{\text{HeII}} n_{\text{e}}, \quad (2.24)$$

$$\begin{aligned} \Gamma_{\text{eHeII}} n_{\text{e}} n_{\text{HeII}} + \Gamma_{\gamma\text{HeII}} n_{\text{HeII}} + (\alpha_{\text{HeII}} + \alpha_{\text{d}}) n_{\text{HeII}} n_{\text{e}} = \\ = \alpha_{\text{HeIII}} n_{\text{HeIII}} n_{\text{e}} + \Gamma_{\text{eHeI}} n_{\text{e}} n_{\text{HeI}} + \Gamma_{\gamma\text{HeI}} n_{\text{HeI}}, \end{aligned} \quad (2.25)$$

$$\alpha_{\text{HeIII}} n_{\text{HeIII}} n_{\text{e}} = \Gamma_{\text{eHeII}} n_{\text{e}} n_{\text{HeII}} + \Gamma_{\gamma\text{HeII}} n_{\text{HeII}}. \quad (2.26)$$

The left-hand sides of Equations (2.23)–(2.26) express the rates at which HI, HeI, HeII and HeIII, respectively, are destroyed by collisional ionization, photoionization or recombination. The right-hand sides express the rates at which these species are created from other species by the same processes. Our collisional ionization ( $\Gamma_{\text{eHI}}$ , etc.) and recombination rates ( $\alpha_{\text{HII}}$ , etc.) are taken from Black (1981) and Cen (1992). The photoionization rates are defined by

$$\Gamma_{\gamma i} \equiv \int_{\nu_i}^{\infty} \frac{4\pi J(\nu)}{h\nu} \sigma_i(\nu) d\nu \quad \text{s}^{-1}, \quad (2.27)$$

where  $J(\nu)$  is the intensity of the UV background at the frequency  $\nu$  (in  $\text{erg s}^{-1} \text{ cm}^{-2} \text{ sr}^{-1} \text{ Hz}^{-1}$ ),  $\nu_i$  and  $\sigma_i(\nu)$  are, respectively, the threshold frequency and cross-section for photoionization of species  $i$ .

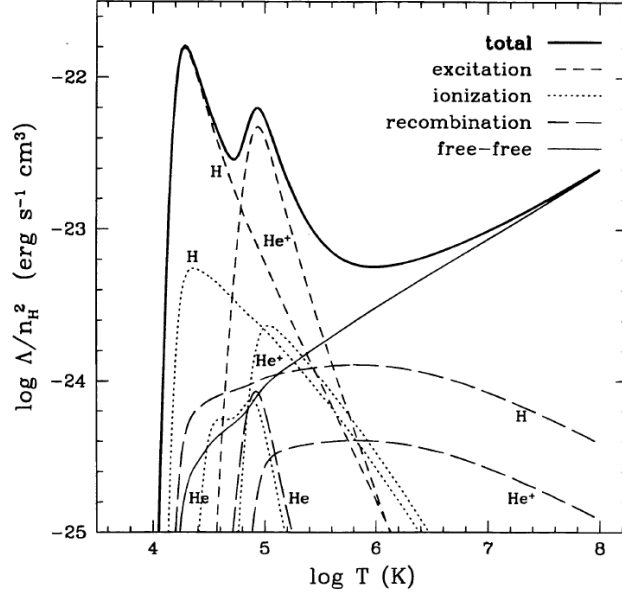


Figure 2.1: Cooling rates as a function of temperature for a primordial composition gas (H + He) in collisional equilibrium (for this plot  $\Lambda = C$ , see Eq. (2.31), and  $\text{H}=\text{HI}$ ,  $\text{He}=\text{HeI}$ ,  $\text{He}^+=\text{HeII}$ ). Heavy solid line shows the total cooling rate. The cooling is dominated by collisional excitation (short-dashed line) at low temperatures and by free-free emission (thin solid line) at high temperatures. Long-dashed and dotted lines show the contributions of recombination and collisional ionization, respectively. From Katz et al. (1996b).

Together with the rate balance Equations (2.23)–(2.26), there are the number conservation equations:

$$n_{\text{HII}} = n_{\text{H}} - n_{\text{HI}}, \quad (2.28)$$

$$n_{\text{e}} = n_{\text{HII}} + n_{\text{HeII}} + 2n_{\text{HeIII}}, \quad (2.29)$$

$$(n_{\text{HeI}} + n_{\text{HeII}} + n_{\text{HeIII}})/n_{\text{H}} = y \equiv Y/(4 - 4Y), \quad (2.30)$$

where  $n_{\text{H}} = \rho X/m_{\text{p}}$  is the number density of hydrogen nuclei ( $m_{\text{p}}$  being the proton mass) and  $Y$  is the helium abundance by mass (we used  $X = 0.76$  and  $Y = 0.24$ ). Without entering into the details, the cooling function  $C$  can be calculated by summing the cooling rates  $c_i$  associated (for every ion species) to the processes presented at the beginning of this Section:

$$C = \sum_{i=1}^{11} c_i [T, \rho_{\text{B}}, J(\nu), T_{\text{CMB}}]. \quad (2.31)$$

We refer to Theuns et al. (1998) for the units and functional dependence on temperature of each  $c_i$ . Figure 2.1 shows the cooling rate of a primordial composition gas in collisional equilibrium, meaning that the abundances of different ionic species were computed from Equations (2.23)–(2.26) and (2.28)–(2.30) with the photoionization rates  $\Gamma_{\gamma_i}$  set to zero (Katz et al. 1996b).

In the presence of photoionization the relative abundances of different species depend on temperature and density, the latter determining the rate at which recombination contrasts the effect of photoionization. In addition to affecting abundances, photoionization injects energy into the gas, since the photoelectrons carry off residual energy. The heating rate from photoionization is

$$H = n_{\text{HI}}\epsilon_{\text{HI}} + n_{\text{HeI}}\epsilon_{\text{HeI}} + n_{\text{HeII}}\epsilon_{\text{HeII}} \quad \text{erg s}^{-1} \text{ cm}^{-3}, \quad (2.32)$$

where

$$\epsilon_i = \int_{\nu_i}^{\infty} \frac{4\pi J(\nu)}{h\nu} \sigma_i(\nu) (h\nu - h\nu_i) d\nu \quad \text{erg s}^{-1}. \quad (2.33)$$

### 2.4.2 The star formation model

In the original GADGET-2 code, Springel & Hernquist (2003) modeled the star formation process through an effective description of the Interstellar Medium (ISM). In this model, the ISM is described as an ambient hot gas containing cold clouds, which provide the reservoir of star formation, the two phases being in pressure equilibrium. The density of the cold and of the hot phase represents an average over small regions of the ISM, within which individual molecular clouds cannot be resolved by simulations sampling cosmological volumes.

In this description, baryons can exist in three phases: hot gas, cold clouds and stars. The mass fluxes between these phases are regulated by three physical processes: (1) hot gas cools and forms cold clouds through radiative cooling; (2) stars are formed from the clouds at a rate given by a Schmidt-type law (see below); (3) stars explode, thereby restoring mass and energy to the hot phase, and evaporating clouds with an efficiency which scales with the gas density. Under the assumption that the timescale to reach equilibrium is much shorter than other timescales, the energy from SNe also sets the equilibrium temperature of the hot gas in the star formation regions.

The original GADGET-2 code only accounts for energy from SNII, that are supposed to promptly explode, with no delay time from the star formation episode. Therefore, the specific energy available per unit mass of stars formed is  $\epsilon_{\text{SNe}} = e_{\text{SNe}} \times n_{\text{SN}}^{\text{II}}$ . Here, the energy produced by a single SN explosion is assumed to be  $e_{\text{SNe}} = 10^{51}$  erg, while the number of stars per solar mass ending in SNII for a Salpeter IMF is  $n_{\text{SN}}^{\text{II}} = 0.0074 M_{\odot}^{-1}$ .

In the effective model by Springel & Hernquist (2003), a gas particle is flagged as star forming whenever its density exceeds a given density threshold, above which that particle is treated as multiphase. Once the clouds evaporation efficiency and the star formation timescale are specified, the value of the threshold is self-consistently computed by requiring: (a) that the temperature of the hot phase at that density coincides with the temperature,  $T_{\text{ti}}$ , at which thermal instability sets on, and (b) that the specific *effective* energy (see Equation (11) of Springel & Hernquist 2003) of the gas changes in a continuous way when crossing that threshold. Accordingly, the value of the density threshold for star formation depends on the value of the cooling function at  $T_{\text{ti}}$ , on the characteristic timescale for star formation, and on the energy budget from SNII. For reference, Springel & Hernquist (2003) computed this threshold to correspond to  $n_{\text{H}} \simeq 0.14 \text{ cm}^{-3}$  for the number density of hydrogen atoms in a gas of primordial composition.

In the simulations presented in this thesis work, we adopt the Tornatore et al. (2007) improved version of the above effective model of star formation from a multiphase medium.

In implementing this more sophisticated model of chemical evolution Tornatore et al. (2007) account explicitly for stellar lifetimes, thereby avoiding the approximation of instantaneous recycling, as well as including the possibility to change the IMF and the yields. Therefore, while the general structure of the Springel & Hernquist (2003) effective model is left unchanged, they have substantially modified it in several aspects. Here below we describe the key features that they have implemented in the code:

- The amount of metals and energy produced by each star particle during the evolution is self-consistently computed for different choices of the IMF. In principle, the code also allows one to treat an IMF which changes with time and whose shape depends on the local conditions (e.g. metallicity) of the star forming gas.
- As in the original Springel & Hernquist (2003) model, self-regulation of star formation is achieved by assuming that the energy of short-living stars is promptly available, while all the other stars die according to their lifetimes. We define as short living all the stars with mass  $\geq M_{\text{SL}}$ , where  $M_{\text{SL}}$  must be considered as a parameter whose value ranges from the minimum mass of core-collapse SNe (we assume  $8 M_{\odot}$ ), up to the maximum mass where the IMF is computed. This allows to parametrize the feedback strength in the self-regulation of the star formation process. We emphasize that the above mass threshold for short living stars is only relevant for the energy available to self-regulate star formation, while metal production takes place by accounting for lifetimes, also for stars with mass  $\geq M_{\text{SL}}$ . In the following runs we set  $M_{\text{SL}} = 8 M_{\odot}$ , thus assuming that all the energy from SNII is used for the self-regulation of star formation.
- The code include the contribution of metals to the cooling function. To this purpose, the implementation of cooling proceeds as follows. The original cooling function provided in the GADGET-2 code is used to account for the photo-ionization equilibrium of Hydrogen and Helium, while the tables by Sutherland & Dopita (1993) are used to account for the contribution of metals to the cooling function<sup>2</sup>.
- A self-consistent computation of the density threshold for star formation implies introducing a complex interplay between different ingredients. Firstly, changing the IMF changes the amount of energy available from short-living stars, in such a way that the threshold increases with this energy. Secondly, including the dependence of the cooling function on the local metallicity causes the density threshold to decrease for more enriched star forming gas. In the following, we fix the value of this threshold at  $n_{\text{H}} = 0.1 \text{ cm}^{-3}$  in terms of the number density of hydrogen atoms, a value that has been adopted in a number of

---

<sup>2</sup>The cooling tables by Sutherland & Dopita (1993) assume the relative proportions of different metal species to be solar. Including more refined cooling rates, which depend explicitly on the individual abundances of different metal species, involves a straightforward modification of the code. Due to the lack of an explicit treatment of metal diffusion, a heavily enriched gas particle does not share its metal content with any neighbour metal poor particle. This may cause a spurious noise in the cooling process, in the sense that close particles may have heavily different cooling rates, depending on how different is their metallicity. To overcome this problem, Tornatore et al. (2007) decided to smooth gas metallicity using the same kernel used for the computation of the hydrodynamical forces (i.e. a B-spline kernel using 64 neighbours), but only for the purpose of the computation of the cooling function. Therefore, while each particle retains its metal mass, its cooling rate is computed by accounting also for the enrichment of the surrounding gas particles.

previous studies of star formation in hydrodynamical simulations (e.g. Navarro & White 1993; Katz et al. 1996b; Kay et al. 2002) and which is comparable to that,  $n_{\text{H}} = 0.14 \text{ cm}^{-3}$ , computed by Springel & Hernquist (2003) in their effective model.

- The computation of the fraction of clouds proceeds exactly as in the original effective model (see Equation (18) in Springel & Hernquist 2003), except that Tornatore et al. (2007) explicitly include the dependence of the cooling function on the local gas metallicity and the SN energy used for the computation of the pressure equilibrium is consistently computed for a generic IMF, as described above.

In order to define the rule to transform star forming gas particles into collisionless star particles, Tornatore et al. (2007) closely follow the implementation by Springel & Hernquist (2003) of the algorithm originally developed by Katz et al. (1996b). This algorithm describes the formation of star particles as a stochastic process, rather than as a “smooth” continuous process. Basically, at a given time the star formation rate of a multiphase gas particle is computed using a Schmidt-type law (Schmidt 1959):

$$\dot{m}_{\star} = \frac{x m}{t_{\star}}. \quad (2.34)$$

Here,  $x$  is the fraction of gas in cold clouds, so that  $x m$  is the mass of cold clouds providing the reservoir for star formation. Within the effective star formation model, the star formation timescale,  $t_{\star}(\rho)$ , is computed as

$$t_{\star}(\rho) = t_0^* \left( \frac{\rho}{\rho_{\text{th}}} \right)^{-1/2}, \quad (2.35)$$

where  $t_0^*$  is a parameter of the model, while  $\rho_{\text{th}}$  is the density threshold for star formation, that we defined above. Springel & Hernquist (2003) showed that the value of  $t_0^*$  should be chosen so as to reproduce the observed relation between the disc-averaged star formation per unit area and the gas surface density (Kennicutt 1998). Following Springel & Hernquist (2003b), we assume  $t_0^* = 1.5 \text{ Gyr}$ .

From Equation (2.34), the stellar mass expected to form in a given time interval  $\Delta t$  is

$$m_{\star} = m \left\{ 1 - \exp \left( -\frac{x \Delta t}{t_{\star}} \right) \right\}. \quad (2.36)$$

Within the stochastic approach to star formation, it is defined the number of stellar generations,  $N_{\star}$ , as the number of star particles which are generated by a single gas particles. Therefore, each star particle will be created with mass

$$m_{\star,0} = m_{\text{g},0} / N_{\star}, \quad (2.37)$$

where  $m_{\text{g},0}$  is the initial mass of the gas particles. Within this approach, a star particle is created once a random number drawn in the interval  $[0,1]$  falls below the probability

$$p = \frac{m_{\text{g},0}}{m_{\star,0}} \left[ 1 - \exp \left( -\frac{x \Delta t}{t_{\star}} \right) \right]. \quad (2.38)$$

After the occurrence of a large enough number of star formation events, the stochastic star formation history will converge to the continuous one. In case a gas particle already spawned  $(N_g^* - 1)$  star particles, then it is entirely converted into a star particle. As we shall discuss in the next Section, star particles are allowed, in the implementation of chemical evolution we used, to restore part of their mass to the gas phase, as a consequence of stellar mass loss. Since this restored mass is assigned to surrounding gas particles, the latter have masses which can change during the evolution. Therefore, in the Equation (2.37) the actual mass  $m_g$  replaces the initial mass  $m_{g,0}$ , which is assumed to be the same for all gas particles. As a consequence, star particles can have different masses due to their mass loss and the mass of their parent gas particles.

Clearly, the larger the number of generations, the closer is the stochastic representation to the continuous description of star formation. In the simulations presented in this work we used  $N_* = 3$  as a reference value for the number of stellar generations.

### 2.4.3 The chemical evolution model

Due to the stochastic representation of the star formation process, each star particle must be treated as a simple stellar population (SSP), i.e. as an ensemble of coeval stars having the same initial metallicity. Every star particle carries all the physical information (e.g. birth time  $t_b$ , initial metallicity and mass) which are needed to calculate the evolution of the stellar populations that they represent, once the lifetime function, the IMF and the yields for SNe and LIMS have been specified. Therefore, it is possible to compute for every star particle at any given time  $t > t_b$  how many stars are dying as SNII and SNIa, and how many stars undergo the AGB phase, according to the equations of chemical evolution that we discuss below. The accuracy with which chemical evolution is followed is set by defining suitable “chemical” timesteps. These timesteps are adaptively computed during the evolution by fixing the percentage of SNe of each type which explode within each time step. In our simulations, we choose this fraction to be 10 per cent for SNII and 2 per cent for SNIa. As such, these timesteps depend both on the choice of the IMF and on the lifetime function.

In the following, it is assumed that SNIa arises from stars belonging to binary systems, having mass in the range  $0.8 - 8 M_\odot$  (Greggio & Renzini 1983), while SNII arise from stars with mass  $> 8 M_\odot$ . Besides SNe, which release energy and metals, it is also accounted for the mass loss by low and intermediate mass stars in the AGB phase. They contribute to metal production, but not to the energy feedback, and are identified with those stars, not turning into SNIa, in the mass range  $0.8 - 8 M_\odot$ .

In summary, the main ingredients that define the model of chemical evolution, as Tornatore et al. (2007) implemented in the code, are the following: the adopted lifetime function (that determines the SNe explosion rates), the adopted yields and the IMF which fixes the number of stars of a given mass. We describe each of these ingredients here in the following.

#### The equations of chemical evolution

We describe here the equations for the evolution of the rates of SNIa, SNII and LIMS, along with their respective metal production. We provide here a short description of the basic results

and of the equations which are actually solved in our simulations, while we refer to the textbook by Matteucci (2003) for a detailed discussion.

Let  $\tau(m)$  be defined as the lifetime function, i.e. the age at which a star of mass  $m$  dies. Accordingly, the the rate of explosions of SNIa reads

$$R_{\text{SNIa}}(t) = - \left. \frac{dm(t)}{dt} \right|_{m_2 \equiv \tau^{-1}(t)} 24m_2^2 A \int_{M_{\text{Bm}}}^{M_{\text{BM}}} \phi(m_{\text{B}}) \frac{1}{m_{\text{B}}^3} dm_{\text{B}}, \quad (2.39)$$

where  $-dm(t)/dt|_{m_2 \equiv \tau^{-1}(t)}$  is the mass of stars dying at the time  $t$ ,  $\tau^{-1}(t)$  is the inverse of the lifetime function  $\tau(m)$ ,  $\phi(m)$  is the IMF (see Eq. 2.45) and  $A$  is the fraction of stars in binary systems of that particular type to be progenitors of SNIa. The integral is over the mass  $m_{\text{B}}$  of the binary system, which runs in the range of the minimum and maximum allowed for the progenitor binary system,  $M_{\text{Bm}}$  and  $M_{\text{BM}}$ , respectively. Following Greggio & Renzini (1983) and Matteucci & Greggio (1986), we assume  $A = 0.1$ ,  $M_{\text{Bm}} = 3 M_{\odot}$  and  $M_{\text{BM}} = 16 M_{\odot}$ . Matteucci & Gibson (1995) applied a model of chemical enrichment of the ICM and found that  $A = 0.1$  was required to reproduce the observed Iron enrichment, by assuming a Scalo IMF (Scalo 1986). Changing the IMF would in principle require to change the value of  $A$ . Here we prefer to fix the value of  $A$  and check the agreement with observations for different IMFs, rather than adjusting by hand its value case by case. Eq. (2.39) holds under the assumption of impulsive star formation. Indeed, since each star particle is considered as a SSP, the associated star formation history,  $\psi(t)$ , is a delta-function,  $\delta(t - t_0)$ , centered on the formation time  $t_0$ .

As for the SNII and the low and intermediate mass stars, the rate is given by

$$R_{\text{SNII,LIMS}}(t) = - \frac{dm(t)}{dt} \phi(m(t)). \quad (2.40)$$

We note that the above expression must be multiplied by a factor of  $(1 - A)$  for LIMS rates if the interested mass  $m(t)$  falls in the same range of masses which is relevant for the secondary stars of SNIa binary systems.

The release of energy and chemical elements by stars (binary systems in case of SNIa) of a given mass is obtained by multiplying the above rates by the yields  $p_{Z_i}(m, Z)$ , which give the mass of the element  $i$  produced by a star of mass  $m$  and initial metallicity  $Z$ . Then, the equation which describes the evolution of the mass  $\rho_i(t)$  for the element  $i$ , holding for a generic form of the star formation history  $\psi(t)$ , reads:

$$\begin{aligned} \dot{\rho}_i(t) = & -\psi(t)Z_i(t) + \\ & A \int_{M_{\text{Bm}}}^{M_{\text{BM}}} \phi(m) \left[ \int_{\mu_{\text{min}}}^{0.5} f(\mu)\psi(t - \tau_{m_2})p_{Z_i}(m, Z) d\mu \right] dm + \\ & (1 - A) \int_{M_{\text{Bm}}}^{M_{\text{BM}}} \psi(t - \tau(m))p_{Z_i}(m, Z)\phi(m) dm + \\ & \int_{M_{\text{L}}}^{M_{\text{Bm}}} \psi(t - \tau(m))p_{Z_i}(m, Z)\phi(m) dm + \\ & \int_{M_{\text{BM}}}^{M_{\text{U}}} \psi(t - \tau(m))p_{Z_i}(m, Z)\phi(m) dm. \end{aligned} \quad (2.41)$$

In the above equation,  $M_L$  and  $M_U$  are the minimum and maximum mass of a star, respectively. In the following we use  $M_L = 0.1 M_\odot$  and  $M_U = 100 M_\odot$ . The term in the first line of Eq. (2.41) accounts for the metals which are locked up in stars. The term in the second line accounts for metal ejection contributed by SNIa. Here we have explicitly written the inner integral that accounts for all the possible mass ratios  $\mu = m_2/(m_1 + m_2)$  between the secondary star mass and the total mass;  $\mu_{\min}$  is the minimum value of  $\mu$  and  $f(\mu)$  is the corresponding distribution function. The terms on the third and fourth lines describe the enrichment by mass-loss from low and intermediate mass stars, while the last line accounts for ejecta by SNII.

The  $\mu$  distribution function is assumed to be

$$f(\mu) = 2^{1+\gamma}(1 + \gamma)\mu^\gamma, \quad (2.42)$$

where  $\gamma = 2$ . This functional form of  $f(\mu)$  has been derived from statistical studies of the stellar population in the solar neighbourhood (Matteucci & Recchi 2001). The value of  $\mu_{\min}$  is calculated for a binary system of mass  $M_B$  as

$$\mu_{\min} = \max\left(\frac{m_2}{m_B}, \frac{m_B - 0.5M_{\text{BM}}}{m_B}\right). \quad (2.43)$$

Taking the impulsive star formation, the terms in Eq. (2.41) must be recast in the form that we actually use for calculating the rates.

In order to solve Equations (2.39), (2.40) and (2.41) in the GADGET-2 code, Tornatore et al. (2007) proceed as follows. At the beginning of each run, two tables, one for SNII and one for SNIa and low and intermediate mass stars, are built to specify at what delay times the chemical evolution should be calculated. The accuracy of these ‘‘chemical timesteps’’ is set by two run-time parameters that specify what fraction of stars must be evolved at each step. Accordingly, during each global timestep of the code only a small fraction (typically few percent) of all stars is processed. This implementation of chemical evolution is quite efficient in terms of computational cost, especially when the number of stars grows. They verified that using  $N_* = 3$  for the number of stellar generations, the overhead associated to the chemical evolution part amounts only to  $\lesssim 10$  per cent of the total computational cost for a typical simulation.

### The lifetime function

We adopted the function given by Padovani & Matteucci (1993),

$$\tau(m) = \begin{cases} 10\left[\left(1.34 - \sqrt{1.79 - 0.22(7.76 - \log m)}\right)/0.11\right]^{-9} & \text{for } m \leq 6.6 M_\odot, \\ 1.2m^{-1.85} + 0.003 & \text{otherwise.} \end{cases} \quad (2.44)$$

We refer to the paper by Romano et al. (2005) for a detailed discussion on the effects of different lifetime functions on the chemical enrichment model of the Milky Way.

We point out that the above lifetime function is independent of metallicity, whereas in principle this dependence can be included in a model of chemical evolution.

## Stellar yields

The stellar yields specify the quantity  $p_{Z_i}(m, Z)$ , which appears in Eq. (2.41) and, therefore, the amount of different metal species which are released during the evolution of each star particle. In the runs presented in this work, we adopt the yields provided by van den Hoek & Groenewegen (1997) for the low and intermediate mass stars, by Thielemann et al. (2003) for SNIa and by Woosley & Weaver (1995) for SNII. We also assume that all the stars having masses  $> 40 M_\odot$  directly end in black holes.

Along with freshly produced elements, stars also release non-processed elements. In order to account for them, whenever necessary, Tornatore et al. (2007) assumed that the non-processed metals are ejected along with Helium and non-processed Hydrogen.

Besides H and He, in the simulations presented in this work we trace the production of C, O, Mg, S, Si and Fe. The code can be easily modified to include other metal species.

## The initial mass function

The initial mass function is one of the most important quantity in modelling the star formation process. It directly determines the relative ratio between SNII and SNIa and, therefore, the relative abundance of  $\alpha$ -elements and Fe-peak elements. The shape of the IMF also determines how many long-living stars will form with respect to massive short-living stars. In turn, this ratio affects the amount of energy released by SNe, the present luminosity of galaxies, which is dominated by low mass stars, and the (metal) mass-locking in the stellar phase.

As of today, no general consensus has been reached on whether the IMF at a given time is universal or strongly dependent on the environment, or whether it is time dependent, i.e. whether local variations of the values of temperature, pressure and metallicity in star forming regions affect the mass distribution of stars.

Nowadays, there are growing evidences that the IMF in the local universe, expressed in number of stars per unit logarithmic mass interval, is likely to be a power-law for  $m_\star > 1 M_\odot$  with slope  $x \sim 1.35$ , while it becomes flat below the  $1 M_\odot$  threshold, possibly even taking a negative slope below  $\sim 0.2 M_\odot$  (e.g. Kroupa 2001). Theoretical arguments (see Larson 1998) suggest that the present day characteristic mass scale  $\sim 1 M_\odot$  should have been larger in the past, so that the IMF at higher redshift was top-heavier than at present. Chiappini et al. (2000) showed that varying the IMF by decreasing the characteristic mass with time, leads to results at variance with observations of chemical properties of the Galaxy. While the shape of the IMF is determined by the local conditions of the interstellar medium, direct hydrodynamical simulations of star formation in molecular clouds are only now approaching the required resolution and sophistication level to make credible predictions on the IMF (e.g. Bate & Bonnell 2005).

In order to explore how the IMF changes the pattern of metal enrichment, Tornatore et al. (2007) implement it in the code in a very general way, so that it is possible to easily use both single-slope and multi-slope IMFs, as well as time-evolving IMFs. In this work we used single-slope IMFs defined as

$$\phi(m) = \frac{dN}{d \log m} \propto m^{-x}, \quad (2.45)$$

with  $x = 1.35$  for the standard Salpeter IMF (Salpeter 1955). In the above equation,  $N$  is the

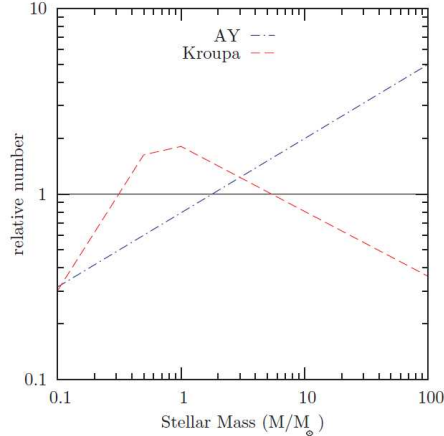


Figure 2.2: The dependence of the shape of the IMF on the stellar mass, relative to the Salpeter (1955) IMF. Blue dot-dashed and red dashed curves are for the IMF by Arimoto & Yoshii (AY, 1987) and by Kroupa (2001), respectively. The horizontal black solid line indicates for reference the Salpeter IMF.

number of stars per unit logarithmic mass interval. We explored the effect of changing the IMF by also using a top-heavier IMF with  $x = 0.95$  (Arimoto & Yoshii 1987, AY), as well as the multi-slope IMF by Kroupa (2001), which is defined as

$$\phi(m) \propto \begin{cases} m^{-1.7} & m \geq 1 M_{\odot}, \\ m^{-1.2} & 0.5 \leq m < 1 M_{\odot}, \\ m^{-0.3} & m < 0.5 M_{\odot}. \end{cases} \quad (2.46)$$

We show in Figure 2.2 the number of stars, as a function of their mass, predicted by the AY and Kroupa IMFs, relative to that predicted by the Salpeter IMF. As expected, the AY IMF predicts a larger number of high-mass stars and, correspondingly, a smaller number of low-mass stars, the crossover taking place at  $\simeq 2 M_{\odot}$ . As a result, we expect that the enrichment pattern of the AY IMF will be characterized by a higher abundance of those elements, like Oxygen, which are mostly produced by SNII. On the other hand, the Kroupa IMF is characterized by a relative deficit of high-mass stars and, correspondingly, a relatively lower enrichment in Oxygen is expected.

#### 2.4.4 Feedback schemes

In the simulations of this thesis work we used three different feedback schemes: two associated to the galactic (energy and momentum driven) winds produced by “starburst” galaxies, and the AGN feedback associated to the energy released by gas accretion onto super-massive black holes. In the following we briefly describe these different models.

## Energy-driven winds

The *energy-driven* implementation of galactic winds is extensively described in Springel & Hernquist (2003). Here we summarize the main aspects of the original model and the modifications that we made.

In the multiphase model of Springel & Hernquist (2003) gas contained in dark matter haloes cool and settle into rotationally supported discs where the baryons are converted into stars. However, in the star forming multiphase medium, it is plausible that not all of the hot gas in supernova remnants remains confined to the disc: supernova bubbles close to the surface of a star forming region may break out of a disc and a galactic-scale wind associated with star formation may develop.

Basically, the wind mass-loss rate  $\dot{M}_w$  is assumed to be proportional to the star formation rate  $\dot{M}_\star$  according to

$$\dot{M}_w = \eta \dot{M}_\star, \quad (2.47)$$

where  $\eta$  is the wind efficiency, and the wind carries a fixed fraction  $\chi$  of SN energy:

$$\frac{1}{2} \dot{M}_w v_w^2 = \chi \epsilon_{\text{SN}} \dot{M}_\star. \quad (2.48)$$

Star forming gas particles are then stochastically selected according to their star formation rate to become part of a blowing wind. Whenever a particle is uploaded to the wind, it is decoupled from the hydrodynamics for a given period of time (calculated as mentioned below) or till the density around it drops below a given fraction of the density threshold set for the onset of the star formation, in order to effectively reach less dense regions. In our case, this limiting density for decoupling is  $0.5\rho_{\text{th}}$ . This allows the wind particle to travel “freely” up to few kpc until it has left the dense star forming phase, without directly affecting it: only outside the disc the hydrodynamical interactions within the halo could stop the wind. Unlike in Springel & Hernquist (2003), we decide here to fix the velocity of the winds,  $v_w$ , instead of the fraction of the energy made available by SNII explosions to power galactic ejecta. Thus, four parameters fully specify the wind model: the wind efficiency  $\eta$ , the wind speed  $v_w$ , the wind free travel length  $l_w$  and the wind free travel density factor  $\delta_w$ .

The maximum allowed time for a wind particle to stay hydrodynamically decoupled is then  $t_{\text{dec}} = l_w/v_w$ . The parameter  $l_w$  has been introduced in order to prevent a gas particle from getting trapped into the potential well of the virialized halo and in order to effectively escape from the ISM, reach the low density IGM and pollute it with metals.

In this thesis work, we used  $l_w = 10 h^{-1}$  kpc and we considered different values for the wind velocity, ranging from  $v_w = 100 \text{ km s}^{-1}$  (weak winds) to  $v_w = 600 \text{ km s}^{-1}$  (strong winds). In our implementation the parameter  $\eta$  is kept fixed to the value 2.

## Momentum-driven Winds

Originally, the energy-driven implementation of galactic winds was the only one included in GADGET-2. Motivated by the work of Oppenheimer & Davé (2006, 2008), we decided to implement inside our version of GADGET-2, as a part of the Ph.D. project, a new and different prescription for the galactic winds: the so called *momentum-driven* winds model. Oppenheimer & Davé (2006, 2008) suggested that, with this scheme of winds, simulations reproduce the

statistics of CIV absorption in the high-redshift IGM better than using the above energy-driven winds.

Observations of outflows from starburst galaxies have improved considerably in recent years. Martin (2005) found that the terminal wind velocity scales roughly linearly with circular velocity, with top winds speeds around three times the galaxy’s circular velocity. Rupke et al. (2005) studied a large sample of luminous infrared galaxies and found that, at least when combined with smaller systems from Martin (2005), those trends continue to quite large systems.

A feasible physical scenario for the wind driving mechanism is derived by noting that the observed scaling are well explained by a momentum-driven wind model such as that outlined by Murray et al. (2005). In such a scenario, the radiation pressure of the starburst drives an outflow, possibly by transferring momentum to an absorptive component (such as dust) that is hydrodynamically coupled with the gas component, which is then dragged out of the galaxy. Following Oppenheimer & Davé (2006, 2008) we test a single model (very close to their “*mzw*” run) based on momentum-driven winds. In such a model the wind speed scales as the galaxy velocity dispersion  $\sigma$ , as observed by Martin (2005). Since in momentum-driven winds the amount of input momentum per unit star formation is constant, this implies that the mass loading factor must be inversely proportional to the velocity dispersion. We therefore use the following relations:

$$v_{\text{wind}} = 3\sigma\sqrt{f_L - 1}; \quad \eta = \frac{\sigma_0}{\sigma}, \quad (2.49)$$

where  $f_L$  is the luminosity factor in units of the galactic Eddington luminosity (i.e. the critical luminosity necessary to expel gas from the galaxy),  $\sigma_0$  is the normalization of the mass loading factor and we add an extra  $2\sigma$  kick to get out of the potential of the galaxy in order to simulate continuous pumping of gas until it is well into the galactic halo. Schaerer (2003) suggested an approximate functional form for far-UV emission which Oppenheimer & Davé (2006, 2008) used to obtain the luminosity factor and which includes a metallicity dependence for  $f_L$  owing to more UV photons output by lower-metallicity stellar populations:

$$f_L = f_{L,\odot} \times 10^{-0.0029(\log Z+9)^{2.5}+0.417694}, \quad (2.50)$$

where Martin (2005) suggests:  $f_{L,\odot} \approx 2$ . The mass loading factor controls star formation at early times, so  $\sigma_0$  can also be set by requiring a match to the observed global star formation rate. Following Oppenheimer & Davé (2008) we set  $\sigma_0 = 150$  km/s. We determine  $\sigma$  directly from the simulation only for the most massive haloes, while for haloes with masses below  $10^3$  dark matter particles (equal to  $1.7 \times 10^9 h^{-1} M_\odot$  for our reference runs in Chapter 3) we use the relation calibrated by Evrard et al. (2008), using a variety of N-body simulations:

$$\sigma_{\text{DM}}(M, z) = \sigma_{\text{DM},15} \left[ \frac{h(z)M_{200}}{10^{15} M_\odot} \right]^\alpha \quad \text{km/s}, \quad (2.51)$$

where  $\sigma_{\text{DM},15} = 1082.9 \pm 4.0$  km/s is the normalization at mass  $10^{15} h^{-1} M_\odot$ ,  $\alpha = 0.3361 \pm 0.0026$  is the logarithmic slope and  $M_{200}$  is defined as the total mass within a sphere with mean interior density  $3M_{200}/4\pi r_{200}^3 = 200\rho_c(z)$  ( $\rho_c(z)$  is the critical density at redshift  $z$ ). Even for this wind implementation the particles are stochastically selected in the same way as for the energy-driven scenario.

## AGN feedback

We also include in our simulations the effect of feedback energy from gas accretion onto super-massive black holes (BHs), following the scheme originally introduced by Springel et al. (2005) (see also Di Matteo et al. 2005). In this model, BHs are represented by collisionless sink particles initially seeded in just resolved dark matter haloes, which subsequently grow via gas accretion and through mergers with other BHs during close encounters. Every new dark matter halo, identified by a run-time friends-of-friends algorithm, above the mass threshold  $M_{\text{th}} = 10^{10} M_{\odot}$ , is seeded with a central BH of initial mass  $10^5 M_{\odot}$ , provided the halo does not contain any BH yet. Each BH can then grow by local gas accretion, with a rate given by

$$\dot{M}_{\text{BH}} = \min \left( \dot{M}_{\text{B}}, \dot{M}_{\text{Edd}} \right). \quad (2.52)$$

Here  $\dot{M}_{\text{B}}$  is the accretion rate estimated with the Bondi-Hoyle-Littleton formula (e.g. Bondi 1952):

$$\dot{M}_{\text{B}} = \frac{4\pi\alpha\rho G^2 M_{\text{BH}}^2}{(c_s^2 + v^2)^{3/2}}, \quad (2.53)$$

where  $\alpha$  is a dimensionless parameter,  $c_s$  is the sound speed and  $v$  is the velocity of the BH relative to the gas; while  $\dot{M}_{\text{Edd}}$  is the Eddington accretion rate:

$$\dot{M}_{\text{Edd}} = \frac{4\pi m_p G M_{\text{BH}}}{\epsilon_r \sigma_{\text{T}} c}, \quad (2.54)$$

with  $m_p$  the proton mass,  $\sigma_{\text{T}}$  the Thomson cross-section and  $\epsilon_r$  the radiative efficiency, which gives the radiated energy  $L_r$  in units of the energy associated to the accreted mass:

$$\epsilon_r = \frac{L_r}{\dot{M}_{\text{BH}} c^2}. \quad (2.55)$$

Following Springel et al. (2005) and Fabjan et al. (2009), we fix  $\epsilon_r = 0.1$  as a reference value, which is typical for a radiatively efficient accretion onto a Schwarzschild BH (Shakura & Sunyaev 1973). The model then assumes that a fraction  $\epsilon_f$  of the radiated energy is thermally coupled to the surrounding gas, so that  $\dot{E}_{\text{feed}} = \epsilon_r \epsilon_f \dot{M}_{\text{BH}} c^2$  is the rate of the energy released to heat the surrounding gas. Using  $\epsilon_f \sim 0.05$ , Di Matteo et al. (2005) were able to reproduce the observed  $M_{\text{BH}} - \sigma$  relation between bulge velocity dispersion and mass of the hosted BH (see also Sijacki et al. 2008; Di Matteo et al. 2008). Gas particle accretion onto the BH is implemented in a stochastic way, by assigning to each neighbouring gas particle a probability of contributing to the accretion, which is proportional to the SPH kernel weight computed at the particle position. In the scheme described above, this stochastic accretion is used only to increase the dynamic mass of the BHs, while their mass entering in the computation of the accretion rate is followed in a continuous way, by integrating the analytic expression for  $\dot{M}_{\text{BH}}$ . Once the amount of energy to be thermalized is computed for each BH at a given timestep, this energy is then distributed to the surrounding gas particles using the SPH kernel weighting scheme.

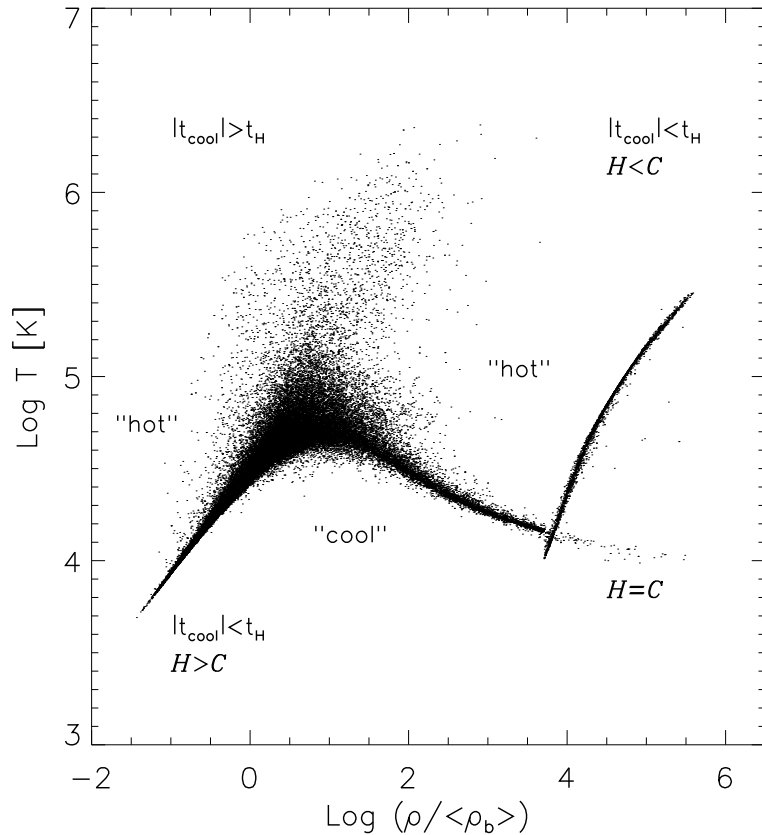


Figure 2.3: Temperature-density distribution at  $z = 3$  for one of our simulations with  $5 h^{-1}$  comoving Mpc box size,  $2 \times 64^3$  (gas + dark matter) particles and momentum-driven winds feedback. Only 1/3 of the particles are plotted.

### 2.4.5 Gas distribution

In Figure 2.3 we show the temperature-density relation of the gas at  $z = 3$ , for one of our simulations with  $5 h^{-1}$  comoving Mpc box size,  $2 \times 64^3$  (gas + dark matter) particles and momentum-driven winds feedback. The overall distribution can be explained in terms of the cooling and heating processes introduced in Section 2.4.1 and of the respective time scales involved. We start by defining the cooling time of gas at temperature  $T$  as

$$t_{\text{cool}} = \frac{u}{\dot{u}} = \frac{3k_{\text{B}}T}{2\mu} \frac{m_{\text{p}}}{\rho(1-Y)^2(C-H)}, \quad (2.56)$$

where  $k_{\text{B}}$  is the Boltzmann's constant,  $\mu$  is the mean molecular weight,  $m_{\text{p}}$  is the proton mass and  $u$  is the thermal energy per unit mass.  $C(u)$  and  $H(\rho, u)$  are, respectively, the normalized cooling and heating rates. The Hubble time is  $t_{\text{H}} = 1/\sqrt{6\pi G\bar{\rho}(z)}$ . In Figure 2.3 is possible to distinguish three separate regions: (a) at low densities and high temperatures the cooling time is longer than the Hubble time, meaning that neither heating nor cooling are able to change the gas temperature significantly; (b) at high densities and high temperatures, bremsstrahlung and

line cooling processes always dominate leading to cooling times shorter than the Hubble time; (c) at low densities and low temperatures, photo-heating is dominant leading to heating times shorter than the Hubble time. If  $H < C$ , the gas is heated and the cooling time in Equation (2.56) is negative; we then define  $-t_{\text{cool}}$  the heating time, and  $|t_{\text{cool}}|$  the “net” cooling time.

Considering the strip of particles indicated by  $H = C$ , i.e. the equilibrium track where cooling balances heating, at high densities: approaching this line from both lower and higher temperatures we start from a region where  $|t_{\text{cool}}| < t_{\text{H}}$  and then pass onto the track where  $t_{\text{cool}} \rightarrow \infty$ , due to the condition  $H = C$  in the denominator of Equation (2.56). As a consequence, we must go through a point where  $t_{\text{cool}} = t_{\text{H}}$  and this explains why the track defined by the latter relation is basically identical to the equilibrium track at sufficiently high densities (see Figure 2 of Theuns et al. 1998). Gas lying just below this line will be heated very quickly on a time scale  $\ll t_{\text{H}}$  onto the track, and the opposite happens for gas slightly hotter than the equilibrium  $T$ .

With this behaviour in mind, we can now explain the distribution of the gas in the  $(\rho, T)$  plane. Efficient photo-heating of under dense gas forces it to remain at those temperatures where  $t_{\text{cool}} = t_{\text{H}}$ . Where gas falls into dark matter potential wells, shock heating generates the large plume of hot gas ( $T > 10^5$  K) present in the figure. Some of this gas may then reach high enough densities so that cooling becomes efficient. This gas condenses onto the equilibrium track where heating balances cooling.

Gas at both low and high densities is forced by photo-heating to remain close to the line where heating is dominant and provides a heating/net cooling time equal to the Hubble time (lower branch of the particles distribution in the left side of Figure 2.3). This zone then defines a minimum temperature at given density,  $T_{\text{min}}(\rho)$ , for the simulated gas distribution. Finally the narrow plume at densities  $> 5 \times 10^3 \langle \rho_{\text{b}} \rangle$  and temperatures  $> 10^4$  K is associated to star forming particles. In this region density is above the threshold for the onset of star formation ( $n_{\text{H}} = 0.1 \text{ cm}^{-3}$ , see Section 2.4.2) and the narrow plume represents the equilibrium track for the multiphase particles. In fact an interesting consequence of our feedback model is that it leads to self-regulated star formation: owing to evaporation, star formation reduces the density in cold clouds, lowering the star formation rate. On the other hand, a higher density of hot gas leads to an increase in the cooling rate, and hence to more rapid replenishing of clouds, increasing the star formation rate. In this manner a self-regulated cycle of star formation is established where, in equilibrium, the growth of clouds is balanced by their evaporation arising from supernova feedback.

To conclude this Chapter, in Figure 2.4 we show the gas density maps at  $z = 3$  for two of our simulations with  $10 h^{-1}$  comoving Mpc box size,  $2 \times 320^3$  (gas + dark matter) particles and energy-driven winds of  $600 \text{ km s}^{-1}$  (strong winds, upper panel) and  $100 \text{ km s}^{-1}$  (weak winds, lower panel). Note in the upper panel the effect of the strong winds which spread the gas around haloes and filaments.

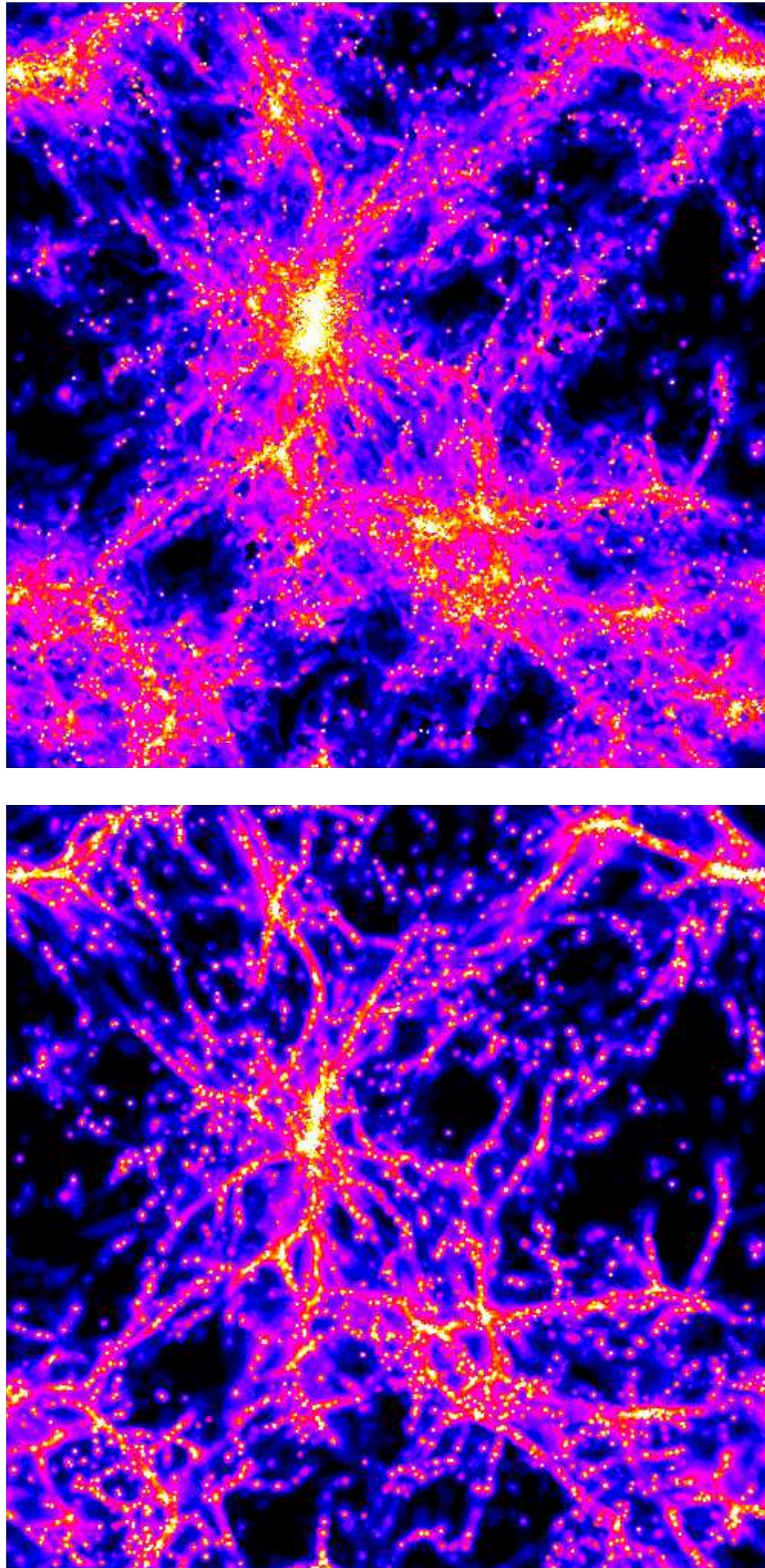


Figure 2.4: Gas density maps at  $z = 3$  for two of our simulations with  $10 h^{-1}$  comoving Mpc box size,  $2 \times 320^3$  (gas + dark matter) particles and energy-driven winds of  $600 \text{ km s}^{-1}$  (strong winds, *upper panel*) and  $100 \text{ km s}^{-1}$  (weak winds, *lower panel*).



# Chapter 3

## DLAs in high-resolution hydrodynamical simulations

In this Chapter we report the results of our work about Damped Lyman- $\alpha$  systems and the chemical enrichment of the intergalactic medium at high redshift. We investigate the properties of DLAs using high-resolution and large box-size cosmological hydrodynamical simulations of a  $\Lambda$ CDM model. The numerical code used is the modification of GADGET-2 with the self consistent implementation of the metal enrichment mechanism (Tornatore et al. 2007) presented in Section 2.4.

What we did is basically an extension of the analysis performed recently by Nagamine et al. (2007) that addressed the properties of DLAs in a  $\Lambda$ CDM universe. The main differences can be summarized as follows and will be more extensively discussed later: *i*) we rely on simulations that have on average a factor 10 better mass resolution; *ii*) we use a different version of the hydrodynamical code GADGET-2 that incorporates the dependence of the radiative cooling function on the global metallicity of the gas (following Sutherland & Dopita 1993) and a self consistent metal enrichment model; *iii*) we explore the effect of varying the stellar initial mass function and most of the parameters describing the wind model. As for the wind model we focus mainly on energy-driven scenarios but we allow for an extra simulation that is based on a momentum-driven wind. At least for the low-density IGM, this model seems to better fit some observational properties (e.g. Oppenheimer & Davé 2006, 2008). The goal is to see which DLAs properties can be reproduced by the hydrodynamical simulations and to investigate closely the impact of galactic winds both on the neutral hydrogen and on the metal distribution around galactic environments in the high redshift Universe (mainly in the range  $z = 2 - 4$ ).

This work is intended as a preliminary quantitative attempt to match some observed properties of the metal and neutral hydrogen distribution using a self consistent chemo-dynamical code that has been already tested for the intra-cluster medium (Tornatore et al. 2007). After having addressed some global properties and evolution of IGM low-ionization species, we will focus on DLAs because their statistical properties are well measured over a wide redshift range and they could provide a useful benchmark for the physics implemented in our simulations.

This Chapter is organized as follows. In Section 3.1 we describe our set of simulations. In Section 3.2 we compare some global properties of the simulations: in particular temperature and metallicity relations (Section 3.2.1), star formation rates and evolution of ion species (Section

3.2.2). In Section 3.3 we focus on the neutral hydrogen distribution around galaxy-sized haloes and we study DLAs properties like the cross-section (Section 3.3.3), the incidence rate (Section 3.3.4) and the column density distribution function (Section 3.3.5). Section 3.4 is dedicated to the simulated QSO spectra extracted from our simulations, to study the velocity width distribution of low-ionization species (Section 3.4.1) and the correlation between metallicity and velocity widths (Section 3.4.2). Finally in Section 3.5 we summarize our main results and we draw some conclusions.

The results of this work are published in the paper: *Damped Lyman- $\alpha$  systems in high-resolution hydrodynamical simulations*, E. Tescari, M. Viel, L. Tornatore & S. Borgani, 2009, MNRAS, 397, 411.

### 3.1 The simulations

We run a number of hydrodynamical simulations in order to explore the effect of changing box-size, numerical resolution, stellar initial mass function, prescription for energy feedback and nature of dark matter. We use the modified version of GADGET-2 described in Section 2.4.

The simulations cover a cosmological volume (with periodic boundary conditions) filled with an equal number of dark matter and gas particles. The cosmological model chosen is a flat  $\Lambda$ CDM with the following parameters:  $\Omega_{0m} = 0.24$ ,  $\Omega_{0b} = 0.0413$ ,  $\Omega_{\Lambda} = 0.76$ ,  $n_s = 0.96$ ,  $H_0 = 73$  km/s/Mpc and  $\sigma_8 = 0.8$ , which are in agreement with the latest results from large scale structure observables such as the cosmic microwave background, weak lensing, the Lyman- $\alpha$  forest and the evolution of mass function of galaxy clusters (Lesgourgues et al. 2007; Komatsu et al. 2009; Vikhlinin et al. 2009; see also Appendix A.5). The input linear dark matter power spectrum for the initial conditions has been generated at  $z = 99$  with CMBFAST (Seljak & Zaldarriaga 1996) and includes baryonic acoustic oscillations. In one case only we change the initial linear dark matter power spectrum by running a warm dark matter (WDM) simulation with a modification (suppression at the small scales) of the initial power spectrum to account for a thermal dark matter particle of mass of 1.2 keV, which is in rough agreement with recent results obtained from Lyman- $\alpha$  high-resolution QSO spectra at redshifts similar to those investigated here (Viel et al. 2008).

Radiative cooling and heating processes are included following the implementation of Katz et al. (1996b). We assume a mean Ultra Violet Background (UVB) produced by quasars and galaxies as given by Haardt & Madau (1996), with the heating rates multiplied by a factor 3.3 in order to better fit observational constraints on the temperature evolution of the intergalactic medium at high redshift. This background gives naturally a  $\Gamma_{-12} \sim 0.8 - 1$  at low redshift in agreement with recent observational measurements (Bolton et al. 2005; Faucher-Giguère et al. 2008). Multiplying the heating rates by the factor above (chosen empirically) results in a larger IGM temperature at the mean density which cannot be reached by the standard hydrodynamical code but aims at mimicking, at least in a phenomenological way, the non-equilibrium ionization effects around reionization (see for example Ricotti et al. 2000; Schaye et al. 2000; Bolton & Haehnelt 2007). We follow self consistently the evolution of the following elements: H, He, C, O, Mg, S, Si and Fe. The contribution of metals is included in the cooling function adopting the tables of Sutherland & Dopita (1993), that assume the solar value for the

Run	Size [ $h^{-1}$ Mpc]	$N_{\text{GAS}}$	$m_{\text{GAS}}$ [ $h^{-1}M_{\odot}$ ]	soft. [ $h^{-1}$ kpc]	Wind [km/s]	IMF	$z_{\text{f}}$
SW	10	$320^3$	$3.5 \times 10^5$	1.5	600	Salpeter	2.25
WW	10	$320^3$	$3.5 \times 10^5$	1.5	100	Salpeter	2.25
MDW	10	$320^3$	$3.5 \times 10^5$	1.5	$\sigma$ -dependent <sup>(a)</sup>	Salpeter	2.25
SW <sub>KR</sub>	10	$320^3$	$3.5 \times 10^5$	1.5	600	Kroupa	2.25
SW <sub>AY</sub>	10	$320^3$	$3.5 \times 10^5$	1.5	600	AY	2.25
SW <sub>10,448</sub>	10	$448^3$	$1.2 \times 10^5$	1	600	Salpeter	3.00
SW <sub>10,256</sub>	10	$256^3$	$6.8 \times 10^5$	2	600	Salpeter	2.25
SW <sub>20,512</sub>	20	$512^3$	$6.8 \times 10^5$	2	600	Salpeter	3.00
SW <sub>5,320</sub>	5	$320^3$	$4.3 \times 10^4$	0.75	600	Salpeter	3.00
SW <sub>WDM</sub> <sup>(b)</sup>	7.5	$320^3$	$1.5 \times 10^5$	0.75	600	Salpeter	3.00

Table 3.1: Summary of the different runs. Column 1, run name: SW, Strong Winds, WW, Weak Winds and MDW, Momentum Driven Winds; column 2, comoving box-size; column 3, number of gas particles; column 4, mass of gas particle; column 5, Plummer-equivalent comoving gravitational softening; column 6, wind speed; column 7, Initial Mass Function (IMF) chosen (see text); column 8, redshift at which the simulation was stopped. (a):  $\sigma$  is the velocity dispersion of the halo that host the “wind” particle (see Section 2.4.4). (b): WDM (Warm Dark Matter) simulation with a modification (suppression at the small scales) of the initial linear dark matter power spectrum to account for a thermal dark matter particle of mass 1.2 keV.

relative abundances. In this work we use the solar metallicity and element abundances given by Asplund et al. (2005).

We used the standard multiphase star formation criterion presented in Section 2.4.2, in which an effective prescription for the interstellar medium is implemented (Springel & Hernquist 2003). In this effective model, a gas particle is flagged as star forming whenever its density exceeds a given density threshold, above which that particle is treated as multiphase. With this prescription baryons are in the form either a hot or a cold phase or in stars, thereby this density threshold marks the onset of cold clouds formation. Following Tornatore et al. (2007) we set the threshold value to  $\rho_{\text{th}} = 0.1 \text{ cm}^{-3}$  in terms of the number density of hydrogen atoms.

The neutral hydrogen fraction  $f_{\text{HI}}$  is associated to each gas particle and is stored in each simulation snapshot. However, we follow Nagamine et al. (2004) to assign a-posteriori a new mass in neutral hydrogen to gas particles above the density threshold which reads:

$$m_{\text{HI}} = f_{\text{HI}} m_{\text{H}} \quad (\rho < \rho_{\text{th}}), \quad (3.1)$$

$$m_{\text{HI}} = f_{\text{c}} m_{\text{H}} \quad (\rho \geq \rho_{\text{th}}), \quad (3.2)$$

with  $f_{\text{HI}}$  the neutral hydrogen fraction that depends on the UVB used,  $m_{\text{H}}$  the hydrogen mass of the particle ( $f_{\text{HI}}$  and  $m_{\text{H}}$  are determined self consistently inside the code),  $f_{\text{c}}$  the fraction of mass in cold clouds and  $\rho_{\text{th}}$  the star formation threshold. Here  $f_{\text{c}} = \rho_{\text{c}}/\rho$ , where  $\rho_{\text{c}}$  is the density of cold clouds and  $\rho$  the total (hot + cold) gas density. Individual molecular clouds

cannot be resolved at the resolution reachable in cosmological simulations, thus  $\rho_c$  represents an average value computed over small regions of the ISM. We refer to Section 2.4.2 to better understand how this cold fraction is related to the physics of the ISM.

Besides including different contributions from SNII, SNIa and LIMS, our model of chemical evolution accounts for the age of various stellar populations. Metals are thereby released over different time-scales by stars of different mass. For the stellar yields we use: SNIa – Thielemann et al. (2003); SNII – Woosley & Weaver (1995); LIMS – van den Hoek & Groenewegen (1997). The mass-range for the SNII is  $m > 8M_\odot$ , while for the SNIa is  $m < 8M_\odot$  with a binary fraction of 10%. We also adopt the lifetime function given by Padovani & Matteucci (1993). Finally we use three distinct stellar initial mass functions (IMFs): a Salpeter, a Kroupa and an Arimoto-Yoshii (AY) IMF (see Section 2.4.3).

In Table 3.1 we summarize the main parameters of the cosmological simulations performed including the mass associated to the gas particles and the gravitational softening. All the simulations start at redshift  $z = 99$ . The reference simulations are SW (“Strong Winds”), WW (“Weak Winds”) and MDW (“Momentum-Driven Winds”) with a total of  $2 \times 320^3$  dark matter and gas particles in a 10 comoving  $h^{-1}\text{Mpc}$  box and Salpeter IMF. Furthermore,  $\text{SW}_{\text{KR}}$  (Kroupa IMF) and  $\text{SW}_{\text{AY}}$  (Arimoto-Yoshii IMF) explore the effects of a different IMF compared to the Salpeter one. Some simulations are intended to explore resolution and box-size effects like  $\text{SW}_{10,448}$ ,  $\text{SW}_{10,256}$ ,  $\text{SW}_{20,512}$  and  $\text{SW}_{5,320}$ . The most CPU-time consuming run is the  $\text{SW}_{20,512}$ , which significantly increase the statistics of dark matter haloes able to host DLAs. Finally, the  $\text{SW}_{\text{WDM}}$  aims at exploring the effect of a modification in the initial linear dark matter power spectrum.

Our reference simulations were run on 128 processors working in parallel for a typical CPU time of about  $5 \times 10^5$  s ( $\sim 6$  days). Numerical computations were done on the COSMOS (SGI Altix 3700) supercomputer at DAMTP and at High Performance Computer Cluster (HPCF) in Cambridge (UK) and at CINECA (Centro Interuniversitario del Nord Est per il Calcolo Elettronico), Italy.

## 3.2 Global properties of the simulations

### 3.2.1 IGM temperature and metallicity relations at $z = 3$

In this Section we investigate two global properties of the IGM, namely its thermal and chemical state, focusing on the differences between the SW, WW and MDW runs at  $z = 3$ .

In Figures 3.1 and 3.2 we show the IGM temperature-density relation and the metallicity-density relation for the WW (upper left panel), SW (upper right panel) and MDW (lower panel) simulations. In these figures it is shown an “effective” temperature for the star-forming particles determined as the mean temperature weighted by the contribution in mass of the cold and the hot phases (see Section 3.1). In all cases the phase diagrams are color coded according to the gas mass fraction, as indicated by the vertical bars. For all the three runs a significant fraction in mass (about 10%) of the IGM resides in the tight power-law relation  $T = T_0(1 + \delta)^{\gamma-1}$  at around the mean density. Gas at this density is usually responsible for Lyman- $\alpha$  forest absorption. At  $z = 3$  the IGM has a temperature at the mean density of about  $T_0 = 15000$  K and the slope  $\gamma$  of the temperature-density relation is around 1.6. In our

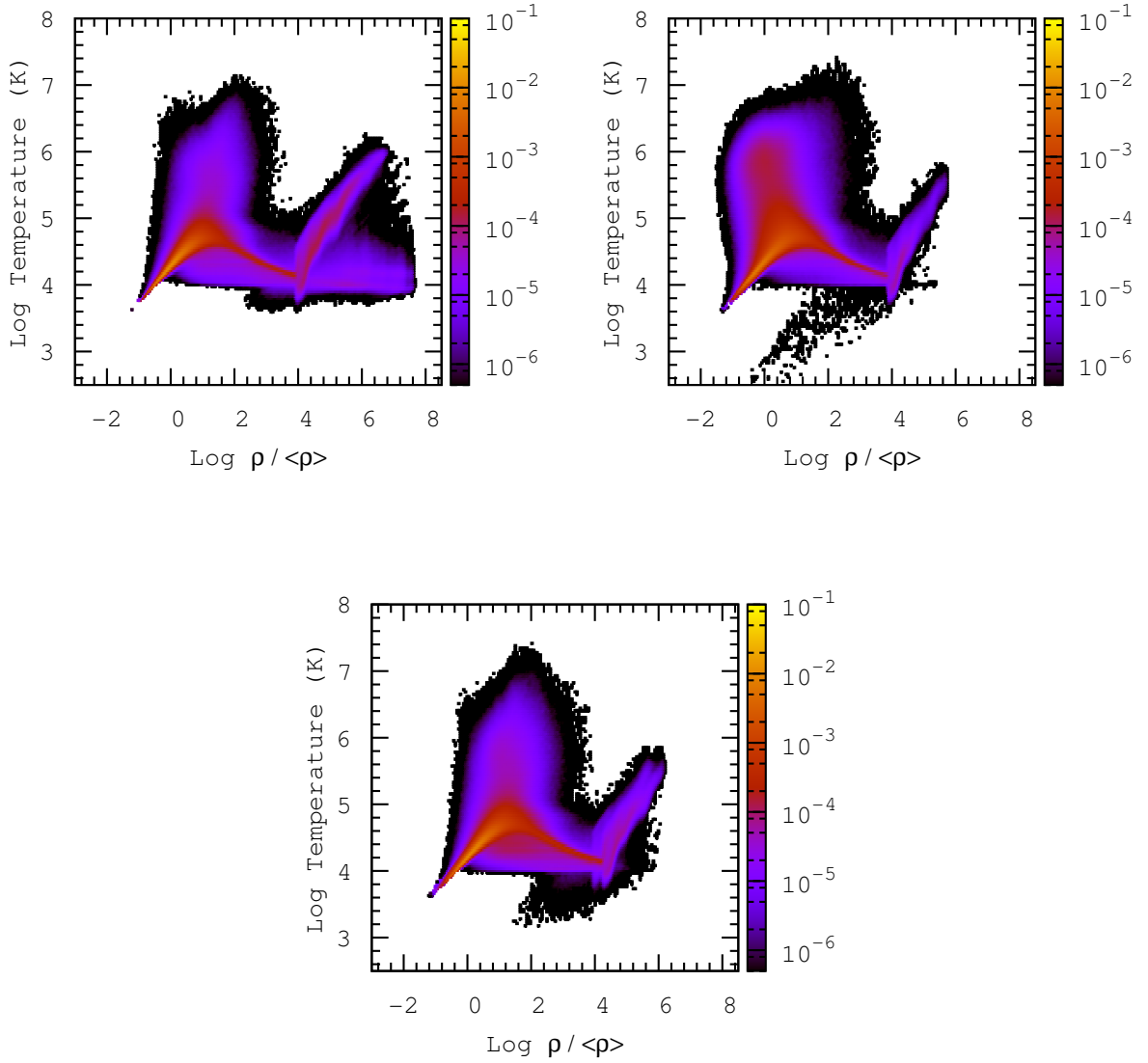


Figure 3.1: Gas (IGM) temperature-density relation (without explicitly splitting the star-forming particles in the hot and the cold phases), for the WW (Weak galactic energy-driven Winds of 100 km/s; upper left panel), SW (Strong galactic energy-driven Winds of 600 km/s; upper right panel) and MDW (Momentum-Driven galactic Winds; lower panel) simulations at  $z = 3$ . The vertical bar indicates the gas mass fraction.

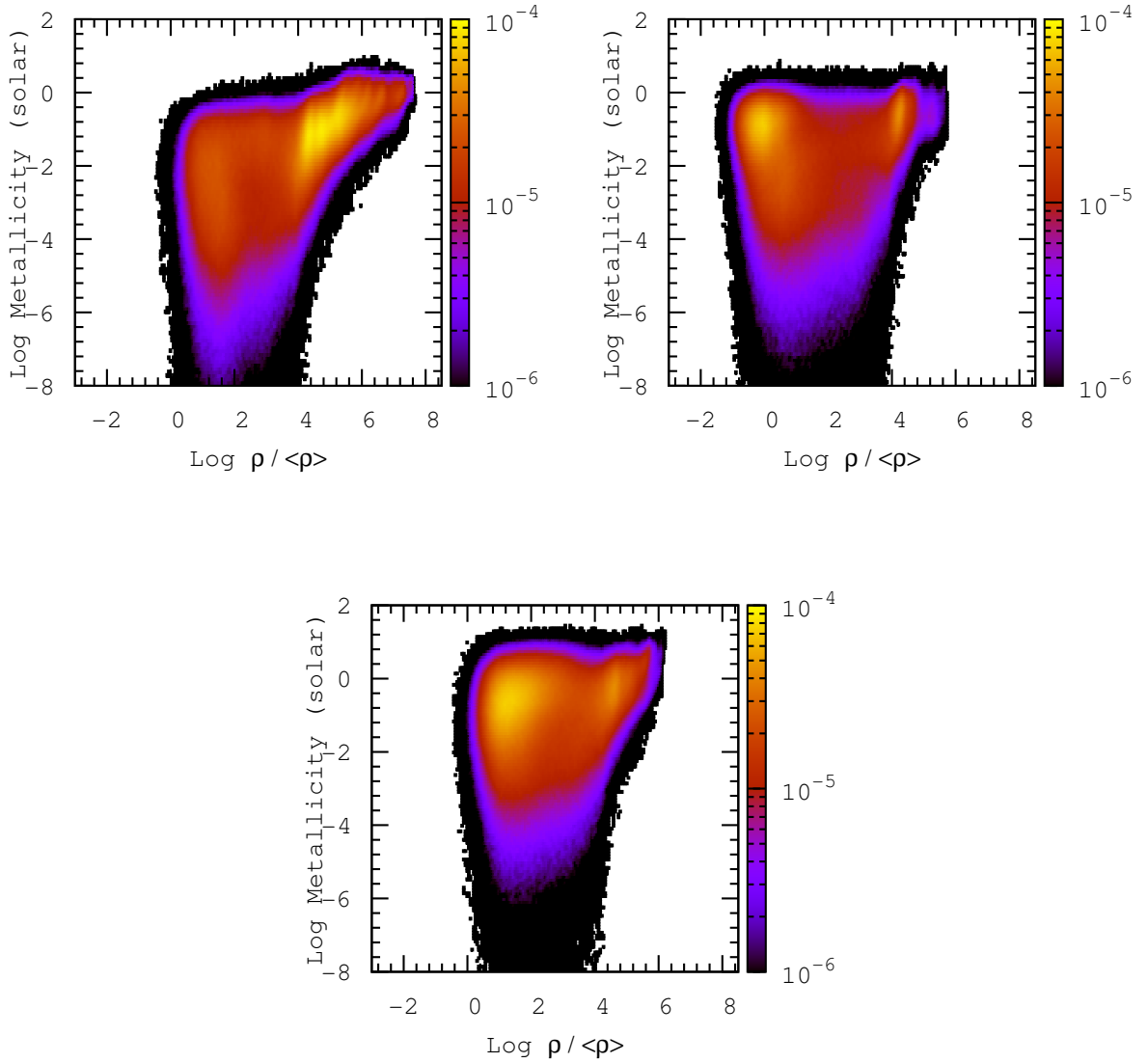


Figure 3.2: Gas (IGM) metallicity-density relation (without explicitly splitting the star-forming particles in the hot and the cold phases), for the WW (Weak galactic Winds of 100 km/s; upper left panel), SW (Strong galactic Winds of 600 km/s; upper right panel) and MDW (Momentum-Driven galactic Winds; lower panel) simulations at  $z = 3$ . The vertical bar indicates the gas mass fraction.

simulations we assume photoionization equilibrium and under this assumption it is difficult to get values of  $\gamma < 1.6$ , which however are in better agreement with the recent measurements of the Lyman- $\alpha$  probability distribution function (Bolton et al. 2008). An IGM fraction between  $10^{-4}$  and  $10^{-3}$  is in the form of shock-heated gas at temperatures higher than  $10^5$  K. The tail of cold gas at large densities resides in the inner parts of the haloes while at even larger densities,  $> 10^4 \langle \rho \rangle$ , and temperature,  $> 10^4$  K, is associated to star-forming regions. We note a plume of cold and overdense gas particles that are below  $10^4$  K and carry a fraction of mass of the order  $10^{-6}$ : these are gas particles that are in the wind phase. After these particles enter the wind regime they become hydrodynamically decoupled for a certain period of time (see Section 2.4.4). During this period they travel “freely” towards regions in which both the density and the temperature are lower. As a consequence, when these particles re-couple to the hydrodynamics, their temperature drop because of the adiabatic expansion.

In Figure 3.2 we show the metallicity-density relation for the three simulations. In the SW case the gas that has been enriched spans a wide range of densities and can attain values that are very close to solar. Also gas that is below the mean density appears to be metal enriched at a high level in this simulation. The bulk ( $10^{-4}$  in mass fraction) of the IGM is either in the form of gas at the mean density or in the form of very dense gas at about  $10^4 \langle \rho \rangle$  with metallicities of about  $0.1 Z_{\odot}$ .

All the previous findings are particularly interesting when the WW (upper left panel) and SW (upper right panel) runs are compared. For the WW temperature-density relation it is clear that the amount of shock-heated gas is significantly reduced and the region of the diagram at temperatures between  $10^5$  and  $10^7$  K is less populated. Thereby, strong galactic winds with speed of order 600 km/s heat the IGM significantly, while weaker winds with speed of order 100 km/s are less effective in doing this. The gas particles in the wind phase at  $T < 10^4$  K are now fewer than in the SW case and at higher overdensity. Moreover, the star-forming high density tail is considerably more extended than in SW case confirming the less efficient feedback of WW in suppressing star formation. In contrast with the SW simulation, in the WW case there is slightly less metal-enriched underdense gas, while the metallicity gradient with density is steeper. Higher values of metallicities are now reached, which attain super-solar values at very high density. In the WW case the bulk of the enriched gas shifts from the mean density values of the SW case to a region which is about  $10^4$  times denser than the mean.

We stress that the difference between the SW and WW simulation is only in the wind speed which is 600 and 100 km/s, respectively, while all the other parameters have been kept fixed. These values of the wind velocity have been chosen in order to embrace values suggested by observational studies of HI and CIV-galaxy correlation and Lyman- $\alpha$  forest in close QSO pairs (Adelberger et al. 2005; Rauch et al. 2005), and observations of interstellar lines in ultraluminous infrared galaxies (Martin 2005).

The lower panels of Figures 3.1 and 3.2 show results for the MDW simulation. Looking at the temperature-density diagram one can easily see a general trend that is intermediate between those of the SW and WW runs. For example, the region associated to wind particles (cold and overdense particles below  $10^4$  K) is less pronounced with respect to SW but not as negligible as the WW run. However the metallicity-density relation is quite different from the energy-driven implementation. In particular the metallicity reaches values slightly higher than SW and WW for the whole range of densities and most importantly there is much more enriched material

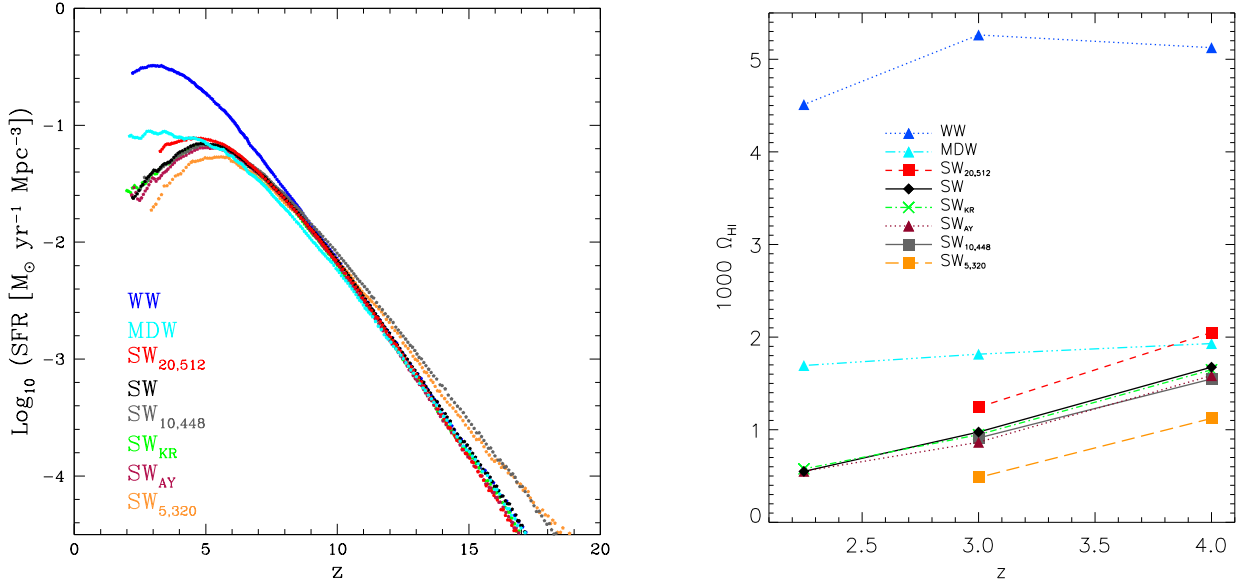


Figure 3.3: *Left Panel:* cosmic star formation rate (SFR) for some of the hydrodynamical simulations of Table 3.1. *Right Panel:* evolution of the total  $\Omega_{\text{HI}}$  ( $\times 1000$ ) as a function of redshift for some of the hydrodynamical simulations of Table 3.1.

around the mean density. This result suggests that MDW is more efficient in polluting the IGM above and around the mean density: this is due to the fact that, unlike for SW and WW, in MDW even small haloes contribute significantly to the enrichment. In fact, such small haloes have small velocity dispersion and correspondingly greater loading factors (see Eq. (2.49)) for their winds.

### 3.2.2 Star formation rates and evolution of ion species

In this Section we analyse the star formation rates (SFR) for the different simulations and the evolution of the neutral hydrogen content and of two ion species, CIV and OVI, that are usually observed in absorption in QSO spectra even at higher redshifts than those explored here (e.g. Becker et al. 2009; Ryan-Weber et al. 2009).

In the left panel of Figure 3.3 we show the total star formation rate of the simulated volume as a function of redshift. The WW simulation has nearly a factor 10 higher star formation rate compared to the others at  $z \sim 3$ . This means that the feedback mechanism induced by strong galactic winds is effective in paupering the metal-rich star-forming gas significantly decreasing the star formation rate. The SW<sub>20,512</sub> and SW<sub>5,320</sub> embrace all the SW runs and this is due to cosmic variance effects. We note negligible differences between the Salpeter IMF and the other two IMFs used (Kroupa and Arimoto-Yoshii), at least at the relatively high redshifts considered here. We underline, however, that we neglect the effect of assuming different IMFs on the observationally inferred cosmic star formation rate; this means that we do not change the star formation efficiency as it would be required in order to match the observables when the number of massive stars per unit mass of formed stars changes. That is because here we

are more interested in the chemical and energetic effect of the IMF. We also point out the intermediate trend of the MDW, in between SW and WW. At very high redshift ( $z > 10$ ) the  $SW_{5,320}$  and  $SW_{10,448}$  show a higher star formation with respect to the other runs. This is due to the improved resolution of these simulations that can resolve higher densities at earlier times. The star formation rate of the  $SW_{10,448}$  at lower redshift agrees very well (in fact the black and the grey curves are nearly indistinguishable) with that of the SW simulation, which has the same box-size but less particles. This confirms the numerical convergence of our simulations.

The behaviour shown in the star formation rate is very similar in nature to that of the total neutral hydrogen evolution of Figure 3.3 (right panel). Here we plot  $\Omega_{\text{HI}}$ , which is defined as the contribution of neutral hydrogen to the total critical density (the values have been multiplied by 1000). The neutral hydrogen fraction is followed in the simulation self consistently with the assumed average UV background and not rescaled a-posteriori using a different UV background. Note again that the neutral hydrogen content of the WW simulation is about a factor 5 higher than that of the SW and this is due to the fact that in the WW simulation the gas is colder and more concentrated in the potential wells of galaxies and thereby is significantly more neutral. Even in this case the  $SW_{20,512}$  and  $SW_{5,320}$  simulations embrace all the SW runs as for the star formation rate plot. The  $SW_{\text{KR}}$  and  $SW_{\text{AY}}$  agree well with the SW confirming that feedback and resolution/box-size effects have more impact on the simulations than effects due to the particular choice of the IMF as long as the stellar spectra are not self consistently taken into account. The difference between WW and SW simulations is somewhat more pronounced than that found by Nagamine et al. (2004) and this is probably due to the fact that our simulations include metal cooling, thereby increasing the neutral hydrogen amount in the haloes (we will come back to this point later). The MDW is in between SW and WW and again the  $SW_{10,448}$  is in good agreement with the SW, demonstrating that, at least for these quantities, numerical convergence has been reached.

At the end of Section 3.3.5 we compute the DLAs contribution to the total neutral hydrogen content ( $\Omega_{\text{DLA}}$ ) and we compare it with the results of Pontzen et al. (2008) and the observational estimates of Prochaska et al. (2005) and Péroux et al. (2005).

As a further check, in Figure 3.4 we plot the evolution of the contribution to the total density of two of the ions that trace the high redshift IGM at relatively low density and for which there are some observational constraints (Schaye et al. 2003; Aguirre et al. 2008): CIV ( $\lambda\lambda$  1548.204, 1550.781 Å) in the upper panels and OVI ( $\lambda\lambda$  1031.927, 1037.616 Å) in the lower panels. Although in the rest of this Chapter we will focus on the distribution of metals around DLA systems, we would like to address briefly the evolution of ionization species in the IGM as a whole. We use the redshift outputs at  $z = 2.25, 3, 4$  and we extract the values for  $\Omega_{\text{CIV}}$  and  $\Omega_{\text{OVI}}$  summing over all the gas particles. In order to obtain the ionization fraction for the two elements it is necessary to multiply the abundance of a given metal, carried by each particle, by its ionization fraction that depends on density and temperature. We use the CLOUDY code (Ferland et al. 1998) to compute a-posteriori the relevant fractions for each gas particles. We choose the HM05 option in CLOUDY, which consists of a UVB made by QSOs and galaxies with a 10% photon escape fraction and which is in agreement with other observational constraints (Bolton et al. 2005).

In Figure 3.4 we explicitly show how different effects impact on  $\Omega_{\text{CIV}}$  and  $\Omega_{\text{OVI}}$ : in the left panels we compare simulation with different wind strength and implementation (SW, WW and

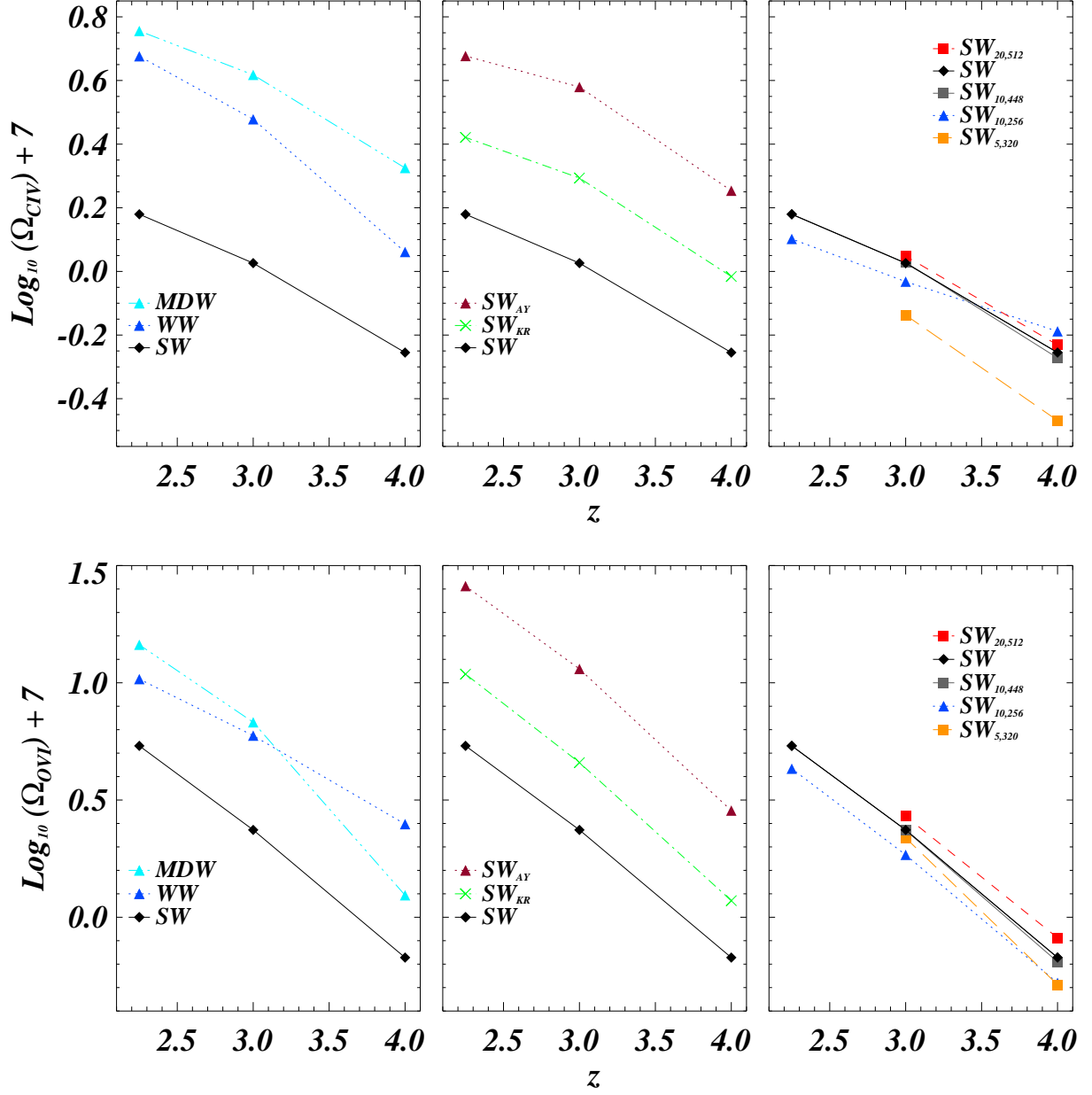


Figure 3.4: Evolution of the total  $\Omega_{\text{CIV}}$  (upper panels) and the total  $\Omega_{\text{OVI}}$  (lower panels) as a function of redshift for some of the hydrodynamical simulations of Table 3.1. *Left Panels:* effect of different wind strengths and implementations. *Middle Panels:* effect of different IMFs. *Right Panels:* resolution tests.

MDW); in the middle panels we test the effect of different IMF (SW, SW<sub>KR</sub> and SW<sub>AY</sub>); in the right panels we present resolution tests for all the SW runs (SW, SW<sub>5,320</sub>, SW<sub>10,256</sub>, SW<sub>10,448</sub> and SW<sub>20,512</sub>). Here we discuss each panel of the figure:

- *Left Panels (feedback physics)*: for the SW simulations the total amount of the two ions increase by a factor of about 3 between  $z = 4$  and  $z = 2.25$ . The WW simulation contain  $\sim 2.5$  times more OVI and CIV compared to the SW case. The reason is that with such weak winds the metals remain very close to the dense environments around galaxies and cannot reach the low-density IGM in contrast with the SW case where the gas is expelled in an explosive way and, for this reason, is also much more heated (see for example Theuns et al. 2002). In these regions close to galaxies the ionization fractions are typically larger than in the voids. The MDW CIV and OVI evolution is similar to the energy driven implementations although it has a higher normalization than SW and WW: this is due to the fact that in the former implementation the winds are more efficient in enriching the IGM around the mean density with metals without heating the gas as much as in the SW case. This produces larger values of  $\Omega_{\text{CIV}}$  and  $\Omega_{\text{OVI}}$  reached at  $z = 2.25$ .
- *Middle Panels (IMF)*: The trend in the redshift dependence of  $\Omega_{\text{CIV}}$  and  $\Omega_{\text{OVI}}$  is the same for SW, SW<sub>KR</sub> and SW<sub>AY</sub>, while there are differences in the normalization. The Kroupa and Arimoto-Yoshii IMFs result in values for the CIV and OVI density that are respectively  $\sim 1.5$  and  $\sim 3$  times higher than the standard Salpeter case. This is due to the fact that Salpeter IMF results in an excess of low mass stars, Kroupa IMF produces a smaller number of massive stars than the other two but twice as many stars in the range of mass  $0.3M_{\odot} < m < 3M_{\odot}$ , while with the Arimoto-Yoshii (or “top-heavy”) IMF there is a larger contribution from massive stars (see Figure 2.2). For these reasons, the SW<sub>AY</sub> run produces more oxygen and carbon than the other simulations, while the SW run (with Salpeter IMF) is less efficient in producing these metal species and SW<sub>KR</sub> is in between the other two. Interestingly the MDW run with Salpeter IMF (triple-dot-dashed cyan lines in the left panels) produces more CIV than the SW<sub>AY</sub>, while the amount of OVI is comparable, confirming the high efficiency of momentum driven winds in enriching the IGM.
- *Right Panels (resolution tests)*: the aim of these two panels is to show that our analysis is robust against box-size and resolution effects. We plot  $\Omega_{\text{CIV}}$  and  $\Omega_{\text{OVI}}$  for all the SW runs and it is clearly evident the convergence of the results (especially for the  $\Omega_{\text{OVI}}$  and the SW<sub>10,448</sub> simulation). As we already found for the SFR and the  $\Omega_{\text{HI}}$ , the SW<sub>20,512</sub> and SW<sub>5,320</sub> simulations embrace all the SW runs.

A comparison of these findings with those by Oppenheimer & Davé (2006, 2008) shows that the evolution of  $\Omega_{\text{CIV}}$  is somewhat faster and the normalization higher than what they find. In particular our MDW is even more discrepant than SW and WW with respect to the analogous momentum-driven winds simulation (“*mzw*”) by Oppenheimer & Davé (2006). However, it is difficult to compare properly given the different resolutions, box-sizes, feedback implementations and details on chemical evolution model used.

In the last part of this Section we briefly discuss the other simulations described in Table 3.1. The simulations SW, SW<sub>10,448</sub> and SW<sub>10,256</sub> are characterised by the same box-size but different number of particles, so that they allow us to carry out a test of stability of our results against numerical resolution. As already mentioned, for the SW<sub>10,448</sub> the star formation rate trend at high redshift is similar to that of SW<sub>5,320</sub> (the simulation with the highest resolution), while it agrees at lower redshift with SW, which has the same box-size. Instead the SW<sub>10,256</sub> has lower SFR (not plotted) than SW at high redshift because, for a given box-size, a lower number of particles means a lower number of structure resolved in the simulation and thereby a lower SFR. As for the evolution of  $\Omega_{\text{HI}}$ ,  $\Omega_{\text{CIV}}$  and  $\Omega_{\text{OVI}}$ , the SW<sub>10,448</sub> follows the results of the SW almost perfectly. This is also true for other analysis made in this work (phase diagrams, haloes properties, etc.), thus further confirming the numerical convergence of our results on these simulations properties. The run SW<sub>WDM</sub> has a different initial power spectrum  $P(k)$  respect all others simulations: power is suppressed at small scales due to free streaming of the dark matter particles that in this case are “warm” and have mass equal to 1.2 keV (corresponding to a suppression scale of around 50 comoving  $h^{-1}\text{kpc}$ ). As a consequence, the star formation rate density at high redshift is significantly reduced with respect to the CDM case, with a correspondingly smaller number of haloes having mass comparable or smaller than the free-streaming mass scale. We run this simulation in order to test whether the modified  $P(k)$  could produce haloes that better fit the column density distribution function for small values of  $N_{\text{HI}}$ , that will be discussed in Section 3.3.5.

### 3.3 The neutral hydrogen distribution

In this Section we focus on the properties of the neutral hydrogen around the simulated galactic haloes. The aim is to study DLAs properties and statistics extracted from our simulations and to compare them with the latest observational data and the simulation results from other groups (Nagamine et al. 2004, 2007; Pontzen et al. 2008).

#### 3.3.1 Identifying haloes

We identify haloes in the simulations by running a parallel Friends-of-Friends (FoF) algorithm with a linking length which is 0.2 times the dark matter mean interparticle spacing. The number of haloes of a given mass per unit mass and per unit volume as a function of their mass is shown in Figure 3.5 for the SW, SW<sub>5,320</sub> and SW<sub>20,512</sub> runs at redshift  $z = 3$ , along with the Sheth & Tormen (1999) mass function, so as to test at the same time the effect of resolution and of box-size. Again, the SW<sub>20,512</sub> and SW<sub>5,320</sub> embrace the reference case SW: the mass function of SW<sub>5,320</sub> extends to small halo masses due to its better resolution, while SW<sub>20,512</sub> produce more massive haloes due to its larger box-size. In our largest simulation we have three haloes above  $10^{12} h^{-1}M_{\odot}$  and about 1000 haloes of masses above  $10^{10} h^{-1}M_{\odot}$  at  $z = 3$ .

We follow the analysis made by Nagamine et al. (2004, 2007) to realize a mock DLA sample: after having identified the haloes and their center of mass, we interpolate with a TSC (Triangular Shaped Cloud) algorithm the comoving neutral hydrogen mass density around the center of mass of each halo on a cubic grid; then we “collapse” the grid along a random direction and we obtain a set of neutral hydrogen column densities for each halo. Thus the column density

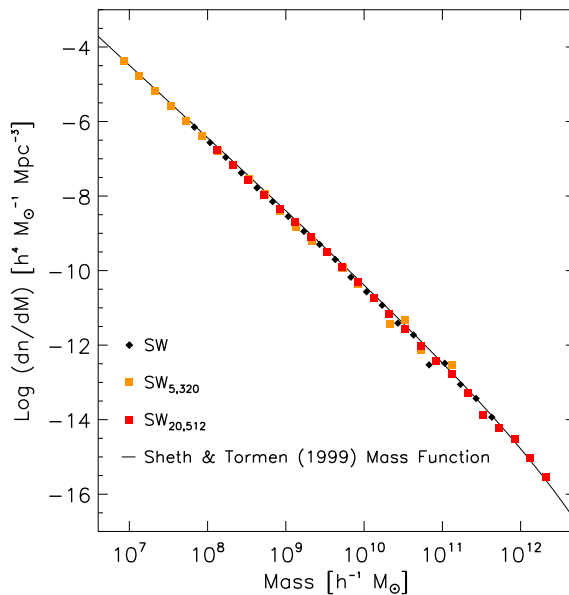


Figure 3.5: Differential halo mass function (number of haloes of a given mass per unit mass [ $h^{-1}M_{\odot}$ ] and per unit volume [ $\text{Mpc}^3/h^3$ ]) for runs SW, SW<sub>5,320</sub>, SW<sub>20,512</sub> at redshift  $z = 3$ , compared with Sheth & Tormen (1999) prediction.

reads:

$$N_{\text{HI}} = \sum_i \rho_{i,\text{HI}} \epsilon / m_p (1+z)^2, \quad (3.3)$$

with  $m_p$  the proton mass and  $\epsilon = l/n_{\text{grid}}$  the linear dimension of the single grid cell. Here  $l$  is the size of the box around the halo and  $n_{\text{grid}}$  is the number of grid points.

Typically, for the most massive haloes, we use cubes of size 200 comoving  $h^{-1}\text{kpc}$  with  $32^3$  grid points ( $\epsilon = 6.25h^{-1}\text{kpc}$ ). In such a way, we increase the DLA total redshift path and we sample  $32^2 \times N_{\text{haloes}}$  HI column densities along lines-of-sight per simulated box.

We have carried out some tests changing the number of grid points in order to study the effect of the sampling size on the neutral hydrogen distribution. The choice of the grid points number is crucial because too many points produce a sampling size below the resolution of the simulation and consequently an “oversampling” of the HI mass density with large statistical fluctuations, while too few points produce a smooth statistic which could not be representative of the real density field. At the end we found that the best compromise was to use  $32^3$  grid points, corresponding to  $\epsilon \gtrsim 4.5 \times \text{softening length}$  (which is also the typical value of the SPH smoothing length in the outskirts of the haloes), differently from Nagamine et al. (2004), who choose instead  $\epsilon \approx \text{softening length}$ .

Figure 3.6 shows the HI column density maps extracted as explained above, but with a finer grid subdivision of 256 points, for the same massive halo in the WW (upper left panel), SW (upper right panel) and MDW (lower panel) runs at  $z = 3$ . The HI density at each pixel has been projected along the line-of-sight in the  $z$  direction. In the figure it is visible the effect of the winds: in the WW run (upper left panel) high column density gas is more concentrated inside the central halo and inside some substructures. Also the column density values reached

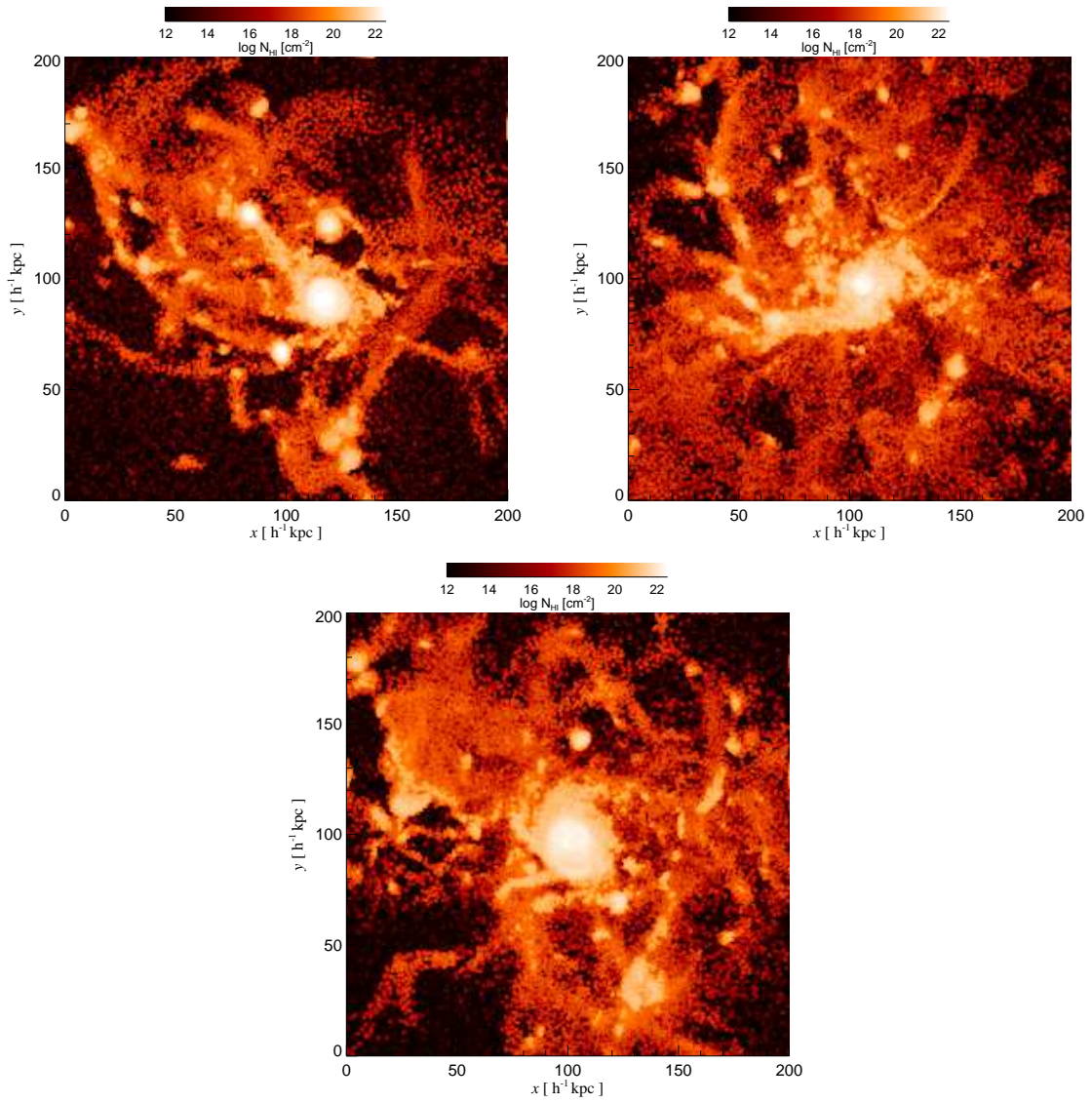


Figure 3.6: HI column density maps in a slice around the same massive halo in the WW (upper left panel), SW (upper right panel) and MDW (lower panel) runs at  $z = 3$ .

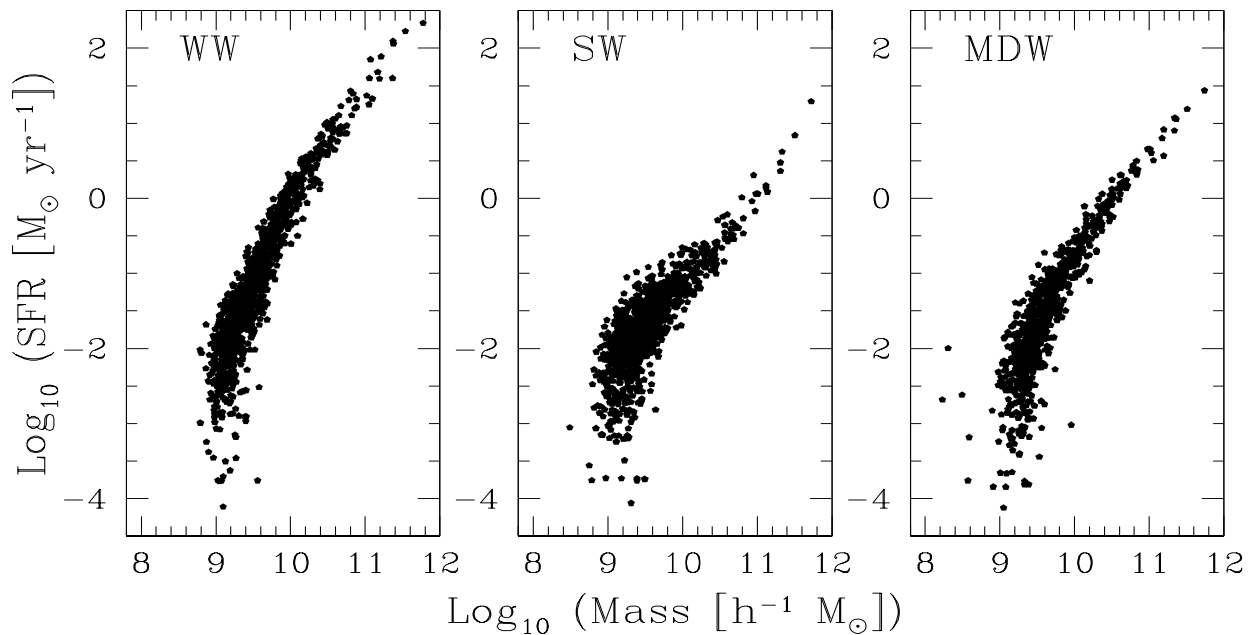


Figure 3.7: Star formation rates (in  $M_{\odot}$  per year) plotted as a function of halo mass for SW, WW and MDW runs at  $z = 3$ .

are higher than for the other runs. In the SW run (upper right panel), the gas is more spread around the central haloes and the substructures. Finally if we consider HI column densities above the DLA limit of  $N_{\text{HI}} = 2 \times 10^{20} \text{ cm}^{-2}$  we see that the central halo in the MDW run has the largest cross-section. We discuss further about this point in Section 3.3.3.

### 3.3.2 Properties of the haloes

For the haloes identified with the FoF algorithm we compute mean quantities that could be relevant for the following analysis, such as the star formation rate inside each halo, the mass-weighted mean total metallicity and the mass-weighted mean neutral fraction of hydrogen (HI/H). We plot in Figures 3.7, 3.8 and 3.9 our findings at redshift  $z = 3$ , only for haloes having mass greater than  $2 \times 10^8 h^{-1} M_{\odot}$ , that are resolved with at least 100 dark matter particles. The properties of the haloes below  $10^9 h^{-1} M_{\odot}$ , resolved with  $\sim 1000$  particles, should not be trusted at a quantitative level, but we prefer to show them in order to appreciate the increase in the scatter at low masses.

For the most massive haloes, the WW simulation shows very high star formation rates that are even a factor 100 larger than that of the corresponding haloes in the SW run: this is expected due to the smaller efficiency of the weak winds in suppressing star formation (see the left panel of Figure 3.3). The MDW run reaches nearly the same SFR values of the SW for the most massive haloes, while for intermediate mass haloes ( $10^{9.5-11} h^{-1} M_{\odot}$ ) the MDW haloes have higher SFR than SW ones. For the smallest haloes of around  $10^9 h^{-1} M_{\odot}$  the SW run shows a slightly larger scatter in the SFR values. Overall, the bulk of the haloes, of masses between  $10^9$  and  $10^{10} h^{-1} M_{\odot}$ , that are likely to host DLA systems, have star formation rates of about

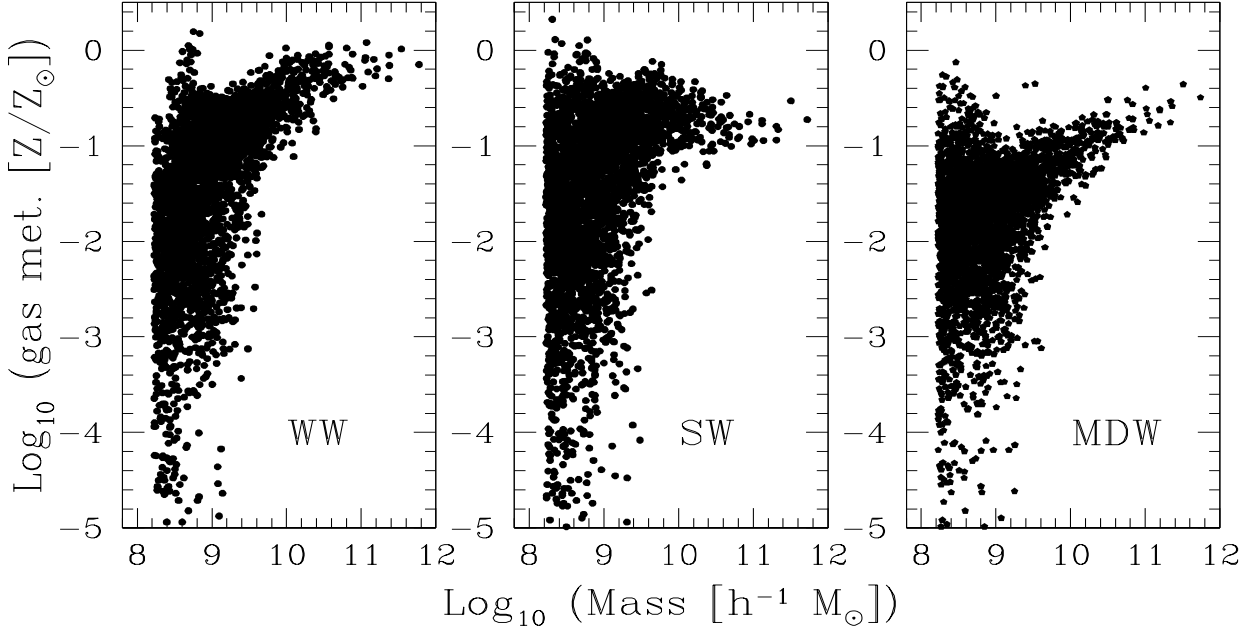


Figure 3.8: Mean total metallicity in solar unit plotted as a function of halo mass for SW, WW and MDW runs at  $z = 3$ .

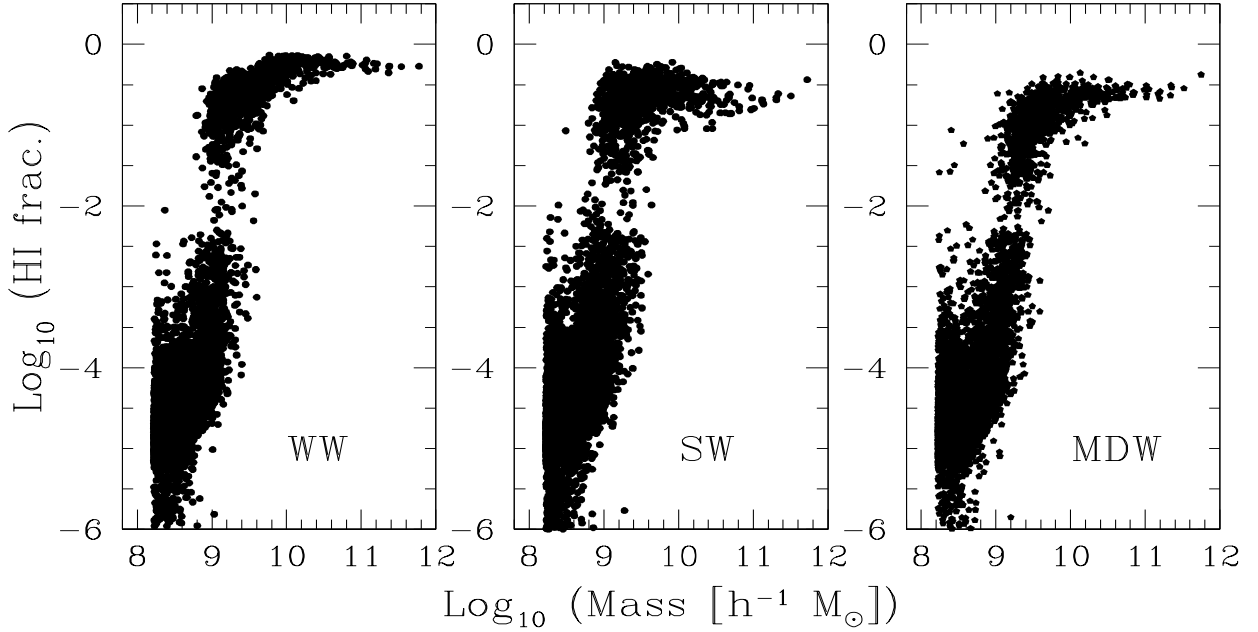


Figure 3.9: Mean neutral fraction of hydrogen (HI/H) plotted as a function of halo mass for SW, WW and MDW runs at  $z = 3$ .

0.1  $M_{\odot}$ /year. For haloes above  $10^{10} h^{-1} M_{\odot}$  the star formation rates are different between the models and usually around 1-30  $M_{\odot}$ /year. These star formation rates are in general agreement with those of the population of faint Lyman- $\alpha$  emitters found recently by Rauch et al. (2008), in which a link between the Lyman- $\alpha$  emitters and the DLAs is suggested.

For the same reasons metallicities of haloes in the WW run are higher than in the SW and MDW simulations (see Figure 3.8). Comparing this result with Figure 3.4, one can derive the following general picture: in the WW run metals remain locked inside the haloes (or stay close to the haloes), while in SW and MDW they are able to reach the IGM and enrich it: this is particularly true for the less massive haloes in the MDW. In fact, the MDW small mass haloes have in general metallicity lower than the corresponding SW and WW haloes. The wind implementation is thereby very effective in devoiding the galaxies of star forming cold gas that is enriched at a level of about 0.1  $Z_{\odot}$ . The most important result of this panel is however that the different wind implementations show different mass-metallicity relations especially for haloes of masses above  $10^{9.5} h^{-1} M_{\odot}$ : while WW and MDW show a correlation (although with different amplitude), the SW results seem to produce very little correlation between mass and metallicity or possibly a weak anti-correlation. This different metallicity pattern in haloes could be important when compared with observation (e.g. Maiolino et al. 2008) and could possibly allow to discriminate between different feedback scenarios.

Finally we note that the largest metallicities appear to occur in haloes of small masses. There are two different motivations for this to happen. The first motivation is numerical: as we mentioned at the beginning of this Section, both these small haloes and the wind model are not well resolved, thereby their large metallicities are, at least partially, the result of some numerical artifact. Furthermore, we also checked that there is a physical motivation: these small haloes are strongly affected both by self enrichment at early epochs and by the metal enriched winds blowing from bigger haloes close to them. Addressing quantitatively these issues would require more numerical work, which is beyond the scope of this work.

In Figure 3.9 we show the mass-weighted mean neutral fraction of hydrogen (HI/H) inside haloes, a quantity which is closely related to the DLA properties. The general trend reflects those of the right panel of Figure 3.3: for a given halo mass the WW simulation displays the highest value, while the SW and the MDW have comparable values. In all the panels, there are present two different sets of values: above and below HI/H  $\sim 0.01$ . The first is associated to the most massive haloes and the second to the least massive ones. This is due to the fact that the most massive haloes contains many particles above the density threshold  $\rho_{\text{th}}$  for which the neutral hydrogen fraction is equal to the fraction of mass in cold clouds  $f_c$  (see Eqs. (3.1) and (3.2) in Section 3.1), boosting in this way the neutral hydrogen content of these haloes. Less massive haloes have instead neutral fractions that are set by the physical conditions of the gas and by the UVB background and are typically more ionized ( $f_{\text{HI}} \ll f_c$ ) than the most massive haloes.

### 3.3.3 The DLA cross-section

For each halo of total mass  $M_{\text{tot}}$  we derive the DLA cross-sections,  $\sigma_{\text{DLA}}$  (in comoving units), by selecting and summing up the area of all the cells with a column density (determined as

Redshift	Run	slope $\alpha$	$\beta$
$z = 4$	SW	0.57	3.83
	WW	0.46	3.79
	MDW	0.69	4.11
$z = 3$	SW	0.77	3.75
	WW	0.49	3.61
	MDW	0.85	4.06
$z = 2.25$	SW	0.62	2.99
	WW	0.52	3.45
	MDW	0.92	3.88

Table 3.2: Fitting parameters  $\alpha$  and  $\beta$  of Eq. (3.4) for runs SW, WW and MDW at redshift  $z = 4, 3$  and  $2.25$ .

explained in Section 3.3.1) above  $10^{20.3} \text{ cm}^{-2}$ . Next we fit a power-law relation of the form:

$$\log \sigma_{\text{DLA}} = \alpha(\log M_{\text{tot}} - 12) + \beta, \quad (3.4)$$

for all the simulations made. Results are shown in Figure 3.10 where we plot the cross-sections as extracted from the SW at  $z = 2.25, 3, 4$  with overplotted fits for SW itself (dashed black line), WW (blue dot-dashed line) and MDW (cyan triple-dot-dashed line). Fitting parameters  $\alpha$  and  $\beta$  for each of these runs are shown in Table 3.2. The continuous red lines in the middle panel fit the upper and lower envelopes of the SW distribution at  $z = 3$  and were drawn with the aim of highlighting the scatter in the distribution of cross-sections especially at low masses. The parameters of the upper envelope line are  $\alpha = 0.5$  and  $\beta = 3.6$  (very similar to the WW case), while those of the lower envelope line are  $\alpha = 1.2$  and  $\beta = 4.02$ . In the next section we discuss the effect of taking into account this scatter in a very conservative way.

It is clear that for the WW simulation the cross-sections are larger than in the SW case for the small mass haloes: this is due to the fact that the wind is more effective in expelling cold gas from small mass haloes than from the most massive ones. For the most massive haloes the content of cold gas is much larger and this trend is inverted: the WW run has a smaller cross-section than in the SW and MDW cases because the cold gas is located very close to the dense galactic environments. The MDW trend reflects the fact that momentum-driven winds are more directly related to the halo properties: smaller mass haloes have greater loading factor and winds become very efficient as in SW case. On the contrary, for massive haloes the MD winds become less efficient: the cold blob of gas around the halo has a more regular shape than in the SW case and determines a larger cross-section than the SW. To sum up, as one can see from Figure 3.6, the qualitative trends are the following: for WW the gas is concentrated in the center of the haloes; the SW expels gas in a quite violent way and the shells of expanding material fragment; the MDW blows less gas but in a more homogeneous way than SW.

A comparison of the results from the SW run with those obtained by Nagamine et al. (2004, 2007) at similar resolution shows that we obtain on average a 20 per cent shallower slopes and 5% smaller  $\beta$  parameters: this is likely to be due to the faster wind speed adopted for the

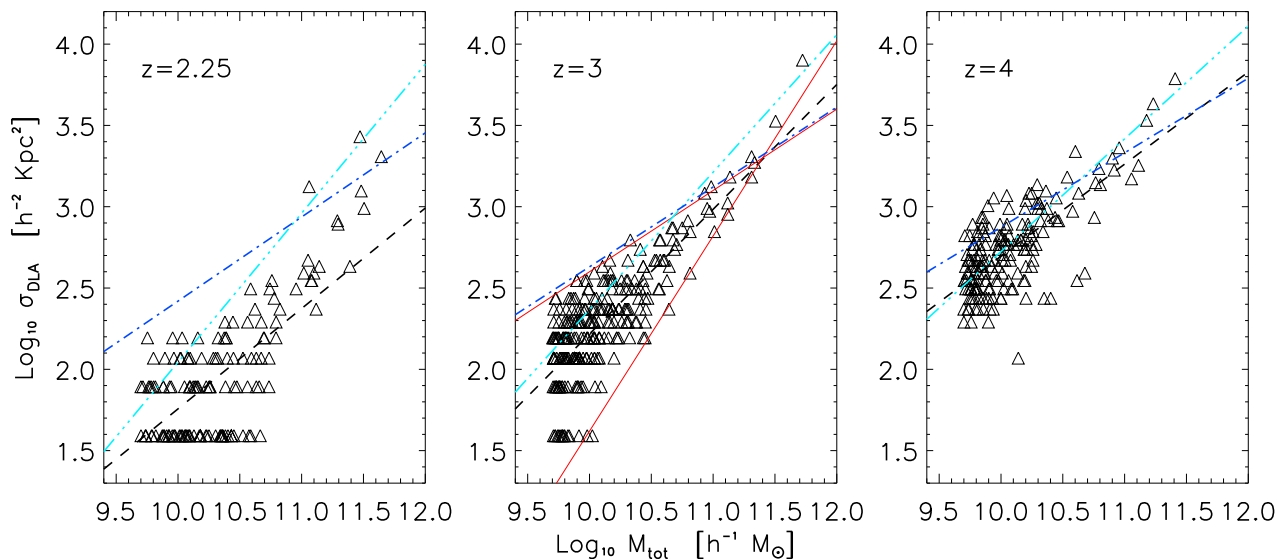


Figure 3.10: Triangles represent the DLA cross-sections (in comoving units) as a function of the total halo mass for the SW run at  $z = 2.25, 3, 4$ . The overplotted lines show power-law fits, of the form  $\log \sigma_{\text{DLA}} = \alpha(\log M_{\text{tot}} - 12) + \beta$ , to the data points for the SW itself (dashed black line), WW (dot-dashed blue line) and MDW (triple-dot-dashed cyan line) runs. The continuous red lines in the middle panel fit the upper and lower envelopes of the SW distribution at  $z = 3$ .

strong wind case (600 km/s vs. 484 km/s) that will probably slightly reduce the normalization  $\beta$  devoiding galaxies of cold gas. Furthermore, the fact that our simulations have the metal cooling implemented could result in a larger cross-section for smaller haloes because the quantity of cold gas increases, while for the most massive haloes the metal cooling enhances the amount of stars at the expenses of cold gas. These two effects determine a shallower slope for the cross-section fitting. In the WW case the run should be compared with the P3 run of Nagamine et al. (2004, 2007) even though the wind speed adopted in this study is 100 km/s vs. 242 km/s and the mass resolution is about 10 times better, but even in this case the trend is confirmed and we find a shallower slope, of about 40 per cent, and a smaller normalization value (by  $\sim 10$  per cent).

In Figure 3.10 it is clearly visible, especially at redshift  $z = 2.25$ , a discretization in the cross-section values, more pronounced than in Nagamine et al. (2004, 2007). This is due to our final choice of the linear dimension of the single grid cell  $\epsilon$  which is somewhat larger than that adopted by Nagamine et al. (2004).

### 3.3.4 The incidence rate of DLA systems

Having obtained the mean relation for the DLA cross-section as a function of halo mass from the previous Section, we are now able to calculate the cumulative number of DLAs per unit redshift (or rate of incidence) using the equation:

$$\frac{dN_{\text{DLA}}(> M, z)}{dz} = \frac{dr}{dz} \int_M^{\infty} n_{\text{h}}(M', z) \sigma_{\text{DLA}}(M', z) dM', \quad (3.5)$$

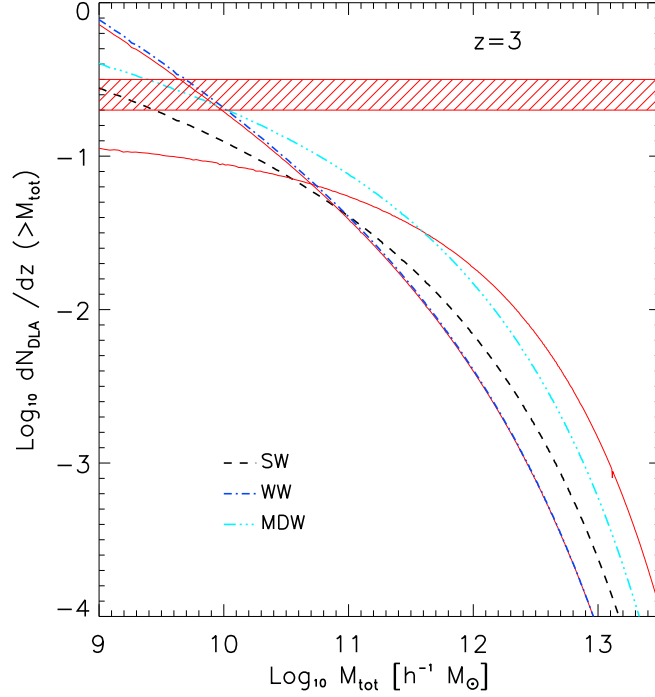


Figure 3.11: Cumulative abundance of DLAs per unit redshift as a function of total halo mass for the SW (dashed black line), WW (dot-dashed blue line) and MDW (triple-dot-dashed cyan line) runs at redshift  $z = 3$ . The continuous red lines show the results considering the scatter (in a conservative way) in the cross-section vs mass relation for the SW run. The red shaded region indicates the observed cumulative DLA abundance of Prochaska et al. (2005) from SDSS data.

where  $n_h(M, z)$  is the Sheth & Tormen (1999) dark matter halo mass function and  $dr/dz = c/H_0 \sqrt{\Omega_m(1+z)^3 + \Omega_\Lambda}$ . Following Nagamine et al. (2004), we use this equation in order not to be sensitive to dark matter haloes with masses below the resolution limit of the simulation. This is a common problem when one tries to compute the number density of DLAs based on a cosmological simulation that does not resolve all small mass haloes that may host a DLA: the underlying assumption in the rest of this work is that haloes below  $10^9 h^{-1} M_\odot$  are not able to produce DLA systems. Moreover small box-size simulations cannot produce very massive haloes. To overcome these limitations in Eq. (3.5) we convolved the Sheth & Tormen (1999) halo mass function with the measured relationship between DLA cross-section and halo mass, thereby correcting for incompleteness in the resolved halo abundance of our simulations. In doing this we extrapolate the power-law fit of Eq. (3.4) both at high and low masses. This relation presents an intrinsic scatter: looking at Figure 3.10 one can note that a given  $\sigma_{\text{DLA}}$  value corresponds to different halo masses, especially at low cross-sections. As mentioned in the previous section we check the impact of this scatter fitting the upper and lower envelopes of the cross-sections distribution of the SW run at  $z = 3$ .

In Figure 3.11 we show  $dN_{\text{DLA}}/dz$  for SW, WW and MDW runs at  $z = 3$ . The three different runs have identical initial power spectrum and cosmological parameters so they all

have the same theoretical dark matter halo mass function. Therefore the differences in Figure 3.11 reflects what we found in previous Section about DLAs cross-sections (see in particular the central panel in Figure 3.10). In fact at low masses WW simulation produce haloes with cross-sections  $\sim 3$  times higher than SW and MDW, and correspondingly  $dN_{\text{DLA}}/dz$  reaches higher values. At greater masses the trend is inverted and WW curve stays below the other two. As we expected  $dN_{\text{DLA}}/dz$  curve for MDW simulation is always above the SW one and well above WW one in the high mass tail. The shaded region shows the observational estimate  $\log(dN/dz) = -0.60 \pm 0.10$  at  $z = 3$  recovered by Nagamine et al. (2007) from the observational results based on SDSS QSO spectra of Prochaska et al. (2005). Finally, the continuous red lines show the results considering the scatter in the cross-section vs mass relation for the SW run. In one case (where the curve is almost equal to that of the WW case) one would need only haloes with mass greater than  $\sim 10^{9.7} h^{-1} M_{\odot}$  to fit the  $dN_{\text{DLA}}/dz$  statistic, while in the other case one should go down to much less massive haloes, that are not well resolved by our simulations.

Our findings for the DLA abundance per unit redshift are slightly different than those obtained by Nagamine et al. (2007): moving to low masses their distribution tend to flatten, while ours are somewhat steeper and this is due both to the different values of the cross-section, the different dimension of the grid cells used, and the different cosmological parameters for the linear dark matter power spectrum (amplitude and slope). As a result, at low masses, the  $dN_{\text{DLA}}/dz$  values in our simulations are about a factor  $\sim 2$  greater than the corresponding ones of Nagamine et al. (2007), while at high mass the trend is inverted and our  $dN_{\text{DLA}}/dz$  decreases somewhat more rapidly than Nagamine et al. results. To summarize, our results reproduce the observational data of Prochaska et al. (2005) slightly better than those of Nagamine et al. (2007) which slightly underpredict  $dN_{\text{DLA}}/dz$  in the range of masses considered.

As far as the redshift evolution of DLA rate of incidence is concerned, the behaviour of the three different simulations reflects that of Figure 3.10. For the sake of brevity we do not show all the plots, but at  $z = 4$  the decreasing in  $dN_{\text{DLA}}/dz$  at high masses is much more pronounced than at  $z = 3$ , due to a lack in massive haloes that have not already formed. At  $z = 2.25$  both WW and MDW curves stay always above the SW one and are more flattened than before down to low masses. The overall trend with redshift is the same of the left panel in Figure 6 of Nagamine et al. (2004).

### 3.3.5 The column density distribution function

In this Section we investigate the column density distribution function for DLAs usually plotted in the form of  $f(N)$ , where  $f(N, X)dNdX$  is the number of DLAs with HI column density in the range  $[N, N + dN]$  and absorption distances in the interval  $[X, X + dX]$ . The absorption distance is given by  $X(z) = \int_0^z (1 + z')^2 H_0/H(z') dz'$ .

In the left panel of Figure 3.12 we show  $f(N)$  for the SW (dashed black line), WW (dot-dashed blue line),  $\text{SW}_{20,512}$  (dotted red line) and MDW (triple-dot-dashed cyan line) runs at  $z = 3$ . The data from SDSS are overplotted along with the  $\Gamma$ -function fit (black diamonds and solid line) of Prochaska et al. (2005).  $\text{SW}_{20,512}$  is plotted to test the effect of different resolution and box-size and its trend is similar to SW. Both are in quite good agreement with data especially at low and high column densities. Instead WW overpredicts the distribution

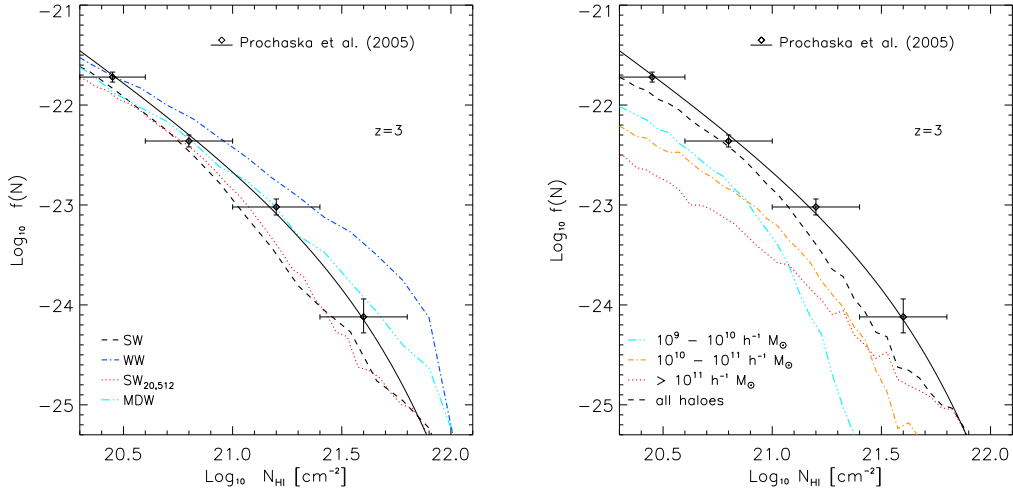


Figure 3.12: *Left Panel:* HI column density distribution function at  $z = 3$  for the SW (dashed black line), WW (dot-dashed blue line), SW<sub>20,512</sub> (dotted red line) and MDW (triple-dot-dashed cyan line) runs. *Right Panel:* Contribution to the HI column density distribution function from haloes of different mass in the SW<sub>20,512</sub> run at  $z = 3$ . Cyan triple dot-dashed line refers to haloes with mass in the range  $10^9 - 10^{10} h^{-1} M_{\odot}$ , orange dot-dashed line refers to haloes with mass in the range  $10^{10} - 10^{11} h^{-1} M_{\odot}$ , red dotted line refers to haloes with mass greater than  $10^{11} h^{-1} M_{\odot}$  while black dashed line refers to all haloes. In both the panels the overplotted black diamonds and the solid line show the data points and the fit of Prochaska et al. (2005).

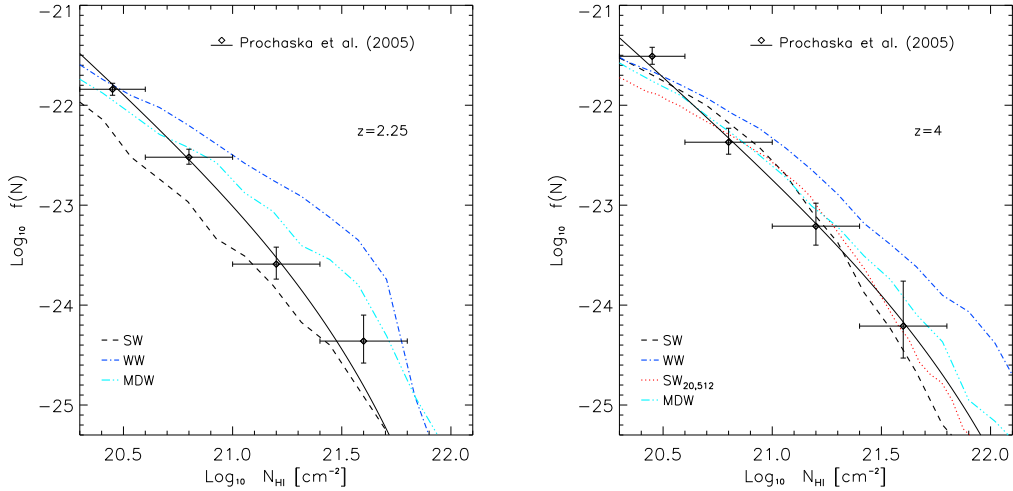


Figure 3.13: *Left Panel:* HI column density distribution function at  $z = 2.25$  for the SW (dashed black line), WW (dot-dashed blue line) and MDW (triple-dot-dashed cyan line) runs. Overplotted black diamonds and solid line show the data points and the fit of Prochaska et al. (2005). Run SW<sub>20,512</sub> is not present here because this simulation was stopped at  $z_f = 3$ . *Right Panel:* the same as the left panel but at redshift  $z = 4$ . Dotted red line refers to the SW<sub>20,512</sub> run.

function at large  $N_{\text{HI}}$  as was already found by Nagamine et al (2004). Finally, MDW agrees extremely well with the data down to the smallest  $N_{\text{HI}}$  values. Comparing with the results of Nagamine et al. (2004, 2007) we find a better agreement with the observational data both for the SW and MDW, especially at low column density and at  $z = 3$ .

In the right panel Figure 3.12 we split the contribution of the different haloes to the total  $f(N)$  for the SW<sub>20,512</sub> at  $z = 3$ . We use the SW<sub>20,512</sub> run because the largest box-size improves the statistics on the haloes. Looking at the figure one can easily see that haloes with masses above  $10^{11} h^{-1}M_{\odot}$  (dotted red line) contribute primarily to the large column densities, while the smallest haloes with masses in the range  $10^9$ - $10^{10} h^{-1}M_{\odot}$  (triple-dot-dashed cyan line) contribute significantly to the lower column densities, below  $N_{\text{HI}} \approx 10^{20.8} \text{ cm}^{-2}$ . This is not surprising since on average more massive haloes have higher gas densities and correspondingly produce larger HI column densities values.

In Figure 3.13 we show the same as Figure 3.12 but at redshift  $z = 2.25$  (left panel) and  $z = 4$  (right panel), to check the redshift evolution of the column density distribution function. In the left panel, the results for SW<sub>20,512</sub> are not shown because this simulation ended at  $z = 3$ . SW fits well the observational data for HI column densities larger than  $10^{21} \text{ cm}^{-2}$ , but at lower column densities there is a discrepancy of about a factor 3. WW and MDW overproduce  $f(N)$  at high  $N_{\text{HI}}$ , but there is a better agreement with data at  $\log N_{\text{HI}} < 20.7$ , especially for the MDW run. At redshift  $z = 4$  (right panel) SW, SW<sub>20,512</sub> and also MDW match very well the data while WW does not. The fact that MDW fits the data as well as SW at  $z = 4$  is due to the fact that high redshift momentum-driven winds behave quite similarly to energy-driven ones, while at lower redshift the two models tend to differ significantly in terms of velocities and loading factors. Thus, we conclude that the different wind implementations of the galactic wind feedback show distinct predictions for the redshift evolution, and in general the differences become larger when moving to  $z \sim 2$ . At the end the feedback model that reproduce better the data is the MDW model.

At the end of Section 3.2.2 we briefly discussed the SW<sub>WDM</sub> simulation. We run this simulation motivated by the poorer fit to observational data for the systems of column densities between  $10^{20.3-20.8} \text{ cm}^{-2}$  that was found in Nagamine et al. (2004, 2007) and Pontzen et al. (2008). Our reference runs (especially the SW) show a similar flattening trend and underproduce the number of these systems, by a smaller amount when compared to Nagamine et al. (2007). The idea is that using a different linear power spectrum we could possibly modify the halo mass function and this could impact on the column density distribution function as well. We perform the same analysis of the other runs for SW<sub>WDM</sub>, but we find no statistical significant difference for the whole column density range. The smaller number of dark matter haloes, compared to  $\Lambda$ CDM cosmology, is thus compensated by an increase in the cross-section, since in WDM the haloes are usually less concentrated. Thereby we decided not to consider this run anymore and we conclude that it appears unlikely that this statistic could be better fit by invoking modifications of the linear dark matter power spectrum such as warm dark matter.

Finally, we compute the total neutral gas mass in DLAs using:

$$\Omega_{\text{DLA}}(z) = \frac{m_{\text{p}} H_0}{c f_{\text{HI}} \rho_{\text{c},0}} \int_{10^{20.3}}^{N_{\text{max}}} f(N_{\text{HI}}, X) N_{\text{HI}} dN_{\text{HI}}, \quad (3.6)$$

where  $m_{\text{p}}$  is the proton mass,  $f_{\text{HI}}$  is the neutral hydrogen fraction of the gas and  $\rho_{\text{c},0}$  is the

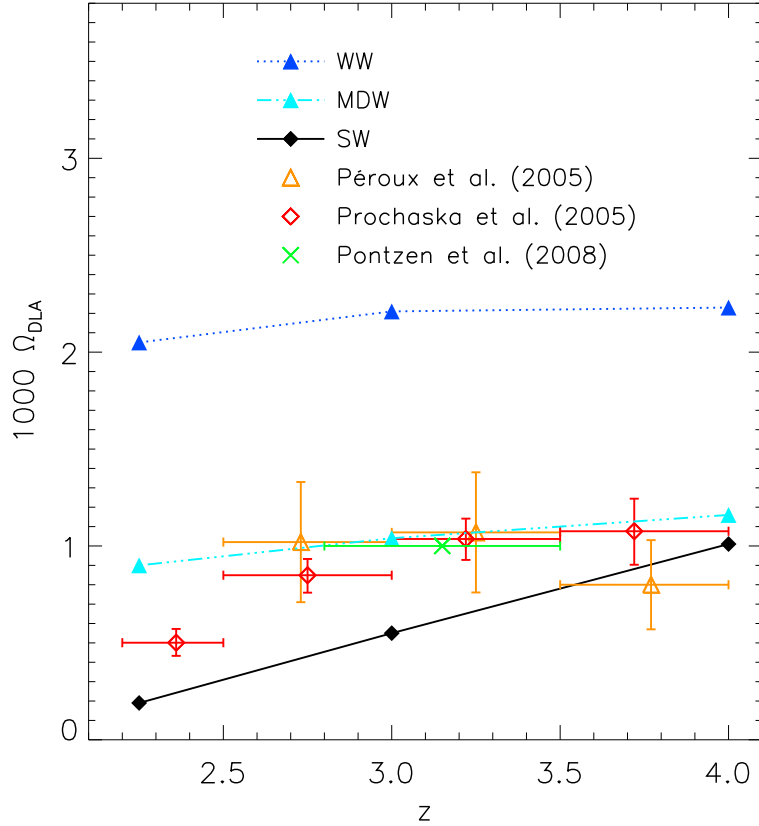


Figure 3.14: Redshift evolution of  $\Omega_{\text{DLA}}$  for the SW (black solid line), WW (blue dotted line) and MDW (cyan triple-dot-dashed line) runs. Overplotted are the result of Pontzen et al. (2008) (green cross) and the observational estimate of Prochaska et al. (2005) (red diamonds) and Péroux et al. (2005) (orange triangles).

critical density at redshift  $z = 0$ . The integration limit goes from  $10^{20.3} \text{ cm}^{-2}$  (the lower column density limit for a system to be identified as DLA) to  $N_{\text{max}} = 10^{21.75} \text{ cm}^{-2}$ , this latter chosen to compare with the results of Pontzen et al. (2008).

In Figure 3.14 we show the evolution with redshift of  $\Omega_{\text{DLA}}$  for the SW (black solid line), WW (blue dotted line) and MDW (cyan triple-dot-dashed line) runs, along with the result of Pontzen et al. (2008) (green cross) and the observational estimate of Prochaska et al. (2005) (red diamonds) and Péroux et al. (2005) (orange triangles). The different simulations' trends reflect those plotted in the right panel of Figure 3.3: the WW run produces the largest  $\Omega_{\text{DLA}}$  values while SW the smallest. The amount of neutral hydrogen in DLAs is about a factor two smaller than the total neutral hydrogen in the simulated volume. The MDW is in good agreement with the value found by Pontzen et al. (2008) ( $1.0 \times 10^{-3}$  in the redshift range  $2.8 < z < 3.5$ ) and with the data by Péroux et al. (2005), while at redshift below  $z \sim 3$  it is slightly larger than the recent measurement made by Prochaska et al. (2005) using DLAs in SDSS spectra.

So far we did not comment much about self-shielding effects. A full treatment of the self-shielding would require radiative transfer and this again would be an approximate (usually a-posteriori) scheme. We decided to rely on the multiphase ISM model to implicitly account for self-shielding motivated by the two following facts: *i*) many observational properties of DLAs have been reproduced in such a way (Katz et al. 1996, Nagamine et al. 2004, 2007); *ii*) the recent results by Pontzen et al. (2008) seem to suggest that even when applying crude radiative transfer approximations the main properties of DLAs do not change significantly. However, to better check the impact of this criterion, we also apply a further approximation that is useful in order to decouple the star formation from the multiphase prescription and assume that the gas particles above densities of  $n_{\text{H}} = 10^{-2} \text{ cm}^{-3}$  are fully neutral (following Haehnelt et al. 1998). We recomputed the column density distribution function for a few simulations and found that the differences are not large. All the column density distribution function increase by a fixed overall amount of about 0.2 dex and are still in broad agreement with the observations. Since we believe that our multiphase ISM model is more refined and more physically motivated than this criterion we decided not to present results for this second simpler assumption.

### 3.4 Simulated QSO spectra

For each simulation performed we have extracted several physical quantities interpolated along lines-of-sight (LOSs) through the box. Given the positions, velocities, densities and temperatures of all SPH particles at a given redshift, we compute spectra along a given LOS through the box following the procedure of Theuns et al. (1998). We divide the sight line into  $N = 1024$  bins of width  $\Delta$  in distance  $x$  along the sight line. For a bin  $i$  at position  $x(i)$  we compute the density and the density weighted temperature and velocity from:

$$\rho_{\text{X}}(j) = a^3 \sum_i X(i) \mathcal{W}_{ij}, \quad (3.7)$$

$$(\rho T)_{\text{X}}(j) = a^3 \sum_i X(i) T(i) \mathcal{W}_{ij}, \quad (3.8)$$

$$(\rho v)_{\text{X}}(j) = a^3 \sum_i X(i) \{a\dot{x}(i) + \dot{a}[x(i) - x(j)]\} \mathcal{W}_{ij}. \quad (3.9)$$

where  $X(i)$  is the abundance of species  $X$  of SPH particle  $i$ , assuming ionization equilibrium, and  $\mathcal{W} = mW(q_{ij})/h_{ij}^3$  is the normalized SPH kernel ( $W$  is the SPH kernel and  $h$  the softening scale). The optical depths of the simulated QSO spectra are drawn in redshift space taking into account the effect of the IGM peculiar velocities along the line-of-sight,  $v_{\text{pec},\parallel}$ . As already mentioned, our simulations follow self consistently the evolution of H, He, C, O, Mg, S, Si and Fe. Using the CLOUDY code (Ferland et al. 1998), we then determine the ionization fractions for some ions that trace the high redshift IGM: CIV ( $\lambda\lambda$  1548.204, 1550.781 Å), OVI ( $\lambda\lambda$  1031.927, 1037.616 Å) and SiIII ( $\lambda$  1526.707 Å), with the possibility to extend the analysis to many others. The simulated flux of a given ion transition at the redshift-space coordinate  $u$  (in km/s) is  $F(u) = \exp[-\tau(u)]$  with:

$$\tau(u) = \frac{\sigma_{0,\text{X}} c}{H(z)} \int_{-\infty}^{\infty} n_{\text{X}}(x) \mathcal{V} [u - x - v_{\text{pec},\parallel}^{\text{IGM}}(x), b(x)] dx, \quad (3.10)$$

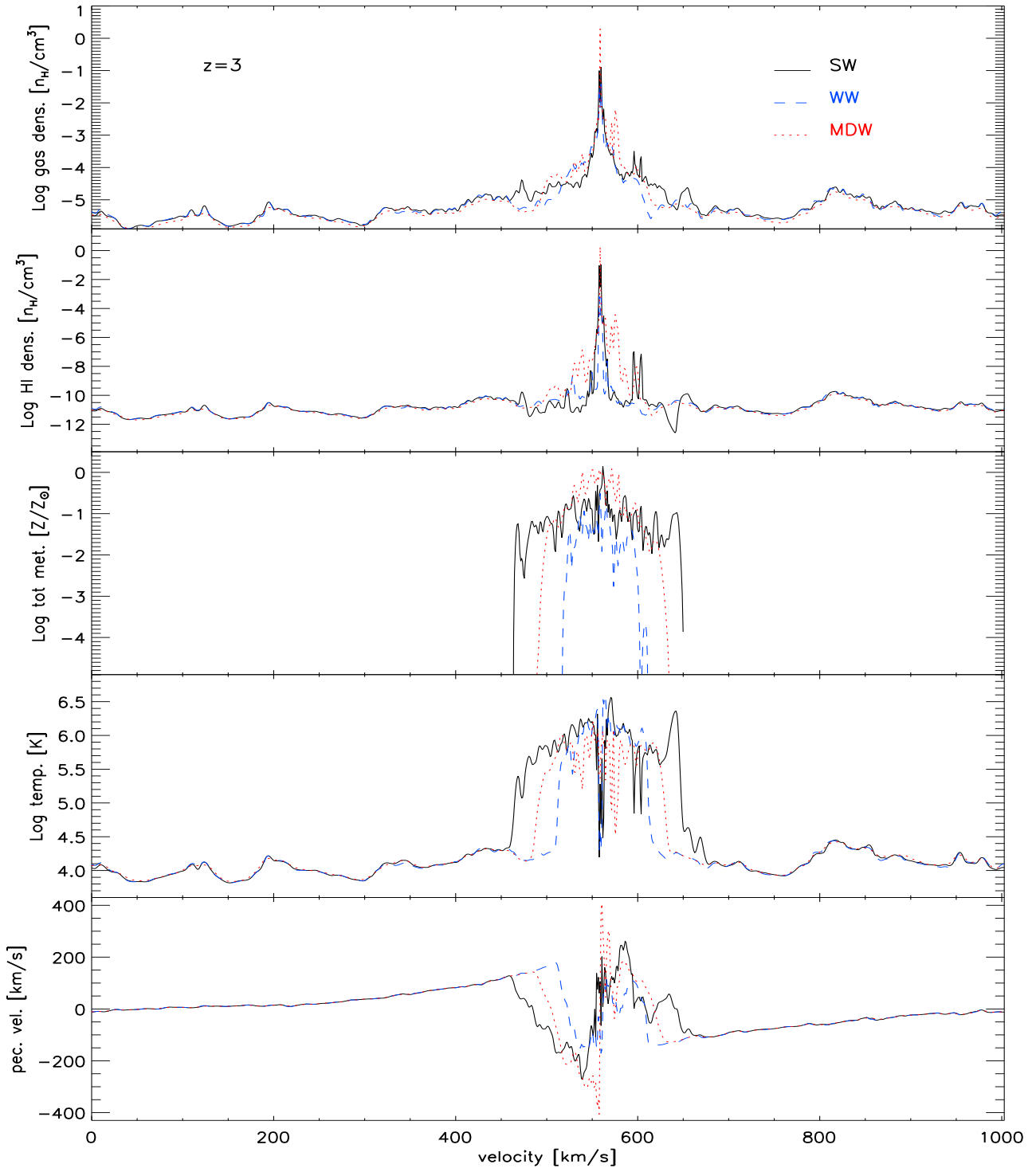


Figure 3.15: Comparison of physical quantities extracted from three simulated LOSs passing through the center of mass of the second most massive halo for the SW (solid black line), WW (dashed blue line) and MDW (dotted red line) runs at  $z = 3$ . From top to bottom the figure shows: total gas density [ $n_{\text{H}}/\text{cm}^3$ ], HI density [ $n_{\text{H}}/\text{cm}^3$ ], total metallicity (in solar unit), temperature [K] and peculiar velocity field [km/s].

where  $\sigma_{0,x}$  is the cross-section of the particular ion transition,  $H(z)$  is the Hubble constant at redshift  $z$ ,  $x$  is the real-space coordinate (in  $\text{km s}^{-1}$ ),  $b = (2k_{\text{B}}T/m_{\text{X}}c^2)^{1/2}$  is the velocity dispersion in units of  $c$ ,  $\mathcal{V}$  is the Voigt profile. These spectra can be converted from velocity  $v$  to observed wavelength  $\lambda$  using  $\lambda = \lambda_0(1+z)(1+v/c)$ .

In Figure 3.15 we compare three LOSs along the center of mass (CM) of the second most massive halo in the SW, WW and MDW simulations, at redshift  $z = 3$ . We interpolate physical quantities along the LOS using the SPH kernel of each particle. The SW is represented by the continuous black line, the WW is represented by the dashed blue line and the MDW by the dotted red line. From top to bottom we show the gas density, neutral hydrogen density, total metallicity, temperature and peculiar velocity. The  $x$ -axis is in  $\text{km/s}$  and represents at a given redshift the size of the box in real space. Looking at the first two top panels it is visible a peak both in the gas and in the neutral hydrogen densities: this corresponds to the CM of the halo. All simulations have more or less the same structure for the peak in density but in the MDW case (red dotted line) it is a bit more extended than the other two. The metallicity panel clearly shows the effect of the different winds implementations and velocities. The SW run produces a distribution of metallicity more extended than MDW and WW while the WW distribution is narrower than the MDW one. This confirms the fact that for massive haloes MDW is less efficient than SW in extracting metals and distributing them in the surrounding IGM (because of the high velocity dispersion of massive haloes that results in a small loading factor for the wind particles even if the corresponding wind velocities are high). The temperature panel presents the same trends as the metallicity panel: the high temperature peak is larger for SW with respect to MDW and WW, demonstrating that the hot SW gas can be spread out to large distances. Quite interesting in this panel is the drop in temperature at the center of the halo where the gas density is high and the cooling efficient. The bottom panel shows the peculiar velocity field. One can clearly see the effect of the expanding wind: a strong discontinuity in the peculiar velocity produced by the shock, with a negative peak (shell coming toward the observer) and a positive one (shell expanding along the LOS in the opposite direction). Again the SW have the larger distribution and WW the narrower. MDW have larger peaks (in absolute values) than SW but not as extended, that are produced by a fast, but less mass-loaded, wind. We note that the peculiar velocity fields account for the observed wind velocities in local starburst galaxies and that these velocities do depend on the wind model.

### 3.4.1 Velocity width distribution

In this Section we compare observational data and simulation predictions on the observed velocity width distribution for low-ionization species. We use the quantity  $\Delta v_{90}$  defined as the extent in velocity (redshift space) that embraces 90% of the total integrated optical depth as in Prochaska & Wolfe (1997). The procedure to recover this statistics is the following: for every simulation we take one thousands spectra extracted along the CMs of the most massive haloes in the box. Then for every spectrum we compute the absorption profile of the ion considered (SiII,  $\lambda$  1526.707 Å) and finally from this we determine the values of  $\Delta v_{90}$  associated with that particular LOS (i.e with that particular DLA). To deal with the fact that SiII occurs in self-shielded regions we use the ISM multiphase model in the same way as we did for the HI.

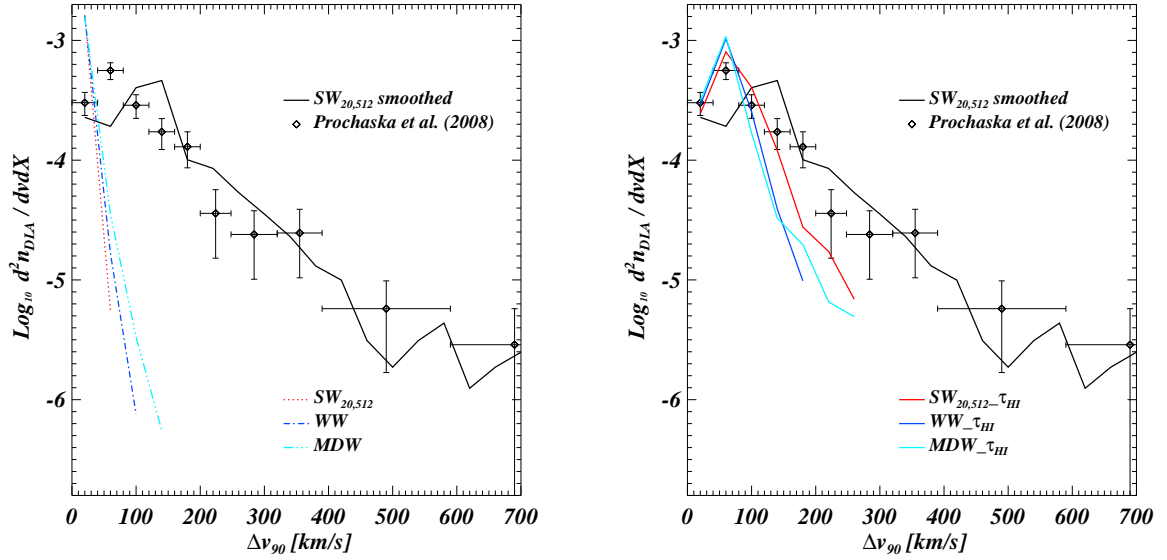


Figure 3.16: *Left Panel:* DLAs velocity width distribution in runs  $SW_{20,512}$  (dotted red line), WW (dot-dashed blue line), MDW (triple-dot-dashed cyan line) and  $SW_{20,512}$  smoothed (solid black line) at  $z = 3$ . *Right Panel:* DLAs velocity width distribution in runs  $SW_{20,512-\tau_{\text{HI}}}$  (solid red line),  $WW_{-\tau_{\text{HI}}}$  (solid blue line),  $MDW_{-\tau_{\text{HI}}}$  (solid cyan line) and  $SW_{20,512}$  smoothed (solid black line) at  $z = 3$ . In both the panels the overplotted black diamonds show the observational data of Prochaska et al. (2008).

Following Eqs. (3.1) and (3.2), we assign to each particle in the LOS a mass in SiII:

$$m_{\text{SiII}} = f_{\text{SiII}} m_{\text{Si}} \quad (\rho < \rho_{\text{th}}), \quad (3.11)$$

$$m_{\text{SiII}} = f_c m_{\text{Si}} \quad (\rho \geq \rho_{\text{th}}), \quad (3.12)$$

where  $m_{\text{Si}}$  is the mass in Si of the particle (determined self consistently inside the code),  $f_{\text{SiII}}$  is the SiII fraction as determined by CLOUDY on the base of the temperature and the density of the particle.  $f_c$  and  $\rho_{\text{th}}$  are, respectively, the fraction of mass in cold clouds and the star formation threshold (see Section 3.1).

It is well known that the observed distribution of velocity widths has a median too large to be accommodated within standard cold dark matter cosmology (Pontzen et al. 2008; Prochaska et al. 2008). In the left panel of Figure 3.16 we show the DLA velocity width distributions at redshift  $z = 3$  for our reference runs  $SW_{20,512}$  (dotted red line), WW (dot-dashed blue line), MDW (triple-dot-dashed cyan line) along with observational data of Prochaska et al. (2008). The latter consist of a set of 113 measurements of metallicity, redshift and  $\Delta v_{90}$  taken with HIRES, ESI and UVES/VLT spectrographs for DLAs in the redshift range  $1.5 < z < 4.6$ . We consider this sample as a whole since it does not show any redshift evolution (Pontzen et al. 2008) and we compare with our  $z = 3$  outputs.

It is clear that our reference runs dramatically fail to reproduce observational data even to a larger extent than found by Pontzen et al. (2008). In fact  $SW_{20,512}$ , WW and MDW overpredict the number of small velocity systems and at the same time they are not able to

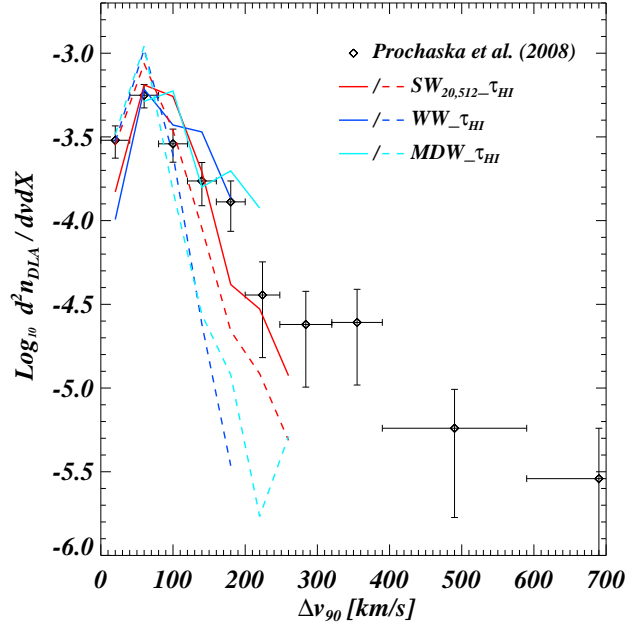


Figure 3.17: Contribution to the DLAs velocity width distribution from haloes of different mass in runs  $SW_{20,512}-\tau_{HI}$  (solid + dashed red lines),  $WW-\tau_{HI}$  (solid + dashed blue lines),  $MDW-\tau_{HI}$  (solid + dashed cyan lines) at  $z = 3$ . For the different runs, dashed lines refer to haloes with mass lower than  $10^{10.5} h^{-1} M_{\odot}$  and solid lines refer to haloes with mass greater than  $10^{10.5} h^{-1} M_{\odot}$ . The overplotted black diamonds show the observational data of Prochaska et al. (2008).

produce systems with velocity width greater than 100 km/s. As we expect, MDW does a better job than the other two runs, since it is more efficient in expelling metals, but it is yet far away from fitting data. Checking one by one a large number of extracted spectra we find that for a given LOS there is a significant number of small regions in the optical depth, all of them with sizes that are too small in redshift space. Basically our simulations, regardless to the particular wind implementation, spread around the haloes small clumps of enriched materials, that are in a wind phase, and are not able to enrich uniformly the surrounding IGM. This of course also results in the overproduction of small velocity systems seen in the left panel of Figure 3.16.

We checked that even using a simulation with higher resolution like  $SW_{10,448}$ , which in principle should start enriching the IGM earlier, we are not able to reproduce observational data. To overcome the problem we follow two other post-processing criteria with the goal of finding out some guidelines to improve our future simulations:  $SW_{20,512}smoothed$  shown in both the panels of Figure 3.16 as the black solid line and the “ $\tau_{HI}$ ” series plotted in the right panel of Figure 3.16.

For the  $\tau_{HI}$  series we take the original  $SW_{20,512}$ , WW and MDW runs and then we follow Pontzen et al. (2008) assuming that SiII is perfectly coupled to HI so that for solar metallicity  $M_X/M_H = 0.0133$  and  $n(\text{SiII})/n(\text{HI}) = n(\text{Si})/n(\text{H}) = 3.47 \times 10^{-5}$ . In this way SiII is spread more efficiently around and inside the haloes. Moreover here we sum, for a given LOS, all

the different  $\Delta v_{90}$  contribution due to the small metal clumps trying to mimic a more uniform enrichment. The results are shown in the right panel of Figure 3.16:  $SW_{20,512-\tau_{\text{HI}}}$  is the solid red line,  $WW_{-\tau_{\text{HI}}}$  the solid blue line and  $MDW_{-\tau_{\text{HI}}}$  the solid cyan line.  $SW_{20,512-\tau_{\text{HI}}}$  works better than the other two mostly because it has a greater number of bigger haloes where the  $\Delta v_{90}$  is correspondingly higher (see below), but as one can see this post-processing procedure is not yet enough to match the observations. We find a trend similar to what Pontzen et al. (2008) showed in their Figure 9: all the different  $\tau_{\text{HI}}$  series reproduce the small velocity tail of the distribution but fail to produce systems with velocity width larger than  $\sim 300$  km/s.

Instead, for  $SW_{20,512\text{smoothed}}$  we extract simulated spectra after having increased the smoothing length associated to each particle along the LOS and having recomputed the metallicity. Basically we set the new smoothing length to  $500 h^{-1}$  comoving kpc and the result is the  $SW_{20,512\text{smoothed}}$  curve (black solid). With this prescription we can fit very well observational data both at high and small velocities. Of course spreading the metals a-posteriori over a scale of hundred  $h^{-1}$ kpc is not self consistent but in this way we just want to see which phenomenological prescription can be used in order to fit the data.

Either a pre-enrichment of the IGM at higher redshift that could pollute the gas particles in a more uniform way (e.g. Tornatore et al. 2007b) or some missing physical ingredient such as small scale turbulence that could be effective in mixing metals in a more efficient way at galactic scales (e.g. Iapichino et al. 2008; Scannapieco & Brügger 2008), could help in reproducing the observed values. From this point of view a smoothing scale of  $500 h^{-1}$ kpc roughly corresponds to a velocity (in redshift space) of  $\sim 50$  km/s, values that are consistent with those presented in Scannapieco & Brügger (2008).

Finally, in Figure 3.17 we test the contribution to the DLAs velocity width distribution from haloes of different mass at  $z = 3$ . We use the three models that fit best the  $\Delta v_{90}$  statistic, the  $\tau_{\text{HI}}$  series:  $SW_{20,512-\tau_{\text{HI}}}$  (solid + dashed red lines),  $WW_{-\tau_{\text{HI}}}$  (solid + dashed blue lines),  $MDW_{-\tau_{\text{HI}}}$  (solid + dashed cyan lines). For the different runs, dashed lines refers to haloes with mass lower than  $10^{10.5} h^{-1} M_{\odot}$  and solid lines refers to haloes with mass larger than  $10^{10.5} h^{-1} M_{\odot}$ . As we expect, massive haloes produce much more systems with great velocity widths, while the less massive haloes produce more smaller velocity systems.

### 3.4.2 Correlation between Metallicity and Velocity Widths

Observational data by Ledoux et al. (2006) and Prochaska et al. (2008) confirmed in the last years the existence of a positive correlation between low-ion velocity width and the metallicity of DLAs along a given sightline. We showed that our reference runs fail to reproduce the DLAs velocity width distribution so we use the two post-processing criteria presented in the previous Section ( $MDW_{-\tau_{\text{HI}}}$  and  $SW_{20,512\text{smoothed}}$ ) to test metallicity-velocity widths correlation. In our simulations we compute the metallicities of DLAs by taking the average metallicity value for the given LOS in a region of  $\pm 100$  km/s in redshift space, centered at the location of the CM of each halo hosting a DLA.

In the left panel of Figure 3.18 we plot metallicities vs. velocity widths for 100 haloes randomly selected in a subsample of haloes with mass  $M > 10^{10} h^{-1} M_{\odot}$  in the  $MDW_{-\tau_{\text{HI}}}$  (green solid squares) and  $SW_{20,512\text{smoothed}}$  (red solid diamonds), along with observational data by Prochaska et al. (2008) (black crosses). Green squares ( $MDW_{-\tau_{\text{HI}}}$ ) show a weak correlation

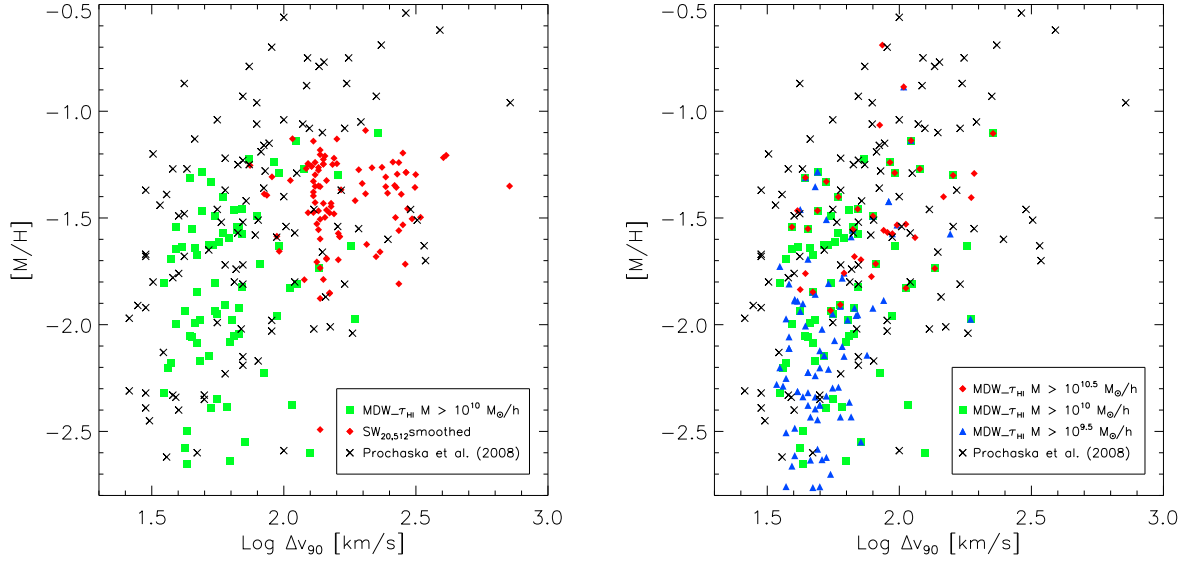


Figure 3.18: *Left Panel:* relationship between metallicity and SiII velocity width of individual sightlines through haloes in MDW\_ $\tau_{\text{HI}}$  (green solid squares) and SW $_{20,512}$ smoothed (red solid diamonds) at  $z = 3$ , compared to the observational data by Prochaska et al. (2008) (black crosses). *Right Panel:* relationship between metallicity and SiII velocity width of individual sightlines through haloes with masses  $M > 10^{10.5} h^{-1} M_{\odot}$  (red solid diamonds),  $M > 10^{10} h^{-1} M_{\odot}$  (green solid squares) and  $M > 10^{9.5} h^{-1} M_{\odot}$  (blue solid triangles) in MDW\_ $\tau_{\text{HI}}$  run at  $z = 3$ , compared to the observational data by Prochaska et al. (2008) (black crosses).

while correlation is negligible for the red diamond (SW $_{20,512}$ smoothed). SW $_{20,512}$ smoothed have in average both metallicities and velocity widths higher than MDW\_ $\tau_{\text{HI}}$  and this is not surprising due to the procedure of smoothing metallicity over a large scale. For this plot we use only haloes with masses above  $M > 10^{10} h^{-1} M_{\odot}$  because we noted that for the most massive haloes the correlation is stronger. In the right panel of Figure 3.18 we clarify this point using the MDW\_ $\tau_{\text{HI}}$  run. Red diamonds refers to all the haloes with mass  $M > 10^{10.5} h^{-1} M_{\odot}$ , green squares are the same green points of the left panel (a subsample of haloes with mass  $M > 10^{10} h^{-1} M_{\odot}$ ), while blue triangles derive from a subsample of haloes with mass  $M > 10^{9.5} h^{-1} M_{\odot}$ . It is evident that the correlation in this case is somewhat weaker. Instead, using a subsample of haloes at larger masses, we increase the value of  $\Delta v_{90}$ , since faster winds are produced by more massive haloes, that usually are more metal rich at least when compared with smaller mass haloes. Thereby, if we restrict ourselves to haloes above  $10^{10.5} h^{-1} M_{\odot}$  the agreement is reasonably good, even though smaller mass haloes, as we saw in the previous sections, contribute to all of the other DLA statistical properties. We also note that in general the mean metallicities recovered from our simulations are somewhat smaller than the observed ones (let say “The show is through the metal is gone...”).

### 3.5 Main results

In this work we investigated the properties of DLAs in high-resolution hydrodynamical cosmological simulations. In particular, we focussed on the role of feedback in the form of galactic winds to quantify their impact on the neutral hydrogen and metal ion species content both on the global IGM and on the IGM around putative DLA sites. The analysis was made by comparing with the recent works of Nagamine et al. (2007) and Pontzen et al. (2008), but with important differences with respect to these previous analyses: *i*) higher resolution simulations (by a factor  $\sim 10$  in mass) than Nagamine et al. (2004, 2007); *ii*) statistics performed in a cosmological setting, like in Nagamine et al. (2004, 2007), but differently from Pontzen et al. (2008), who relied mainly on simulations of single objects; *iii*) inclusion of metal cooling and an accurate chemo-dynamical code that follows self consistently the IGM enrichment Tornatore et al. (2007); *iv*) inclusion of different wind prescriptions (energy driven and momentum driven); *v*) modification of the stellar IMFs and the linear dark matter power spectrum in the initial conditions to explore the parameter space further.

The conclusions that we draw from our analysis can be summarized as follows.

- The different feedback prescriptions that we explored (WW, weak energy-driven winds of 100 km/s; SW, strong energy-driven winds of 600 km/s; MDW, momentum driven winds) give distinct predictions for the gas distribution in metallicity-temperature and density. SW are effective in heating the gas particles at temperatures of  $10^5$  K to a larger extent than MDW and WW. Also the metallicity-density distribution is different: WW and MDW show correlations in high-density regions (denser regions being more metal rich), while SW is more efficient in polluting the low-density IGM (Figures 3.1 and 3.2).
- WW, SW and MDW have also an impact on global quantities of the simulations such as the cosmic star formation rates and the neutral hydrogen content. As for the latter, MDW and SW show agreement with data while in the WW the HI is clearly overproduced since the feedback is not as efficient. Also, the star formation rate for the WW run is higher than for the SW one (see Figures 3.3 and 3.14).
- The evolution with redshift of CIV and OVI (two of the most common ion species observed in QSO absorption spectra) is similar in shape between the different runs but the normalization differ by up to a factor 3 (see Figure 3.4).
- Focusing on the properties of the haloes that could host DLAs we find that haloes between  $10^9 - 10^{10} h^{-1} M_\odot$  at  $z = 3$  have similar SFR for the different wind models of about  $0.01 - 0.1 M_\odot/\text{yr}$ , with large scatter, while more massive haloes have larger SFRs and the trend with mass depends on the specific wind model (Figure 3.7). The metallicities of the haloes as a function of mass is correlated for haloes of masses  $> 10^{9.5} h^{-1} M_\odot$  in the WW and MDW runs, while no correlation or possibly a weak anti-correlation is seen for the SW model. For less massive haloes below  $10^{9.5} h^{-1} M_\odot$  the scatter in metallicity is huge and span several orders of magnitude (Figure 3.8).
- The cross-sections inferred from the different runs are in overall agreement with the results of Nagamine et al. (2004, 2007), although the values for shape and normalization are

somewhat smaller for similar runs. This is likely to be due to the different prescriptions of the wind implementation and the metal cooling. The DLA incidence rate is in good agreement with the observed one by Prochaska et al. (2005) from SDSS data for MDW and SW, while is larger for WW. The incidence rate results clearly show that all the haloes whose masses are above  $10^9 h^{-1} M_{\odot}$  contribute to the cross-section (Figures 3.10 and 3.11).

- The column density distribution function at  $z = 3$  is in rough agreement with the data points for all the models (for MDW the agreement is better), while at lower redshifts there are larger differences and SW (WW) underpredicts (overpredicts) the number of DLAs. The WW run shows the largest discrepancies especially for the high column density DLAs, a feature that was already found by Nagamine et al. (2004). The contribution of haloes of masses between  $10^9 - 10^{10} h^{-1} M_{\odot}$  is particularly relevant for DLAs below  $N_{\text{HI}} \approx 10^{20.8} \text{ cm}^{-2}$ , another hint that less massive haloes contribute to reproduce DLAs statistical properties (Figures 3.12 and 3.13).
- Qualitatively, physical quantities interpolated along LOS that pierce the haloes show different behaviours (particularly in temperature and metallicity) in different models. Also the peculiar velocity fields look different (Figure 3.15) and the gas velocity gradient is in agreement with the observed wind velocities.
- The distribution of velocity widths of low ionization species (in our case SiII) reproduces the observed one Prochaska et al. (2008) only for velocity widths below 100 km/s, while larger values are dramatically under-reproduced by our simulations. A slightly better agreement is obtained when SiII is supposed to faithfully trace the HI distribution (as done by Pontzen et al. 2008), but even in this case the observed distribution is underestimated. We can fit the observed velocity widths well only if we empirically smooth the metallicity of each gas particle over a region of 500 comoving  $h^{-1} \text{kpc}$  (Figure 3.16). We also find a trend of  $\Delta v_{90}$  with the halo mass that goes in the expected direction: more massive haloes produce the larger values for  $\Delta v_{90}$  (Figure 3.17).
- The metallicity-velocity width correlations is broadly reproduced by the two models discussed above, even if the metallicity values are somewhat lower than the observed ones. If we split the contribution to the correlation by taking into account different ranges of masses, we find that there is good agreement if we restrict ourselves to the most massive haloes with  $M > 10^{10.5} h^{-1} M_{\odot}$  (Figure 3.18). This is in agreement with Barnes & Haehnelt (2009), but in disagreement with other statistical properties of DLAs, that in order to be reproduced need less massive haloes as well.

Overall, we succeeded in reproducing most of the observed properties of DLAs in particular the column density distribution function and the incidence rate. It appears that the best agreement is given either by the SW or the MDW implementation, while the WW does not seem to fit the data. For the metal distributions, as traced by the velocity widths, the agreement is not good. This could be the hint that there are some pieces of physics missing in our treatment. Possible ingredients that are not considered here and that could help in easing the discrepancy are: *i*) radiative transfer effects in DLAs that have been either neglected so far (e.g. Nagamine

et al. 2004) or approximately modelled (e.g. Pontzen et al. 2008): even if their impact seems to be not dramatic at least using our effective model description of the ISM, since the cold clouds are assumed to be fully self-shielded and the ambient medium to be optically thin, they could be important for large column density systems, especially when affecting the molecular hydrogen in star forming regions (Gnedin et al. 2009); *ii*) small-scale turbulence and its impact on the metal diffusion at large scales, which has been recently investigated by Scannapieco & Brügger (2008) and that can be effective in smoothing the metal distribution around DLAs; *iii*) a pre-enrichment of the IGM, possibly produced by PopIII stars, at higher redshift than those considered here that could result in a smoother metallicity for the particles that are in a wind phase (e.g. Tornatore et al. 2007b). We stress that all these effects are not considered in our simulations and their accurate description could be important to match the remaining still unexplained DLA properties.

# Chapter 4

## Cosmic evolution of the CIV

In this Chapter we present our work about the cosmic evolution of the triply ionized carbon, CIV. The numerical code used is the same of Chapter 3, but now we added a new set of hydrodynamical simulations that incorporate both new feedback models, like the AGN feedback associated to the energy released by gas accretion onto super-massive black holes, and different physical prescriptions, as in the case of a pre-enriched run. This work is basically the theoretical counterpart of the D’Odorico et al. (2009) paper, in which the authors present a new measurement of the CIV cosmological mass density,  $\Omega_{\text{CIV}}$ , in the redshift range  $[1.5, 4]$ , based on a sample of 25 high resolution high signal-to-noise QSO spectra plus an additional sample of 8 QSO spectra from the literature.

The cosmological mass density of CIV, observed as a function of redshift is a fundamental quantity closely related to the metal enrichment of the intergalactic medium (IGM). Its apparent lack of evolution in the redshift interval  $z \simeq [1.5, 5]$  (Songaila 2001; Pettini et al. 2003; Boksenberg et al. 2003) is puzzling since both the physical conditions of the IGM and the properties of the ionizing background are thought to evolve between these epochs.

Remarkable efforts have been spent in recent years to extend the measure of  $\Omega_{\text{CIV}}$  to redshift larger than five (Ryan-Weber et al. 2006; Simcoe 2006) where a decrease of the star formation rate density is observed (Bunker et al. 2006). If  $\Omega_{\text{CIV}}$  is dominated by the metals produced *in situ* by the observed star forming galaxies, we would expect a decrease of its value at those redshifts. *Vice versa*, the value of  $\Omega_{\text{CIV}}$  could remain constant if it reflects the metallicity of a diffuse medium pre-enriched at very high redshift. It should be noted, however, that this is a simplified scenario since, as redshift increases, the observed CIV absorptions likely trace gas in structures of decreasing overdensity and also the ionizing spectrum evolves in shape and intensity. As a consequence, the behaviour of  $\Omega_{\text{CIV}}$  could be different from that of  $\Omega_{\text{C}}$  and of the mean IGM metallicity (see e.g. Schaye et al. 2003). The most recent measurements of CIV absorptions in spectra of QSOs at  $z \sim 6$  seem to indicate a downturn in the CIV mass density at  $z > 5$  (Becker et al. 2009; Ryan-Weber et al. 2009), though based only on 3 detected CIV lines.

At redshift  $z \lesssim 4.5$ , a fundamental measurement of  $\Omega_{\text{CIV}}$  has been carried out by (Songaila 2001). However, the redshift interval  $1.5 < z < 2$  is poorly sampled by the considered QSO spectra. A more uniform redshift coverage is provided by the sample of Boksenberg et al. (2003) although with fewer QSO spectra. Both analysis are consistent with a constant behaviour of

$\Omega_{\text{CIV}}$  in the range [1.5, 4.5]. At  $z < 1$ , recent results based on HST UV data (Cooksey et al. 2010) give  $\Omega_{\text{CIV}} = (6 \pm 1) \times 10^{-8}$  corresponding to a  $2.8 \pm 0.5$  increase over the  $1.5 < z < 5$  values.

The cosmological simulations of Oppenheimer & Davé (2006, 2008) reproduce the  $\Omega_{\text{CIV}}$  behaviour in the redshift interval [1.5, 6] without assuming a pre-enrichment of the IGM. In these simulations, metals are expelled from galaxies with momentum-driven winds (proportional to the star formation rate) which are very effective in transporting the gas without heating it too much. In this work we attempt to reproduce the observed different CIV statistics using our self consistent chemo-dynamical code and exploring different feedback prescriptions.

This Chapter is organized as follows. In Sections 4.1 and 4.2 we present, respectively, the observational data sample of D’Odorico et al. (2009) and our set of simulations. We start by reproducing the neutral hydrogen observed statistics in Section 4.3 and then move to the CIV. In Sections 4.4 and 4.5 we investigate the CIV column density distribution function and the  $\Omega_{\text{CIV}}$  evolution with redshift, respectively. In Section 4.6 we study the probability distribution function of the CIV Doppler parameter and, in Section 4.7, we focus on the CIV column density-Doppler parameter relation. Finally, in Section 4.8 we summarize our main results and we give some final remarks.

A paper containing the results of this work will be soon submitted to MNRAS (Tescari et al. 2010, in preparation).

## 4.1 Observational data sample

The core of the D’Odorico et al. (2009) sample is formed by the high resolution, high signal-to-noise QSO spectra already described in Saitta et al. (2008) and D’Odorico et al. (2008). Most of them were obtained with the UVES spectrograph (Dekker et al. 2000) at the Kueyen unit of the ESO VLT (Cerro Paranal, Chile) in the framework of the ESO Large Programme (LP): “The Cosmic Evolution of the IGM” (Bergeron et al. 2004).

In D’Odorico et al. (2009) work, three more QSOs were added to that sample, mainly to increase the redshift extension above  $z \sim 3$ . UVES spectra of the QSO: Q0055-269, PKS2000-330 and PKS1937-101, were downloaded from the ESO Archive and reduced with the UVES pipeline following the standard procedure. The continuum level was determined by interpolating with a cubic spline the region of the spectrum free from evident absorption features.

For all the QSO in the sample, the CIV forest was defined as the interval between the Lyman- $\alpha$  emission and  $5000 \text{ km s}^{-1}$  from the CIV emission to avoid the proximity region where most of the intrinsic systems are found. The absorption features present in this wavelength interval were identified inspecting the spectra by eye to look for the most common doublets (CIV, MgII and SiIV). Then, other lines were identified testing their compatibility with the CIV, MgII and SiIV redshifts. Finally, lines whose identity was still unknown after this operation, were associated with metal systems detected in the Lyman- $\alpha$  forest or recognized as part of other multiplets (e.g. FeII).

The CIV doublets were fitted with Voigt profiles using the context LYMAN of the MIDAS reduction package (Fontana & Ballester 1995). A minimum number of components was adopted to fit the velocity profile in order to reach a normalized  $\chi^2 \sim 1$ . D’Odorico et al. (2009) distinguished the CIV *components* or *lines*, meaning the velocity components in which every

QSO	$z_{\text{em}}$	$\Delta z_{\text{CIV}}$
HE 1341-1020	2.142	1.467-2.090
Q0122-380	2.2004	1.513-2.147
PKS 1448-232	2.224	1.531-2.171
PKS 0237-23	2.233	1.538-2.179
J2233-606	2.248	1.550-2.194
HE 0001-2340	2.265	1.564-2.211
HS 1626+6433 <sup>a</sup>	2.32	1.607-2.265
HE 1122-1648	2.40	1.665-2.344
Q0109-3518	2.4057	1.674-2.349
HE 2217-2818	2.414	1.681-2.357
Q0329-385	2.435	1.697-2.378
HE 1158-1843	2.448	1.707-2.391
HE 1347-2457	2.5986	1.826-2.539
Q1442+2931 <sup>a</sup>	2.661	1.875-2.600
Q0453-423	2.669	1.881-2.608
PKS 0329-255	2.696	1.902-2.635
HE 0151-4326	2.763	1.955-2.701
Q0002-422	2.769	1.959-2.707
HE 2347-4342	2.880	2.067-2.816
SBS 1107+487 <sup>a</sup>	2.966	2.114-2.900
HS 1946+7658	3.058	2.181-2.991
HE 0940-1050	3.0932	2.214-3.025
Q0420-388	3.1257	2.239-3.057
S4 0636+68 <sup>a</sup>	3.175	2.278-3.106
SBS 1425+606 <sup>a</sup>	3.199	2.297-3.129
PKS 2126-158	3.292	2.370-3.221
B1422+231	3.623	2.630-3.546
Q0055-269	3.66	2.659-3.583
PKS 2000-330	3.783	2.756-3.704
PKS 1937-101	3.787	2.770-3.400
PSS J1646+5514 <sup>a</sup>	4.059	2.972-3.975
PSS J1057+4555 <sup>a</sup>	4.131	3.029-4.046
BR 2237-0607 <sup>a</sup>	4.559	3.365-4.467

Table 4.1: Relevant properties of the QSOs forming the D’Odorico et al. (2009) observational sample. (a) QSOs from Boksenberg et al. (2003).

Run	Size [ $h^{-1}$ Mpc]	$N_{\text{GAS}}$	$m_{\text{GAS}}$ [ $h^{-1}M_{\odot}$ ]	soft. [ $h^{-1}$ kpc]	Feedback	IMF	$z_f$
<i>S1</i>	10.0	$320^3$	$3.5 \times 10^5$	1.5	PRE-EN.+EDW <sup>a</sup>	Salpeter	1.8
<i>B1</i>	37.5	$256^3$	$3.6 \times 10^7$	7.5	AGN+EDW <sup>b</sup>	Kroupa	1.5
<i>B2</i>	37.5	$256^3$	$3.6 \times 10^7$	7.5	NO FEEDBACK	Kroupa	1.5
<i>B3</i>	37.5	$256^3$	$3.6 \times 10^7$	7.5	COUPLED EDW <sup>c</sup>	Kroupa	1.5
<i>B4</i>	37.5	$256^3$	$3.6 \times 10^7$	7.5	EDW	Kroupa	1.5
<i>B5</i>	37.5	$256^3$	$3.6 \times 10^7$	7.5	EDW	AY <sup>f</sup>	1.5
<i>B6</i>	37.5	$256^3$	$3.6 \times 10^7$	7.5	MDW <sup>d</sup>	Kroupa	1.5
<i>B8</i>	37.5	$256^3$	$3.6 \times 10^7$	7.5	AGN <sup>e</sup>	Kroupa	1.5
<i>B9</i>	37.5	$256^3$	$3.6 \times 10^7$	7.5	EDW	Salpeter	1.5

Table 4.2: Summary of the different runs. Column 1, run name; column 2, comoving box size; column 3, number of gas particles; column 4, mass of gas particle; column 5, Plummer-equivalent comoving gravitational softening; column 6, type of feedback implemented; column 7, Initial Mass Function (IMF) chosen; column 8, redshift at which the simulation was stopped. For the runs *B3*, *B4*, *B5* and *B9* the velocity of the energy-driven winds (EDW) is set to  $v_w = 500 \text{ km s}^{-1}$ . (*a*): pre-enriched run with energy-driven winds of  $600 \text{ km s}^{-1}$ . (*b*): combined effect of energy-driven winds of  $300 \text{ km s}^{-1}$  and AGN feedbacks. (*c*): energy-driven winds not decoupled from the hydrodynamics (see the text). (*d*): momentum-driven winds (MDW) feedback in which wind velocity scales roughly with  $3\sigma$  ( $\sigma$  being the velocity dispersion of the halo that host the “wind” particle, see Section 2.4.4). (*e*): AGN feedback in which the energy is released by gas accretion onto super-massive black holes. (*f*): Arimoto-Yoshii IMF.

absorption profile has been decomposed, and the CIV *systems*, formed by groups of components. CIV *systems* were defined in the following way: for each list of CIV components corresponding to a single QSO, the velocity separations among all the lines have been computed and sorted in ascending order. If the smallest separation is less than  $dv_{\text{min}} = 50 \text{ km s}^{-1}$  (corresponding to the velocity separation adopted by Songaila 2001) the two lines are merged into a new line with column density equal to the sum of the column densities, and redshift equal to the average of the redshifts weighted with the column densities of the components. The velocity separation are then computed again and the procedure is iterated till the smallest separation results larger than  $dv_{\text{min}}$ .

The sample consists of 1023 CIV velocity components with column densities  $10^{12} \lesssim N_{\text{CIV}} \lesssim 10^{15} \text{ cm}^{-2}$  and of 508 CIV systems in the same column density range. The CIV absorptions in the spectra of 19 of the QSOs forming the sample were already identified and fitted by Scannapieco et al. (2006) using the software package VPFIT<sup>1</sup>.

In order to further increase the number of CIV lines and to extend the sample to higher redshift, D’Odorico et al. (2009) have considered the CIV lines fitted in 9 QSO spectra observed with HIRES at Keck at a resolution and signal-to-noise ratio similar to those of their spectra

<sup>1</sup><http://www.ast.cam.ac.uk/~rfc/vpfit.html>

and reported in Boksenberg et al. (2003). The fit with Voigt profiles was carried out by Boksenberg et al. (2003) with VPFIT. The main difference between LYMAN and VPFIT is that the number of components fitted to a given velocity profile is, in general, larger using the latter (see also the discussion in Saitta et al. 2008). This is seen also in the analysis of D’Odorico et al. (2009), in particular from the comparison of the CIV lines detected in the spectrum of the QSO B1422+231, which is the only object in common between the two samples. D’Odorico et al. (2009) find that in all cases the number of components found with VPFIT is larger or equal to that found with LYMAN. However, when the total column density of each absorption system is considered the difference between the two fitting procedures becomes negligible.

All the QSOs forming the observational sample are reported in Table 4.1 with their emission redshift and the redshift range covered by the CIV forest.

## 4.2 The simulations

In Table 4.2 we summarize the main parameters of the cosmological simulations performed including the mass associated to the gas particles and the gravitational softening. All the simulations start at redshift  $z = 99$ .

The simulations cover a cosmological volume (with periodic boundary conditions) filled with an equal number of dark matter and gas particles. The cosmological model chosen is a flat  $\Lambda$ CDM with the parameters already stated in Chapter 3:  $\Omega_{\text{om}} = 0.24$ ,  $\Omega_{\text{ob}} = 0.0413$ ,  $\Omega_{\Lambda} = 0.76$ ,  $n_s = 0.96$ ,  $H_0 = 73$  km/s/Mpc and  $\sigma_8 = 0.8$ .

While we refer to Section 3.1 for the basic characteristics of the simulations, in the following we briefly describe the runs used in this work. To better appreciate the effects of the various feedback prescriptions on the CIV statistics, we divided our simulations in two sets: “regular” and “non regular”. “Regular runs” are those in which the feedback prescriptions were already tested to be stable and physically reasonable, and that generally agree with each other in reproducing the CIV statistics:

- *B1*: In this simulation two different feedback models are combined: the energy-driven (EDW) galactic winds of velocity  $v_w = 300$  km s<sup>-1</sup>, and the new AGN feedback associated to the energy released by gas accretion onto super-massive black holes. Even if the AGN feedback is a new model, we consider “regular” this simulation because, as it will be clear in the next sections, it follows the general trend of all the other regular runs. This is due to the fact that winds start to be effective at higher redshift than the AGN feedback, devoiding of gas the haloes and in this way reducing the efficiency of the black holes accretion and the power of the AGN feedback.
- *B3*: This simulation has energy-driven winds of velocity  $v_w = 500$  km s<sup>-1</sup>, never decoupled from the hydrodynamics. In a normal EDW run (like the *B4*), whenever a particle is uploaded to the wind, it is decoupled from the hydrodynamics for a given period of time or till the density around it drops below a given fraction of the density threshold set for the onset of the star formation, in order to effectively reach less dense regions (see Section 2.4.4 for further details). Otherwise, in this simulation wind particles are always affected by the hydrodynamics like all the other gas particles.

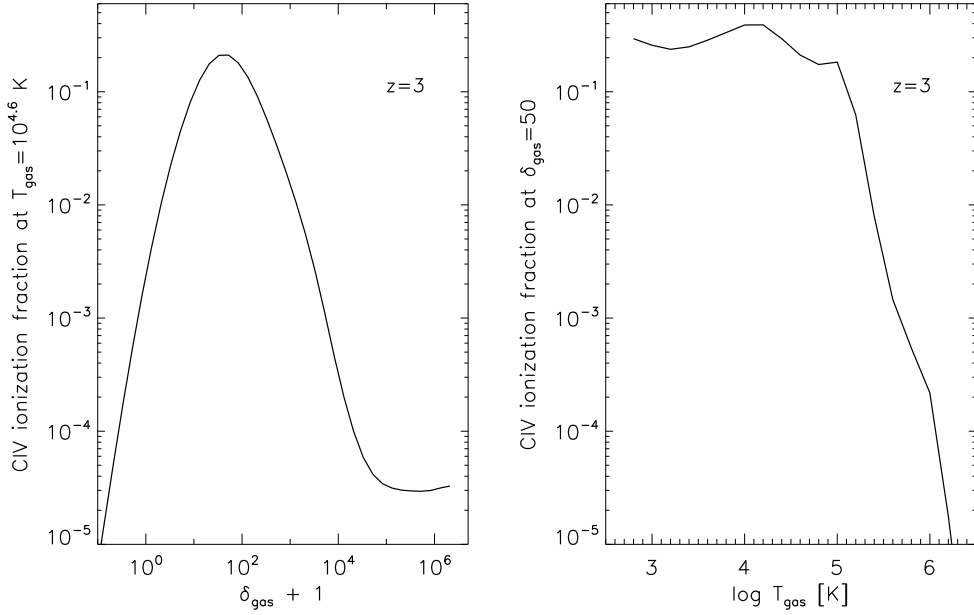


Figure 4.1: *Left panel:* CIV ionization fraction, as a function of the gas overdensity, at  $z = 3$  for a gas temperature of  $10^{4.6}$  K. *Right panel:* CIV ionization fraction, as a function of the gas temperature, at  $z = 3$  for an overdensity of  $\delta_{\text{gas}} \sim 50$ .

- *B4:* Energy-driven winds of velocity  $v_w = 500 \text{ km s}^{-1}$  and Kroupa IMF (the reference IMF for this work).
- *B5:* Energy-driven winds of velocity  $v_w = 500 \text{ km s}^{-1}$  and Arimoto-Yoshii IMF.
- *B6:* Momentum-driven winds (MDW) and Kroupa IMF.
- *B9:* Energy-driven winds of velocity  $v_w = 500 \text{ km s}^{-1}$  and Salpeter IMF (runs *B4*, *B5* and *B9* are identical except for the IMF).

Otherwise, the “non regular” are the runs with new feedback models or which explore some extreme physical solutions:

- *S1:* Pre-enriched simulation with energy-driven winds of velocity  $v_w = 600 \text{ km s}^{-1}$ . At redshift  $z = 9$  all the particles with overdensity  $\delta + 1 > 20$  are enriched to a metallicity of 0.2 in solar units. As a result, the dense regions associated with haloes and filaments in the box are strongly enriched at high redshift.
- *B2:* This simulation was run without any winds or AGN feedback. In this way we wanted to test how big is the effect of the different feedback prescriptions on the CIV statistics.
- *B8:* In this simulation only the AGN feedback mechanism (see Section 2.4.4) is active. In the *B1* case, the effect of the galactic winds overcomes and covers that of the AGN, with the result that *B1* run behaves very similarly to a regular energy-driven winds simulation. In this case we explored for the first time this new feedback prescription in relation to

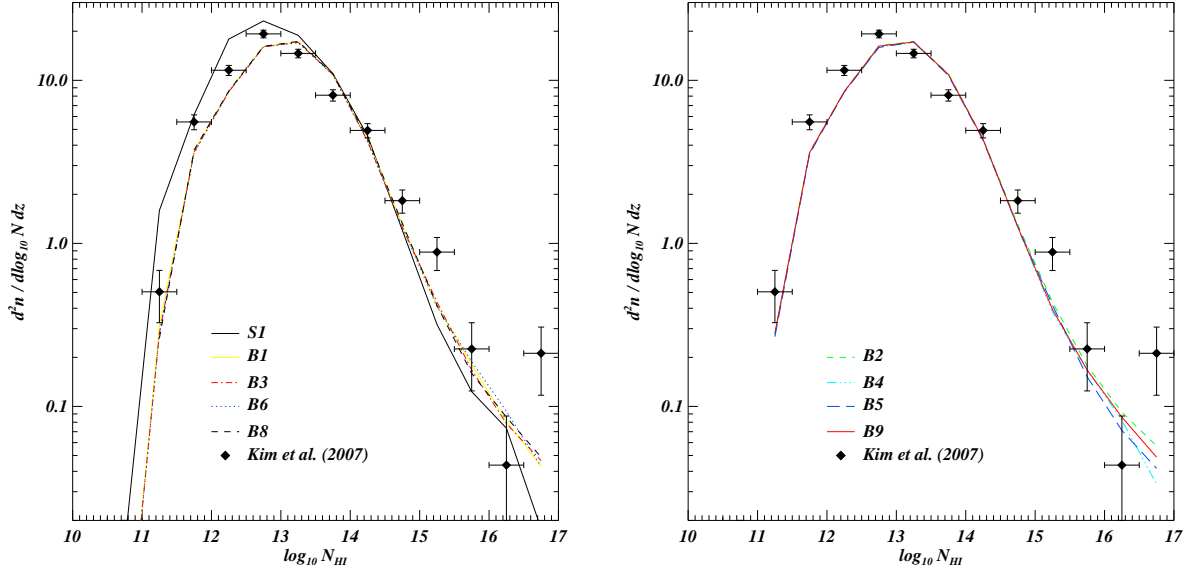


Figure 4.2: HI column density distribution function at  $z = 3$ . *Left panel*: part I. *Right panel*: part II. Data from Kim et al. (2007).

the high redshift properties of the intergalactic medium (while Tornatore et al. 2009 have studied the impact of this feedback mechanism on the low redshift IGM).

We use the CLOUDY code (Ferland et al. 1998) to compute a-posteriori the CIV ionization fractions for each gas particles. As for the work presented in Chapter 2, we choose the HM05 option in CLOUDY, which consists of a UVB made by QSOs and galaxies with a 10% photon escape fraction and which is in agreement with other observational constraints (Bolton et al. 2005). In Figure 4.1 we show the CIV ionization fraction at  $z = 3$  for a gas temperature of  $10^{4.6}$  K (left panel) and for an overdensity of  $\delta_{\text{gas}} \sim 50$  (right panel). This latter value is representative of the outskirts of dark matter haloes.

## 4.3 Statistics of HI

We start by reproducing some statistics related to the neutral hydrogen. We feel quite confident that our simulations can catch the properties and the evolution of the HI in the IGM so basically this Section is a test for our analysis methods of the absorption lines in quasar spectra.

### 4.3.1 The HI column density distribution function

In this Section we investigate the Lyman- $\alpha$  forest column density distribution function (HI CDDF)  $d^2n/d\log N dz$ , namely the number of absorbers with HI column density in the range  $[\log N, \log N + d \log N]$  and redshift path in the interval  $[z, z + dz]$ . The redshift path at a given

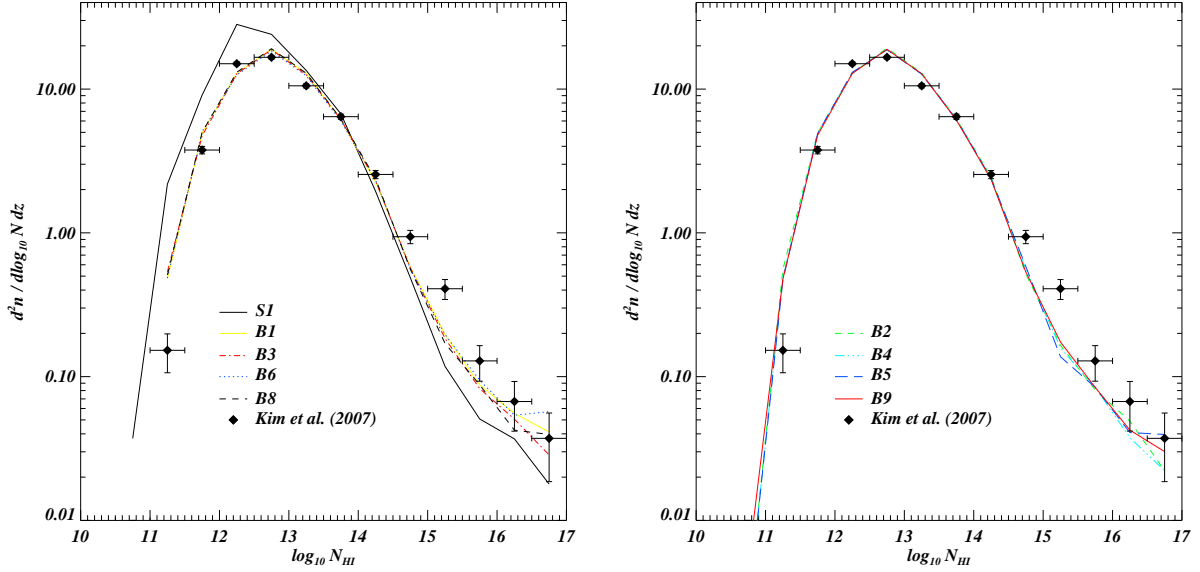


Figure 4.3: HI column density distribution function at  $z = 2.25$ . *Left panel*: part I. *Right panel*: part II. Data from Kim et al. (2007).

redshift  $z$  is given by:

$$dz = n_{\text{spec}}(1+z)\frac{\Delta v}{c}, \quad (4.1)$$

where  $c$  is the speed of light (in  $\text{km s}^{-1}$ ) and  $n_{\text{spec}}$  is the number of spectra taken at  $z$  for a simulation with box size in  $\text{km s}^{-1}$  equal to  $\Delta v$ .

In Figure 4.2 we show the HI CDDF at redshift  $z = 3$  for all the simulations of Table 4.2 splitted in two groups for the sake of clarity (left panel: part I, right panel: part II). In the left panel the S1 simulation (the pre-enriched run) has different (higher) resolution, number of particles and (smaller) box-size with respect to the other runs plotted. In particular the effect of the higher resolution is visible in the low column density tail of the distribution: S1 simulation produce more small systems than the others and this result in a larger statistics at these column densities. Otherwise at high column densities it is visible the effect of the box-size: run S1 has smaller box size than the other runs therefore missing large-scale power and producing lower statistics. In general all the simulations fit well the observational data by Kim et al. (2007) and are all in agreement confirming the fact (already found by Theuns et al. 2002) that the HI column density distribution function is quite insensitive to the different feedback prescriptions. Even though the galaxies drive strong winds or AGN feedbacks, there is no discernible effect on the Lyman- $\alpha$  forest. This because winds or black hole ejecta expand preferentially into the lower density regions and so keep the filaments that produce the hydrogen lines intact (Theuns et al. 2002). The volume filling factor of the winds is thus quite small and does not impact strongly on Lyman- $\alpha$  lines. In Figure 4.3 we show the HI CDDF at redshift  $z = 2.25$ : all the previous trends are confirmed.

### 4.3.2 Probability distribution function of the HI Doppler parameter

In this Section we analyse the Lyman- $\alpha$  Doppler parameter probability distribution function. The Doppler parameter  $b_{\text{HI}}$  is defined (see Section 1.3.1) as:

$$b_{\text{HI}} = \sqrt{\frac{2k_{\text{B}}T}{m_{\text{HI}}} + b_{\text{kin}}^2}, \quad (4.2)$$

where  $m_{\text{HI}}$  is the neutral hydrogen particle mass and  $k_{\text{B}}$  is the Boltzmann’s constant. The first term under the square root is the “thermal” contribution and the second is the “kinetical” term describing the contribution from turbulence. Therefore, omitting the kinetical contribution, the Doppler parameter basically measures the temperature of the gas. In Figures 4.4 and 4.5 we show the Lyman- $\alpha$  Doppler parameter distribution function at redshifts  $z = 3$  and  $z = 2.25$  for all the simulations of Table 4.2, splitted in two groups (left panels: part I, right panels: part II) and compared with the data by Kim et al. (2007). All runs are in good agreement, but shifted towards higher  $b_{\text{HI}}$  with respect to the observational data. This is the same to say that our simulations produce too hot gas compared to the observations. There can be many reasons for this, both physical and numerical. Regarding the former, it is very important to stress the effect of the UV background on the gas: if the UV background is too strong the gas will be heated too much, however in this case we believe that most of the discrepancy is due to the lines fitting procedure. In particular, sometimes it happens that VPFIT has problems in reconstructing the continuum outside a given line and adds broad components with large equivalent width but very low optical depth. These components have negligible impact on the column density distribution function because of their small column density, but they can bias the Doppler parameter probability distribution function. We will show later how this numerical effect is important in explaining some features of the  $b_{\text{CIV}} - N_{\text{CIV}}$  relation.

### 4.3.3 Column density-Doppler parameter relation

To conclude this part on the HI statistics, in Figures 4.6 and 4.7 we plot the  $b_{\text{HI}} - N_{\text{HI}}$  relation, at redshift  $z = 3$  and  $z = 2.25$  respectively, for some of the simulations in Table 4.2. In the upper left panel of both the Figures are overplotted (purple diamonds) the observational data of Kim et al. (2007). Both at redshifts  $z = 3$  and  $z = 2.25$  all runs are in good agreement between each other and reproduce well the observations, even if the simulations present an excess of low column density-low Doppler parameter systems. Again this can be a numerical effect: in order to fit a given line, VPFIT uses a lot of small components to minimize the  $\chi^2$  statistics (in addition to the single broad component that fit the line “at the first order”). This results in the excess we see in these plots. The slope of the data envelope in the column density range  $11.5 < \log N_{\text{HI}} < 15$  measures the slope of the  $T - \rho$  relation for the gas (Schaye 2001), and all the runs show the same right slope of the data at the two redshifts.

To sum up, the fact that for our simulations all the different HI statistics are in agreement with the observational data, confirms that we are catching the physics of the gas traced by the neutral hydrogen. The discrepancies are due to two different numerical effects introduced by VPFIT and affecting our analysis of the absorption lines in quasar spectra. We will discuss in more detail the impact of this effects in the next sessions regarding the CIV absorption lines statistics.

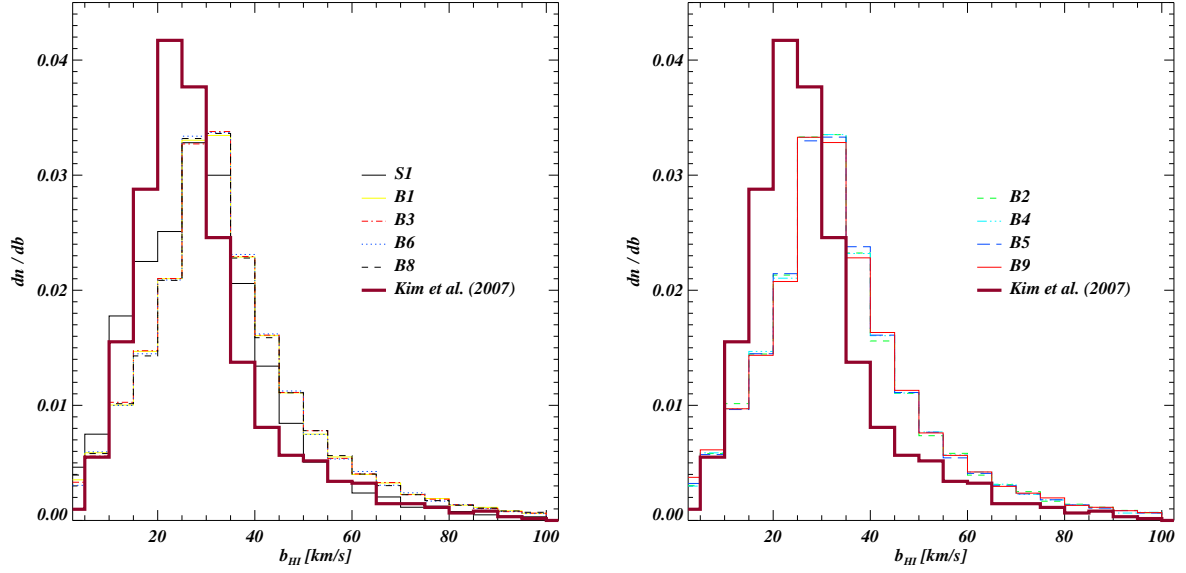


Figure 4.4:  $b_{\text{HI}}$  probability distribution function at  $z = 3$ . *Left panel*: part I. *Right panel*: part II. In both panels, data from Kim et al. (2007) are showed by the purple solid line.

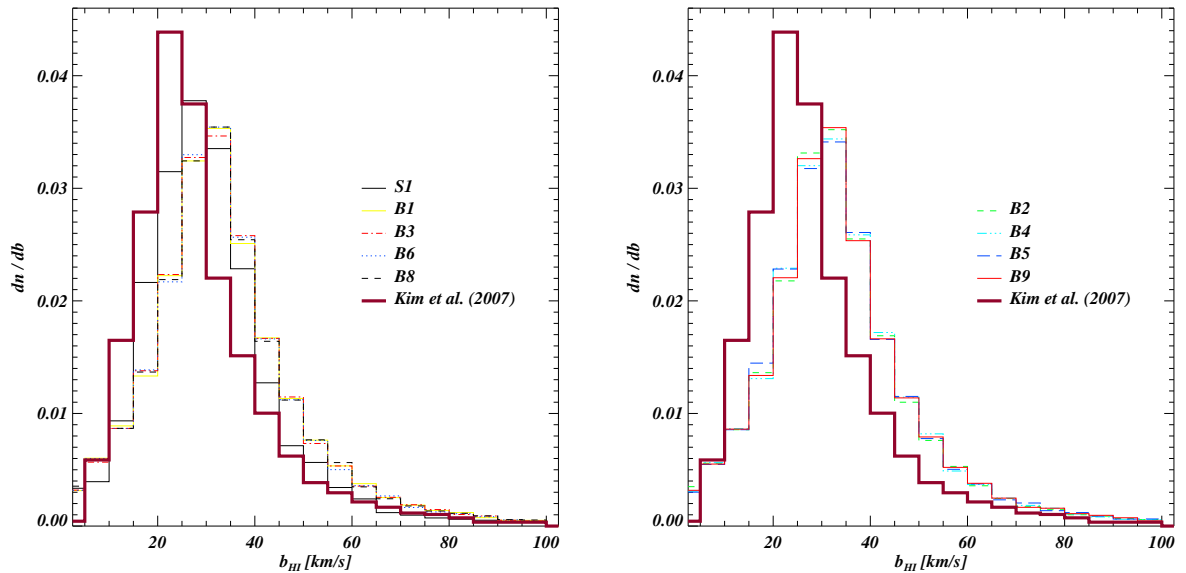


Figure 4.5:  $b_{\text{HI}}$  probability distribution function at  $z = 2.25$ . *Left panel*: part I. *Right panel*: part II. In both panels, data from Kim et al. (2007) are showed by the purple solid line..

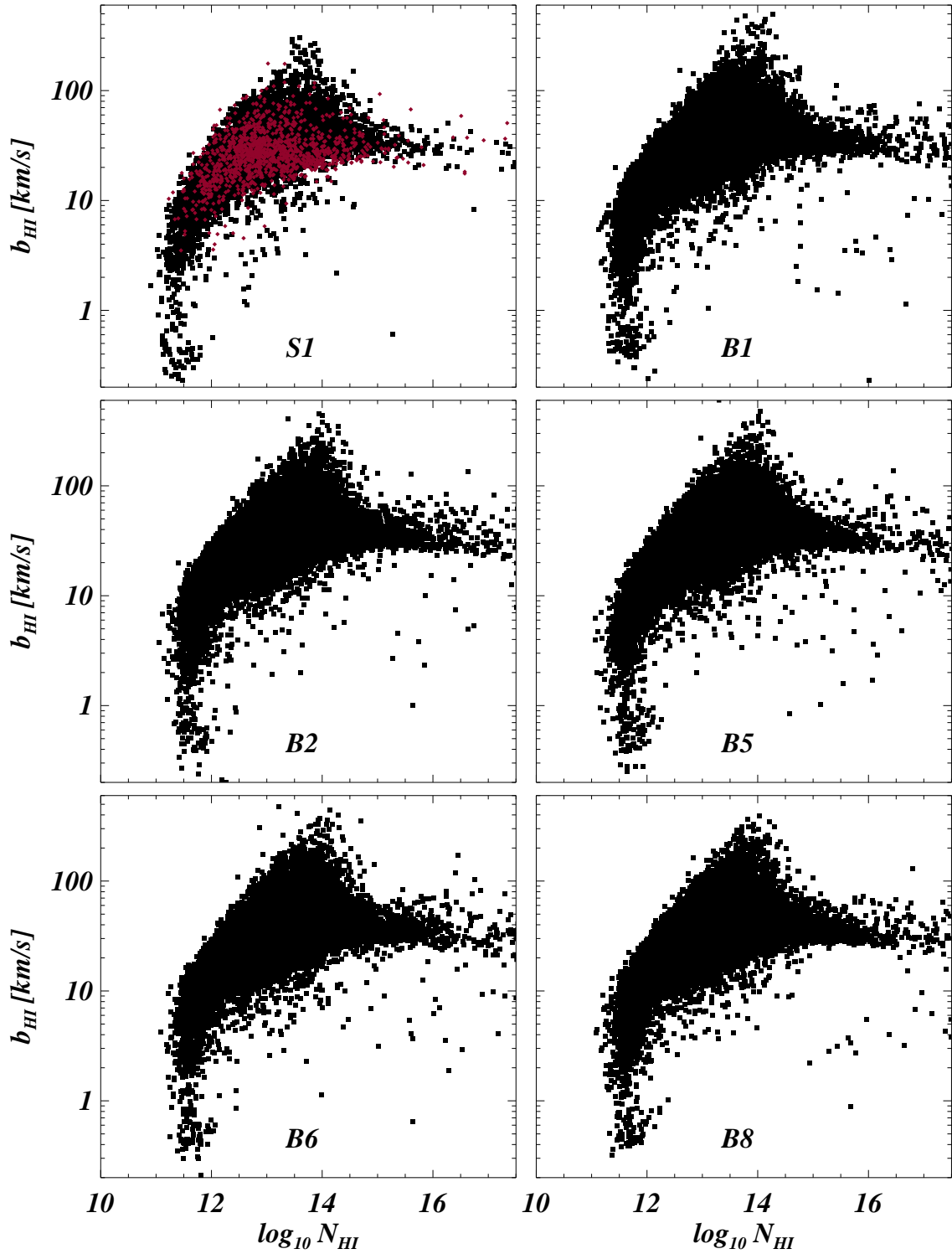


Figure 4.6:  $b_{\text{HI}} - N_{\text{HI}}$  relation at  $z = 3$ . The overplotted purple diamonds in upper left panel show the observational data of Kim et al. (2007).

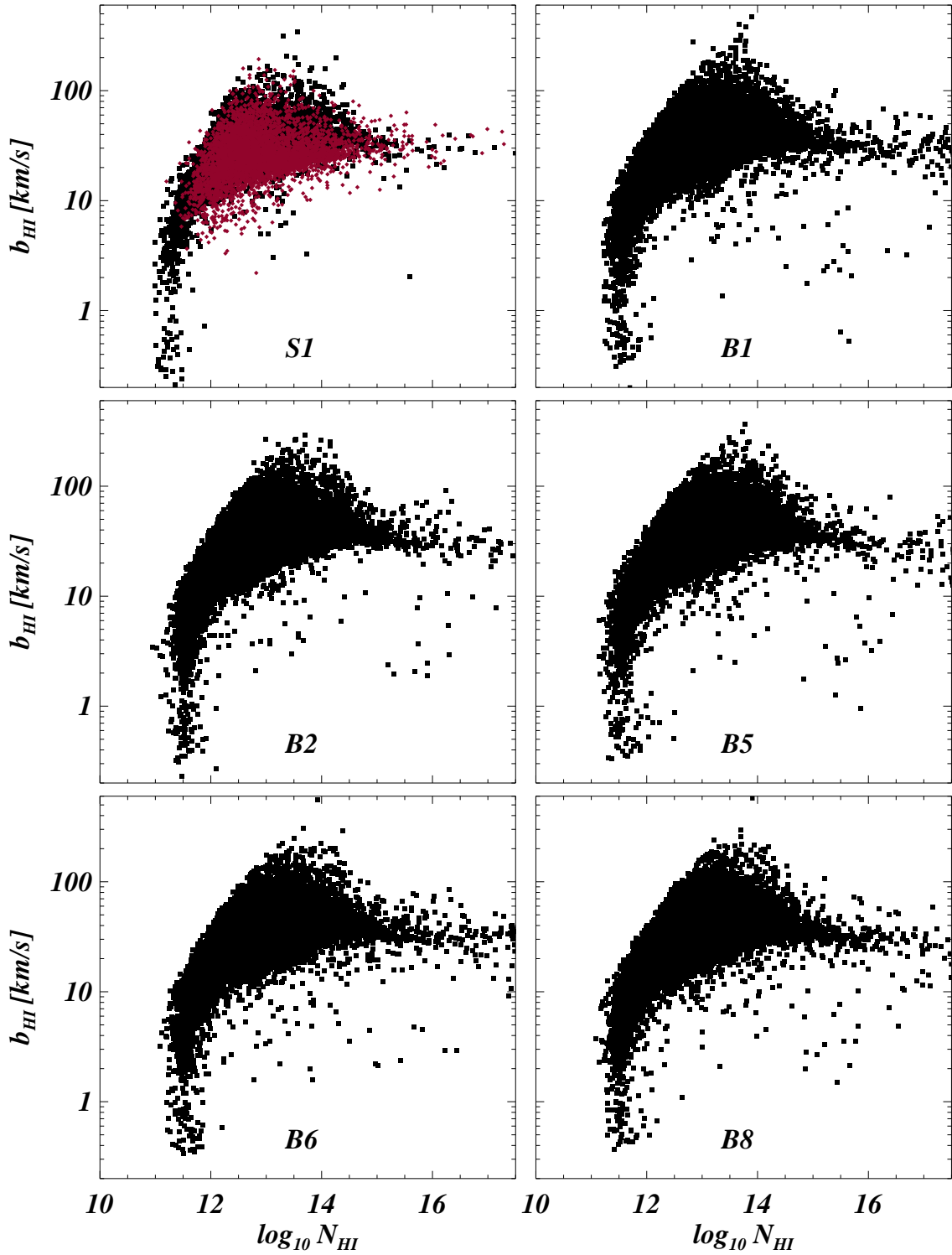


Figure 4.7:  $b_{\text{HI}} - N_{\text{HI}}$  relation at  $z = 2.25$ . The overplotted purple diamonds in upper left panel show the observational data of Kim et al. (2007).

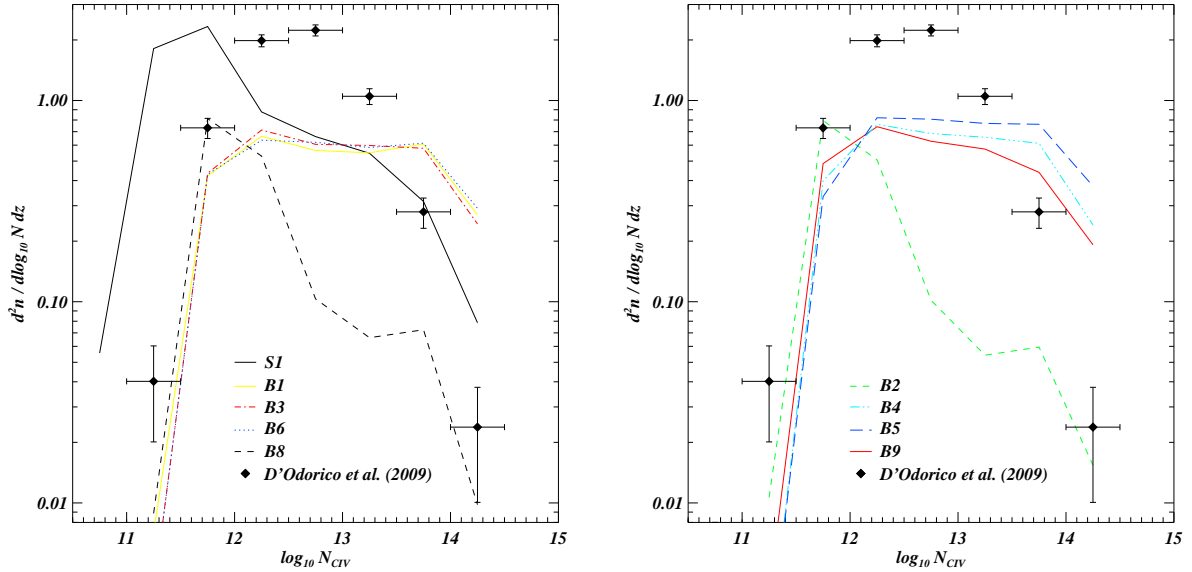


Figure 4.8: CIV column density distribution function at  $z = 3$ . *Left panel*: part I. *Right panel*: part II. Data from D’Odorico et al. (2009).

## 4.4 The CIV column density distribution function

In this Section we investigate the CIV column density distribution function (CIV CDDF, already defined in Section 4.3.1), plotted at redshift  $z = 3$ , 2.25 and 1.5, respectively and along with the D’Odorico et al. (2009) data, in Figures 4.8, 4.9 and 4.10. From these Figures is clear that, differently than for the HI, we have some problems in reproduce the CIV column density distribution function.

At redshift  $z = 3$  (Figure 4.8) all the simulations fail to fit the data in the intermediate range of the distribution  $12 < \log N_{\text{CIV}} < 13.5$ : the normalization of the simulated distributions is too low compared with the one of the data. In the range  $\log N_{\text{CIV}} > 13.5$  there are some small differences between the “regular” runs (part I, left panel)  $B1$  (AGN + energy-driven winds),  $B3$  (coupled energy-driven winds),  $B6$  (momentum-driven winds) and (part II, right panel)  $B4$  (energy-driven winds, Kroupa IMF),  $B5$  (energy-driven winds, Arimoto-Yoshii IMF),  $B9$  (energy-driven winds, Salpeter IMF), but in general all these runs are in agreement between each other. Instead for the “non regular” (in the sense of the feedback prescriptions chosen) simulations  $S1$ ,  $B2$  and  $B8$  problems are even worse. Run  $S1$  (Figure 4.8 left panel, black solid line) is the pre-enriched one: at redshift  $z = 9$  all the particles with overdensity  $\delta + 1 > 20$  assumed a metallicity  $Z = 0.2Z_{\odot}$  or, in other words, the dense regions associated with haloes and filaments in the box were strongly enriched. Differently from what one could expect, this only results in an overproduction of low column density systems. The reason is that all the enriched gas can cool very efficiently producing a burst of star formation that “consumes” the gas itself. Therefore, going to lower redshift, haloes are devoided of gas and, even when the winds feedback becomes effective, present small and enriched cores. The case is different for runs  $B2$  and  $B8$ . Simulation  $B2$  (Figure 4.8 right panel, green dashed line) was run, as a test,

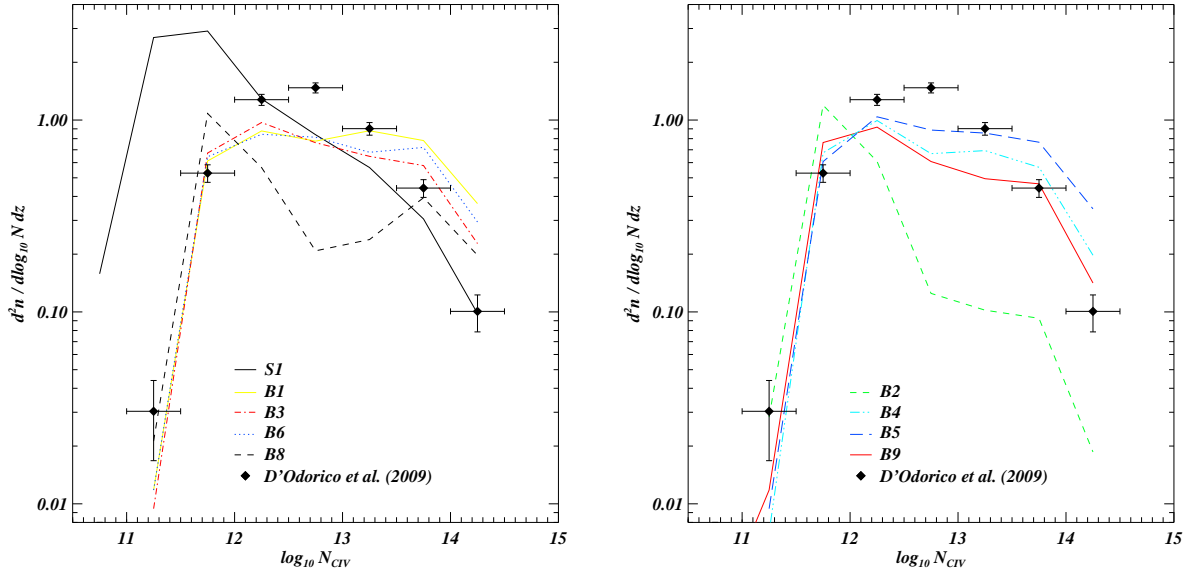


Figure 4.9: CIV column density distribution function at  $z = 2.25$ . *Left panel*: part I. *Right panel*: part II. Data from D’Odorico et al. (2009).

without any winds or AGN feedback: so there is no effective mechanism able to quench the star formation and spread the enriched gas outside the haloes. The result is that all the gas is trapped at high temperature inside high density haloes and most of the carbon is used up by the star and convert in other species, leaving only the lot of small clumps seen in the Figure. In run *B8* (Figure 4.8 left panel, black dashed line) the feedback mechanism is the AGN feedback, associated to the energy released by gas accretion onto super-massive black holes. Comparing the resulting distribution with the one of the just mentioned “no feedback” *B2*, they are very similar (at least at this redshift), but for completely different reasons. While in the *B2* there is no feedback, for the *B8* the AGN feedback at  $z = 3$  is very powerful: gas around haloes is heated too much and a lot of CIV gets ionized to CV. We do not see high column density systems in the distribution because they are not produced at all. Interestingly, run *B1* (AGN + energy-driven winds) follow all the other “regular” runs even if in this case we have the joined effect of winds and AGN feedbacks: this is due to the fact that winds start to be effective at higher redshift than the AGN feedback, devoiding of gas the haloes and in this way reducing the efficiency of the black holes accretion and the power of the AGN feedback.

At redshift  $z = 2.25$  (Figure 4.9) the agreement is better than at redshift  $z = 3$ , but we still fail in reproducing the CIV column density distribution function in the intermediate range  $12 < \log N_{\text{CIV}} < 13.5$ . Again the normalization of the simulated distributions is too low compared with the observational data. *S1* (pre-enriched, left panel solid black line) and *B2* (no feedback, right panel dashed green line) runs suffer of the same problems described before, while for the *B8* (AGN feedback, left panel dashed black line) run the discrepancies with the regular runs decreased: a first hint that going to lower redshift AGN feedback becomes less and less efficient in heating the intergalactic gas and the behaviour of this simulation starts to follow the regular ones.

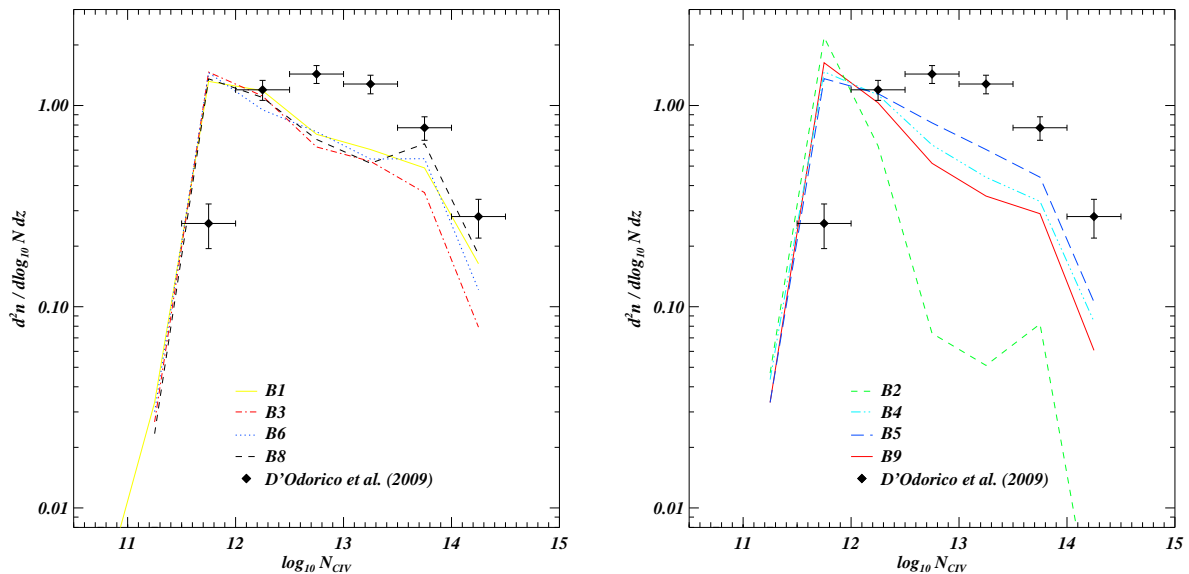


Figure 4.10: CIV column density distribution function at  $z = 1.5$ . *Left panel*: part I. Run *S1* (pre-enriched) is not present here because this simulation was stopped at  $z_f = 1.8$ . *Right panel*: part II. Data from D’Odorico et al. (2009).

At redshift  $z = 1.5$  (Figure 4.10) all the simulations produce too many systems with low column density and systematically fall short off reproducing the distribution at  $\log N_{\text{CIV}} > 12.5$ . Now the *B8* run (AGN feedback, left panel dashed black line) closely follows the other regular runs, confirming that at this low redshift AGN feedback does not heat too much the gas anymore, while *B2* run (no feedback, right panel dashed green line) is still wrong and has to be discarded. If we consider all the redshifts, the *B6* run with momentum-driven winds reproduces better than all the other runs the CIV column density distribution function.

Looking at the Figures 4.8, 4.9 and 4.10 it is possible to note that our simulations fail to reproduce the CIV CDDF at the various redshift in two different modes: (a) they present an overproduction of small column density systems and (b) the normalization of the distributions is always too low. There can be many reasons for this, but basically we need both to “rise” and “shift towards higher column densities” the distribution. Regarding the point (a) we think that the numerical effect mentioned in Section 4.3.3 can play an important role: in order to fit a given line, along with a single broad component, VPFIT could use a lot of small components to minimize the  $\chi^2$  statistics. This plethora of small components can contribute significantly to the low column density tail of the distribution. As a first improvement, we will try to discriminate all the spurious components and to control the fitting procedure both checking VPFIT and the statistical analysis of the fitted lines. Regarding the point (b), a different choice of the UV background can be crucial in helping to “rise” the distribution to the level seen in the observational data. In this thesis we always assumed a mean UVB produced by quasars and galaxies as given by Haardt & Madau (1996), with the heating rates multiplied by a factor 3.3 in order to better fit observational constraints on the temperature evolution of the IGM at high redshift. For the future we want to test the updated version of this Haardt & Madau ultraviolet

background: namely a new refined UVB that takes into account the HeII reionization. With this new UVB, before redshift  $\sim 3$  a lot of hard photons are captured and used to reionize HeII; after the reionization is complete the same photons are again available and free to affect the IGM evolution. We do not know what will be the effect on the CIV statistics, but of course the new UV background is more realistic of the one we used so far and can help to improve this and other statistics of different metal ion species.

In Figure 4.11 we show a first very simple attempt of “varying” the UV background. The procedure for fitting a compilation of CIV absorption spectra, for a given simulation at a given redshift, was the following: we started considering the corresponding compilation of HI absorption spectra and rescaling all the HI optical depths by a constant factor  $A_{\text{HI}}$ , in such a way that their mean value was equal to the HI effective optical depth at that redshift  $z$ , given by the Kim et al. (2007) fitting formula:

$$\tau_{\text{HI}}^{\text{eff}} = (0.0023 \pm 0.0007)(1+z)^{3.65 \pm 0.21}. \quad (4.3)$$

Then we rescaled all the CIV optical depths for the same constant factor  $A_{\text{HI}}$ . Vary the value of  $\tau_{\text{HI}}^{\text{eff}}$  is equivalent to vary the strength of the UV background because  $\tau_{\text{HI}}^{\text{eff}} \propto 1/\Gamma_{-12}$  ( $\Gamma_{-12}$  being the HI photoionization rate depending on the emissivity at the Lyman edge and on the spectral index of the UV background just shortward of the Lyman edge). For this reason we took the momentum-driven winds run *B6* and produced two new sets of absorption spectra in which all the CIV optical depths were rescaled considering both the upper and the lower limit of the relation (4.3). The result is plotted, along with the data of D’Odorico et al. (2009), at redshift  $z = 3$  (left panel),  $z = 2.25$  (middle panel),  $z = 1.5$  (right panel) in Figure 4.11: blue solid line is the original *B6* run, while blue dashed and dotted lines refer respectively to the upper and lower limit. From the Figure is clear that the effect of such a change in the CIV CDDF is very small: increasing  $\tau_{\text{HI}}^{\text{eff}}$  (and therefore lowering the UVB strength) results in a shift of systems from the low to the high column density tail of the distribution, with respect to the original run. The opposite is true when one considers the lower limit of Eq. (4.3). Of course what we did was not a real physically consistent variation of the UV background, but only a simple attempt to check the impact of different assumptions on the normalization of our synthetic spectra: in this sense we were “varying” the UVB. To sum up, the effect is present but not very strong and does not help to solve the discrepancies between the real and the simulated distributions at the various redshift.

## 4.5 The evolution of the CIV cosmological mass density

In Figure 4.12 we show, for all the different simulations, the evolution with redshift of the CIV cosmological mass density as a fraction of the critical density today:

$$\Omega_{\text{CIV}}(z) = \frac{H_0 m_{\text{CIV}}}{c \rho_{\text{crit}}} \int N f(N) dN, \quad (4.4)$$

where  $H_0 = 100 h \text{ km s}^{-1} \text{ Mpc}^{-1}$  is the Hubble constant,  $m_{\text{CIV}}$  is the mass of a CIV ion,  $c$  is the speed of light,  $\rho_{\text{crit}} = 1.88 \times 10^{-29} h^2 \text{ g cm}^{-3}$  and  $f(N)$  is the CIV CDDF. Since  $f(N)$  cannot be recovered correctly for all column densities due to incompleteness and poor statistics,

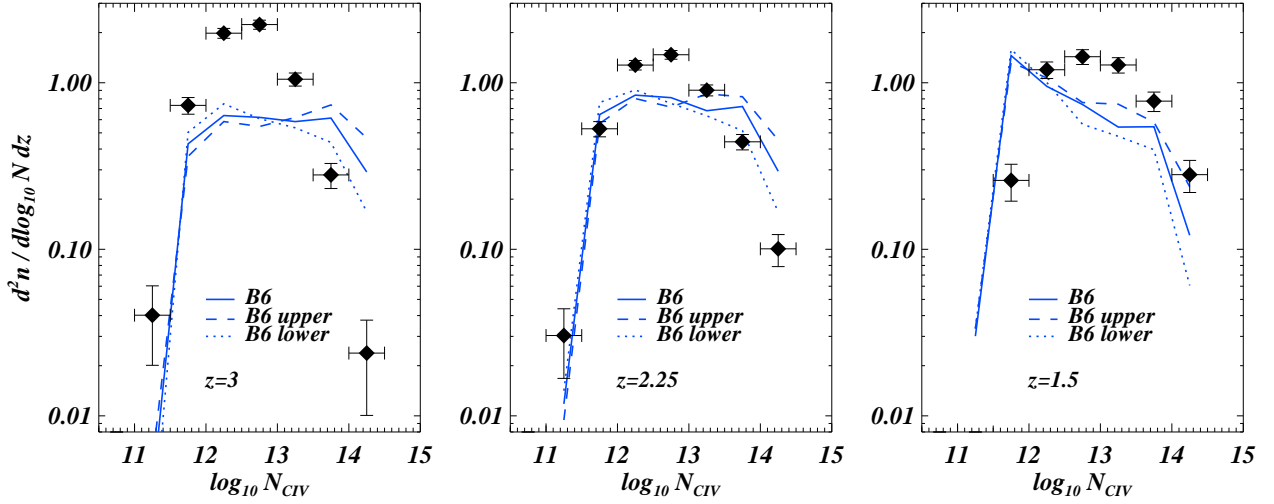


Figure 4.11: CIV column density distribution functions at  $z = 3$  (*left panel*),  $2.25$  (*middle panel*) and  $1.5$  (*right panel*) for the *B6* (momentum-driven winds) run. In each panel solid blue line refers to the original run while the dashed and dotted blue lines were calculated rescaling all the optical depths for, respectively, the upper and the lower limit of the Kim et al. (2007) fitting formula for the HI effective optical depth  $\tau_{\text{HI}}^{\text{eff}}$ , Eq. (4.3). The black diamonds show the observational data of D’Odorico et al. (2009).

the integral in the previous Equation can be approximated by a sum (Storrie-Lombardi et al. 1996):

$$\Omega_{\text{CIV}}(z) = \frac{H_0 m_{\text{CIV}} \sum_i N_i(\text{CIV})}{c \rho_{\text{crit}} \Delta X}, \quad (4.5)$$

with  $\Delta X \equiv \int (1+z)^2 [\Omega_{\text{om}}(1+z)^3 + \Omega_{0\Lambda}]^{-1/2} dz$ , the redshift absorption path.

In Figure 4.12 the overplotted black diamonds show the observational data of D’Odorico et al. (2009). The value of  $\Omega_{\text{CIV}}$  significantly depends on the column density range over which the sum or the integration is carried out and, as a consequence, on the resolution and signal-to-noise ratio of the available spectra. In order to address this aspect, D’Odorico et al. (2009) have computed three sets of values to be compared consistently with different data in the literature. Here we compared  $\Omega_{\text{CIV}}$  obtained from the simulated CIV components lying in the column density range  $12 \leq \log N_{\text{CIV}} \leq 15$ , with the  $\Omega_{\text{CIV}}$  computed from the CIV systems of the total D’Odorico et al. (2009) sample, in the same range of column densities. As we introduced in Section 4.1, CIV systems have been built adopting a minimum lines velocity separation of  $50 \text{ km s}^{-1}$ . Apart from the no feedback simulation *B2* (green crosses and dashed line), all the other runs reproduce the observational data around redshift  $z = 2.25$ . If we consider lower redshift, all the simulations, except the *B8* (AGN feedback, black crosses and dashed line), show a decreasing trend at variance with the data. At redshift  $z = 3$  the AGN feedback of run *B8* is very strong and heats too much the gas around haloes, in this way lowering the CIV content (as we explained in the previous Section). At the same time this strong AGN feedback quenches efficiently the star formation, therefore the gas is no longer reprocessed from the stars and the CIV is not converted in other ions. For this reason, going to lower redshift

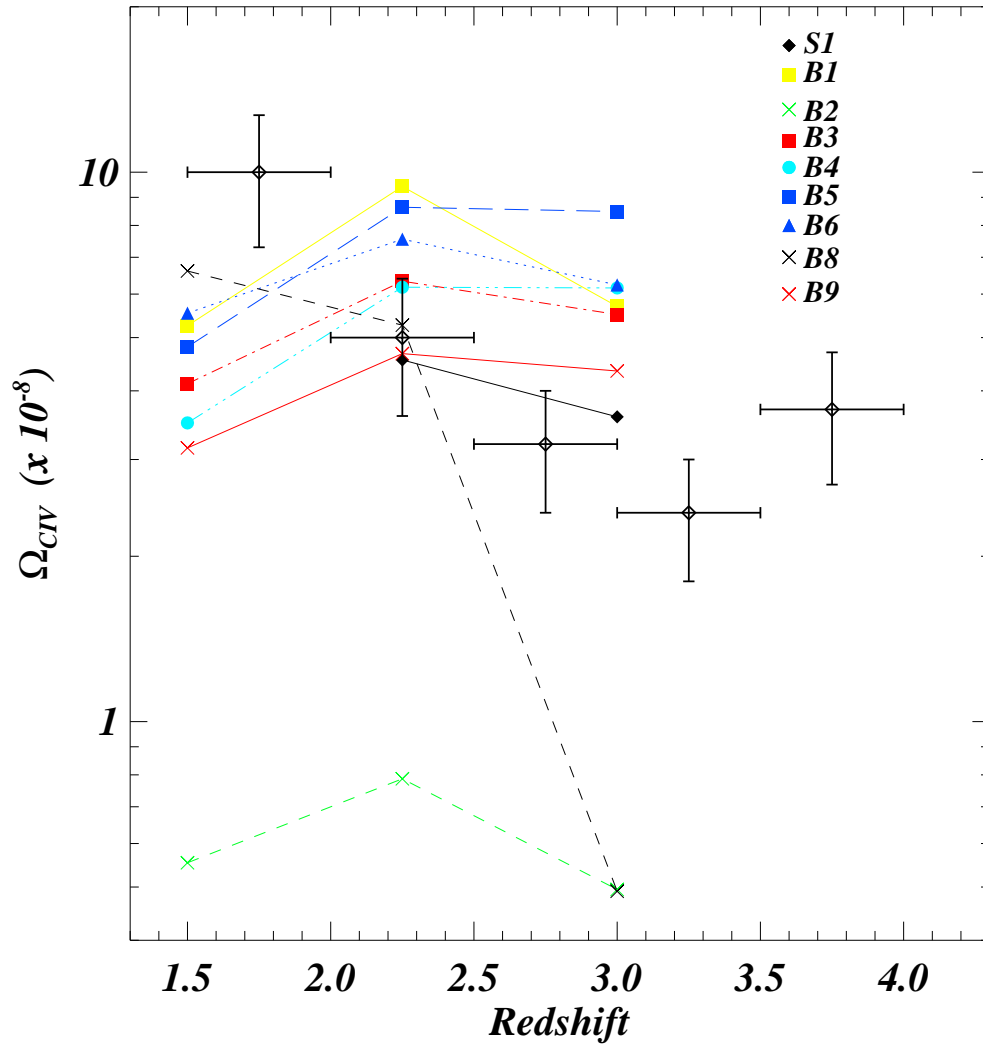


Figure 4.12:  $\Omega_{CIV}$  evolution with redshift, calculated considering the absorption lines in 1000 lines-of-sight through each box, for the different simulation boxes. The overplotted black diamonds show the observational data of D'Odorico et al. (2009).

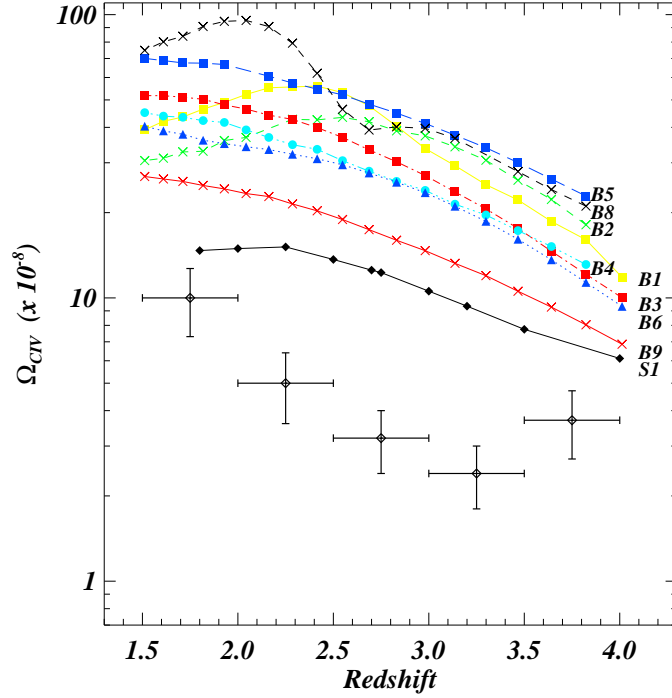


Figure 4.13:  $\Omega_{\text{CIV}}$  evolution with redshift, calculated considering all the CIV content inside each box, for the different simulation boxes. The overplotted black diamonds show the observational data of D’Odorico et al. (2009).

$\Omega_{\text{CIV}}(z)$  for the *B8* run continues to increase. A way to improve the situation for all the other runs is related to the effect of the UV background, and we believe that with the updated UVB described in Section 4.4 we can improve the situation and invert the decreasing trend.

Interestingly run *S1* (pre-enriched, black diamonds and solid line) fits the data better than all the other runs in the redshift range [2.25, 3] (data point at redshift  $z = 1.5$  is missing because this simulation was stopped at redshift  $z_f = 1.8$ ). This run fails to reproduce most of the CIV statistics, mainly because it produces too many small CIV enriched clumps, but in this case, where we are treating with the total content of CIV, it fits the data: other improved and more physically motivated pre-enrichment recipes, will be presented in a future publication.

We want to point out that in our present analysis we considered simulated CIV single components and not systems of components like D’Odorico et al. (2009). Even if the differences in the observational data are very small, they could be important for the simulations, especially considering the numerical effects introduced by VPFIT (see Section 4.3.3) that can be alleviated when taking into account groups of lines instead of single lines. For the future, will be of crucial importance the implementation of an automatic procedure able to find and isolate CIV systems in the simulated spectra.

In Figure 4.13 we show  $\Omega_{\text{CIV}}(z)$ , now calculated considering the entire CIV content inside each cosmological box. Observational data are again from D’Odorico et al. (2009), but now plotted only for reference. The difference with Figure 4.12 is that here, without taking into

account the CDDF, we considered the CIV content of every gas particle in the simulation and then we added together all the contributions. Of course in this case simulations data are well above the observational data recovered by means of the CIV absorption lines using Eq. (4.5), but it is interesting to compare the different simulations. Energy-driven winds runs *B4* (cyan circles and triple dot-dashed line), *B5* (blue squares and dashed line) and *B9* (red crosses and solid line) are identical except for the IMF: in fact the evolution of  $\Omega_{\text{CIV}}$  is the same but with different normalization: *B5* has Arimoto-Yoshii IMF and produces more CIV than *B4* run (Kroupa IMF) which itself produces more CIV than *B9* (Salpeter IMF). The same trend is visible in the middle upper panel of Figure 3.4 in Chapter 3. Runs *B3* (coupled energy-driven winds, red squares and dot-dashed line) and *B6* (momentum-driven winds, blue triangles and dotted line) follow almost the same trend of *B4*, which has the same IMF of them. For the *B2* simulation (no feedback, green crosses and dashed line),  $\Omega_{\text{CIV}}$  starts to decrease at redshift  $z \sim 2.7$ , while *S1* run (black diamonds and solid line) has the lowest normalization even if was pre-enriched at high redshift. It is interesting to note that for the simulation *B8* (AGN feedback, black crosses and dashed line)  $\Omega_{\text{CIV}}$  suddenly increases after a small decrement at redshift  $z \sim 2.8$ . This again is due to the star formation quenching effect produced by the powerful AGN feedback. Going to lower redshift AGN feedback becomes less efficient and the CIV cosmological density starts to follow all the other runs. The same effect is visible in the *B1* run (AGN + energy-driven winds, yellow squares and solid line). In this case the effect is weaker because, as we explained in Section 4.4, winds devoid haloes of gas and therefore reduce the efficiency of the black holes accretion and thus the power of the AGN feedback.

## 4.6 Probability distribution function of the CIV Doppler parameter

In this Section we focus on the CIV Doppler parameter probability distribution function, plotted at redshift  $z = 3$ , 2.25 and 1.5 in Figures 4.14, 4.15 and 4.16, respectively. The data from D’Odorico et al. (2009) are also overplotted in these Figures with a purple solid line.

At redshift  $z = 3$  (Figure 4.14) all the “regular” runs are quite in agreement with the data even if there are some small discrepancies. In particular regular runs tend to: (a) slightly overestimate the observed distribution at very low  $b_{\text{CIV}}$ ; (b) underestimate the distribution in the range  $10 < b_{\text{CIV}} < 20 \text{ km s}^{-1}$ ; (c) overestimate it for  $b_{\text{CIV}} > 20 \text{ km s}^{-1}$ . We already found a similar behaviour for the  $b_{\text{HI}}$  probability distribution function (see Section 4.3.2), but now the effect is considerably smaller. Again the “non regular” runs *S1*, *B2* and *B8* show a different trend with respect to the others, for exactly the same reasons mentioned in the previous sections. Simulation *S1* (pre-enriched, left panel black solid line) has a marked excess of low CIV Doppler parameter lines, while the *B2* (no feedback, right panel green dashed line) and *B8* (AGN feedback, left panel black dashed line) distributions are shifted towards higher  $b_{\text{CIV}}$  than the observed one. At this redshift AGN feedback is very powerful and heats the intergalactic gas too much (we remember that the Doppler parameter measures the temperature of the gas), while in the no feedback case of *B2* the gas remains trapped inside haloes at high density and temperature.

The situation for the regular runs is quite the same both at redshift  $z = 2.25$  (Figure 4.15)

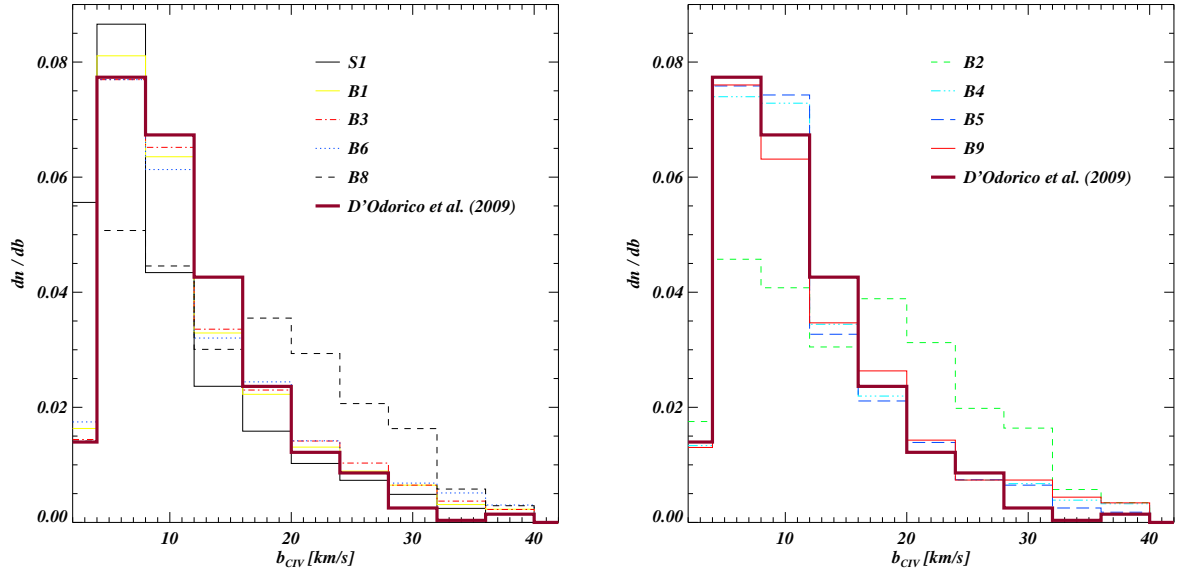


Figure 4.14:  $b_{\text{CIV}}$  probability distribution function at  $z = 3$ . *Left panel*: part I. *Right panel*: part II. In both panels, data from D’Odorico et al. (2009) are showed by the purple solid line.

and  $z = 1.5$  (Figure 4.16). Moreover, while going to lower redshift  $B2$  simulation (no feedback, right panels green dashed lines) is still wrong, run  $B8$  (AGN feedback, left panels black dashed lines) at redshift  $z = 2.25$  fits better the data and it finally approaches all the other runs at  $z = 1.5$ , further confirming the decreasing efficiency of the AGN feedback at low redshift.

## 4.7 The CIV column density-Doppler parameter relation

In Figures 4.17, 4.18 and 4.19 we plot the  $b_{\text{CIV}} - N_{\text{CIV}}$  relation, at redshift  $z = 3$ ,  $z = 2.25$  and  $z = 1.5$  respectively, for some of the simulations in Table 4.2. The observational data of D’Odorico et al. (2009) are also reported as purple diamonds in the upper left panel of the Figures.

At redshift  $z = 3$  (Figure 4.17), regular runs  $B1$  (AGN + energy-driven winds),  $B5$  (energy-driven winds, Arimoto-Yoshii IMF) and  $B6$  (momentum-driven winds) are in agreement and generally reproduce the spread of the data. We stress that in the  $B1$  run the effect of the winds overcomes that of the AGN and this run has the same distribution of the other two. Anyway, in the simulated data is visible a sort of bimodality: (a) a plume of lines at high CIV column densities for which the Doppler parameters increase as  $N_{\text{CIV}}$  increases; (b) a clump of systems with various  $b_{\text{CIV}}$  at low column density. We interpret the plume in (a) as a  $T - \rho$  relation: lines with higher column densities (i.e. associated to denser regions) have higher Doppler parameters (i.e. temperature). The fact that this relation appears only at high column densities is not a surprise: for high values of  $N_{\text{CIV}}$  absorption lines are very strong and well resolved, so they are good tracers of the physical state of the intergalactic gas and also they are better fit by VPFIT.

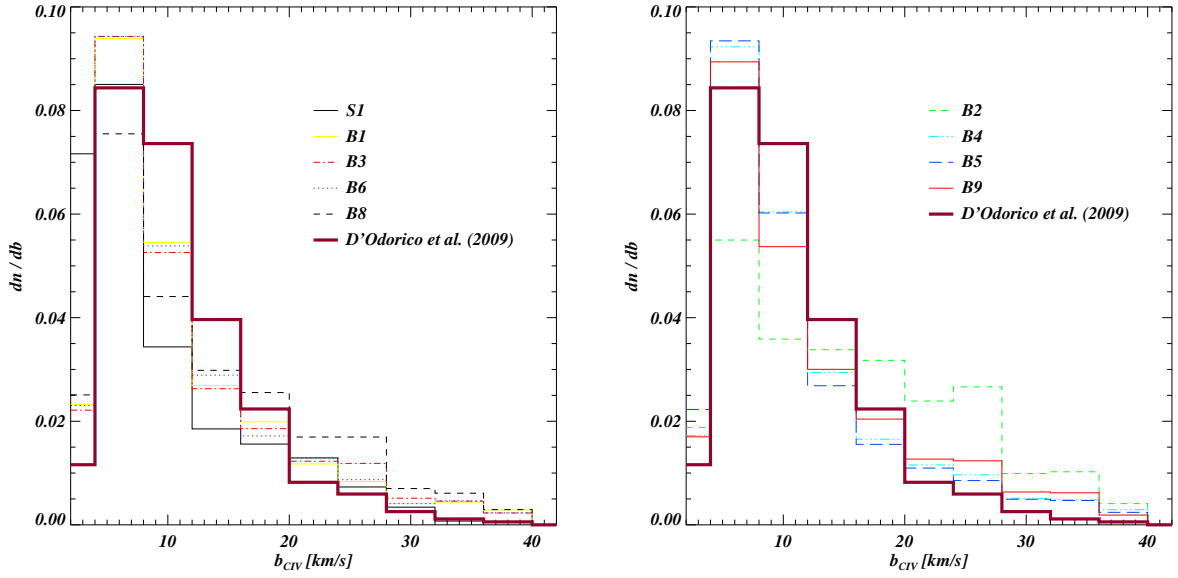


Figure 4.15:  $b_{\text{CIV}}$  probability distribution function at  $z = 2.25$ . *Left panel*: part I. *Right panel*: part II. In both panels, data from D'Odorico et al. (2009) are showed by the purple solid line.

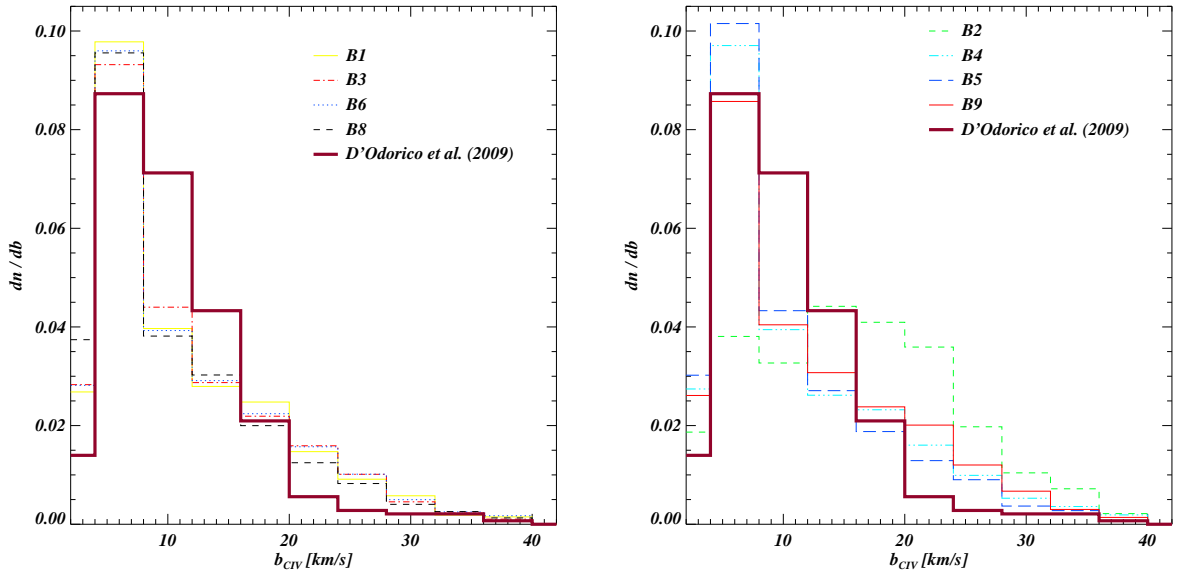


Figure 4.16:  $b_{\text{CIV}}$  probability distribution function at  $z = 1.5$ . *Left panel*: part I. Run S1 (pre-enriched) is not present here because this simulation was stopped at  $z_{\text{f}} = 1.8$ . *Right panel*: part II. In both panels, data from D'Odorico et al. (2009) are showed by the purple solid line.

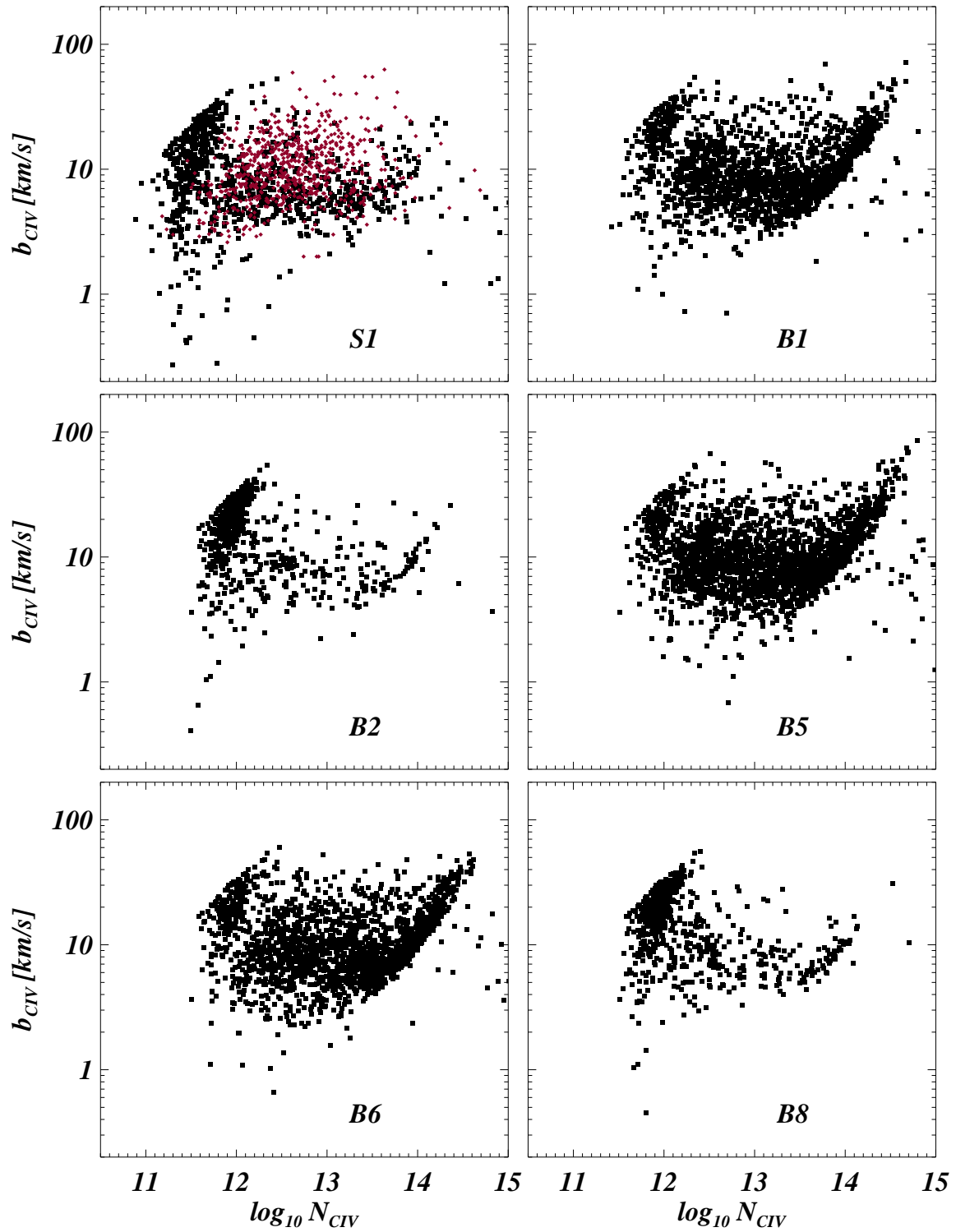


Figure 4.17:  $b_{\text{CIV}} - N_{\text{CIV}}$  relation at  $z = 3$ . The overplotted purple diamonds in upper left panel show the observational data of D'Odorico et al. (2009).

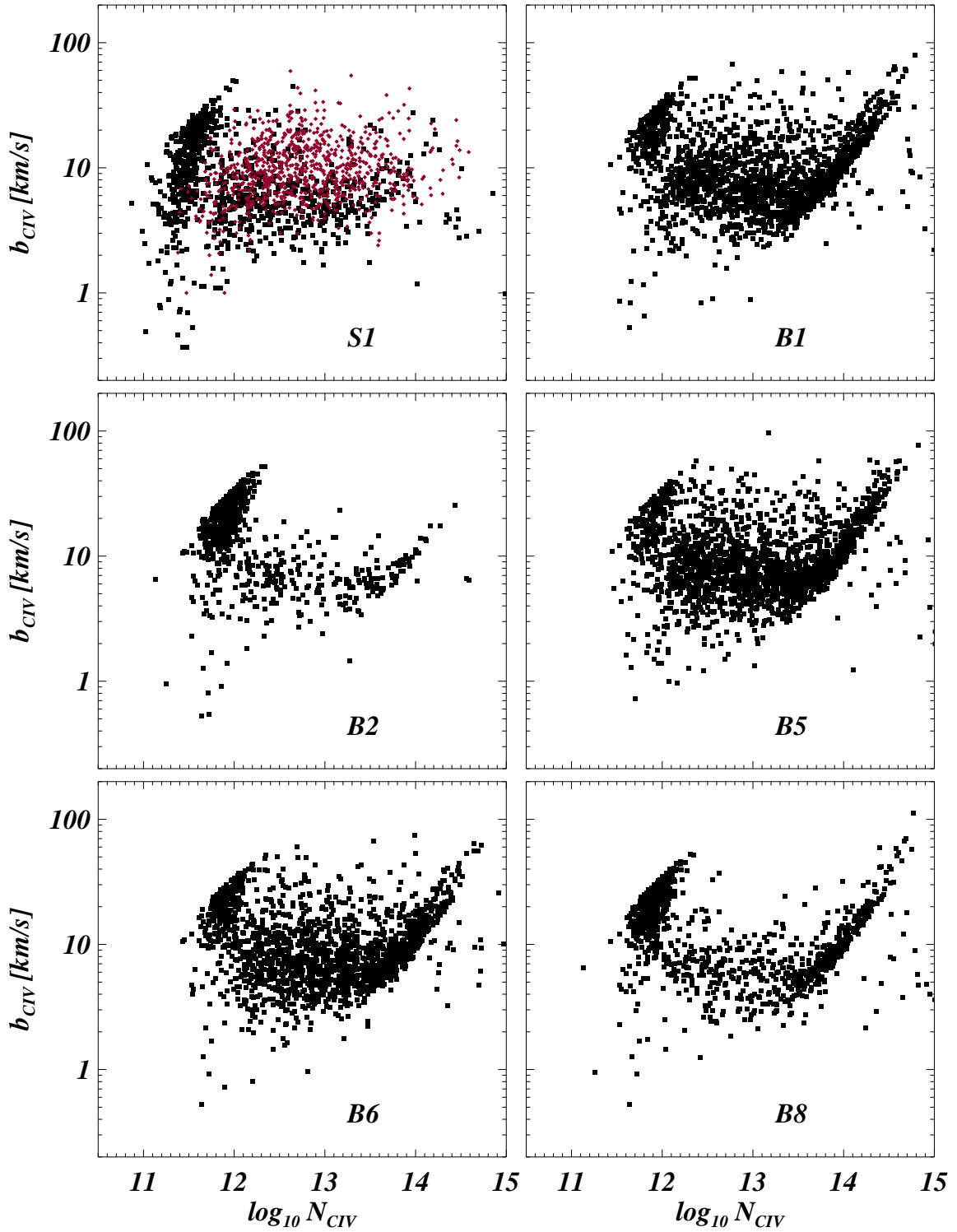


Figure 4.18:  $b_{\text{CIV}} - N_{\text{CIV}}$  relation at  $z = 2.25$ . The overplotted purple diamonds in upper left panel show the observational data of D'Odorico et al. (2009).

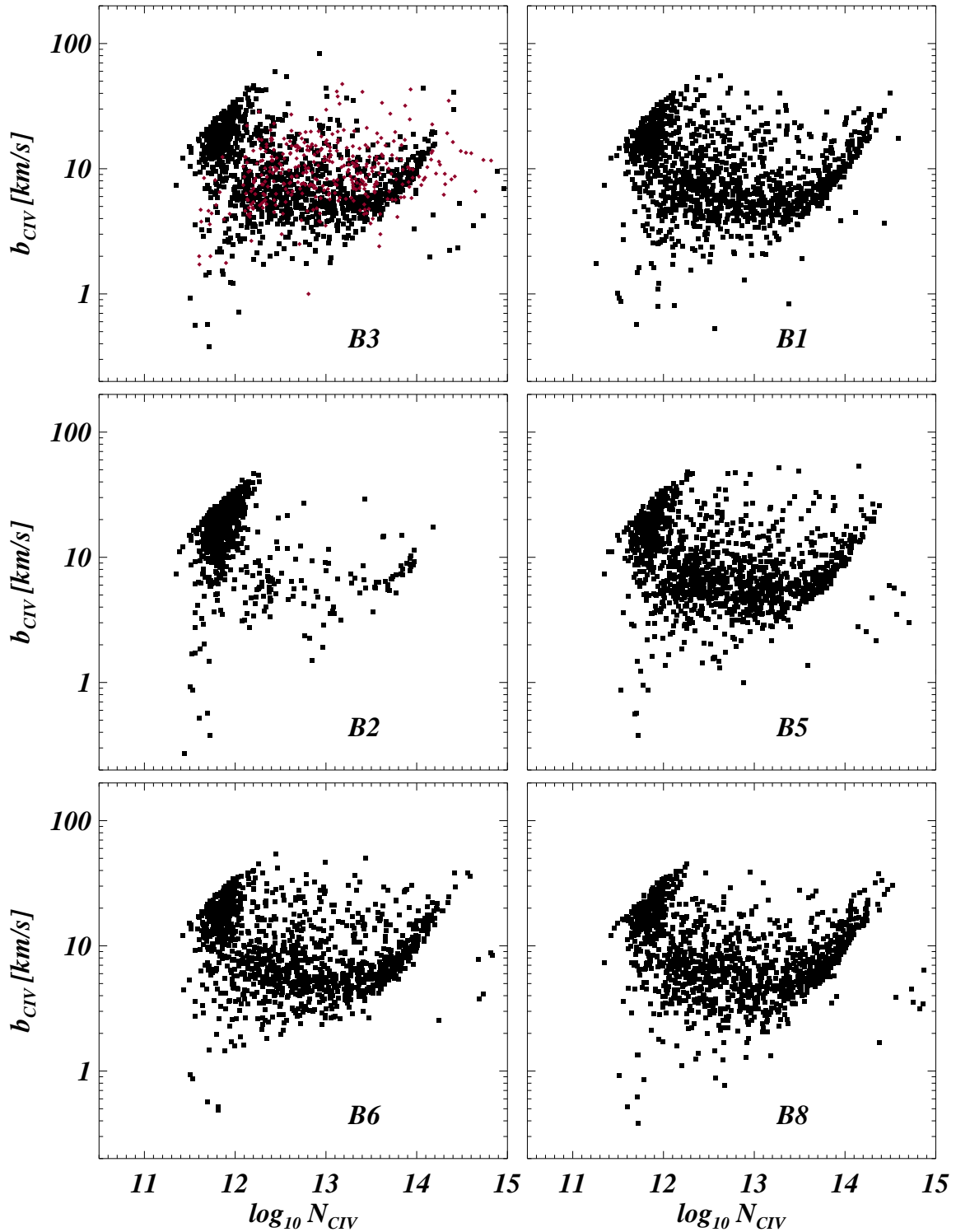


Figure 4.19:  $b_{\text{CIV}} - N_{\text{CIV}}$  relation at  $z = 1.5$ . The overplotted purple diamonds in upper left panel show the observational data of D’Odorico et al. (2009). Run  $S1$  (pre-enriched, stopped at  $z_f = 1.8$ ) is substituted in the upper left panel with run  $B3$  (coupled energy-driven winds).

Regarding the point (b), it is interesting to note that all the panels present the clump of systems at low column density, supporting the idea that this effect is a numerical artifact introduced by VPFIT. As we reported in Section 4.3.2, when VPFIT is not able to reconstruct correctly the continuum outside a given line, it adds some very broad components with low column density. While the effect is less evident (but present) in the case of the  $b_{\text{HI}} - N_{\text{HI}}$  relation, it is now much more critical. Of course, observational data do not present such a clump, because in the “by eye” procedure of fitting these spurious lines are discarded. We need for the future to improve our automatic fitting procedure in order to alleviate this problems.

The case of non regular runs *B2* (no feedback) and *B8* (AGN feedback) is different. Both the simulations present a clump of systems at low column density but they do not show the  $T - \rho$  relation for large  $N_{\text{CIV}}$  values. They show the same data distribution but for completely different reasons. As we just stated, AGN feedback at redshift  $z = 3$  is very powerful and heats too much the gas around haloes ionizing the CIV, while in the no feedback case all the gas resides inside high density high temperature cores of the haloes where is reprocessed by the stars. Finally the distribution of the *S1* (pre-enriched) simulation is shifted towards lower column densities with respect to all the others, and in this case the  $T - \rho$  relation is missing because this run has too much star formation at high redshift that consumes all the gas and leaves only an excess of small CIV clumps.

The situation is similar at redshift  $z = 2.25$  (Figure 4.18) and  $z = 1.5$  (Figure 4.19). As for the other CIV statistics discussed in the previous sections, moving to lower redshift *B8* run with AGN feedback approaches the regular runs, while the no feedback run *B2* fails to reproduce the correct data distribution.

## 4.8 Final Remarks

In this Chapter we have focussed on the global properties of triply ionized carbon (CIV) as an IGM tracer at  $z > 1$ . From the theoretical/numerical point of view we presented results from a new set of hydrodynamical simulations that incorporate feedback either in the form of galactic winds or in the form of black holes accretion (AGN feedback). From the observational point of view we relied on recent high-resolution data sets obtained with the UVES spectrograph. The main results can be summarized as follows:

- The statistics of HI are weakly affected by the feedback prescription implemented: both the CDDF and the Doppler width distributions do not change significantly when considering the different simulations. We regard this as a geometrical effect: winds and AGN feedback are stronger at the intersection of IGM filaments and these sites have usually small filling factor. Only very strong lines differ noticeably, than in less dense environments, between the different runs, but this does not affect the statistics significantly.
- The fact that overall our simulations reproduce very well all the HI statistics confirms that we are catching the physics of the gas traced by the neutral hydrogen. The remaining small discrepancies with the observational data are due to numerical effects introduced by the line-fitting software VPFIT.

- Differently from the HI, The statistics of CIV do depend on feedback. To clarify this, we divided our simulations in two sets: “regular” and “non regular”. For the regular runs the feedback prescriptions were already tested to be stable and physically reasonable, as for example the strong energy-driven or the momentum driven winds. Otherwise the “non regular” are the runs with new feedback models, like the AGN feedback, or runs which explore some extreme solutions as the pre-enriched or the no feedback runs.
- At redshift  $z = 3$  and  $z = 2.25$  the regular runs fit well the low column density tail of the CIV column density distribution function, but fail to fit the data in the intermediate range of the distribution:  $12 < \log N_{\text{CIV}} < 13.5$ . The non regular runs always overproduce the low column density tail of the distribution, like the regular runs do at redshift  $z = 1.5$ , but moving to lower redshift, the AGN feedback simulation follows all the other regular runs. Momentum-driven winds simulation reproduce best this statistics, therefore we used it to test a simple attempt of “varying” the UV background changing the constant factor that we use to rescale all the CIV optical depths. The effect on the column density distribution function is not very strong and does not help to solve the discrepancies between the real and the simulated distributions at the redshift considered.
- In the redshift range  $z = 2 - 3$ , our simulations fit the  $\Omega_{\text{CIV}}(z)$  evolution, but at lower redshift we found a decreasing trend (with the exception of the AGN feedback run, for the reasons explained in Session 4.5) at variance with the increasing trend shown by the observational data. We think that an updated version of the UV background used for this work (Haardt & Madau 1996) will be crucial to improve this result.
- At all the redshift considered, the CIV Doppler parameter distribution is in quite good agreement with the observational data, in the case of the regular runs. The pre-enriched simulation shows a marked excess of low Doppler parameter lines, while no feedback and AGN feedback simulations (the latter only at high redshift) result in distributions shifted towards higher  $b_{\text{CIV}}$  than the observed ones: this is because these runs basically produce too hot gas.
- The overall data distribution of the  $b_{\text{CIV}} - N_{\text{CIV}}$  relation is reproduced by our simulations, even if all of them present a clump of low column density systems with different Doppler parameters. We think that this effect is a numerical artifact introduced by VPFIT when placing the continuum level. Moreover the regular runs (and also the AGN feedback run at low redshift) show a plume of lines at high CIV column densities, for which the Doppler parameters increase as  $N_{\text{CIV}}$  increases: the sign of a well defined temperature-density relation for the high density gas.

In the future we will try to improve the CIV statistics by using a more physically motivated UV background that takes into account HeII reionization at  $z \sim 3$ . Furthermore, while the agreement is far from being perfect for the CIV statistics we will try to refine the metal distribution by including physical processes like turbulence, metal diffusion and radiative transfer, that can help in polluting with metals the low-density IGM. We also plan to improve the post-processing line-fitting analysis by removing the spurious numerical effects introduced by VPFIT.



# Chapter 5

## Conclusions

In this thesis work we investigated the chemical and physical evolution of the Intergalactic Medium. We used high-resolution and large box-size hydrodynamical cosmological simulations to explore the mechanisms responsible for the IGM metal enrichment and we proposed some physically motivated theoretical models and then compared the prediction of the models with the latest observational data. In the following the main conclusions of this work are reported.

### Feedback models

We focussed on two different types of enrichment: galactic (energy and momentum driven) winds produced by “starburst” galaxies at redshift  $z = 1.5 - 4$  and AGN feedback associated to the energy released by gas accretion onto super-massive black holes.

In Chapter 3 we compared the two distinct implementations (energy and momentum driven) of the galactic winds and also different choices for the winds strength, ranging from weak to strong winds. We found that in the weak wind case (energy-driven with wind velocity  $v_w = 100 \text{ km s}^{-1}$ ), feedback is not able to spread the gas around haloes, failing also to quench the star formation: all the gas is concentrated at high density and at relatively high temperature in the centre of the haloes. Instead in the strong winds case (energy-driven with wind velocity  $v_w = 100 \text{ km s}^{-1}$ ) the gas is expelled in a quite violent way and the shells of expanding material fragment (we recall that, in the energy-driven implementation, the wind velocity is set to a fixed value for every wind particle, regardless the mass of the haloes containing the particle itself). In this way the star formation is efficiently quenched, but the resulting enrichment is very patchy and inhomogeneous. With the momentum-driven winds implementation, in which the wind speed and mass load is related to the properties of the dark matter haloes, the situation is slightly improved: less gas is blown by the winds but in a more homogeneous way and also this implementation is more efficient in polluting the IGM above and around the mean density. Anyway some problems are still present when trying to fit the data. For example, with our best models for the galactic winds feedback (strong energy-driven and momentum-driven) we succeeded in reproducing many of the observed IGM properties and in particular those related to the DLAs and the CIV cosmic evolution, but currently we are not able to enrich uniformly the gas around haloes, at least at a level comparable with that suggested by the observations.

In Chapter 4 we considered also other feedback mechanisms such as the AGN feedback along with galactic winds. The AGN-feedback is very powerful at high redshift: black holes inject a

huge amount of energy to the surrounding particles, which leave the inner region of the haloes and heat efficiently the intergalactic gas. Even in this case and especially at lower redshift, when the AGN feedback efficiency decreases, the resulting enrichment is not as uniform as observations suggest and metals are present in clumps within the simulated cosmic volume.

To sum up, in our simulations the resulting IGM enrichment, far from a smooth metallicity pattern, consists of many small and isolated metal clumps located around haloes. Related to this, we fail in reproducing both the observed distribution of velocity widths of low ionization species (like SiII) and the metallicity-velocity width correlation. We also overproduce low column density systems in the CIV column density distribution function at redshift  $z = 1.5$ . However, when the IGM metallicity is a-posteriori smoothed over a scale of about 500 comoving kpc the observational properties are reasonably well reproduced.

Along with the well known problem of metal mixing in the SPH simulations, this could be a hint that there are some pieces of physics missing in our treatment, as we stated at the end of Chapter 3. For example in our simulations we did not consider the radiative transfer effects and the small-scale turbulence and its impact on the metal diffusion at large scales, that can be effective in smoothing the metal distribution around haloes. From this point of view the above smoothing scale of  $\sim 500$  kpc roughly corresponds to a velocity (in redshift space) of  $\sim 50 \text{ km s}^{-1}$ , values that are consistent with those presented in Scannapieco & Brügggen (2008). The accurate description of these phenomena could be important to improve the results and the physical consistency of our work.

### IGM global properties

The different feedback prescriptions that we explored give distinct predictions for the gas in the metallicity-temperature and density distributions. Strong energy-driven winds are effective in heating the gas particles at temperature of  $10^5$  K and the effect is even more dramatic in the presence of AGN feedback: this is because black holes release a large amount of energy in a relatively short time interval at around  $z \sim 3$ . This sudden energy release turns out to be much more efficient than winds to heat metal-enriched gas to high temperatures, thus displacing it from the haloes of star-forming regions to low-density regions. Once brought to high entropy by AGN feedback, this enriched gas is prevented from reaccreting into collapsed haloes at lower redshift. The star forming high-density tail is considerably more extended in the no feedback and weak winds case due to the small (or absent) efficiency of the feedback in quenching the star formation.

The metallicity-density relation at redshift  $z = 3$  is quite different for the momentum-driven winds simulation, with respect to all the other runs. In particular the metallicity reaches values slightly higher than the energy-driven case for strong and weak winds and for the whole range of densities and most importantly for this run there is much more enriched material around the mean density: this due to the fact that in the momentum-driven implementation even small haloes contribute significantly to the enrichment. In fact, such haloes have small velocity dispersion and correspondingly greater loading factor (see Equation (2.49)) for their winds than the massive ones. Otherwise strong winds and AGN feedback are more efficient than all the other simulations in polluting low-density IGM due to the stronger power of these feedback models.

For a fixed feedback prescription if we change the (Initial Mass Function) IMF, the evolution

with redshift of  $\Omega_{\text{OVI}}$  and  $\Omega_{\text{CIV}}$  remains the same while there are differences in the normalization. The Kroupa and Arimoto-Yoshii IMFs result in values for the CIV and OVI density that are respectively  $\sim 1.5$  and  $\sim 3$  times higher than the Salpeter case. This is due to the fact that Salpeter IMF results in an excess of low mass stars, Kroupa IMF produces a smaller number of massive stars than the other two but twice as many stars in the range of mass  $0.3M_{\odot} < m < 3M_{\odot}$ , while with the Arimoto-Yoshii (or “top-heavy”) IMF there is a larger contribution from massive stars (see Figure 2.2). For these reasons, the Arimoto-Yoshii IMF produces more oxygen and carbon, while the Salpeter IMF is less efficient in producing these metal species and Kroupa IMF is in between the other two. It is interesting to note that in the cosmic (or total) star formation history (see left panel of Figure 3.3) there are negligible differences between the three IMFs, at least at the relatively high redshift considered in this thesis. We stress that this is due to the fact that we neglected the effect of assuming different IMFs on the observationally inferred cosmic star formation rate. This means that we did not change the star formation efficiency as it would be required in order to match the observables when the number of massive stars per unit mass of formed stars changes since we were more interested in the chemical and energetic effect of the IMF.

## HI statistics and Damped Lyman- $\alpha$ systems

In Chapter 3 we showed that both the total HI cosmological density and the one recovered from DLAs column density distribution function change with the feedback prescription. The neutral hydrogen fraction is followed in the simulations self consistently with the assumed average ultra violet background and not rescaled a-posteriori using a different UVB. The HI content of the weak energy-driven winds simulation is considerably higher than that of the strong energy-driven and of the momentum-driven winds and this is due to the fact that in the weak winds run the gas is more concentrated in the potential wells of galaxies, where it can cool very efficiently, and thereby is significantly more neutral with respect to the other simulations.

Even the DLAs properties depend on the feedback models. In the weak winds simulation high column density gas is highly concentrated inside the central halo and inside some substructures. Also the column density values reached are higher than for the other runs. In the strong winds run, the gas is spread all around the central haloes and the substructures. Finally, considering HI column densities above the DLA limit of  $N_{\text{HI}} = 2 \times 10^{20} \text{ cm}^{-2}$ , we found that the central halo in the momentum-driven winds run has the largest cross-section. The DLA incidence rate is in good agreement with the observed one by Prochaska et al. (2005) from SDSS data for the strong and momentum-driven winds, while is larger for the weak winds run. The incidence rate results clearly show that all the haloes whose masses are above  $10^9 h^{-1} M_{\odot}$  contribute to the DLA cross-section: in agreement with Pontzen et al. (2008) findings but at variance with Barnes & Haehnelt (2009) results, which using a semi-analytical model claimed instead that, in order to reproduce the velocity widths distribution, the cross-section of haloes less massive than  $10^{10} h^{-1} M_{\odot}$  should be exponentially suppressed. The column density distribution function at  $z = 3$  is in rough agreement with the data points for strong and momentum-driven winds models, while at lower redshifts there are some differences and strong winds (weak winds) underpredicts (overpredicts) the number of DLAs. The weak winds run shows the largest discrepancies especially for the high column density DLAs, a feature that was already found by Nagamine et al. (2004). The contribution of haloes of masses between

$10^9 - 10^{10} h^{-1} M_\odot$  is particularly relevant for DLAs below  $N_{\text{HI}} \approx 10^{20.8} \text{ cm}^{-2}$ , another hint that less massive haloes contribute to reproduce DLAs statistical properties.

While the overall neutral hydrogen content of the simulations and the DLAs properties are sensitive to the feedback prescription, the situation is different when randomly oriented mock QSO spectra are extracted from the cosmological boxes. In this case we found the same result of Theuns et al. (2002): the statistics of HI are weakly affected by the feedback prescription. Both the HI column density distribution function and Doppler parameter probability distribution function do not change significantly when considering different feedback models. This is because the winds or black holes ejecta expand preferentially into the lower density regions and so keep the filaments that produce the hydrogen lines intact. Only very strong lines differ noticeably between the different runs, but this does not affect the statistics significantly. Anyway, our simulations reproduce very well all the HI statistics and this confirms that we are catching the physics of the gas traced by the neutral hydrogen. Moreover, we think that the remaining small discrepancies with the observational data are due to numerical effects introduced by the line-fitting software VPFIT.

### Cosmic evolution of CIV

In Chapter 4 we studied the cosmic evolution of the CIV (triply ionized carbon), which is considered the best tracer of the IGM metallicity. Differently from the HI, the CIV statistics do depend on feedback. In this respect we divided our simulations in two sets: “regular” and “non regular”. Regular runs are those in which the feedback prescriptions were already tested to be stable and physically reasonable, as for example the strong energy-driven or the momentum driven winds. Otherwise the “non regular” ones are those runs with new feedback models, like the AGN feedback, or runs which explore some extreme solutions as the pre-enriched or the no feedback runs.

At redshift  $z = 3$  and  $z = 2.25$  the regular runs fit well the low column density tail of the CIV column density distribution function, but fail to fit the data of D’Odorico et al. (2009) in the intermediate range of the distribution:  $12 < \log N_{\text{CIV}} < 13.5$ . The non regular runs always overproduce the low column density tail of the distribution, like the regular runs do at redshift  $z = 1.5$ , but moving to lower redshift, the AGN feedback simulation follows all the other regular runs. With the aim of improving the accord with the data, we tried a very simple attempt of “varying” the UV background changing the constant factor that we use to rescale all the CIV optical depths, but the effect on the column density distribution function is not very strong.

Our simulations fit the  $\Omega_{\text{CIV}}(z)$  evolution in the redshift range  $z = 2 - 3$ , but at lower redshift we found a decreasing trend (with the exception of the AGN feedback run) at variance with the increasing trend shown by the observational data. We think that an updated version of the UV background used for this work (Haardt & Madau 1996) will be crucial to improve this result.

As far the CIV Doppler parameter ( $b_{\text{CIV}}$ ) distribution function is concerned: at all the redshift considered our regular runs are quite in good agreement with the observational data of D’Odorico et al. (2009). The pre-enriched simulation shows a marked excess of low Doppler parameter lines, while no feedback and AGN feedback simulations (the latter only at high redshift) result in distributions shifted towards higher  $b_{\text{CIV}}$  than the observed ones, since these runs basically produce too hot gas.

Finally, the overall data distribution of the  $b_{\text{CIV}} - N_{\text{CIV}}$  relation is reproduced by our simulations, even if all of them present a clump of low column density systems with different Doppler parameters. Again, we think that this effect is a numerical artifact introduced by VPFIT. Moreover the regular runs (and also the AGN feedback run at low redshift) show a plume of lines at high CIV column densities, for which the Doppler parameters increase as  $N_{\text{CIV}}$  increases: the signature of a well defined temperature-density relation for the high density gas.

In conclusion, different feedback prescriptions impact largely on CIV statistics: AGN feedback and no feedback runs heat too much the gas (the latter more locally, producing a lot of small hot systems), while momentum-driven winds run reproduces best all the statistics. The accord of the CIV statistics with the observational data can be surely improved and for the future we plan to refine both our physical models (UV background and feedback prescriptions) and the post-processing analysis (line-fitting procedure with VPFIT).



# Appendix A

## First Principles

### A.1 Standard Model

Gravitation exerts the same force per unit mass on all bodies and the essence of the Einstein's General Theory of Relativity is to transform it from being a force to being a property of space-time. The interval between two events can be written as

$$ds^2 = g_{ij} dx^i dx^j, \quad (\text{A.1})$$

where repeated suffixes imply summation and  $i, j$  both run from 0 to 3:  $x^0 = ct$  is the time coordinate and  $x^1, x^2, x^3$  are space coordinates. The tensor  $g_{ij}$  is the *metric tensor* describing the space-time geometry.

One can show from simple geometrical considerations only (i.e. without making use of any field equations) that the most general space-time metric describing a universe in which the cosmological principle is obeyed is the Robertson-Walker ones:

$$ds^2 = (c dt)^2 - a^2(t) \left[ \frac{dr^2}{1 - Kr^2} + r^2(d\vartheta^2 + \sin^2\vartheta d\varphi^2) \right], \quad (\text{A.2})$$

where we have used spherical polar coordinates:  $r, \vartheta$  and  $\varphi$  are the comoving coordinates (these label observers who follow the Hubble expansion;  $r$  is by convention dimensionless),  $t$  is the proper time,  $a(t)$  is a function to be determined which has the dimensions of a length and is called *the cosmic scale factor* or the *expansion parameter*, the *curvature parameter*  $K$  is a constant which can be scaled in such a way it takes only the values 1 (close universe), 0 (flat universe) or -1 (open universe).

The Einstein equations (without the cosmological constant we will introduce in the next Section) are

$$R_{ij} - \frac{1}{2} g_{ij} R = \frac{8\pi G}{c^4} T_{ij}, \quad (\text{A.3})$$

where  $R_{ij}$  and  $R$  are, respectively, the Ricci tensor and Ricci scalar and  $T_{ij}$  is the energy-momentum tensor. In cosmology, the energy-momentum tensor which is of greatest relevance is that of a perfect fluid

$$T_{ij} = (p + \rho c^2) U_i U_j - p g_{ij}, \quad (\text{A.4})$$

where  $p$  is the pressure,  $\rho c^2$  is the energy density (which includes the rest-mass energy) and  $U_i$  is the fluid four-velocity

$$U_i = g_{ik} \frac{dx^k}{ds}. \quad (\text{A.5})$$

If the metric is of Robertson-Walker type, the Einstein Equations (A.3) then yield

$$\ddot{a} = -\frac{4\pi}{3}G \left( \rho + 3\frac{p}{c^2} \right) a, \quad (\text{A.6})$$

for the time-time component ( $i, j = 0$ ), and

$$a\ddot{a} + 2\dot{a}^2 + 2Kc^2 = 4\pi G \left( \rho - \frac{p}{c^2} \right) a^2, \quad (\text{A.7})$$

for the space-space components ( $i, j = 1, 2, 3$ ). The space-time components ( $i = 1, 2, 3, j = 0$  or  $j = 1, 2, 3, i = 0$ ) merely give  $0 = 0$ . Eliminating  $\ddot{a}$  from (A.6) and (A.7) we obtain:

$$\dot{a}^2 + Kc^2 = \frac{8}{3}\pi G \rho a^2. \quad (\text{A.8})$$

Eqs. (A.6) and (A.8) are called the *Friedmann equations* and allow to determine the temporal evolution of  $a(t)$ ,  $p(t)$  and  $\rho(t)$ , once is known the equation of state that connect pressure and density. In many cases of physical interest, the appropriate equation of state can be cast in the form

$$p = w\rho c^2, \quad (\text{A.9})$$

where the parameter  $w$  is a constant which lies in the range

$$0 \leq w \leq 1, \quad (\text{A.10})$$

often called the *Zel'dovich interval*. The  $w = 0$  case represents *dust* (pressureless material) and is also a good approximation to the behaviour of any form of non-relativistic fluid or gas. At the other extreme, a fluid of non-degenerate, ultrarelativistic particles in thermal equilibrium has an equation of state of the type

$$p = \frac{1}{3}\rho c^2. \quad (\text{A.11})$$

For instance, this is the case for a gas of photons. A fluid with an equation of state of this type is usually called a *radiative fluid*, though it may comprise relativistic particles of any form.

In reality, the Friedmann equations are not independent: the second can be recovered from the first if one takes the adiabatic expansion of the universe into account, i.e.

$$d(\rho c^2 a^3) = -p da^3. \quad (\text{A.12})$$

## A.2 The Cosmological Constant

Einstein formulated his theory of general relativity without a cosmological constant in 1916; at this time it was generally accepted that the Universe was static. A glance at the equation (A.6) shows that universes evolving according to this theory cannot be static, unless

$$\rho = -3\frac{p}{c^2}, \quad (\text{A.13})$$

in other words, either the energy density or the pressure must be negative. Given that this type of fluid does not seem to be physically reasonable, Einstein (1917) modified the Equation (A.3) by introducing the cosmological constant term  $\Lambda$ :

$$R_{ij} - \frac{1}{2} g_{ij} R - \Lambda g_{ij} = \frac{8\pi G}{c^4} T_{ij}. \quad (\text{A.14})$$

With an appropriate choice of  $\Lambda$ , one can obtain a static cosmological model. The Equation (A.14) can be written in a form similar to the Equation (A.3), by modifying the energy-momentum tensor

$$R_{ij} - \frac{1}{2} g_{ij} R = \frac{8\pi G}{c^4} \tilde{T}_{ij}, \quad (\text{A.15})$$

with  $\tilde{T}_{ij}$  formally given by:

$$\tilde{T}_{ij} = T_{ij} + \frac{\Lambda c^4}{8\pi G} g_{ij} = -\tilde{p} g_{ij} + (\tilde{p} + \tilde{\rho} c^2) U_i U_j, \quad (\text{A.16})$$

where the effective pressure  $\tilde{p}$  and the effective density  $\tilde{\rho}$  are related to the corresponding quantities for a perfect fluid by

$$\tilde{p} = p - \frac{\Lambda c^4}{8\pi G}, \quad (\text{A.17})$$

$$\tilde{\rho} = \rho + \frac{\Lambda c^2}{8\pi G}. \quad (\text{A.18})$$

From these relations results that  $|\Lambda|^{-1/2}$  has the dimensions of a length. One can then show, for a universe described by the Robertson-Walker metric, we can get equations which are analogous to Eqs. (A.6) and (A.8), respectively:

$$\ddot{a} = -\frac{4\pi}{3} G \left( \tilde{\rho} + 3\frac{\tilde{p}}{c^2} \right) a, \quad (\text{A.19})$$

$$\dot{a}^2 + K c^2 = \frac{8}{3} \pi G \tilde{\rho} a^2. \quad (\text{A.20})$$

These equations admit a static solution for

$$\tilde{\rho} = -3\frac{\tilde{p}}{c^2} = \frac{3Kc^2}{8\pi G a^2}. \quad (\text{A.21})$$

For a “dust” universe ( $p = 0$ ), which is a good approximation to our Universe at present time, Equations (A.17), (A.18) and (A.21) give

$$\Lambda = \frac{K}{a^2}, \quad (\text{A.22})$$

$$\rho = \frac{Kc^2}{4\pi G a^2}. \quad (\text{A.23})$$

Since  $\rho > 0$ , we must have  $K = 1$  and therefore  $\Lambda > 0$ . The value of  $\Lambda$  which makes the universe static is just

$$\Lambda_E = \frac{4\pi G \rho}{c^2}. \quad (\text{A.24})$$

The model just described is called the *Einstein universe*. This universe is static (but unfortunately unstable, as one can show), has positive curvature and curvature radius

$$a_E = \Lambda_E^{-1/2} = \frac{c}{(4\pi G \rho)^{1/2}}. \quad (\text{A.25})$$

After the discovery of the expansion of the Universe in the late 1920s (Hubble 1929) there was no longer any reason to seek static solutions to the field equations. The motivation which had led Einstein to introduce his cosmological constant term therefore failed. Since then, however,  $\Lambda$  has not

died but has been the subject of much interest and serious study on both conceptual and observational grounds.

Today the cosmological constant is invoked to explain the accelerated expansion of the Universe, inferred by detailed analysis of the CMB fluctuations, the large scale structure of the galaxy distribution and observations of supernovae type Ia. Practically the cosmological constant can be treated as a fluid with equation of state

$$p = -\rho c^2 \quad (\text{A.26})$$

i.e. with  $w = -1$ , and its physical meaning is often associated with the energy of the vacuum (even if the nature of the cosmological constant is an hardly debated open problem).

To conclude, solving Eqs. (A.19) and (A.20) gives

$$\ddot{a} = -\frac{4\pi}{3}G\left(\rho + 3\frac{p}{c^2}\right)a + \frac{\Lambda c^2 a}{3}, \quad (\text{A.27})$$

$$\dot{a}^2 + Kc^2 = \frac{8\pi G}{3}\rho a^2 + \frac{\Lambda c^2 a^2}{3}. \quad (\text{A.28})$$

Now considering only the  $p$  and  $\rho$  terms, Equation (A.28) can be rewritten, in the case  $a = a_0$  (i.e. at the reference time  $t_0$ , usually taken as the present time), as:

$$\left(\frac{\dot{a}_0}{a_0}\right)^2 - \frac{8\pi}{3}G\rho\left(\frac{a_0}{a_0}\right)^2 = H_0^2\left(1 - \frac{\rho_0}{\rho_{0c}}\right) = H_0^2(1 - \Omega_0) = -\frac{Kc^2}{a_0^2}, \quad (\text{A.29})$$

where  $H_0 = \dot{a}_0/a_0$  is the *Hubble constant*,  $\Omega_0$  is the *density parameter*, both considered at the present day, and

$$\rho_{0c} = \frac{3H_0^2}{8\pi G}, \quad (\text{A.30})$$

is the (present) *critical density*, i.e the density for which the curvature parameter  $K$  is equal to zero, and therefore the universe is flat. If we ignore the original terms in  $p$  and  $\rho$  and we consider only the cosmological constant term we obtain:

$$\left(\frac{\dot{a}_0}{a_0}\right)^2 - \frac{\Lambda c^2}{3} = H_0^2\left(1 - \frac{\Lambda}{\Lambda_c}\right) = H_0^2(1 - \Omega_{0\Lambda}) = -\frac{Kc^2}{a_0^2}. \quad (\text{A.31})$$

In this case the “critical” value is

$$\Lambda_c = \frac{3H_0^2}{c^2}, \quad (\text{A.32})$$

so that:  $\Omega_{0\Lambda} = \Lambda c^2/3H_0^2$ . If we now reinstate the “ordinary” matter we began with, we can see that the curvature is zero as long as  $\Omega_{0\Lambda} + \Omega_0 = 1$ . The cosmological constant therefore breaks the relationship between the matter density and the curvature. Even if  $\Omega_0 < 1$ , a suitably chosen value of  $\Omega_{0\Lambda} = 1 - \Omega_0$  can be invoked to ensure flat space sections.

### A.3 Dark Matter

A lot of evidence indicate that the ordinary baryonic “visible” matter is only a tiny fraction of the matter content of the Universe. The predominant matter component in the Universe is in fact the so called *dark matter*. With “dark” is intended that this kind of matter does not take part into radiative process and therefore its presence is only detectable by means of gravitational

phenomena. The existence of the dark matter is invoked to reconcile the low value of the baryon density parameter  $\Omega_{\text{ob}} < 0.12$ , predicted by the Big Bang nucleosynthesis and measured to high precision by the Wilkinson Microwave Anisotropy Probe (WMAP) experiment<sup>1</sup> ( $\Omega_{\text{ob(WMAP)}} = 0.0441 \pm 0.0030$ , Hinshaw et al. 2009), to the “dynamical” one,  $\Omega_{0\text{m(dyn)}} \approx 0.3$ , recovered from the mass estimates of spiral galaxies and clusters of galaxies. Basically the high rotation velocities of the spirals and the high orbital velocities of the galaxies inside the clusters require for these systems gravitational fields (and therefore total masses) much higher than the ones obtained taking into account only the contribution of the visible baryonic matter. Since baryons alone cannot give  $\Omega_{0\text{m}} \approx 0.3$ , due to the upper limits given by the cosmological nucleosynthesis, it is commonly assumed that the missing part is in the form of a non baryonic dark component and that this component is gravitationally dominant.

In the last years, the improvement of the theoretical models and the needs to reproduce correctly the observational data, have lead to the definition of the specific characteristics that dark matter should have. For this reason we considered only *non-collisional*, *non-baryonic* and *cold* dark matter (CDM). “Cold” means that the dark matter particles are non relativistic at any epochs of cosmological interest. “Non-collisional” means that the motion of these particles is determined only by the average gravitational field and therefore the cross-section for the elastic collisions between particles is negligible (differently than the case of a perfect gas, in which the microscopic motion is governed by the collisions). Finally, “non-baryonic” means that the particles are of exotic origin and belong to the fauna of elementary particles predicted by the supersymmetric field theory. Lately the most promising candidate seems to be the neutralino, a particle which mass is of the order of 100 GeV.

## A.4 Structure formation and evolution

In the gravitational instability scenario of structure formation, cosmological structures grow from smaller structures through gravity. The growth of structures is governed by the coupled gravity-fluid equations describing both the collisionless gravitating matter component and the collisional baryonic component. Because of the enormous change in spatial scales as the Universe expands, it is most convenient to solve the equations in a frame comoving with the expansions (Peebles 1993). The physical position  $\mathbf{r}$  and velocity  $\mathbf{u}$  are then expressed in terms of the comoving position  $\mathbf{x}$  and peculiar velocity  $\mathbf{v}$  according to

$$\mathbf{r} = a(t)\mathbf{x}, \quad \mathbf{u} = \dot{\mathbf{r}} = \dot{a}\mathbf{x} + \mathbf{v}, \quad (\text{A.33})$$

where  $\mathbf{v} = a\dot{\mathbf{x}}$  and  $a(t) = 1/(1+z)$  is the cosmological expansion factor corresponding to the cosmological epoch at the redshift<sup>2</sup>  $z$ .

The dynamical equations for the dark matter component are

$$\frac{d\mathbf{x}_d}{dt} = \mathbf{v}_d(\mathbf{x}, t), \quad (\text{A.34})$$

$$\frac{d\mathbf{v}_d(\mathbf{x}, t)}{dt} + \frac{\dot{a}}{a}\mathbf{v}_d = -\frac{1}{a}\nabla\phi(\mathbf{x}, t), \quad (\text{A.35})$$

where  $\phi(\mathbf{x}, t)$  is the gravitational potential, and the gradient is with respect to the comoving coordinate

<sup>1</sup><http://map.gsfc.nasa.gov>

<sup>2</sup>We define the redshift of a luminous source, such as a distant galaxy, by the quantity  $z = \frac{\lambda_0 - \lambda_e}{\lambda_e}$ , where  $\lambda_0$  is the wavelength of radiation from the source observed at 0 at time  $t_0$  and emitted ( $\lambda_e$ ) by the source at some earlier time  $t_e$ .

system. The fluid equations expressing mass and momentum conservation are

$$\frac{\partial \rho(\mathbf{x}, t)}{\partial t} + 3\frac{\dot{a}}{a}\rho + \frac{1}{a}\nabla \cdot [\rho(\mathbf{x}, t)\mathbf{v}(\mathbf{x}, t)] = 0, \quad (\text{A.36})$$

$$\begin{aligned} \frac{\partial \mathbf{v}(\mathbf{x}, t)}{\partial t} + \frac{\dot{a}}{a}\mathbf{v}(\mathbf{x}, t) + \frac{1}{a}[\mathbf{v}(\mathbf{x}, t) \cdot \nabla]\mathbf{v}(\mathbf{x}, t) = \\ -\frac{1}{\rho a}\nabla p(\mathbf{x}, t) - \frac{1}{a}\nabla \phi(\mathbf{x}, t), \end{aligned} \quad (\text{A.37})$$

where  $\rho(\mathbf{x}, t)$  and  $p(\mathbf{x}, t)$  are the gas density and pressure at  $\mathbf{x}$  and at cosmological time  $t$ . Finally, in the presence of heat transfer at the rate  $(G - L)/n$  per particle, where  $G$  and  $L$  are, respectively, the thermal gain and loss functions per volume and  $n$  is the particle density, the second law of thermodynamics requires the entropy per particle  $s$  to change at the rate

$$\frac{\partial s}{\partial t} + \frac{1}{a}[\mathbf{v}(\mathbf{x}, t) \cdot \nabla]s = \frac{1}{nT}(G - L), \quad (\text{A.38})$$

where  $T$  is the temperature of the system. For an ideal gas, the entropy per particle is  $s = (\gamma - 1)^{-1}k_B \ln(p/\rho^\gamma) + s_0$ , where  $p$  is the gas pressure,  $\rho$  is the mass density,  $\gamma$  is the ratio of specific heats at constant pressure to constant volume ( $\gamma = 5/3$  for a monoatomic gas),  $k_B$  is the Boltzmann's constant and  $s_0$  is an arbitrary additive constant.

The dark matter and fluid are coupled through Poisson's equation for the gravitational potential

$$\nabla^2 \phi = 4\pi G a^2 [\rho_{\text{tot}}(\mathbf{x}, t) - \langle \rho_{\text{tot}} \rangle], \quad (\text{A.39})$$

where  $\rho_{\text{tot}} = \rho_d + \rho$  is the total mass density of the dark matter and fluid combined,  $\langle \rho_{\text{tot}} \rangle$  is the spatial average of  $\rho_{\text{tot}}$  over the Universe and  $p \ll (\rho_{\text{tot}} - \langle \rho_{\text{tot}} \rangle)c^2$  has been assumed. In terms of the present day matter closure parameter  $\Omega_{0m}$ ,  $\langle \rho_{\text{tot}} \rangle = 3H_0^2 \Omega_{0m} / (8\pi G a^3)$ . Eqs. (A.34), (A.35), (A.36), (A.37) and (A.39) are valid for any Friedman-Robertson-Walker universe, including those with non-zero vacuum energy (such an effective cosmological constant).

These are the same equations that describe the mix of dark matter, baryons and radiation that give rise to the CMB except for the addition of the radiation energy density and pressure. The principal difference is that while the density fluctuations are linear for the CMB up to the time the baryons begin to recombine and decouple from the radiation, the description of the growth of cosmological structures extends the computations of the fluctuations into the non-linear regime. Numerical solutions to Eqs. (A.34), (A.35), (A.36), (A.37) and (A.39) generally begin at a sufficiently high redshift that the primordial density fluctuations are still linear on the scales of interest, but after the matter and radiation have decoupled.

No structures will form unless the matter is initially inhomogeneous. The inhomogeneity is usually specified in terms of a primordial power spectrum of matter fluctuations, which is the ensemble average of the squared modulus of the Fourier modes of the density field. The mass density expanded in Fourier modes within a periodic Cartesian volume  $V_{\text{box}}$  may be expressed as

$$\rho(\mathbf{x}, t) = \langle \rho \rangle \left[ 1 + \sum_{\mathbf{k} \neq 0} \delta_{\mathbf{k}}(t) \exp(-i\mathbf{k} \cdot \mathbf{x}) \right], \quad (\text{A.40})$$

where the Fourier amplitudes  $\delta_{\mathbf{k}}(t)$  are assumed to have random phases and to be distributed according to a gaussian random process. The power spectrum, which quantifies the amplitude of the density fluctuations, may be defined as  $P(k) = V_{\text{box}} \langle |\delta_{\mathbf{k}}|^2 \rangle$ , where the average is over independent statistical realizations of the Fourier amplitudes.

The real space analogue of the power spectrum is the spatial correlation function  $\xi(r)$  of the density field

$$\langle \rho(\mathbf{x}' + \mathbf{x})\rho(\mathbf{x}') \rangle = \langle \rho \rangle^2 [1 + \xi(\mathbf{x})], \quad (\text{A.41})$$

where the average is carried out over all spatial locations  $\mathbf{x}'$ . The correlation function is related to the power spectrum through a Fourier transform

$$\xi(\mathbf{x}) = \frac{1}{(2\pi)^3} \int P(k) \exp(-i\mathbf{k} \cdot \mathbf{x}) d^3k. \quad (\text{A.42})$$

It is convenient to define the amplitude of density fluctuations

$$\Delta^2(k) = \frac{k^3}{2\pi^2} P(k). \quad (\text{A.43})$$

The amplitude of mass fluctuations  $(\delta M/M)^2$  in a sphere of radius  $r_f$  is then given by

$$\sigma_{r_f}^2 = \int_0^\infty \Delta^2(k) \left[ \frac{3j_1(kr_f)}{kr_f} \right]^2 \frac{dk}{k}, \quad (\text{A.44})$$

where  $j_1(x) = (\sin x)/x^2 - (\cos x)/x$  is a spherical Bessel function. A common fiducial normalization measure is the mass fluctuation  $\sigma_8$  filtered on a scale of  $r_f = 8 h^{-1}$  Mpc, where  $h = H_0/100 \text{ km s}^{-1} \text{ Mpc}^{-1}$ . The spectrum of matter fluctuations may be expressed in the form

$$\Delta^2(k, z) = \delta_H^2 \left( \frac{ck}{H_0} \right)^{3+n_s} \frac{D^2(z)}{D^2(0)} T^2(k), \quad (\text{A.45})$$

where  $T(k)$  is the transfer function describing the evolution of density perturbations as they cross the present day horizon scale with amplitude  $\delta_H$ ,  $n_s$  is the spectral index and  $D(t) = (\dot{a}/a) \int^a da/\dot{a}^3$  is the growth factor for the density perturbations. The transfer function for a Cold Dark Matter dominated universe was first computed by Peebles (1981).

## A.5 $\Lambda$ CDM model

Throughout this thesis work we adopted a  $\Lambda$ CDM model, dominated at low redshift by the cosmological constant and in which, as we just stated, dark matter is composed of cold, weakly interacting, massive particles. The cosmological model is completely defined once the value of the following parameters is specified: the present day adimensional density of the universe,  $\Omega_0 = \Omega_{0m} + \Omega_{0\Lambda}$  (where  $\Omega_{0m}$  and  $\Omega_{0\Lambda}$  are the contribution from matter and vacuum, respectively), the Hubble constant,  $H_0 = 100 h \text{ km s}^{-1} \text{ Mpc}^{-1}$ , the (present day) adimensional baryon density,  $\Omega_{0b}$ , the just quoted root mean square of the mass fluctuations on  $8 h^{-1}$  Mpc scale,  $\sigma_8$ , and the spectral index of the primordial density fluctuations,  $n_s$ . Recent observations have set stringent constraints on the values allowed for these parameters and in the thesis we used the following:

- $\Omega_{0m} = 0.24$
- $\Omega_{0b} = 0.0413$
- $\Omega_{0\Lambda} = 0.76$
- $n_s = 0.96$

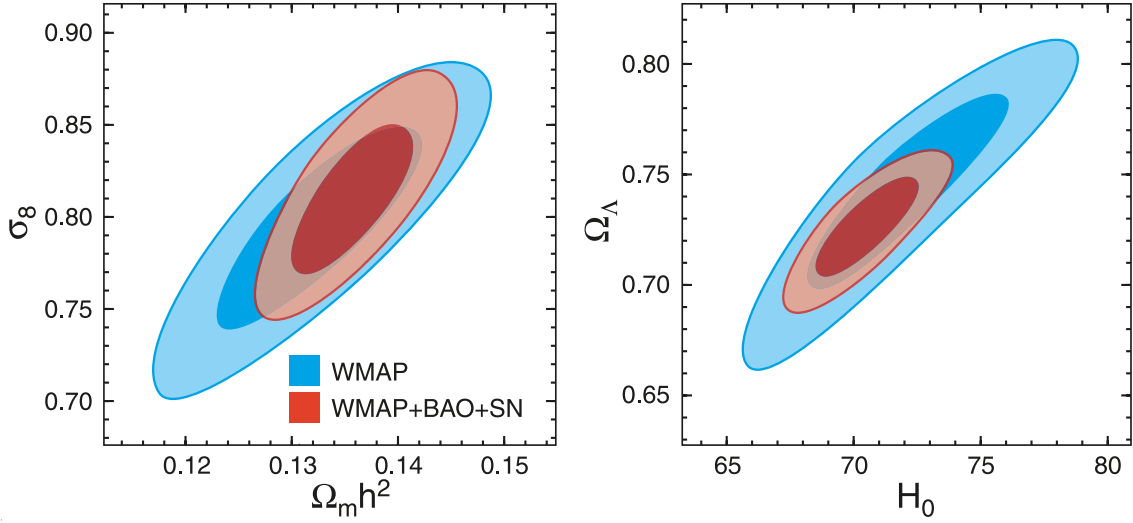


Figure A.1: Four representative cosmological parameters that have improved significantly using WMAP five-year data along with the Baryonic Acoustic Oscillations (BAO) and Supernovae (SN) data. The contours show the 68% and 95% confidence levels. The WMAP-only constraint is shown in blue, while WMAP+BAO+SN in red. *Left panel:*  $\sigma_8 - \Omega_{\text{m}} h^2$  constraint. *Right panel:*  $\Omega_{0\Lambda} - H_0$  constraint. From Komatsu et al. (2009).

- $H_0 = 73 \text{ km s}^{-1} \text{ Mpc}^{-1}$
- $\sigma_8 = 0.8$

which are in agreement with the latest results from large scale structure observables such as the CMB, weak lensing, the Lyman- $\alpha$  forest and the evolution of mass function of galaxy clusters (Lesgourgues et al. 2007; Komatsu et al. 2009, see Figure A.1; Vikhlinin et al. 2009). With the cosmology fixed we focussed on the astrophysics.

# List of Figures

1.1	Illustrative example of high redshift QSO spectrum with both hydrogen (blueward, i.e. at lower redshifts, of the Lyman- $\alpha$ emission of the quasar) and metal (redward of the Lyman- $\alpha$ emission) absorption lines. . . . .	16
1.2	Distribution of Lyman- $\alpha$ forest column densities with fits for different ranges, for absorption systems in the redshift range $0.5 < z < 1.9$ . For $12.90 < \log N_{\text{HI}} < 15.70$ , $\beta = 1.60 \pm 0.03$ . For $12.90 < \log N_{\text{HI}} < 17.20$ , $\beta = 1.59 \pm 0.02$ . Here $f$ is the number of absorption systems per unit column density and per unit of absorption distance. From the work by Janknecht et al. (2006), where the authors used high-resolution ( $R \geq 30000$ ) UV (STIS) and optical (VLT/UVES and Keck/HIRES) spectra of nine bright quasars with $z_{\text{em}} < 1.94$ . . . . .	19
1.3	Distribution of the Lyman- $\alpha$ Doppler parameters in intervals $\Delta b = 5 \text{ km s}^{-1}$ , varying redshift ranges. Data are the same of Figure 1.2, from Janknecht et al. (2006). CANDALF was used for the analysis of all quasar spectra except for HE 0515-4414. The lines found in the HST/STIS and VLT/UVES spectra of HE 0515-4414 were fit with the MIDAS software package FITLYMAN (Fontana & Ballester 1995). . . . .	20
1.4	Evolution of the number density of Lyman- $\alpha$ systems with $13.10 < \log N_{\text{HI}} < 14.00$ , including best-fits to the solid and open circles over the ranges indicated, as represented by the solid and dashed lines, respectively, taking $dN/dz \propto (1+z)^\gamma$ . The dotted line extrapolates the lower redshift fit to $z = 0$ . From Janknecht et al. (2006). . . . .	22
1.5	Evolution of the number density of Lyman- $\alpha$ systems with $\log N_{\text{HI}} > 13.64$ , including best-fits to the solid and open circles over the ranges indicated, as represented by the solid and dashed lines, taking $dN/dz \propto (1+z)^\gamma$ . The additional low redshift dashed line is the best fit to the open triangles. The open square, left-pointing solid triangle, and stars correspond to systems with $\log N_{\text{HI}} > 14.00$ . From Janknecht et al. (2006). . . . .	22
1.6	Best fit to the flux PDF for the two fiducial models (continuous blue and dashed green lines) of Viel et al. (2009), in the three redshift bins at $\langle z \rangle = (2.07, 2.52, 2.94)$ . Data used for these investigations consist mainly of two kinds of sets of quasars spectra: the Sloan Digital Sky Survey low-resolution, low signal-to-noise ratio sample, and UVES/VLT or HIRES/KECK samples of high-resolution spectra. From Viel et al. (2009). . . . .	24
1.7	Example Voigt profile fits to two DLAs of the sample from Prochaska et al. (2003). In the y-axis is shown the relative flux. The vertical dashed line indicates the line centroid determined from metal-line transitions identified outside the Lyman- $\alpha$ forest. The dotted line traces the continuum of the QSO and the green and red lines trace the Voigt profile solution and the fits corresponding to $1\sigma$ changes to $N_{\text{HI}}$ . The fluctuations at the bottom of the damped Lyman- $\alpha$ absorption troughs indicate the level of sky noise. . . . .	27

2.1	Cooling rates as a function of temperature for a primordial composition gas (H + He) in collisional equilibrium (for this plot $\Lambda = C$ , see Eq. (2.31), and H=HI, He=HeI, He <sup>+</sup> =HeII). Heavy solid line shows the total cooling rate. The cooling is dominated by collisional excitation (short-dashed line) at low temperatures and by free-free emission (thin solid line) at high temperatures. Long-dashed and dotted lines show the contributions of recombination and collisional ionization, respectively. From Katz et al. (1996b). . . . .	51
2.2	The dependence of the shape of the IMF on the stellar mass, relative to the Salpeter (1955) IMF. Blue dot-dashed and red dashed curves are for the IMF by Arimoto & Yoshii (AY, 1987) and by Kroupa (2001), respectively. The horizontal black solid line indicates for reference the Salpeter IMF. . . . .	59
2.3	Temperature-density distribution at $z = 3$ for one of our simulations with $5 h^{-1}$ comoving Mpc box size, $2 \times 64^3$ (gas + dark matter) particles and momentum-driven winds feedback. Only 1/3 of the particles are plotted. . . . .	63
2.4	Gas density maps at $z = 3$ for two of our simulations with $10 h^{-1}$ comoving Mpc box size, $2 \times 320^3$ (gas + dark matter) particles and energy-driven winds of 600 km s <sup>-1</sup> (strong winds, <i>upper panel</i> ) and 100 km s <sup>-1</sup> (weak winds, <i>lower panel</i> ). . . . .	65
3.1	Gas (IGM) temperature-density relation (without explicitly splitting the star-forming particles in the hot and the cold phases), for the WW (Weak galactic energy-driven Winds of 100 km/s; upper left panel), SW (Strong galactic energy-driven Winds of 600 km/s; upper right panel) and MDW (Momentum-Driven galactic Winds; lower panel) simulations at $z = 3$ . The vertical bar indicates the gas mass fraction. . . . .	71
3.2	Gas (IGM) metallicity-density relation (without explicitly splitting the star-forming particles in the hot and the cold phases), for the WW (Weak galactic Winds of 100 km/s; upper left panel), SW (Strong galactic Winds of 600 km/s; upper right panel) and MDW (Momentum-Driven galactic Winds; lower panel) simulations at $z = 3$ . The vertical bar indicates the gas mass fraction. . . . .	72
3.3	<i>Left Panel:</i> cosmic star formation rate (SFR) for some of the hydrodynamical simulations of Table 3.1. <i>Right Panel:</i> evolution of the total $\Omega_{\text{HI}}$ ( $\times 1000$ ) as a function of redshift for some of the hydrodynamical simulations of Table 3.1. . . . .	74
3.4	Evolution of the total $\Omega_{\text{CIV}}$ (upper panels) and the total $\Omega_{\text{OVI}}$ (lower panels) as a function of redshift for some of the hydrodynamical simulations of Table 3.1. <i>Left Panels:</i> effect of different wind strengths and implementations. <i>Middle Panels:</i> effect of different IMFs. <i>Right Panels:</i> resolution tests. . . . .	76
3.5	Differential halo mass function (number of haloes of a given mass per unit mass [ $h^{-1}M_{\odot}$ ] and per unit volume [ $\text{Mpc}^3/h^3$ ]) for runs SW, SW <sub>5,320</sub> , SW <sub>20,512</sub> at redshift $z = 3$ , compared with Sheth & Tormen (1999) prediction. . . . .	79
3.6	HI column density maps in a slice around the same massive halo in the WW (upper left panel), SW (upper right panel) and MDW (lower panel) runs at $z = 3$ . . . . .	80
3.7	Star formation rates (in $M_{\odot}$ per year) plotted as a function of halo mass for SW, WW and MDW runs at $z = 3$ . . . . .	81
3.8	Mean total metallicity in solar unit plotted as a function of halo mass for SW, WW and MDW runs at $z = 3$ . . . . .	82
3.9	Mean neutral fraction of hydrogen (HI/H) plotted as a function of halo mass for SW, WW and MDW runs at $z = 3$ . . . . .	82

3.10	Triangles represent the DLA cross-sections (in comoving units) as a function of the total halo mass for the SW run at $z = 2.25, 3, 4$ . The overplotted lines show power-law fits, of the form $\log \sigma_{\text{DLA}} = \alpha(\log M_{\text{tot}} - 12) + \beta$ , to the data points for the SW itself (dashed black line), WW (dot-dashed blue line) and MDW (triple-dot-dashed cyan line) runs. The continuous red lines in the middle panel fit the upper and lower envelopes of the SW distribution at $z = 3$ . . . . .	85
3.11	Cumulative abundance of DLAs per unit redshift as a function of total halo mass for the SW (dashed black line), WW (dot-dashed blue line) and MDW (triple-dot-dashed cyan line) runs at redshift $z = 3$ . The continuous red lines show the results considering the scatter (in a conservative way) in the cross-section vs mass relation for the SW run. The red shaded region indicates the observed cumulative DLA abundance of Prochaska et al. (2005) from SDSS data. . . . .	86
3.12	<i>Left Panel:</i> HI column density distribution function at $z = 3$ for the SW (dashed black line), WW (dot-dashed blue line), SW <sub>20,512</sub> (dotted red line) and MDW (triple-dot-dashed cyan line) runs. <i>Right Panel:</i> Contribution to the HI column density distribution function from haloes of different mass in the SW <sub>20,512</sub> run at $z = 3$ . Cyan triple dot-dashed line refers to haloes with mass in the range $10^9 - 10^{10} h^{-1} M_{\odot}$ , orange dot-dashed line refers to haloes with mass in the range $10^{10} - 10^{11} h^{-1} M_{\odot}$ , red dotted line refers to haloes with mass greater than $10^{11} h^{-1} M_{\odot}$ while black dashed line refers to all haloes. In both the panels the overplotted black diamonds and the solid line show the data points and the fit of Prochaska et al. (2005). . . . .	88
3.13	<i>Left Panel:</i> HI column density distribution function at $z = 2.25$ for the SW (dashed black line), WW (dot-dashed blue line) and MDW (triple-dot-dashed cyan line) runs. Overplotted black diamonds and solid line show the data points and the fit of Prochaska et al. (2005). Run SW <sub>20,512</sub> is not present here because this simulation was stopped at $z_{\text{f}} = 3$ . <i>Right Panel:</i> the same as the left panel but at redshift $z = 4$ . Dotted red line refers to the SW <sub>20,512</sub> run. . . . .	88
3.14	Redshift evolution of $\Omega_{\text{DLA}}$ for the SW (black solid line), WW (blue dotted line) and MDW (cyan triple-dot-dashed line) runs. Overplotted are the result of Pontzen et al. (2008) (green cross) and the observational estimate of Prochaska et al. (2005) (red diamonds) and Péroux et al. (2005) (orange triangles). . . . .	90
3.15	Comparison of physical quantities extracted from three simulated LOSs passing through the center of mass of the second most massive halo for the SW (solid black line), WW (dashed blue line) and MDW (dotted red line) runs at $z = 3$ . From top to bottom the figure shows: total gas density [ $n_{\text{H}}/\text{cm}^3$ ], HI density [ $n_{\text{H}}/\text{cm}^3$ ], total metallicity (in solar unit), temperature [K] and peculiar velocity field [km/s]. . . . .	92
3.16	<i>Left Panel:</i> DLAs velocity width distribution in runs SW <sub>20,512</sub> (dotted red line), WW (dot-dashed blue line), MDW (triple-dot-dashed cyan line) and SW <sub>20,512</sub> <i>smoothed</i> (solid black line) at $z = 3$ . <i>Right Panel:</i> DLAs velocity width distribution in runs SW <sub>20,512</sub> - $\tau_{\text{HI}}$ (solid red line), WW- $\tau_{\text{HI}}$ (solid blue line), MDW- $\tau_{\text{HI}}$ (solid cyan line) and SW <sub>20,512</sub> <i>smoothed</i> (solid black line) at $z = 3$ . In both the panels the overplotted black diamonds show the observational data of Prochaska et al. (2008). . . . .	94

3.17	Contribution to the DLAs velocity width distribution from haloes of different mass in runs SW <sub>20,512-<math>\tau_{\text{HI}}</math></sub> (solid + dashed red lines), WW- $\tau_{\text{HI}}$ (solid + dashed blue lines), MDW- $\tau_{\text{HI}}$ (solid + dashed cyan lines) at $z = 3$ . For the different runs, dashed lines refer to haloes with mass lower than $10^{10.5} h^{-1} M_{\odot}$ and solid lines refer to haloes with mass greater than $10^{10.5} h^{-1} M_{\odot}$ . The overplotted black diamonds show the observational data of Prochaska et al. (2008). . . . .	95
3.18	<i>Left Panel:</i> relationship between metallicity and SiII velocity width of individual sightlines through haloes in MDW- $\tau_{\text{HI}}$ (green solid squares) and SW <sub>20,512smoothed</sub> (red solid diamonds) at $z = 3$ , compared to the observational data by Prochaska et al. (2008) (black crosses). <i>Right Panel:</i> relationship between metallicity and SiII velocity width of individual sightlines through haloes with masses $M > 10^{10.5} h^{-1} M_{\odot}$ (red solid diamonds), $M > 10^{10} h^{-1} M_{\odot}$ (green solid squares) and $M > 10^{9.5} h^{-1} M_{\odot}$ (blue solid triangles) in MDW- $\tau_{\text{HI}}$ run at $z = 3$ , compared to the observational data by Prochaska et al. (2008) (black crosses). . . . .	97
4.1	<i>Left panel:</i> CIV ionization fraction, as a function of the gas overdensity, at $z = 3$ for a gas temperature of $10^{4.6}$ K. <i>Right panel:</i> CIV ionization fraction, as a function of the gas temperature, at $z = 3$ for an overdensity of $\delta_{\text{gas}} \sim 50$ . . . . .	106
4.2	HI column density distribution function at $z = 3$ . <i>Left panel:</i> part I. <i>Right panel:</i> part II. Data from Kim et al. (2007). . . . .	107
4.3	HI column density distribution function at $z = 2.25$ . <i>Left panel:</i> part I. <i>Right panel:</i> part II. Data from Kim et al. (2007). . . . .	108
4.4	$b_{\text{HI}}$ probability distribution function at $z = 3$ . <i>Left panel:</i> part I. <i>Right panel:</i> part II. In both panels, data from Kim et al. (2007) are showed by the purple solid line. . . . .	110
4.5	$b_{\text{HI}}$ probability distribution function at $z = 2.25$ . <i>Left panel:</i> part I. <i>Right panel:</i> part II. In both panels, data from Kim et al. (2007) are showed by the purple solid line.. . . .	110
4.6	$b_{\text{HI}} - N_{\text{HI}}$ relation at $z = 3$ . The overplotted purple diamonds in upper left panel show the observational data of Kim et al. (2007). . . . .	111
4.7	$b_{\text{HI}} - N_{\text{HI}}$ relation at $z = 2.25$ . The overplotted purple diamonds in upper left panel show the observational data of Kim et al. (2007). . . . .	112
4.8	CIV column density distribution function at $z = 3$ . <i>Left panel:</i> part I. <i>Right panel:</i> part II. Data from D’Odorico et al. (2009). . . . .	113
4.9	CIV column density distribution function at $z = 2.25$ . <i>Left panel:</i> part I. <i>Right panel:</i> part II. Data from D’Odorico et al. (2009). . . . .	114
4.10	CIV column density distribution function at $z = 1.5$ . <i>Left panel:</i> part I. Run S1 (pre-enriched) is not present here because this simulation was stopped at $z_{\text{f}} = 1.8$ . <i>Right panel:</i> part II. Data from D’Odorico et al. (2009). . . . .	115
4.11	CIV column density distribution functions at $z = 3$ ( <i>left panel</i> ), 2.25 ( <i>middle panel</i> ) and 1.5 ( <i>right panel</i> ) for the B6 (momentum-driven winds) run. In each panel solid blue line refers to the original run while the dashed and dotted blue lines were calculated rescaling all the optical depths for, respectively, the upper and the lower limit of the Kim et al. (2007) fitting formula for the HI effective optical depth $\tau_{\text{HI}}^{\text{eff}}$ , Eq. (4.3). The black diamonds show the observational data of D’Odorico et al. (2009). . . . .	117
4.12	$\Omega_{\text{CIV}}$ evolution with redshift, calculated considering the absorption lines in 1000 lines-of-sight through each box, for the different simulation boxes. The overplotted black diamonds show the observational data of D’Odorico et al. (2009). . . . .	118

4.13	$\Omega_{\text{CIV}}$ evolution with redshift, calculated considering all the CIV content inside each box, for the different simulation boxes. The overplotted black diamonds show the observational data of D’Odorico et al. (2009). . . . .	119
4.14	$b_{\text{CIV}}$ probability distribution function at $z = 3$ . <i>Left panel:</i> part I. <i>Right panel:</i> part II. In both panels, data from D’Odorico et al. (2009) are showed by the purple solid line. . . . .	121
4.15	$b_{\text{CIV}}$ probability distribution function at $z = 2.25$ . <i>Left panel:</i> part I. <i>Right panel:</i> part II. In both panels, data from D’Odorico et al. (2009) are showed by the purple solid line. . . . .	122
4.16	$b_{\text{CIV}}$ probability distribution function at $z = 1.5$ . <i>Left panel:</i> part I. Run <i>S1</i> (pre-enriched) is not present here because this simulation was stopped at $z_f = 1.8$ . <i>Right panel:</i> part II. In both panels, data from D’Odorico et al. (2009) are showed by the purple solid line. . . . .	122
4.17	$b_{\text{CIV}} - N_{\text{CIV}}$ relation at $z = 3$ . The overplotted purple diamonds in upper left panel show the observational data of D’Odorico et al. (2009). . . . .	123
4.18	$b_{\text{CIV}} - N_{\text{CIV}}$ relation at $z = 2.25$ . The overplotted purple diamonds in upper left panel show the observational data of D’Odorico et al. (2009). . . . .	124
4.19	$b_{\text{CIV}} - N_{\text{CIV}}$ relation at $z = 1.5$ . The overplotted purple diamonds in upper left panel show the observational data of D’Odorico et al. (2009). Run <i>S1</i> (pre-enriched, stopped at $z_f = 1.8$ ) is substituted in the upper left panel with run <i>B3</i> (coupled energy-driven winds). . . . .	125
A.1	Four representative cosmological parameters that have improved significantly using WMAP five-year data along with the Baryonic Acoustic Oscillations (BAO) and Supernovae (SN) data. The contours show the 68% and 95% confidence levels. The WMAP-only constraint is shown in blue, while WMAP+BAO+SN in red. <i>Left panel:</i> $\sigma_8 - \Omega_{0\text{m}} h^2$ constraint. <i>Right panel:</i> $\Omega_{0\Lambda} - H_0$ constraint. From Komatsu et al. (2009). . . . .	142



# Bibliography

- [1] Abel T., Bryan G. L., Norman M. L., 2002, *Sci*, 295, 93
- [2] Adelberger K. L., et al., 2005, *ApJ*, 629, 636
- [3] Aguirre A., Dow-Hygelund C., Schaye J., Theuns T., 2008, *ApJ*, 689, 851
- [4] Allende Prieto C., Lambert D. L., Asplund M., 2001, *ApJ*, 556, L63
- [5] Allende Prieto C., Lambert D. L., Asplund M., 2002, *ApJ*, 573, L137
- [6] Arimoto N. & Yoshii Y., 1987, *A&A*, 173, 23
- [7] Asplund M., 2003, *ArXiv Astrophysics e-prints*, astro-ph/0302409v1
- [8] Asplund M., Grevesse N., Sauval A. J., 2005, *ASPC*, 336, 25
- [9] Atwood B., Baldwin J. A., Carswell R. F., 1985, *ApJ*, 292, 58
- [10] Bahcall J. N. & Salpeter E. E., 1965, *ApJ*, 142, 1677
- [11] Bahcall J. N., Greenstein J. L., Sargent W. L. W., 1968, *ApJ*, 153, 689
- [12] Balsara D. S., 1995, *JCoPh*, 121, 357
- [13] Barnes L. A., Haehnelt M. G., 2009, *MNRAS*, 397, 511
- [14] Baron E., Carswell R. F., Hogan C. J., Weymann R. J., 1989, *ApJ*, 337, 609
- [15] Bate M. R. & Bonnell I. A., 2005, *MNRAS*, 356, 1201
- [16] Becker G. D., Rauch M., Sargent W. L. W., 2009, *ApJ*, 698, 1010
- [17] Bergeron J., et al., 2004, *Msngr*, 118, 40
- [18] Bertone S., et al., 2009, *ArXiv Astrophysics e-prints*, astro-ph/0910.5723v1
- [19] Bi H. & Davidsen A. F., 1997, *ApJ*, 479, 523
- [20] Bianchi S., Cristiani S., Kim T.-S., 2001, *A&A*, 376, 1
- [21] Black J. H., 1981, *MNRAS*, 197, 553
- [22] Boksenberg A., Sargent W. L. W., Rauch M., 2003, *ArXiv Astrophysics e-prints*, astro-ph/0307557v1

- [23] Bolton J. S., Haehnelt M. G., Viel M., Springel V., 2005, MNRAS, 357, 1178
- [24] Bolton J. S. & Haehnelt M. G., 2007, MNRAS, 374, 493
- [25] Bolton J. S., Viel M., Kim T.-S., Haehnelt M. G., Carswell R. F., 2008, MNRAS, 386, 1131
- [26] Bolton J. S., Oh S. P., Furlanetto S. R., 2009, MNRAS, 396, 2405
- [27] Bond J. R., Szalay A. S., Silk J., 1988, ApJ, 324, 627
- [28] Bondi H., 1952, MNRAS, 112, 195
- [29] Bunker A., et al., 2006, NewAR, 50, 94
- [30] Calura F., Matteucci F., Vladilo G., 2003, MNRAS, 340, 59
- [31] Carswell R. F., Morton D. C., Smith M. G., Stockton A. N., Turnshek D. A., Weymann R. J., 1984, ApJ, 278, 486
- [32] Carswell R. F., Webb J. K., Baldwin J. A., Atwood B., 1987, ApJ, 319, 709
- [33] Carswell R. F., Lanzetta K. M., Parnell H. C., Webb J. K., 1991, ApJ, 371, 36
- [34] Cen R., 1992, ApJS, 78, 341
- [35] Chen H.-W. & Lanzetta K. M., 2003, ApJ, 597, 706
- [36] Chiappini C., Matteucci F., Padoan P., 2000, ApJ, 528, 711
- [37] Christensen L., et al., 2007, A&A, 468, 587
- [38] Ciardi B. & Ferrara A., 2005, SSRv, 116, 625
- [39] Coles P. & Jones B., 1991, MNRAS, 248, 1
- [40] Coles P. & Lucchin F., *Cosmology (The Origin and Evolution of Cosmic Structure)*, Second Edition, John Wiley & Sons, Chichester, 2003
- [41] Cooksey K. L., Thom C., Prochaska J. X., Chen H.-W., 2010, ApJ, 708, 868
- [42] Cowie L. L. & Songaila A., 1998, Nature, 394, 44
- [43] Cristiani S., Giallongo E., Buson L. M., Gouiffes C., La Franca F., 1993, A&A, 268, 86
- [44] Croft R. A. C., Weinberg D. H., Katz N., Hernquist L., 1998, ApJ, 495, 44
- [45] Croft R. A. C., et al., 2002, ApJ, 581, 20
- [46] Danforth C. W. & Shull J. M., 2008, ApJ, 679, 194
- [47] Davé R. & Tripp T. M., 2001, ApJ, 553, 528
- [48] Dekker H., D'Odorico S., Kaufer A., Delabre B., Kotzlowski H., 2000, SPIE, 4008, 534
- [49] Dessauges-Zavadsky M., Prochaska J. X., D'Odorico S., Calura F., Matteucci F., 2006, A&A, 445, 93

- [50] Di Matteo T., Springel V., Hernquist L., 2005, *Nature*, 433, 604
- [51] Di Matteo T., Colberg J., Springel V., Hernquist L., Sijacki D., 2008, *ApJ*, 676, 33
- [52] D’Odorico V., et al., 2008, *MNRAS*, 389, 1727
- [53] D’Odorico V., Calura F., Cristiani S., Viel M., 2009, *ArXiv Astrophysics e-prints*, astro-ph/0910.2126v1
- [54] Einstein A., 1917, *SPAW*, 142
- [55] Evrard A. E., et al., 2008, *ApJ*, 672, 122
- [56] Fabjan D., et al., 2009, *ArXiv Astrophysics e-prints*, astro-ph/0909.0664v1
- [57] Fang L. Z., Bi H. G., Xiang S. P., Börner G., 1993, *ApJ*, 413, 477
- [58] Fang T., Marshall H. L., Lee J. C., Davis D. S., Canizares C. R., 2002, *ApJ*, 572, L127
- [59] Fang T., Canizares C. R., Yao Y., 2007, *ApJ*, 670, 992
- [60] Faucher-Giguère C.-A., Lidz A., Hernquist L., Zaldarriaga M., 2008, *ApJ*, 688, 85
- [61] Fechner C. & Reimers D., 2007, *A&A*, 463, 69
- [62] Ferland G. J., et al., 1998, *PASP*, 110, 761
- [63] Fontana A. & Ballester P., 1995, *Msngr*, 80, 37
- [64] Fransson C. & Epstein R., 1982, *MNRAS*, 198, 1127
- [65] Fry J. N., 1994, *PhRvL*, 73, 215
- [66] Fynbo J. U., Møller P., Warren S. J., 1999, *MNRAS*, 305, 849
- [67] Gardner J. P., Katz N., Weinberg D. H., Hernquist L., 1997, *ApJ*, 486, 42
- [68] Gardner J. P., Katz N., Hernquist L., Weinberg D. H., 2001, *ApJ*, 559, 131
- [69] Giallongo E., Cristiani S., Fontana A., Trevese D., 1993, *ApJ*, 416, 137
- [70] Gingold R. A. & Monaghan J. J., 1977, *MNRAS*, 181, 375
- [71] Gnedin N. Y. & Hui L., 1998, *MNRAS*, 296, 44
- [72] Gnedin N. Y., Tassis K., Kravtsov A. V., 2009, *ApJ*, 697, 55
- [73] Greggio L. & Renzini A., 1983, *A&A*, 118, 217
- [74] Grevesse N. & Sauval A. J., 1998, *SSRv*, 85, 161
- [75] Gunn J. E. & Peterson B. A., 1965, *ApJ*, 142, 1633
- [76] Haardt F. & Madau P., 1996, *ApJ*, 461, 20
- [77] Haehnelt M. G., Steinmetz M., Rauch M., 1998, *ApJ*, 495, 647

- [78] Hernquist L., Hut P., Makino J., 1993, ApJ, 402, L85
- [79] Hinshaw G., et al., 2009, ApJS, 180, 225
- [80] Holweger H., 2001, AIPC, 598, 23
- [81] Hu E. M., Kim T.-S., Cowie L. L., Songaila A., Rauch M., 1995, AJ, 110, 1526
- [82] Hubble E., 1929, PNAS, 15, 168
- [83] Hui L. & Gnedin N. Y., 1997, MNRAS, 292, 27
- [84] Iapichino L., Adamek J., Schmidt W., Niemeyer J. C., 2008, MNRAS, 388, 1079
- [85] Ikeuchi S., 1986, Ap&SS, 118, 509
- [86] Ikeuchi S. & Ostriker J. P., 1986, ApJ, 310, 522
- [87] Janknecht E., Reimers D., Lopez S., Tytler D., 2006, A&A, 458, 427
- [88] Katz N., Weinberg D. H., Hernquist L., Miralda-Escudé J., 1996, ApJ, 457, L57
- [89] Katz N., Weinberg D. H., Hernquist L., 1996b, ApJS, 105, 19
- [90] Kay S. T., Pearce F. R., Frenk C. S., Jenkins A., 2002, MNRAS, 330, 113
- [91] Kennicutt R. C. Jr., 1998, ApJ, 498, 541
- [92] Kim T.-S., Hu E. M., Cowie L. L., Songaila A., 1997, AJ, 114, 1
- [93] Kim T.-S., Carswell R. F., Cristiani S., D'Odorico S., Giallongo E., 2002, MNRAS, 335, 555
- [94] Kim T.-S., Bolton J. S., Viel M., Haehnelt M. G., Carswell R. F., 2007, MNRAS, 382, 1657
- [95] Kirkman D. & Tytler D., 1997, ApJ, 484, 672
- [96] Kirkman D., Tytler D., Burles S., Lubin D., O'Meara J. M., 2000, ApJ, 529, 655
- [97] Komatsu E., et al., 2009, ApJS, 180, 330
- [98] Kravtsov A. V., Klypin A., Hoffman Y., 2002, ApJ, 571, 563
- [99] Kroupa P., 2001, MNRAS, 322, 231
- [100] Kulkarni V. P., et al., 2007, ApJ, 661, 88
- [101] Larson R. B., 1998, MNRAS, 301, 569
- [102] Ledoux C., Petitjean P., Fynbo J. P. U., Møller P., Srianand R., 2006, A&A, 457, 71
- [103] Lesgourgues J., Viel M., Haehnelt M. G., Massey R., 2007, JCAP, 11, 008
- [104] Lodders K., 2003, ApJ, 591, 1220
- [105] Lu L., Sargent W. L. W., Womble D. S., Takada-Hidai M., 1996, ApJ, 472, 509
- [106] Lu. L., Sargent W. L. W., Barlow T. A., Churchill C. W., Vogt S. S., 1996b, ApJS, 107, 475

- [107] Lu L., Sargent W. L. W., Barlow T. A., Rauch M., 1998, ArXiv Astrophysics e-prints, astro-ph/9802189v1
- [108] Lucy L. B., 1977, AJ, 82, 1013
- [109] Maiolino R., et al., 2008, A&A, 488, 463
- [110] Maller A. H., Prochaska J. X., Somerville R. S., Primack J. R., 2001, MNRAS, 326, 1475
- [111] Mandelbaum R., McDonald P., Seljak U., Cen R., 2003, MNRAS, 344, 776
- [112] Martin C. L., 2005, ApJ, 621, 227
- [113] Mather J.C., et al., 1994, ApJ, 420, 439
- [114] Matteucci F., *The Chemical Evolution of the Galaxy*, Astrophysics and Space Science Library Volume 253, reprint Kluwer Academic Publishers, Dordrecht, 2003
- [115] Matteucci F. & Greggio L., 1986, A&A, 154, 279
- [116] Matteucci F. & Gibson B. K., 1995, A&A, 304, 11
- [117] Matteucci F., Molaro P., Vladilo G., 1997, A&A, 321, 45
- [118] Matteucci F. & Recchi S., 2001, ApJ, 558, 351
- [119] McDonald P. & Miralda-Escudé J., 2001, ApJ, 549, L11
- [120] McGill C., 1990, MNRAS, 242, 544
- [121] McQuinn M., et al., 2009, ApJ, 694, 842
- [122] Meiksin A., 1994, ApJ, 431, 109
- [123] Meiksin A., 2009, RvMP, 81, 1405
- [124] Meiksin A. & Madau P., 1993, ApJ, 412, 34
- [125] Meiksin A., Bryan G., Machacek M., 2001, MNRAS, 327, 296
- [126] Miralda-Escudé J. & Rees M. J., 1993, MNRAS, 260, 617
- [127] Mo H. J. & Miralda-Escudé J., 1996, ApJ, 469, 589
- [128] Monaghan J. J., 1992, ARA&A, 30, 543
- [129] Monaghan J. J., 1997, JCoPh, 136, 298
- [130] Monaghan J. J. & Gingold R. A., 1983, JCoPh, 52, 374
- [131] Monaghan J. J. & Lattanzio J. C., 1985, A&A, 149, 135
- [132] Morris S. L. & van den Bergh S., 1994, ApJ, 427, 696
- [133] Motl P. M., Burns J. O., Loken C., Norman M. L., Bryan G., 2004, ApJ, 606, 635
- [134] Murray N., Quataert E., Thompson T. A., 2005, ApJ, 618, 569

- [135] Nagamine K., Springel V., Hernquist L., 2004, MNRAS, 348, 435
- [136] Nagamine K., Wolfe A. M., Hernquist L., Springel V., 2007, ApJ, 660, 945
- [137] Navarro J. F. & White S. D. M., 1993, MNRAS, 265, 271
- [138] Okoshi K. & Nagashima M., 2005, ApJ, 623, 99
- [139] Olive K. A. & Skillman E. D., 2004, ApJ, 617, 290
- [140] O'Meara J. M., et al., 2001, ApJ, 552, 718
- [141] Oppenheimer B. D. & Davé R., 2006, MNRAS, 373, 1265
- [142] Oppenheimer B. D. & Davé R., 2008, MNRAS, 387, 577
- [143] Padovani P. & Matteucci F., 1993, ApJ, 416, 26
- [144] Peacock J.A., *Cosmological Physics*, Fifth Reprint, Cambridge University Press, Cambridge, 2003
- [145] Peebles P. J. E., 1974, ApJ, 392, 15
- [146] Peebles P. J. E., *The large scale structure of the Universe*, Princeton, NJ: Princeton University Press, 1980
- [147] Peebles P. J. E., 1981, ApJ, 248, 885
- [148] Peebles P. J. E., *Principles of physical cosmology*, Princeton Series in Physics, Princeton, NJ: Princeton University Press, 1993
- [149] Penton S. V., Shull J. M., Stocke J. T., 2000, ApJ, 544, 150
- [150] Penton S. V., Stocke J. T., Shull J. M., 2004, ApJS, 152, 29
- [151] Péroux C., McMahon R. G., Storré-Lombardi L. J., Irwin M. J., 2003, MNRAS, 346, 1103
- [152] Péroux C., Dessauges-Zavadsky M., D'Odorico S., Kim T.-S., McMahon R. G., 2005, MNRAS, 363, 479
- [153] Petitjean P., Webb J. K., Rauch M., Carswell R. F., Lanzetta K. M., 1993, MNRAS, 262, 499
- [154] Pettini M., et al., 2003, ApJ, 594, 695
- [155] Pierleoni M., Branchini E., Viel M., 2008, MNRAS, 388, 282
- [156] Pontzen A., et al., 2008, MNRAS, 390, 1349
- [157] Prochaska J. X. & Wolfe A. M., 1997, ApJ, 487, 73
- [158] Prochaska J. X., et al., 2001, ApJS, 137, 21
- [159] Prochaska J. X., Castro S., Djorgovski S. G., 2003, ApJS, 148, 317
- [160] Prochaska J. X., Herbert-Fort S., Wolfe A. M., 2005, ApJ, 635, 123

- [161] Prochaska J. X., Chen H.-W., Wolfe A. M., Dessauges-Zavadsky M., Bloom J. S., 2008, *ApJ*, 672, 59
- [162] Prochaska J. X. & Wolfe A. M., 2009, *ApJ*, 696, 1543
- [163] Rao S. M. & Turnshek D. A., 2000, *ApJS*, 130, 1
- [164] Rauch M. 1998, *ARA&A*, 36, 267
- [165] Rauch M., et al., 1992, *ApJ*, 390, 387
- [166] Rauch M., Carswell R. F., Webb J. K., Weymann R. J., 1993, *MNRAS*, 260, 589
- [167] Rauch M., Sargent W. L. W., Womble D. S., Barlow T. A., 1996, *ApJ*, 467, L5
- [168] Rauch M., Haehnelt M. G., Steinmetz M., 1997, *ApJ*, 481, 601
- [169] Rauch M., et al., 2005, *ApJ*, 632, 58
- [170] Rauch M., et al., 2008, *ApJ*, 681, 856
- [171] Rees M. J., 1986, *MNRAS*, 218, 25P
- [172] Refregier A. & Teyssier R., 2002, *PhRvD*, 66, 043002
- [173] Ricotti M., Gnedin N. Y., Shull J. M., 2000, *ApJ*, 534, 41
- [174] Romano D., Chiappini C., Matteucci F., Tosi M., 2005, *A&A*, 430, 491
- [175] Rupke D. S., Veilleux S., Sanders D. B., 2005, *ApJS*, 160, 115
- [176] Ryan-Weber E. V., Pettini M., Madau P., 2006, *MNRAS*, 371, L78
- [177] Ryan-Weber E. V., Pettini M., Madau P., Zych B. J., 2009, *MNRAS*, 395, 1476
- [178] Saitta F., et al., 2008, *MNRAS*, 385, 519
- [179] Salpeter E. E., 1955, *ApJ*, 121, 161
- [180] Salpeter E. E., 1993, *AJ*, 106, 1265
- [181] Sarazin C. L. & Bahcall J. N., 1977, *ApJS*, 34, 451
- [182] Sargent W. L. W., Young P. J., Boksenberg A., Tytler D., 1980, *ApJS*, 42, 41
- [183] Scalo J. M., 1986, *FCPh*, 11, 1
- [184] Scannapieco E., et al., 2006, *MNRAS*, 365, 615
- [185] Scannapieco E. & Brügggen M., 2008, *ApJ*, 686, 927
- [186] Schaerer D., 2003, *A&A*, 397, 527
- [187] Schaye J., 2001, *ApJ*, 559, 507
- [188] Schaye J., Theuns T., Rauch M., Efstathiou G., Sargent W. L. W., 2000, *MNRAS*, 318, 817

- [189] Schaye J., et al., 2003, *ApJ*, 596, 768
- [190] Schaye J., Carswell R. F., Kim T.-S., 2007, *MNRAS*, 379, 1169
- [191] Schmidt M., 1959, *ApJ*, 129, 243
- [192] Scott J., Bechtold J., Dobrzycki A., Kulkarni V. P., 2000, *ApJS*, 130, 67
- [193] Seljak U. & Zaldarriaga M., 1996, *ApJ*, 469, 437
- [194] Seljak U., Slosar A., McDonald P., 2006, *JCAP*, 10, 014
- [195] Shakura N. I. & Sunyaev R. A., 1973, *A&A*, 24, 337
- [196] Sheth R. K. & Tormen G., 1999, *MNRAS*, 308, 119
- [197] Sijacki D., Pfrommer C., Springel V., Enßlin T. A., 2008, *MNRAS*, 387, 1403
- [198] Simcoe R. A., 2006, *ApJ*, 653, 977
- [199] Simcoe R. A., Sargent W. L. W., Rauch M., 2002, *ApJ*, 578, 737
- [200] Simcoe R. A., Sargent W. L. W., Rauch M., 2004, *ApJ*, 606, 92
- [201] Smoot G. F., et al., 1992, *ApJ*, 142, 419
- [202] Songaila A., 2001, *ApJ*, 561, L153
- [203] Songaila A. & Cowie L. L., 1996, *AJ*, 112, 335
- [204] Springel V., 2005, *MNRAS*, 364, 1105
- [205] Springel V., Yoshida N., White S. D. M., 2001, *NewA*, 6, 79
- [206] Springel V. & Hernquist L., 2002, *MNRAS*, 333, 649
- [207] Springel V. & Hernquist L., 2003, *MNRAS*, 339, 289
- [208] Springel V. & Hernquist L., 2003b, *MNRAS*, 339, 312
- [209] Springel V., Di Matteo T., Hernquist L., 2005, *MNRAS*, 361, 776
- [210] Steinmetz M., 1996, *MNRAS*, 278, 1005
- [211] Stengler-Larrea E. A., et al., 1995, *ApJ*, 444, 64
- [212] Storrie-Lombardi L., McMahon R. G., Irwin M., 1996, *MNRAS*, 283, 79
- [213] Storrie-Lombardi L. J. & Wolfe A. M., 2000, *ApJ*, 543, 552
- [214] Sutherland R. S. & Dopita M. A., 1993, *ApJS*, 88, 253
- [215] Tepper-García T., 2006, *MNRAS*, 369, 2025
- [216] Tescari E., Viel M., Tornatore L., Borgani S., 2009, *MNRAS*, 397, 411
- [217] Theuns T., Leonard A., Efstathiou G., Pearce F. R., Thomas P. A., 1998, *MNRAS*, 301, 478

- [218] Theuns T., et al., 2002, *ApJ*, 578, L5
- [219] Thielemann F.-K., et al., 2003, *NuPhA*, 718, 139
- [220] Tornatore L., Borgani S., Dolag K., Matteucci F., 2007, *MNRAS*, 382, 1050
- [221] Tornatore L., Ferrara A., Schneider R., 2007b, *MNRAS*, 382, 945
- [222] Tornatore L., Borgani S., Viel M., Springel V., 2009, *ArXiv Astrophysics e-prints*, astro-ph/0911.0699v2
- [223] Tytler D., 1987, *ApJ*, 321, 49
- [224] Tytler D., 1987b, *ApJ*, 321, 69
- [225] Tytler D., et al., 1999, *AJ*, 117, 63
- [226] Valageas P., Schaeffer R., Silk J., 2002, *A&A*, 388, 741
- [227] van den Hoek L. B., Groenewegen M. A. T., 1997, *A&AS*, 123, 305
- [228] Verde L., et al., 2002, *MNRAS*, 335, 432
- [229] Viel M., et al., 2003, *MNRAS*, 341, 792
- [230] Viel M., Haehnelt M. G., Springel V., 2004, *MNRAS*, 354, 684
- [231] Viel M., et al., 2004b, *MNRAS*, 347, L26
- [232] Viel M., et al., 2005, *MNRAS*, 360, 1110
- [233] Viel M., et al., 2008, *PhRvL*, 100, 041304
- [234] Viel M., Bolton J. S., Haehnelt M. G., 2009, *MNRAS*, 399, L39
- [235] Viel M., et al., 2009b, *MNRAS*, 393, 774
- [236] Vikhlinin A., et al., 2009, *ApJ*, 692, 1060
- [237] Vladilo G. & Péroux C., 2005, *A&A*, 444, 461
- [238] Vladilo G., et al., 2006, *A&A*, 454, 151
- [239] Vladilo G., Prochaska J. X., Wolfe A. M., 2008, *A&A*, 478, 701
- [240] Wagoner R. V., 1967, *ApJ*, 149, 465
- [241] Walker T. P., Steigman G., Schramm D. N., Olive K. A., Kang H. S., 1991, *ApJ*, 376, 51
- [242] Wang B., 1993, *ApJ*, 415, 174
- [243] Wang B., 1995, *ApJ*, 444, L17
- [244] Weisheit J. C., 1978, *ApJ*, 219, 829
- [245] Weymann R. J., et al., 1998, *ApJ*, 506, 1

- [246] Williams R. J., Mathur S., Nicastro F., Elvis M., 2007, ApJ, 665, 247
- [247] Wolfe A. M., Turnshek D. A., Smith H. E., Cohen R. D., 1986, ApJS, 61, 249
- [248] Wolfe A. M., Lanzetta K. M., Foltz C. B., Chaffee F. H., 1995, ApJ, 454, 698
- [249] Wolfe A. M., Gawiser E., Prochaska J. X., 2005, ARA&A, 43, 861
- [250] Wolfe A. M. & Chen H.-W., 2006, ApJ, 652, 981
- [251] Wolfe A. M., Prochaska J. X., Jorgenson R. A., Rafelski M., 2008, ApJ, 681, 881
- [252] Wolfire M. G., McKee C. F., Hollenbach D., Tielens A. G. G. M., 2003, ApJ, 587, 278
- [253] Woosley S. E. & Weaver T. A., 1995, ApJS, 101, 181
- [254] York D. G., Green R. F., Bechtold J., Chaffee F. H. Jr., 1984, ApJ, 280, L1
- [255] York D. G., Dopita M., Green R., Bechtold J., 1986, ApJ, 311, 610
- [256] Zaldarriaga M., Seljak U., Hui L., 2001, ApJ, 551, 48
- [257] Zel'dovich Y. B., 1970, A&A, 5, 84
- [258] Zhang Y., Anninos P., Norman M. L., Meiksin A., 1997, ApJ, 485, 496
- [259] Zheng W., et al., 2004, ApJ, 605, 631
- [260] Zwaan M., et al., 2008, AJ, 136, 2886

Tuned half step down

Rhy. Fig. 1:

G	C
-3---3-----3-----3-----	-----3---3---3-----
-0-----0-----0-----0---0-	-1-----1-----1-----1---1-
-0-----0-----0-----0---0-	-0-----0-----0-----0---0-
-0-----0-----0-----0---0-	-0h2---2-----0-----0---0-
-2-----0-----0-----0---0-	-----3-----0-----0---0-
-3-----0-----0-----0---0-	-----0-----0-----0---0-

Fadd9	C	G
-----3-----0-----0---0-	-----3-----0-----0---0-	-3---3-----0-----0---0-
-1---1---1---1---1---1---1---0-	-0---0---0---0---0---0---0---0-	-0---0---0---0h2---0---0---0-
-0h2-----2---0-----0---0-	-0h2-----0h2-----0h2---0-	-0h2-----0h2-----0h2---0-
-0h3-----0h2-----0h2---0-	-----3-----0-----0---0-	-2-----0-----0---0-
-----0-----0-----0---0-	-----0-----0-----0---0-	-3-----0-----0---0-